The effects of soil macroporosity on the hydrology of infrastructure slopes

Muddle, David

Award date:
2018

Awarding institution:
University of Bath

The effects of soil macroporosity on the hydrology of infrastructure slopes

David Edward Muddle

A thesis submitted for the degree of Doctor of Philosophy

University of Bath

Department of Architecture and Civil Engineering

July 2017

COPYRIGHT

Abstract

In order for infrastructure owners to be able to properly assess the risk of slope failures within their network of assets it is essential that the hydrological processes within slopes can be accurately modelled. Hydrological modelling is, in turn, dependent on a fundamental understanding of soil physics and flow at the soil structure scale.

It is well known that flow within soils is strongly related to a soil's physical structure and pore space architecture and is therefore affected by the presence and interconnectivity of macropores. However, macropore influence on governing flow has traditionally been hard to define within laboratory experiments, particularly on representative and undisturbed samples. Additionally, quantitative descriptions of the dynamic nature of soil pore architecture and the effects of saturation on altering internal pore networks have proven elusive.

This thesis uses detailed numerical modelling of a case study infrastructure slope in conjunction with field data to assess the key influences on flow within infrastructure slopes. The results of this investigation reinforce the importance of determining how the hydraulic conductivity of clay soils varies with depth and with saturation, in order to be able to correctly model the hydrological response of earthworks to climate conditions. Determining the extent to which pore structure and connectivity influence hydraulic conductivity and the evolution of this pore architecture with changes in saturation and depth is therefore of great importance.

This thesis builds on recent developments in X-ray computed tomography (CT) in order to progress the technique as a means of visualising and quantifying macropore characteristics in a non-intrusive manner. A microCT scanning technique which allows for the scanning of large undisturbed clay fill samples is developed, as well as an image analysis procedure that allows for the quantification of internal macropore architecture. It is shown that 100 mm diameter clay cores are at the limit of microCT capabilities as a result of achievable spatial resolution and phase contrast. The use of subsampling and image improvement techniques allows for the pores above 63 microns in size present within the samples to be visualized and quantified.

A further novel development within this thesis is the assessment of the evolution of the internal macropore structure of undisturbed clay fill samples with saturation. Scans were conducted on 100 mm diameter clay fill samples at different states of saturation at microCT

resolution for the first time. It was found that the saturation procedure reduced overall measured total macroporosity as well as the number of macropores within the samples. Additionally, the saturation procedure was observed to decrease the size of largest macropores within the samples and to make the samples more uniform in structure throughout their height.

MicroCT determined macropore property metrics of the clay fill samples were compared to saturated hydraulic conductivity tests of the samples. Saturated hydraulic conductivity was found to correlate strongly with microCT derived mean macropore length, which represents the connectivity of the macropores within the samples. The results also indicate that the length of the macropores within a sample has more influence on the saturated hydraulic conductivity than the quantity of macropores (total macroporosity).

Acknowledgements

I would like to thank my supervisor Dr Kevin Briggs, whose support, guidance, and encouragement throughout the PhD experience, both academically and otherwise, have been invaluable. I am grateful to the EPSRC and the University of Bath Alumni Fund for funding this research, as well as the British Geological Survey for providing samples and data. I would like to thank all those within iSMART whose collaboration and willingness to share data and knowledge have been remarkable. I wish to thank the technicians within the University's Civil and Mechanical Engineering labs for their help with experimental work, particularly, David Surgenor and Clare Ball.

I would also like to thank all those new friends I have made at conferences throughout my studies for inspiring me and expanding my knowledge, and all those with whom I have shared an office over the past four years, for the many fun experiences and the new cultural traditions I have learnt along the way.

Finally, I wish to thank my parents Andrew and Susan for their support and Caroline for being the best teammate that I could ask for.

Contents

List of figures

List of tables

1 Introduction

The failure of infrastructure slopes poses a risk to the safety of transport users and can lead to delays, economic losses for industry, and the need for expensive remediation (Glendinning et al., 2014). The disruption caused by slope failures is exacerbated by the fact that the UK's transport infrastructure is one of the most heavily used in the world, often relying on old and poorly constructed earthworks (Briggs et al., 2017). Indeed, it is estimated that two-thirds of the transport network is supported by, or adjacent to, engineered slopes such as embankments and cuttings (Perry et al., 2003). Many of these slopes suffer from age-related deterioration and were constructed to standards considerably different to those used today and, as a result, suffer from high incidents of instability, which are becoming increasingly frequent (Loveridge et al., 2010). Although maintenance of such infrastructure is costly, the benefits of proactive works far outweigh the costs of remedial works after failure (Glendinning et al., 2015). Therefore, research which enables asset managers to better prioritise maintenance and investments is needed in order to help improve the resilience of the country's transport network. Such advancements require an upgrading of the knowledge surrounding slope hydrology, instability, and modelling capability (Dijkstra et al., 2014).

The hydrology of slopes is key to their structural behaviour. Infiltration into a slope can reduce the negative pore water pressures (suctions) present within the soil which contribute to stabilising the slope. This can lead to a reduction in strength which may, in turn, result in failure (Fredlund et al., 2012). Cycles of pore water pressure and effective stress change have also been shown to lead to progressive failure of infrastructure slopes over several years (e.g. Potts et al., 1997). However, there are many potential causes of failure and many factors that influence the water flow within slopes and their response to climate, some of which we have a limited understanding of.

To realise the development of a fundamental understanding of material and system behaviour it is necessary to integrate research across a range of spatial scales, including studies of soil fabric, whole slope modelling, and upscaling to transport networks (Glendinning et al., 2015). This involves an improved comprehension of flow within soils (particularly clay fills) and system behaviour at a slope scale.

An enhanced understanding of the physical processes involved within slope systems and identification of key soil parameters from field and laboratory tests is required to facilitate

the development of robust models capable of predicting slope response to current and future climate conditions (Dijkstra and Dixon, 2010).

One of the most important and lesser understood elements within slope systems that affects the flow of water is the role of macroporosity. Macropores are large pores created as a result of many processes, including soil fauna, decay of plant roots, wetting and drying cycles, freeze–thaw cycles, or the erosive action of subsurface flow (Beven and Germann, 1982).

Flow within soils is strongly dependent on a soil's physical structure and pore space architecture and is therefore affected by the presence and interconnectivity of macropores (Beven and Germann, 2013). Macropores can result in non-equilibrium, or preferential, flow which does not obey the Darcy-Richard's equations of flow on which the majority of saturated and unsaturated hydrological modelling is based (Jarvis, 2007). However, the influence of macropores is hard to define accurately because it is difficult to measure in a non-destructive manner (Weiler, 2017). Moreover, quantitative descriptions of the dynamic nature of soil pore architecture (i.e. macropore networks) and the evolution of internal pore structure with changes in saturation are still lacking.

Recently, X-ray computed tomography has developed as a means for non-destructive observation and analysis of the internal pore space architecture of soil samples in three dimensions (Cnudde and Boone, 2013). This technique allows high resolution imaging of soil structure and macropore networks. The imaging data can then be used to provide quantitative estimates of many properties associated with the pore architecture including macroporosity and pore connectivity (Helliwell et al., 2013). It therefore offers the potential to link soil structure and pore architecture to flow and hydraulic conductivity, and to improve our understanding of flow within soils.

This thesis uses detailed numerical modelling of a case study infrastructure slope in conjunction with field data to assess the assumptions regarding soil heterogeneity in the model and the key influences on flow within infrastructure slopes. Using a field representative model and sensitivity analysis, the influence of anisotropy of hydraulic conductivity, unsaturated soil behaviour characteristics, and hydraulic conductivity variation at the surface and at depth within the model are explored. This process informs the direction of the laboratory work carried out to subsequently understand the complex role of macropores.

Although quantitative measures of macropore networks calculated from X-ray tomography images can provide useful information on soil structure, they are dependent on the sample size, scanning procedure, image quality, and image processing methods used (Wildenschild and Sheppard, 2013).

This thesis develops a microCT scanning and analysis procedure to investigate the use of computed tomography as a means to visualise and quantify macropore networks in large (100 mm) and relatively undisturbed clay fill cores from an embankment for the first time.

In a further novel development, clay fill cores of this size were scanned repeatedly at different water contents using the non-destructive nature of the microCT technique to investigate the evolution of macropore structure with increases in saturation.

The work undertaken also explores variation in macroporosity with depth throughout the embankment and examines the influence of macropores on the saturated hydraulic conductivity of the samples using triaxial and oedometer permeability tests. The pore property metrics (total macroporosity, macropore density, mean macropore length, macropore surface area density, and mean volume of the largest pores) derived from the microCT image data which have the strongest relationship to saturated hydraulic conductivity are investigated.

1.1 Thesis aim

The fundamental ambition of the work presented here is to help to progress research within this field towards achieving a complete picture of transient water movement within infrastructure slopes, based on a fundamental understanding of earthwork material and systems behaviour. Such an understanding could subsequently be used to create a more robust, resilient, and cost-effective transport network.

1.2 Overall methodology

To achieve the stated aim, the work presented within this thesis comprises several individual studies, at varying scales, to identify the key unknowns and to research methods which can further our knowledge of these aspects.

Chronologically, the first of these investigations was a large-scale study of slope failures within the UK using the British Geological Survey landslide database in conjunction with climate data (see Appendix). During the course of this study it became apparent that site-specific heterogeneity in terms of soil structure, composition, and vegetation, mean that in order to achieve improved network-scale assessments of risk it is first necessary to explore modelling of site-specific cases and to examine the implications of the assumptions involved current modelling practice in terms of flow and unsaturated behaviour.

To do this, a comprehensive modelling analysis using Darcy-Richard's type flow equations was carried out on a clay cutting. This research uses clay as it comprises much of UK infrastructure (embankments and cuttings), has higher incidences of failure, and exhibits behaviour which is lesser understood than other soils. The propensity of clay earthworks for shrink-swell behaviour, desiccation cracking, and heterogeneity due to construction methods (particularly within embankments) mean that they can suffer from preferential flow.

The theory and assumptions used within the model are discussed in the literature review in Chapters 2 and 3, whilst the inputs and results of the modelling processing are explored in Chapter 5. As a result of the learning outcomes from the modelling process it was found that models which use more physically-based flow theories are needed if we want to improve our modelling capability of slope hydrology. It is essential that the effects of macropores, their structural properties, and their interaction with the soil matrix can be properly described within models. However, this has historically been difficult to achieve due to the lack of non-destructive measurement techniques.

After researching potential solutions to this problem, it was found that microCT scanning represents a new technique which could be used to provide quantitative estimations of the physical properties of macropores within samples as well as the evolution of this structure over time (Chapter 4).

To ensure that the macropore networks analysed were representative of the type of natural pore structures found within infrastructure slopes, relatively undisturbed, large clay fill samples were used for the experimental work in this thesis.

As microCT scanning of clay fill has never been done before, several problems were encountered during this research. It was necessary to make sure that processing and analysing scan data, as well as the physical scans themselves, were as consistent and repeatable as possible. Two detailed studies were conducted, firstly to determine the optimal scan procedure for such large inhomogeneous samples (Chapter 6), and secondly to determine the optimal image data analysis procedure for these samples (Chapter 7).

Having established the consistent procedures necessary to use microCT scanning to analyse large clay fill samples, this thesis finally examines the achievable results of scans of a series of different embankment samples (Chapter 8). The samples were scanned at different states of saturation which uses the repeatable nature of the technique to explore the dynamic changes within the soil macropore structure. The quantified macropore properties were also compared to hydraulic conductivity tests to take advantage of the non-destructive nature of CT and to examine the relationship between the quantity, size, and connectivity of macropores and flow. This provides a basis for improving our description of slope hydrology in the future.

1.3 Thesis objectives

The specific objectives of this work were to:

- Use a field representative slope-scale model to compare simulated pore water pressures and volumetric water contents with field measured data, in order to explore the implications of the assumptions regarding soil heterogeneity made within hydrological models.
- Use the modelling process to determine the key parameters that affect slope hydrology and pore water pressures within models. Particularly, to examine the importance of hydraulic conductivity and the unsaturated soil behaviour characteristics.
- Investigate the capabilities of microCT for geotechnical research and the non-invasive imaging of macropore networks within large clay samples, with regards to sample size and image quality. From this investigation, to devise a microCT scanning method for scanning large undisturbed clay fill samples which allows for repeated scanning of samples.
- Devise a consistent and repeatable image analysis procedure in order to quantify the macropore structure of large clay fill samples and compare results from multiple microCT scans.
- Assess the change of macroporosity and macropore properties with depth throughout an embankment (between 1.5 - 6.5 m) and to comment on the heterogeneity of the macropores using the microCT technique.
- Assess the evolution of the macropore structure within clay fill samples due to changes in saturation.
- Investigate the relationship between the internal macropore structure of clay fill (measured using microCT derived macropore property metrics) and the saturated hydraulic conductivity of samples.

1.4 Thesis structure

Firstly, in Chapter 2, this thesis gives an overview of some of the established theories describing water flow and storage within saturated and unsaturated soils which are commonly used within hydrological models.

Chapter 3 describes the processes associated with slope hydrology, hydrological triggering of failures, the influence of climate and vegetation in relation to modelling slope hydrological behaviour, and observations of the influence of macroporosity.

Chapter 4 explores the use of computed tomography within the geoscience research field for the non-invasive quantification of soil architecture.

Chapter 5 discusses the detailed hydrological modelling of a roadside clay cutting conducted to explore the uncertainties involved in slope hydrology, with particular emphasis on the influence of hydraulic conductivity and the assumptions of continuum behaviour within hydrological models.

Chapter 6 presents an investigation into the use of microCT to image large-scale clay fill samples from an embankment in order to establish microCT capabilities and scanning procedures.

Chapter 7 presents an investigation into the detailed image analysis procedure required in order to accurately quantify the macropore structure present within 100mm diameter clay fill samples.

Chapter 8 presents the results of a series of scans of clay fill samples from different depths within an embankment. The cores were scanned in partially saturated and saturated conditions using the repeatable method established in Chapters 6 and 7. The association between microCT derived pore property metrics and saturated hydraulic conductivity test results is examined to explore macropore influence on flow.

Chapter 9 provides an overall discussion which integrates the findings from the different studies within this thesis and discusses the progress made towards the aim of this work.

Finally, Chapter 10 presents the conclusions drawn from the work conducted and Chapter 11 identifies the areas of interest for future research.

2 Flow in soils

2.1 Introduction

This chapter presents an overview of some of the fundamental concepts involved in flow through saturated and unsaturated soils with a view to modelling the hydrology of slopes. Equations describing the flow of water, vapour, and heat are explored and estimations of hydraulic conductivity and soil water storage with changes in saturation are discussed. Additionally, this chapter explores the knowledge surrounding macropores and flow within them. Methods for measuring saturated hydraulic conductivity and pore size distributions are also discussed. The flow and unsaturated behaviour descriptions discussed here are the Darcy-Richard's type flow equations which are most commonly used in hydrological modelling. They are presented here so that the assumptions and uncertainties associated with the modelling later in this thesis are evident (Chapter 5).

2.2 Soil structure

In essence, a soil is comprised of soil particles and the voids in between them. When all these voids are filled with water, a soil is described as being saturated. However, if a saturated soil is allowed to dry out, water evaporates from the surface leaving some voids filled with air. In this state, a soil is described as unsaturated (or partially saturated). In the case of an unsaturated soil, the soil structure can be thought of as having three phases: soil particles, air, and water (Figure 2.1).

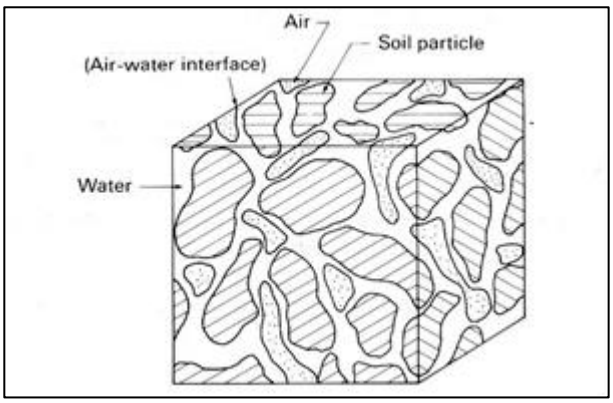

Figure 2.1 – Representation of an element of unsaturated soil with continuous air phase (Fredlund et al., 2012)

Due to the hydrological cycle, within nature there usually exists a region at a depth below the ground's surface in which the soil is completely saturated and the pore water pressure is positive. The upper surface of this region is known as the water table, although water is often

held within voids above this region at negative pressures (i.e. in the capillary fringe) (Figure 2.2).

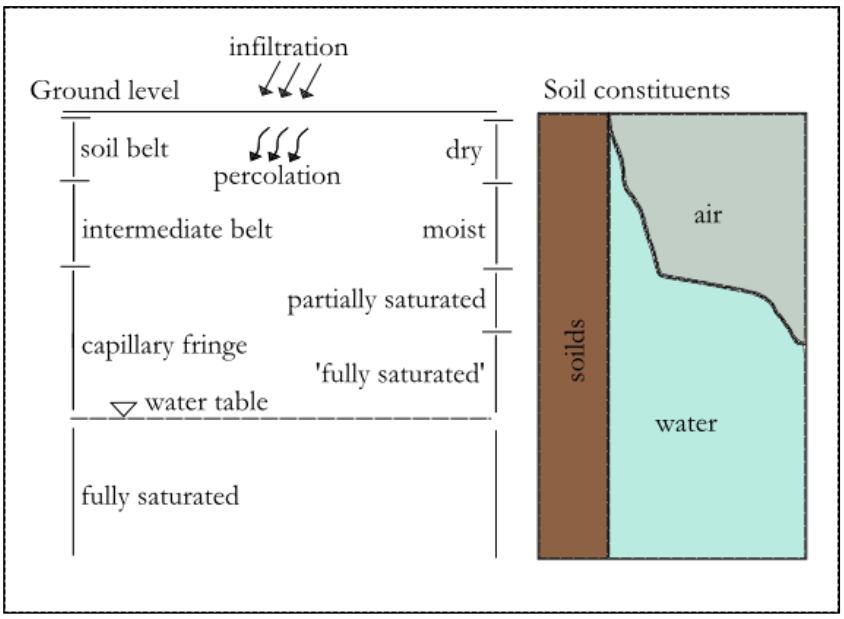

Figure 2.2 – Diagram of the zones of saturation present within the ground showing the capillary rise above the water table and the makeup of phases within the soil (Barnes, (2010))

The rate at which water passes through a soil is not directly dependent on the amount of voids present within a soil. For example the porosity (the proportion of void within a soil) of a clay is usually greater than that of a sand despite the sand having a coefficient of permeability several degrees of magnitude larger (Hillel, 1998).

Unsaturated soils display different hydrological properties than the same soils when saturated. This is because the air inside the pores interacts with infiltrating water, altering its path, and therefore the soil's hydraulic conductivity (Gens 2010). An example of the increased resistance to flow is shown in Figure 2.3.

A soil will begin to desaturate when exposed to the atmosphere at a value of negative pore water pressure (PWP) referred to as the air entry value. Once the air-entry value is exceeded, air enters the largest pores and the air-filled pores become non-conductive conduits to flow and increase the tortuosity of the flow path. As a result, the ability of the soil to transport water (the hydraulic conductivity) decreases. As the soil dries and more pores become air-filled, water will tend to retreat into the smallest pores and the hydraulic conductivity decreases further.

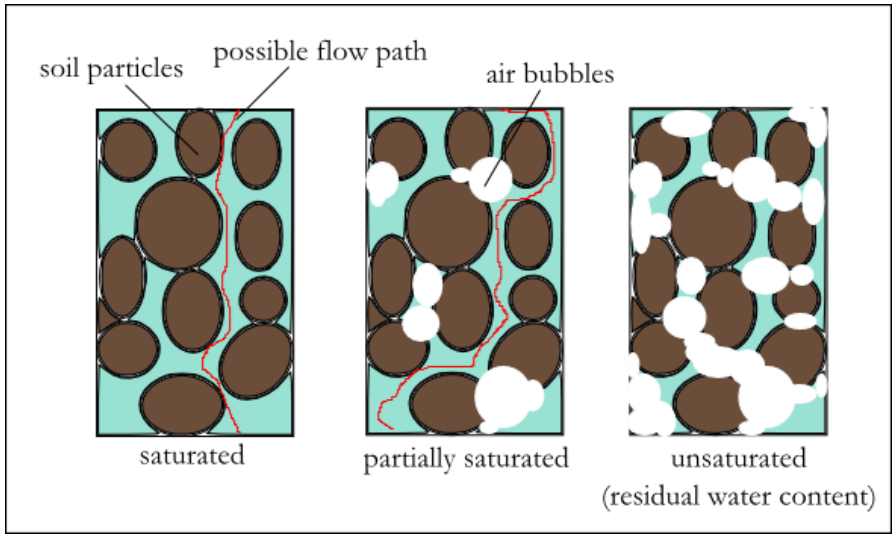

Figure 2.3 – The decrease in hydraulic conductivity due to the restriction of flow paths with desaturation

Within a partially saturated soil, water molecules move between the liquid and vapour phases with changes in heat (Wilson, 1990). It is therefore necessary to consider liquid, water vapour and heat flow through the pores when describing overall flow in unsaturated soils.

2.3 Phase relationships

The division of soil structure into three phases gives rise to a series of fundamental relationships which can be used to characterise the state of the soil. If the volume of soil, water, and air within a unit volume of soil are defined as V_s, V_w, and V_a respectively, then the water and air phases can also be combined as the volume of voids, V_v.

The following five important relationships can be defined:

1. Void ratio (e) is the ratio of the volume of voids to the volume of solids (soil particles)

$$e = \frac{V_v}{V_s} \tag{1}$$

2. Porosity (n) is the volume of voids per unit volume (total of voids and solids)

$$n = \frac{V_v}{V_s + V_v} = \frac{e}{1 + e} \tag{2}$$

3. The degree of saturation (S_r) is the ratio of the volume of water to the volume of voids. It must be a value between zero and one, a fully saturated soil having an S_r of one, whilst a completely dry soil would have an S_r of zero

$$S_r = \frac{V_w}{V_v} \tag{3}$$

4. Gravimetric water (or moisture) content (w) is the ratio of the mass of water (m_w) to the mass of solids (m_s)

$$w = \frac{m_w}{m_s} \tag{4}$$

5. Volumetric water content (θ) is the ratio of the volume of water to the total volume within an element of soil.

$$\theta = \frac{V_w}{V_t} = \frac{V_w}{V_v} \times \frac{V_v}{V_t} = S_r n = \frac{w G_s}{1 + e} \tag{5}$$

Where, G_s, the specific gravity, is the ratio of particle density to that of water

2.4 Soil suction

Within an unsaturated soil, pore water pressures exist at negative values relative to atmospheric pressure (suctions). Suction has been shown to increase the strength of soil and therefore maintain the stability of slopes (Leroueil, 2001). There are two primary constituents of soil suction, namely, matric and osmotic suction.

Matric suction arises from the interaction between liquid and solid within a soil. Specifically, from the pressures generated by the capillary menisci and the adsorption forces on particle surfaces. Matric suction therefore can be thought of as having two components, a capillary component, and an adsorptive component.

The capillary component is a result of the difference in water and air pressure caused by menisci which develop between solids due to surface tension and interface curvature (Gens, 2010). The difference in pressure generates inter-particle forces which are roughly aligned with the normal of the contact and therefore have a stabilising effect on the soil structure (Gens, 2010). The adsorptive component is a result of a combination of solid-water interactions by which soil particles acquire a layer of water molecules on their surface. These

include electrostatic and van der Waals forces, hydrogen bonding and surface-dipole attraction (Gili and Alonso, 2002)

The relative importance of each component depends on the type of soil and the magnitude of suctions. Some research has shown that the adsorptive component will tend to predominate in fine-grained soils (Nitao and Bear, 1996). However, due to the intricate nature of the soil pore space architecture, matric suction has to be evaluated experimentally, and the distinction between the two components is largely conceptual. It is therefore possible to express matric suction as the difference between atmospheric and water pressures (u_a-u_w).

Osmotic suction results from the effects of a semi-permeable membrane. If one solution has a higher concentration of solute than another on either side of a membrane then a hydrostatic pressure will be created due to diffusion. Due to their small pore sizes, clay soils may, in some cases, exhibit these type of membrane properties (Gens, 2010). Matric suction is usually considered the most important component of suction within soils.

2.5 The capillary fringe

The region immediately above a water table is known as the capillary zone or fringe (Figure 2.2). In this region the soil may still be completely saturated as water is held within the voids due to surface tension (Aubertin et al., 2003). In the capillary zone, soil voids can sustain a negative pore water pressure without drawing in air. Above this region the water will start to recede and air will enter some of the pore space. At greater height above the water table only the finer capillaries can sustain water and the soil may be dry or the degree of saturation governed largely by surface effects (see Chapter 3).

The height of the capillary fringe is related to the soil particle size. A finer-grained soil with more intricate pore space architecture will have a larger capillary zone than other soils (e.g. granular soils). This is because the air entry value is found to increase as the pore size of the soil decreases (Powrie, 2013). As a consequence of this, fine soils (silts and clays) may remain saturated several meters above the water table, with pore water pressures continuing to decrease until the air entry value is reached. If the groundwater is at rest, the pore water pressure will decrease approximately hydrostatically with height above the water table (Figure 2.4). However, in reality this is not a static condition. Flow through the capillary fringe and unsaturated zones may take place by infiltration and percolation of rainwater through the soil, changing PWPs. Evaporation and transpiration may also occur from the near-surface, altering PWPs in the unsaturated zone.

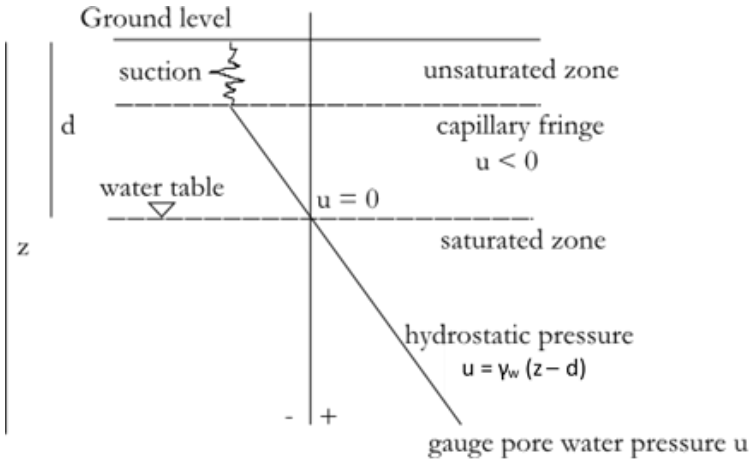

Figure 2.4 – Pore water pressures in a fine soil above the water table (the suction shown in the unsaturated zone indicates uncertainty rather than actual values) (Powrie, 2013)

2.6 Effective stress

A fundamental concept in soil mechanics is that of effective stress (Equation (6)) (Terzaghi, 1925). The effective stress represents the component of the total normal stress taken by the soil skeleton and controls the volumetric and strength behaviour of a soil.

$$\sigma' = \sigma - u \tag{6}$$

Where, σ' is the effective stress, σ is the total stress, and u is the gauge pore water pressure

Above the water table, effective stresses are enhanced and can increase the stability of partially saturated soils (Bishop, 1960).

2.7 Water flow in soils

Water flow in soils is driven by differences in hydraulic head, which consist of pressure head, elevation head, and velocity head. Since the velocity of flow through soils is very low, velocity head is usually ignored (Smith, 2014). Therefore flow in soils is governed by differences in soil water pressure and elevation.

2.7.1 Equations describing flow

The flow of water in saturated soil is commonly calculated using Darcy's law (Equation (7)). Darcy's law states that the rate of water flow through a soil mass is proportional to the hydraulic head gradient.

$$\frac{Q}{A} = v = ki \tag{7}$$

Where, v = the discharge velocity of water (ms^{-1}), k = the coefficient of permeability (ms^{-1}), and i = the hydraulic head gradient (the ratio of head loss h over a distance l). The discharge velocity (v) is defined as the quantity of water Q percolating through a cross-sectional area A in unit time.

The coefficient of permeability is dependent on the nature of voids and the properties of the permeating fluid. It is given by Equation (8):

$$k = K\frac{\gamma_w}{\eta} \tag{8}$$

Where, k is the coefficient of permeability (m/s), γ_w = the unit weight of fluid (kN/m^3), η = viscosity of fluid kNs/m^2, and K = absolute or intrinsic permeability (not dependent on the properties of the permeating fluid) (m^2)

In this thesis the terms permeability and hydraulic conductivity are used interchangeably, however, it should be noted that when the permeating fluid is water, the coefficient of permeability (k) is more correctly termed the saturated hydraulic conductivity. The coefficient of permeability describes the special case of hydraulic conductivity when the soil is saturated, as hydraulic conductivity then decreases with increasing suction. As k is dependent on the viscosity of fluid (Equation (8)) it is conventional to report a k value measured at 20°C.

If Darcy's law is combined with laws of mass conservation, conservation of energy and the second law of thermodynamics, equations describing groundwater flow and consolidation in saturated soils can be obtained (Jacob 1950 cited: Freeze & Cherry (1977)):

$$k_x\frac{\partial^2 h}{\partial x^2} + k_y\frac{\partial^2 h}{\partial y^2} = S_s\frac{\partial h}{\partial t} \tag{9}$$

Where, k_x and k_y = Coefficient of hydraulic conductivity in the x and y directions respectively (ms^{-1}), h = Total hydraulic head (m), and S_s = Specific storage (m^{-1}).

Specific Storage (S_s) describes the change in the volume of water stored within a unit volume due to the expansion of water or compression of the soil matrix caused by a change in head Freeze & Cherry (1977):

$$S_s = \rho g(\alpha + n\beta) \tag{10}$$

Where, ρ = Fluid density (kgm^{-3}), α = Compressibility of porous medium ($m^2\ N^{-1}$), n = Porosity (m^3m^{-3}), and β = Compressibility of the fluid (m^2N^{-1}).

The flow of water in a compressible, saturated soil was presented as the 'theory of one-dimensional consolidation' by Terzaghi (1943). Consolidation theory provides a differential equation governing the gradual reduction of volume of a fully saturated soil with time (one dimensional consolidation) as water is removed from pore space due to a dissipation of excess pore pressure (u_e) (and a corresponding gradual increase in effective stress) (Terzaghi, 1943a);

$$\frac{\partial u_e}{\partial t} = \frac{k}{m_v \gamma_w}\frac{\partial^2 u_e}{\partial z^2} = c_v \frac{\partial^2 u_e}{\partial z^2} \tag{11}$$

Where, c_v is the coefficient of consolidation (m^2/s), m_v is the coefficient of compressibility (m^2/kN), and k is the coefficient of permeability (m/s), and γ_w = the unit weight of pore fluid (kN/m^3).

The consolidation equation is a solution to Equation (9) where the rate of increase of effective stress is considered equal to the rate of dissipation of excess pore pressure (Domenico, 1972).

Darcy's Law was originally derived for saturated soil, but later research has shown that it can also be applied to flow through unsaturated soil. In 1931, Richards combined Darcy's law with an equation of continuity to derive a general equation for transient unsaturated water flow in soil (Equation (12)). This is based on the assumption of homogeneity, that unique values of water potential, water content, and hydraulic conductivity can adequately characterize a representative elementary volume at a given soil depth (Jarvis, 2007).

The only difference between the unsaturated and saturated flow equations is that under conditions of unsaturated flow, the hydraulic conductivity (k) is no longer a constant, but varies with changes in soil water content and therefore pore-water pressure. In the case of heat flow, the thermal conductivity becomes a function of soil water, air and ice content;

while for vapour and gas flow the coefficient of diffusion becomes a function of degree of saturation (GEO-SLOPE, 2008).

Since the hydraulic conductivity is no longer a constant and varies with changes in soil water content, the conservation equations must be altered to contain terms for both the rate of change of moisture content and the rate of change of soil water storage.

Richards' equation in terms of pressure head h_ψ in two dimensions (Richards, 1931):

$$\frac{\partial}{\partial x}\left[k_\varphi \frac{\partial h_\varphi}{\partial x}\right] + \frac{\partial}{\partial y}\left[k_\varphi \left(\frac{\partial h_\varphi}{\partial y} + 1\right)\right] = C_\varphi \frac{\partial h_\varphi}{\partial t} \qquad (12)$$

The solution to Richards' equation requires knowledge of the characteristic curve relating hydraulic conductivity k_ψ to pressure head, and the characteristic curve relating specific moisture capacity C_ψ to pressure head. Specific moisture capacity represents the unsaturated storage property of the soil and is derived from the slope of the Soil Water Retention Curve (SWRC), relating moisture content to pressure head. Equation (12) can be converted to one in terms of total hydraulic head $h_{(x,y,t)}$ through the relation $h = h_\psi + z$ (where z is the elevation).

Richards' equation, considers only liquid phase transport and as mentioned previously, unsaturated soil descriptions must provide for water vapour and heat flow as well. Several researchers have formulated differential equations governing vapour, heat and liquid flow in unsaturated soils. (e.g. Dakshanamurthy and Fredlund, 1981). Wilson (1990) presented a flow model which comprised a modified Richards' equation with vapour components and a heat flow equation. Under reducing assumptions (see Wilson 1990) it is:

For moisture flow:

$$\frac{\partial h}{\partial t} = C_w^1 \frac{\partial}{\partial y}\left[k \frac{\partial h}{\partial y}\right] + C_w^2 \frac{\partial}{\partial y}\left[D_{vap} \frac{\partial P_{vap}}{\partial y}\right] \qquad (13)$$

For Heat flow:

$$c \frac{\partial T}{\partial t} = \frac{\partial}{\partial t}\left[\lambda \frac{\partial T}{\partial t}\right] - L_v \left[\frac{P + P_{vap}}{P}\right] \frac{\partial}{\partial y}\left[D_{vap} \frac{\partial P_{vap}}{\partial y}\right] \qquad (14)$$

Where,

h = Hydraulic head (m), C_w^1 = Coefficient of consolidation with respect to liquid phase $= \left(\frac{1}{\rho_w g m_2^w}\right)$,

C_w^2 = Coefficient of consolidation with respect to vapour phase $= \left(\frac{P+P_{vap}}{P(\rho_w)^2 g m_2^w}\right)$, m_2^w = Slope of the soil water retention curve (1/kPa), k = Coefficient of permeability (ms^{-1}), D_{vap} = Coefficient of diffusion for water vapour

through soil (kgm/kNs), P = Total pressure in the bulk air phase (kPa), P_{vap} = Partial pressure in the soil due to water vapour (kPa), c = Volumetric heat capacity (Jm^{-3} $\circ C^{-1}$), T = Temperature ($\circ C$), λ = Thermal conductivity ($Wm^{-1}\circ C^{-1}$), L_v = Latent heat of vaporisation (Jkg^{-1})

If Equation (13) is rewritten as a function of pressure rather than in terms of head it becomes:

$$\frac{1}{\rho}\frac{\partial}{\partial x}\left[D_{vap}\frac{\partial P_{vap}}{\partial x}\right]+\frac{1}{\rho}\frac{\partial}{\partial y}\left[D_{vap}\frac{\partial P_{vap}}{\partial y}\right] + \frac{\partial}{\partial x}\left[k_x\frac{\partial\left[\frac{P}{\rho g}+y\right]}{\partial x}\right]+\frac{\partial}{\partial y}\left[k_y\frac{\partial\left[\frac{P}{\rho g}+y\right]}{\partial y}\right] + Q = \lambda\frac{\partial P}{\partial t} \tag{15}$$

Where,

m_v= slope of the soil water retention function, k_x= hydraulic conductivity in the x-direction,

k_y = hydraulic conductivity in the y-direction, Q = applied boundary flux, D_v = vapour diffusion coefficient as described by Wilson (1990), y = elevation head, ρ = density of water, g = acceleration due to gravity, and t = time.

Similarly Equation (14) for heat flow becomes,

$$L_v\frac{\partial}{\partial x}\left[D_{vap}\frac{\partial P_{vap}}{\partial x}\right]+L_v\frac{\partial}{\partial y}\left[D_{vap}\frac{\partial P_{vap}}{\partial y}\right]+\frac{\partial}{\partial x}\left[k_{tx}\frac{\partial T}{\partial x}\right] + \frac{\partial}{\partial y}\left[k_{ty}\frac{\partial T}{\partial y}\right]+Q_t+\rho cV_x\frac{\partial T}{\partial x}+\rho cV_y\frac{\partial T}{\partial y}=\lambda_t\frac{\partial T}{\partial t} \tag{16}$$

Where,

ρ_c = volumetric specific heat value, k_x = thermal conductivity in the x-direction, k_y = thermal conductivity in the y direction and assumed equal to k_{tx}, V_{xy} = the Darcy water velocity in x and y directions and Q_t = applied thermal boundary flux.

The equations described above can be solved using a finite difference approach and validated using evaporation pan experiments (Wilson, 1990).

These equations have been incorporated into a number of finite element programs including Vadose/W, which is used later in Chapter 5 of this thesis to model pore water pressures within a case study infrastructure slope.

Coupling heat and mass flow (Equations (13) and (14)) can be achieved by

(Edlefsen et al. 1943 cited: GEO-SLOPE 2008):

$$P_{vap} = P_{vs} e^{-\frac{Pw}{\rho RT}} = P_{vs} h_{rair} \quad (17)$$

Reformed by (Joshi et al., 1993):

$$\nabla P_{vap} = D_1 \nabla(-P) + D_2 \nabla T \quad (18)$$

Where,

$D_l = D_v(W/\rho_w RT)P_{vap}$, $D_2 = D_v\{h_r \delta P_{vs}/\delta T - P_{vap}\Psi W/\rho_w RT^2\}$, $D_v = \alpha\beta D_{vap}\,(W/RT)$,

β = the volumetric air content, α = the tortuosity factor, P_{vs} = saturated vapour pressure of pure free water, W = molecular mass of water vapour, R = universal gas constant, T = temperature (K) for the term in the exponent, h_{rair} = relative humidity of air and D_{vap} is the coefficient of water vapour diffusion in free air.

Wilson (1990) made several assumptions in order to reduce the complexity of Equations (13) and (14). Specifically, air and partial vapour pressure change due to changes in soil volume have been ignored. As a consequence of this, Wilson's model may not represent clay soils undergoing rapid volume change such as high plasticity clays near the ground surface where high moisture gradients may exist.

2.8 Measuring saturated hydraulic conductivity

For a cohesive soil in a laboratory, the coefficient of permeability can be obtained from consolidation tests either in a oedometer or a triaxial cell from Terzaghi's (1943) theory of one-dimensional consolidation (Equation (11):

$$k = c_v m_v \gamma_w \quad (19)$$

Where, k = coefficient of permeability (m/s), c_v = coefficient of consolidation (m^2/s), m_v = the coefficient of compressibility (m^2/kN), and γ_w = the unit weight of water (kN/m^3).

Indeed, Terzaghi originally produced his theory for this purpose, as he noted that smear on the specimen boundaries greatly affected the measured soil permeability in his permeameter tests, and used an oedometer cell in order that all water flow would occur out of the sample. (Clayton et al., 1995)

The hydraulic conductivity of clays can be measured with a greater degree of accuracy using a constant head permeability test as described in (BS 1377:1990). This test can also be carried out either in a triaxial cell (Figure 2.5) or in an oedometer cell.

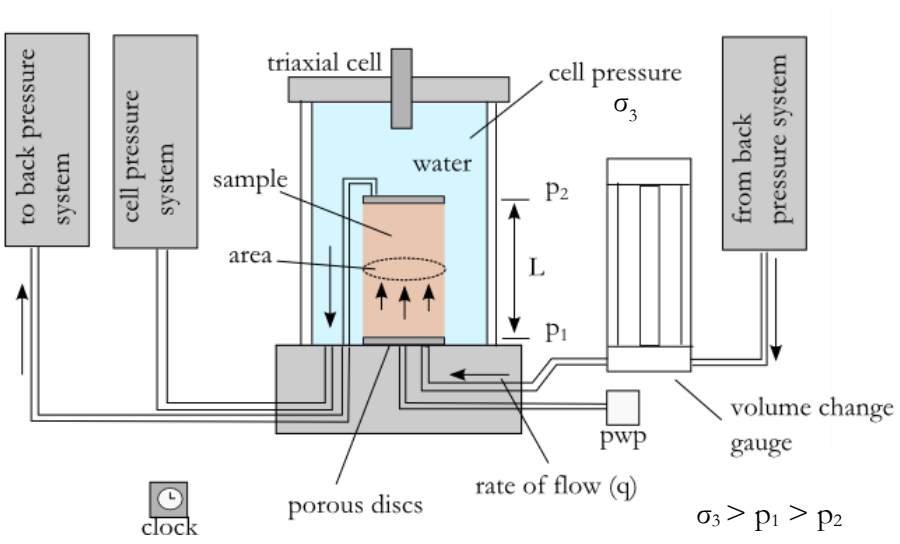

Figure 2.5 – Diagram of a typical triaxial cell setup

In a constant head permeability test, a 100 mm diameter sample is subjected to a total stress level approximating to that of the in-situ ground conditions, and a hydraulic gradient is applied across the height of the sample. The volume of water flowing through the sample is then measured over a timed period and it is possible to use Darcy's law (Equation (7)) to calculate the saturated hydraulic conductivity of the sample. In this situation the accuracy of the test is very much affected by the differences in effective stress across the specimen. The applied pressure difference should be kept to less than 10 % of the average effective stress on the specimen (Krstelj, 1994).

Changes of effective stress at the start of the test introduce consolidation or swelling (or both), and the test must therefore be run until steady flow is achieved. The test should be carried out using de-aired water and a back pressure can be used to drive air into solution and achieve full saturation (Sivakumar et al., 2015). The test can include measurements of the incremental volume and moisture content (or density) changes of the specimen during the test, and the degree of saturation (B value). The measured k values should be corrected for any variation in the viscosity of water and for the rubber membrane edge effects depending on the sample size (Krstelj, 1994).

Samples of 100 mm diameter size will contain some macropores networks but may not contain all the macrostructure present in the field. This may cause a discrepancy between laboratory and field measured values. A drawback of the test is that it only measures hydraulic conductivity in one direction, which is unlikely to occur in the field. Additionally, sample edge disturbance is unavoidable when loading the samples into the cell and the structure of the soil will therefore be altered. Lastly, the membrane surrounding the sample can trap air bubbles, reducing flow or providing a pathway for preferential flow, giving a false indication of the true hydraulic conductivity.

2.9 Soil moisture retention curves and hydraulic conductivity functions

To model water flow through unsaturated soils using the equations described above, it is necessary to define the ability of a soil to store water as it desaturates. This relationship can be described using a Soil Water Retention Curve (SWRC), also known as a Soil Water Characteristic Curve (SWCC), which along with a hydraulic conductivity function, forms a conceptual model for understanding unsaturated soil behaviour.

A typical SWRC curve is presented in Figure 2.6. There are different curves associated with a soil depending on if it is currently subject to wetting or drying. It can be seen that each curve is comprised of four main components, the saturated water content θ_s, the air entry value, the gradient of the slope (slope function), and the residual water content θ_r.

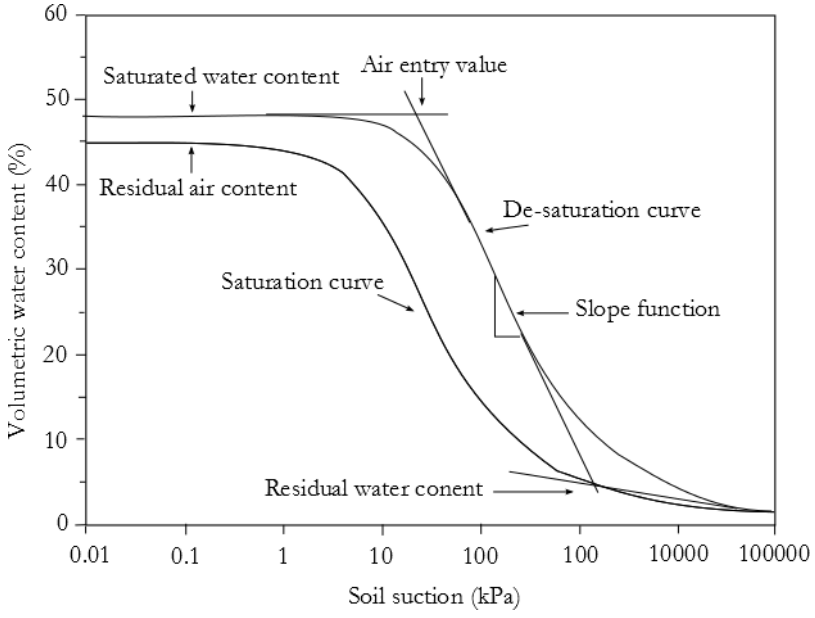

Figure 2.6 – The soil water retention curve (Fredlund and Xing, 1994)

The saturated water content is the amount of water in the soil when all voids are completely filled with water. The air-entry value is the suction at which air starts to enter the larger pores within the soil, and it begins to desaturate. The slope function is the gradient of the curve after the air entry value and is governed by the degree of uniformity of pore sizes within the soil (Fredlund and Xing, 1994). The residual water content is the amount of water at which an increase in suction produces no further reduction in water content within the soil.

SWRC measurement methods are based on bringing the soil specimen to thermodynamic equilibrium with a reservoir of water at a known energy state (Barbour, 1998). Methods include the pressure plate, the capillary potentiometer (high suction tensiometer) and osmotic desiccator (Gens, 2010). Different methods are suited to different ranges of suctions (Fredlund et al., 2012). SWRCs are usually plotted in terms of volumetric rather than gravimetric water content (Equation (5)). Although it has been observed that the density may vary at different suctions so Equation 5 may not hold for some samples.

One key point to note with respect to soil water retention curves, is that it is not a unique relationship, it is actually hysteretic, as shown in Figure 2.7. Hysteresis is caused mainly by the variation in pore sizes. Hillel (1998) considers a large void connected to a smaller void such that they form the shape of an ink bottle. When the soil is drying, the surface tension of the water in the small void can maintain the water in the large void and can sustain higher suction.

However, at the same moisture content, if the soil is wetting, the larger void will be filled first and the suction in the smaller void is not as effective. The contact angle of the water meniscus on the walls of soil pores also plays a role in causing hysteresis, as it tends to be greater in an advancing, wetting meniscus than a receding, drying one, resulting in greater suctions in drying than wetting (Smith, 2015). Hillel (1998) also notes entrapped air and changes in soil structure due to volume changes as possible causes of hysteresis.

Hysteresis means that there are an infinite number of soil water retention curves for a given soil, as the path followed depends on its current stress state. Therefore wetting and drying curves in effect act only as bounding curves for the soil's real behaviour. That is, that the soil will actually follow a path from one of these curves to another via a scanning curve (Figure 2.7).

Hysteresis is often ignored in geotechnical analysis due to its complexity and the difficulties associated with deriving wetting SWRCs (Likos et al., 2014). Soil water retention

curves are therefore commonly assumed to refer to drying curves (Pham et al., 2005). However, as the wetting curve is of importance when considering slope instability, the effect of altering this characterisation is explored further in the hydrological modelling discussed in Chapter 5.

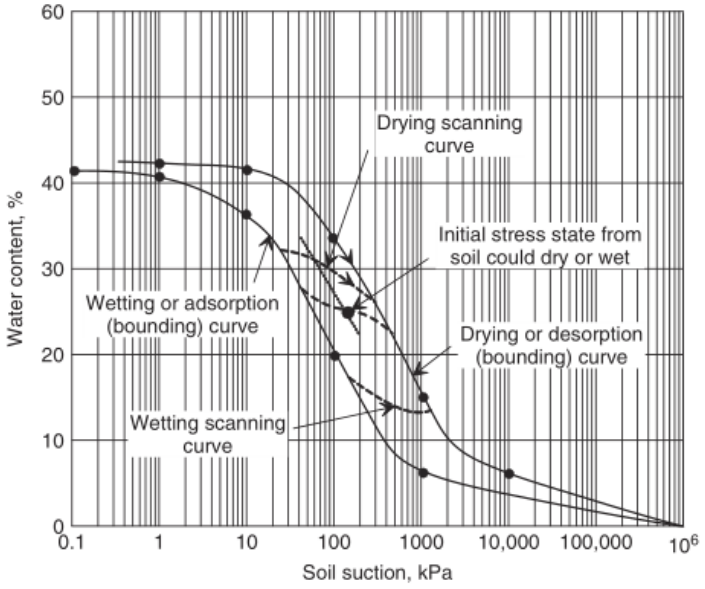

Figure 2.7 - Relationship of initial stress state to hysteresis loops of the soil water retention curve (Fredlund et al., 2012)

As discussed earlier, the quantity of water and air in the soil pores affects the ability of a soil to transport water and changes its hydraulic conductivity. Therefore, as well as the soil water retention curve, it is necessary to define how the hydraulic conductivity of a soil varies with the degree of suction. This relationship is known as the hydraulic conductivity function (HCF) and typical HCFs along with corresponding SWRCs for common soils are shown in Figure 2.8.

For either air or water to be able to flow through a soil, the phase must be continuous throughout the pore space. Therefore a near-saturated soil may be impermeable to air and a nearly-dry soil may still have some residual water present but may not be permeable until the water content increases enough that the water becomes continuous. As a soil dries water drains from within the largest pores before leaving the smallest ones. The largest pores are the most important for flow so the hydraulic conductivity will reduce rapidly. After the water within the pore space dries to the extent that it is no longer continuous the hydraulic conductivity will reduce to zero.

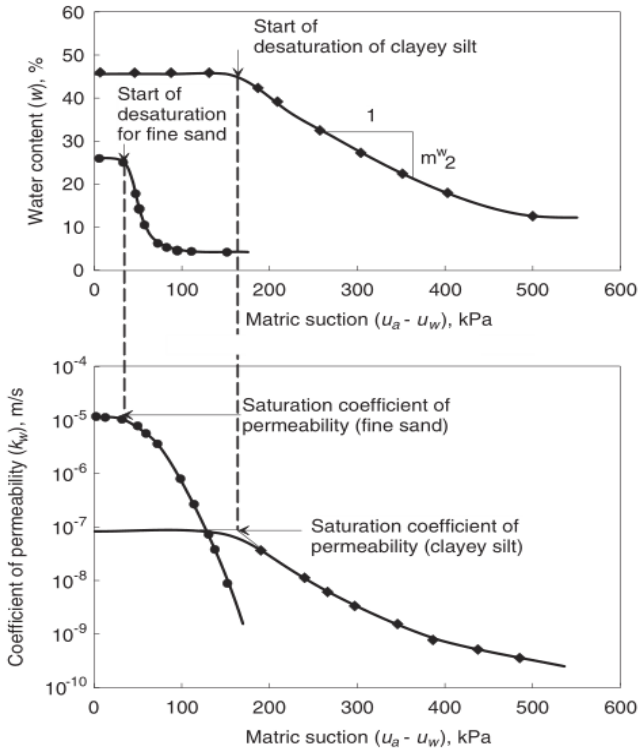

Figure 2.8 – A typical relationship between soil water retention curves and hydraulic conductivity functions for sand and clayey silt (Fredlund et al., 2012)

2.10 Methods for estimating unsaturated properties

The process of experimentally determining a complete SWRC and HCF is time consuming, difficult, and expensive (Fredlund et al., 2012). This is due to the large range of suctions which need to be generated in order to fully describe a soil's behaviour. A different technique is required to generate extremely low suctions (less than 10 kPa) than is necessary to generate suctions in the hundreds of thousands of kPa. An additional difficultly is that samples cannot be disturbed, otherwise, as Croney (1952) showed, the ability of the soil to absorb and release water is drastically altered.

For these reasons, many researchers have proposed methods to estimate the two functions. With regards to the soil water retention function, Aubertin et al. (2003) derived estimations based on grain size distributions, while Fredlund & Xing (1994) and van Genuchten (1980) used closed form equations derived for curve fitting.

For the hydraulic conductivity function, estimations have been made based on those water retention formulations, or on actual measured water retention functions. For instance, Mualem (1976) and Fredlund & Xing (1994) developed closed form analytical expressions of the hydraulic conductivity function.

Therefore, there are complete closed form equation formulations which can describe the unsaturated characteristics of a soil.

One such formulation is the van Genuchten-Mualem model (Schaap & van Genuchten 2006) which proposes that the soil water retention curve is given by:

If $h \leq 0$

$$\theta = \theta_r + \frac{\theta_s - \theta_r}{[1 + |\alpha h|^n]^m} \quad (20)$$

If $h > 0$

$$\theta = \theta_s$$

Where,

θ = the volumetric water content, θ_s = the saturated volumetric water content, θ_r = the residual volumetric water content, h = the pressure head (cm), and α, n, m = curve fitting parameters (α is related to the inverse of the air entry value (cm^{-1}), n is a measure of pore size distribution (>1) and m = 1-1/n)

The corresponding hydraulic conductivity function in the formulation is given by:

If $h \leq 0$

$$K(S_e) = K_{sat} S_e^L \left[1 - \left(1 - S_e^{\frac{1}{m}}\right)^m\right]^2 \quad (21)$$

If $h > 0$

$$K(S_e) = K_{sat}$$

In which L is a pore-connectivity parameter (commonly fixed at 0.5) (Mualem, 1976) and S_e is the effective saturation given by:

$$S_e(h) = \frac{\theta(h) - \theta_r}{\theta_s - \theta_r} \quad (22)$$

It can be seen that it is only necessary for the user to define the three curve fitting parameters, α, n and m, along with saturated and residual soil water contents, in order to fully define the two functions.

2.11 Flow within macropores

The relationships describing flow within soils presented in this Chapter have used concepts and governing equations formed from fluid mechanics and continuum assumptions (e.g. Richards's equation). However, due to the heterogeneity often found in real world slopes many instances of flow which do not obey these laws have been observed (Beven and Germann, 1982). This phenomenon is termed preferential, or non-equilibrium, flow and has been a topic of interest for researchers for many decades now. Hendrickx and Flury (2001)

define preferential flow as 'all phenome where water and solute move along certain pathways while bypassing a fraction of the porous matrix'.

Preferential flow results from significant spatial variations in water velocities due to heterogeneities in soil properties (Jarvis et al., 2016). The point at which water will start to flow into a macropore is determined by the surface tension of water, the radius of curvature of the air-water interface, and its contact angle with the solid pore walls (Beven and Germann, 2013). As water starts to flow into macropores, the sharp contrast in pore size and tortuosity with the surrounding textural pores leads to an abrupt increase in water flow rate for only a small increase in soil water pressure (Larsbo et al., 2014).

Experimental evidence suggests that pores larger than around 0.3 – 0.5 mm in equivalent cylindrical diameter are the pores most responsible for rapid non-equilibrium flow (Jarvis, 2007). These pores also tend to be characterized by relatively large length (high continuity) and low tortuosity (pore length divided by sample length) (Perret et al., 1999; Clothier et al., 2008).

The soil macroporosity is rarely full of water even under nominally saturated flow conditions because not all macropores form continuous pathways (Beven and Germann, 1982). Some researchers have shown that only 10 – 50 % of the total macroporosity conducts water during saturated flow through intact cores, with different types of macrostructure showing significantly different flow phenomena (Bouma and Wösten., 1979; Mori et al., 1999; Perret et al., 1999). However, these assessments of sample macroporosity were made using 2-D analysis or rudimentary imaging techniques.

Some researchers have developed conceptual models which suggest that the strongest preferential transport is predicted to occur in soils which contain large continuous macropores but lack well-connected networks of smaller macropores (Jarvis et al., 2016). A well-connected network of smaller pores reduces the likelihood of soil water potentials increasing sufficiently to trigger flow in the largest macropores. However flow within macropores and the relationship between macropore properties (e.g. size and connectivity) and hydraulic conductivity is still an area of research of which we require an improved understanding in order to construct new descriptions of flow within soils (Beven and Germann, 2013).

2.12 Measuring porosity at different scales

It is clear that the range of pore sizes within a soil and their connectivity has an important impact on the hydraulic conductivity and storage properties of that soil. Several techniques exist which allow for the pore (also known as void) size distribution and porosity of a soil sample to be determined. A void size distribution shows the volume of voids corresponding to any given size of void. A standard laboratory technique for determining the void size distribution for soil is mercury intrusion porosimetery (MIP). MIP involves applying an absolute pressure to mercury (a non-wetting fluid) in order to force it to enter pores within the sample. If pores are assumed to be of cylindrical shape then the Washburn equation applies:

$$P = \frac{-n\,\sigma_{Hg}\,\cos\theta_{nw}}{x} \qquad (23)$$

Where, P is the absolute pressure, σ_{Hg} is the surface tension of mercury (equal to 0.484 N/m at 25°C), θ_{nw} is the contact angle between mercury and the pore wall (between 139° and 147° for clays (Diamond, 1970)) and x is the pore entrance diameter (n = 4).

MIP is a widely trusted technique for determining the void size distribution of a soil between 4 nm and 0.4 mm, however, it does have several limitations. Namely, that isolated pores which are completed enclosed by solids are not measured by the test and neither are pores that are only accessible through smaller ones (until p is large enough to penetrate the smaller pores). Some pores are also not intruded as the machine does not have the capability of high enough pressures. Furthermore, the minimum practical pressure of the machine may limit the largest size of pore measured and during low pressure application, before initial intrusion has taken place, some alteration in pore geometry may occur (Romero and Simms, 2008). MIP requires the use of very small samples (less than 1g) which must be oven or freeze dried prior to testing. Additionally, a typical MIP derived void size distribution relates the volume of intruded mercury against the void entrance diameter size. This can be very different from a true volumetric pore size distribution (Lapierre et al., 1990)

Figure 2.9 shows two different pores which would give the same entrance radius and volume but would likely have very different permeabilities. MIP results cannot therefore directly be linked to permeability, without using another technique (e.g. CT imaging) to quantify other aspects of the pores which are related to permeability.

Computed tomography is an emerging technique within geotechnical research that is capable of determining void size distributions within much larger soil samples than MIP and has the potential to provide three-dimensional quantitative data regarding the macrostructure of any scanned samples (Helliwell et al., 2013). Chapter 4 of this thesis provides a detailed overview of the CT technique including its capabilities and limitations.

For all experimental techniques exploring pore size, the measured porosity values of samples depend on the size of sample investigated and the scale of experimental technique. For instance imaging techniques such as Electron Microscopy and X-ray Computed Tomography provide differing indications of sample porosity due to the size of sample scanned and the smallest pores which can be visualised. The increase in connectivity, porosity, and observable features with different measurement techniques (using different scales) is an aspect which is explored further in Chapter 8 as clay fill contains a wide range of pore and particle sizes.

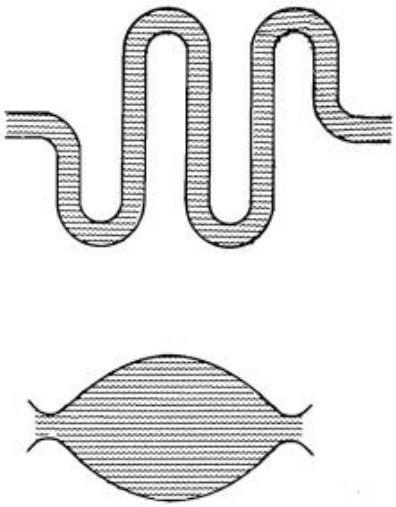

Figure 2.9 - Example of two different pores which would lead to similar MIP test results (Lapierre et al., 1990)

2.13 Critical discussion

A detailed background literature review has provided an overview of some of the fundamental concepts involved in the structure of soils and the flow of water through saturated and unsaturated soils. It was shown that Wilson's (1990) equations provide simplified descriptions describing the flow of water, vapour, and heat. In conjunction with SWRCs and HCFs these flow equations provide a basis for modelling unsaturated flow (based on Darcy-Richards assumptions).

However, the commonly used descriptions of flow and unsaturated soil behaviour presented in this Chapter have several drawbacks.

The flow equations are not based on the physical reality of many real soils as no allowance is made for the presence of macropores. Macropores have been observed to result in non-equilibrium flow which does not obey the relationships described here. The equations do not take into account the structure of the soil and it is instead assumed to be a homogenous continuum based of the representative elemental volume theory. The hydraulic conductivity is also assumed to remain constant throughout time when, in reality, it can change over time (as can the strength of soils).

Additionally, SWRCs are not physically based (depending on the pore structure) as they are curves fitted to a series of one-off test results on remoulded soils (where the nature of soil has been changed). The air entry point is also an approximation (see Figure 2.6) which does not precisely define the point at which the pores begin to desaturate. The complexity of the real world is not fully reflected in these curves as hysteresis and the effects of the current stress state are not captured. The van Genuchten-Mualem model approximation of HCF has also been shown to be inaccurate at low suctions, possibly due to the effects of macropores (Schaap et al., 2006).

The implications of these assumptions regarding flow and unsaturated behaviour on modelling the hydrology of slopes is explored further in Chapter 5.

The limitations of experimental methods for measuring hydraulic conductivity and porosity should also be noted. The size of the sample used for experimental work is of great importance, to avoid edge effects and to provide representative results. Additionally, anisotropy within field soils may not be captured during laboratory tests (see Section 5.4.8)

The limitations of current flow theory are a consequence of the experimental difficulty in accurately determining the direct influence of soil structure. There is a need for better understanding of these limitations and research into techniques which can overcome them. The relationship between the macropore properties and the hydraulic conductivity of clay fill is explored further in Chapter 8.

Prior to this however, in order to model the hydrology of infrastructure slopes fully, it is necessary to examine slope scale processes and flow at the soil-atmosphere boundary as well as the theories discussed here. The following chapter describes these processes, including the hydrological triggering of failures, the influence of climate and vegetation, and observations of the influence of macroporosity at a slope scale.

3 Systems of slope hydrology

3.1 Introduction

To properly analyse the hydrology of infrastructure slopes it is necessary to build on the understanding of water flow in soils explored in Chapter 2 by introducing the influence of other factors within the slope hydrological system. This Chapter explores the effects of processes at the soil-atmosphere boundary including climate and vegetation in relation to modelling slope hydrological behaviour. This chapter also discusses observations of preferential flow and the influence of macroporosity at the slope scale.

3.2 The role of climate and the hydrological cycle

The hydrological cycle (Figure 3.1) describes the continual cyclical movement of water between land, sea and air. This process is driven by energy from the sun, changing the state of the water present in the environment. Evaporation causes liquid water within the oceans and on land to change to water vapour in the air, whilst precipitation returns this moisture to the land surface. Water can then complete the hydrological cycle by evaporating or being transpired by plants back into the atmosphere or by flowing as a liquid into the oceans.

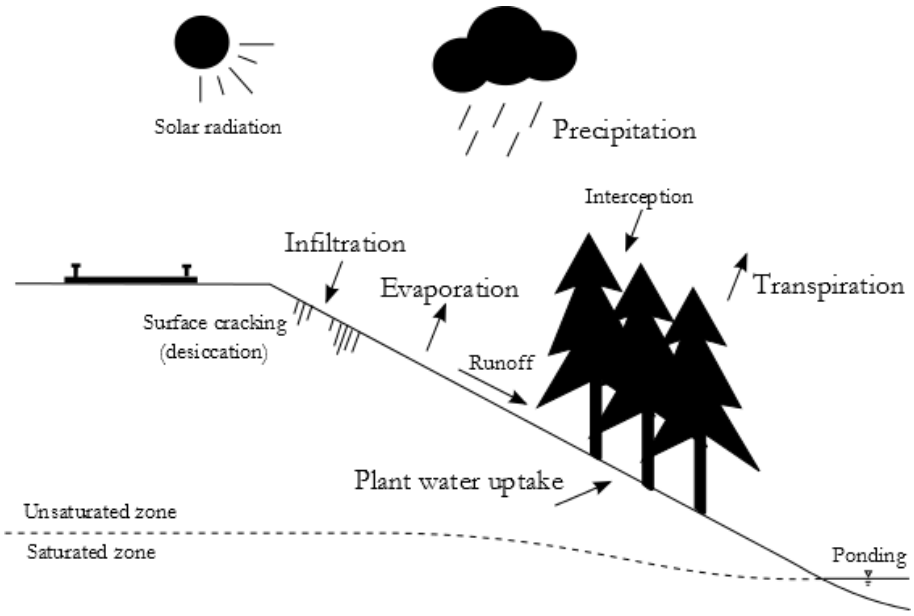

Figure 3.1 – The hydrological cycle of a railway embankment

When rain falls on a slope, some of it will be intercepted by vegetation and will not penetrate the soil. A further proportion will run off the surface depending on how much water is already in the soil and how intensive the rainfall is. The rest will infiltrate the soil and produce

a change in water content which will then result in a change in pore water pressure. The magnitude of this pore water pressure change is dependent on a number of other factors (e.g. soil permeability, saturation, vegetation properties which influence transpiration, and aspects of climate which govern evaporation).

Within earthworks, the hydrological regime can also vary depending on the construction methods used. Two primary types of earthwork used as infrastructure slopes are embankments and cuttings. Embankments are formed by placing a mound of fill material above ground to maintain the vertical alignment of road, rail, and canal routes. As a result they often remain largely unsaturated with a water table at depth. Cuttings are formed by excavating below ground level and soil and groundwater conditions will be determined by the natural geology at the site.

Railway embankments in the UK were typically constructed in the late 19th and early 20th centuries (Skempton, 1996). They can therefore often be comprised of poorly compacted fills placed upon unprepared foundations. As a consequence of this, the permeability of fill is commonly found to be higher than soils within other infrastructure slopes and it is likely that these railway embankments contain a greater degree of heterogeneity in structure and pore size (Loveridge et al., 2010). The change in macropore structure with depth within a clay fill embankment is explored further in Chapter 8.

3.3 Hydrological triggering of failures

Hydrological triggering is considered to be a principle landslide initiation mechanism for both natural and engineered slopes (Asch et al. 1999). Several different failure mechanisms have been observed for earthworks (Briggs et al., 2017).

Infiltration (Figure 3.1) can cause an increase in pore-water pressure (i.e. a decrease in suction) and a decrease in shear strength, which can lead to failure (Leroueil, 2001). Pore water pressure increase within a slope can occur from above, through rainfall infiltration and a temporary perched water table, or from below through a rise in the groundwater table (Toll et al., 2011). Transient near-surface pore water pressure changes may be sufficient to induce landslides, even though they are likely to be shallow in nature (like many slope failures in the UK) (Pennington et al., 2014).

Slopes which are subjected to seasonal wetting and drying cycles, and therefore cycles of effective stress, can experience a degradation in strength over time, termed ‘progressive failure’ (Potts et al., 1997; Vaughan et al., 2004; Take and Bolton, 2011; Harley et al., 2014)

Clay slopes which undergo regular seasonal volume changes (shrink-swell behaviour), either due to vegetation or climate influence, can also suffer from serviceability failures due to deformation (Glendinning et al., 2014).

These failure mechanisms are inter-related and can occur in combination with one-another or sequentially (e.g. shrink-swell deformation may lead to progressive failure of an embankment, with the final slide triggered by an increase in pore water pressure) (Briggs et al., 2017).

Potential earthwork failure mechanisms depend upon the nature of the construction of the earthwork, including its parent geology (Loveridge et al., 2010). In the UK the dominant source materials generating unstable slopes include mud rocks such as the London Clay formation, the Lias group, and the Gault formation (Dijkstra and Dixon, 2010).

3.4 Hydrological triggering thresholds

The assessment and mitigation of landslide hazards requires an understanding of triggering factors and how these may vary spatially (e.g. due to local geology) and temporally (e.g. in response to extreme weather or changing climate patterns).

By examining historical records of landslides in combination with climate data it is possible to define threshold values to identify periods of increased slope instability. These thresholds can be in terms of daily rainfall, antecedent rainfall, hydrological conditions, or a combination. A common approach is to estimate a meteorological threshold based on rainfall intensity and duration (e.g. Guzzetti et al., 2007).

However, the rate and quantity of surface water infiltration (causing increased pore water pressures) is influenced by the geological conditions (e.g. soil type, saturation and permeability) and the antecedent weather conditions (Zhang et al. 2011). This can affect the time of landslide occurrence and the type of landslide failure mechanism (Leroueil 2001).

As this thesis aims to help advance understanding of slope hydrology in the direction of upscaling to the network scale, a landside inventory study of recent UK failures was conducted. The aims of this study were to consider the influence of long term weather, extreme rainfall and the underlying slope geology on the type and time of landslide occurrence, for comparison with existing landslide trigger thresholds. The type, time and location of 441 landslide events recorded by the BGS over ten years (2004 - 2014) were

compared with rainfall data, geological permeability indices and calculated soil moisture deficit (see Section 3.7.1).

The results showed that a combined rainfall intensity and water balance assessment can be a useful proxy for predicting slope failure occurrence when daily rainfall is above the long term average and the soil moisture deficit is close to 0 mm. The methodology and further results of this study can be found in the Appendix.

3.5 Field monitoring of slope hydrology

From the study described in Section 3.4. It can be seen that rainfall by itself can only give a rough indication of likely slope failures. However, it is the easiest parameter to measure from a field site. Similarly, even if water content within the soil is measured directly it does not give a reliable indication of failures, because the relationship between water content and suction (the SWRC) is hysteretic (see Section 2.9). The best parameter to monitor within field study sites is therefore pore water pressure which is the most reliable indicator of failure and can be used in early warning systems (Toll et al., 2011).

A number of different instruments have been developed for measuring pore water pressures in the field some using direct and some using indirect techniques (Lourenco et al., 2011). Widely used direct measurement devices include tensiometers and flushable piezometers. The instruments are commonly limited in the range of suctions they can measure by cavitation and cannot measure suctions greater than 100 kPa (Ridley, 2004). Cavitation occurs when water breaks down at negative pressure and bubbles of vapour are produced. In recent years, high-capacity tensiometers have been developed. Which allow measurement up to several hundred kPa before cavitation (Toll et al., 2011).

All instrumentation is location specific and installation can have significant effects on the quality of data gathered (Ridley, 2004). An example of this might be if an observation tube used to take probe measurements is poorly installed in the soil then preferential flow paths may exist for infiltration from the surface, meaning that soil around the tube could be wetter than elsewhere in the slope (Hughes et al., 2009). Similarly, each type of instrument varies with respect to resolution.

There is a lack of high quality field data regarding PWP and hydraulic conductivity variation at the near-surface of infrastructure slopes, so the selection of sites when conducting site-specific modelling is restricted.

3.6 The role of vegetation

Trees cover many of the earthworks that support the UK's transport infrastructure and dense vegetation has become more established since the 1960's, when aggressive management of such vegetation was phased out (Briggs and Smethurst, 2013). Vegetation has been shown to have a very significant impact on the hydrology of slopes (Blight, 2003). Vegetation affects slope hydrology by intercepting rainfall, by transpiring soil moisture from within the root zone, and by altering hydraulic conductivity through physical transformation of the soil by roots (Glendinning et al., 2009).

The effects of vegetation with regards to infrastructure asset management are far from clear cut in a positive or negative sense. In periods of dry weather, excessive suctions due to high water demand trees often cause significant serviceability issues and track deformation (Scott et al., 2007). This is particularly the case for clay embankments which suffer from large volume changes as water content changes (Briggs et al., 2013).

However, in periods of wet weather it has been observed that some high water demand trees can help maintain suctions within embankments throughout the winter months and therefore can prevent slope instability (Biddle, 1998; Briggs and Smethurst, 2013). Additionally, tree roots have been shown to act as a mechanical reinforcement to slopes. (Glendinning et al., 2009). On the other hand, vegetation sometimes causes disruption due to leaves falling onto tracks, or prevents the necessary access to maintain drainage systems. It is also worth noting that vegetation is generally popular with those people who live adjacent to railway lines or major roads, as it often provides a visual and audial screen. Its removal can be therefore be unwelcome.

The complex impact of vegetation on hydrology and its temporal effects on pore water pressure and stability, are areas which are still poorly understood and have been identified as requiring further research (Dijkstra and Dixon, 2010). Modelling of these impacts is explored in the Appendix.

3.7 Modelling the soil-atmosphere boundary

As discussed in Chapter 2, flow within soils is driven by differences in hydraulic head within a soil. Within infrastructure slopes, hydraulic head varies the most within the unsaturated zone above the water table where soil moisture is largely governed by the effects of atmospheric conditions at the soil surface (Figure 3.1). Therefore in order to model flow and

changes in pore water pressure within slopes it is necessary to define how water infiltrates at the soil-atmosphere boundary and is abstracted from the near-surface.

3.7.1 Soil water balance and soil moisture deficit

The soil water balance (Equation (24)) describes the effects of the hydrological cycle on the total quantity of water stored within a soil (Blight, 2003)

$$\sum(R - I - RO) - \sum ET + S - RE = 0 \qquad (24)$$

Where,

R is the sum of rainfall, I is the canopy interception, RO is the runoff, ET is the Evapotranspiration which is a function of the interaction between vegetation, soil and climate, RE is recharge to the water table, and S is the change in total water stored within the soil (all in mm/day).

Soil moisture deficit (SMD) is a further simplified water balance calculation (Equation (25)) and represents the volume of water required to keep a soil at its field capacity (the equilibrium moisture content within a soil that is allowed to drain freely under gravity). A soil's field capacity is dependent on pore size, as the water is held by capillary action (Clarke and Smethurst, 2010). SMD is strongly related to changes in pore water pressures, for many soils when SMD is zero there is usually a suction present of around 10 - 30kPa (Kabat and Beekma, 1994). As a result, SMD can be useful proxy for the hydrological conditions of a slope. SMD can be calculated using:

$$\sum(R - RO) - \sum ET + S = 0 \qquad (25)$$

Where,

R is the rainfall, RO is the runoff, ET is the amount of actual evapotranspiration and S is the change in stored moisture within the soil (all in mm/day). Thus the current soil moisture deficit is then the previous day's SMD + S.

SMD can be derived from water content measurements in the field as well as from weather data. SMD derived from weather data provides a tool for understanding and comparing the wetness and dryness of the soil for different years and seasonal cycles without the need for field measurement equipment. This is of use to engineers and infrastructure owners when assessing seasonal risk to infrastructure and identifying SMD thresholds where seasonal problems may occur (Birch and Dewar, 2002). However, this water balance does not take

into account permeability when calculating infiltration/runoff which means its use is limited to larger scale applications rather than site specific cases.

Water abstraction from the soil, shown in Equation (24) as evapotranspiration (ET), occurs due to evaporation from the soil surface and from transpiration through the root zone by vegetation. These are two independent processes, however, due to the difficulties of separating measurement of evaporation and transpiration, the combined term evapotranspiration is used (Hillel, 1998). Both of these water removal processes are controlled by available energy, vapour gradients and air movement but can be limited by soil water availability. Conditions where evaporation and transpiration are at their maximum possible value, given the available solar energy and climate conditions, are termed 'potential'. Where evaporation and transpiration rates fall below the potential, due to lack of available water, the rate is described as 'actual' (Clarke and Smethurst, 2010).

3.7.2 Potential evapotranspiration

If evaporation and transpiration are combined the total contribution of each individual process to total evapotranspiration will vary seasonally. For instance Allen et al. (1998) found that during a crop growing cycle, evaporation can contribute 100 % to total evapotranspiration at sowing time but only 10 % when full crop cover is achieved. A number of models exist for estimating evapotranspiration (e.g. (Penman, 1948; Blaney and Criddle, 1962).

One of the most commonly used models is the Penman-Monteith equation (Equation (27)) which allows for the calculation of potential evapotranspiration (PET) from daily weather data (Allen et al., 1998).

$$PET = \frac{\Delta(R_n - G) + \left(86{,}400\,\frac{\rho_a C_\rho (e_s^0 - e_a)}{r_{av}}\right)}{\Delta + \gamma\left(1 + \frac{r_s}{r_{av}}\right)} \qquad (26)$$

Where,

ρ_a = air density (kg m^{-3}), $C\rho$ = specific heat of dry air, e_s^o = mean saturated vapour pressure (kPa) computed as the mean e^o at the daily minimum and maximum air temperature (°C), r_{av} = bulk surface aerodynamic resistance for water vapour (s m^{-1}), e_a = mean daily ambient vapour pressure (kPa), and r_s = the canopy surface resistance (s m^{-1}). Δ = slope of the vapour pressure curve, kPa $°C^{-1}$; γ = psychrometric constant, kPa $°C^{-1}$.

The surface resistance (r_s) describes the resistance of water vapour flowing through stomata openings, leaf area, and root zones. Aerodynamic resistance (r_{av}) describes the friction from

air flowing over vegetated surfaces (Allen et al., 1998). Further details on the theory and parameters defining this equation can be found in Zotarelli & Dukes (2010). These resistance factors describe a continually changing complex process which depends on environmental conditions and vegetation growth (McMahon et al., 2013).

An updated equation was recommended by the Food and Agriculture Organisation of the United Nations (FAO) (Allen et al., 1998). The FAO-56 Penman-Monteith Equation (Equation (27) simplifies Equation (26) by utilizing some assumed constant parameters for a clipped grass reference crop (See appendix for more details).

$$ET_o = \frac{0.408(R_n - G) + y\frac{900}{T+273}u_2(e_s - e_a)}{\Delta + (1 + 0.34u_2)} \qquad (27)$$

Where,

PET = reference evapotranspiration (mm/day), T = mean daily air temperature at 2 m height (°C), R_n = net radiation at the crop surface (MJ m^{-2} d^{-1}), G = soil heat flux density (MJ m^{-2} d^{-1}), u_2 = wind speed at 2m height (ms^{-1}), e_s = saturation vapour pressure (kPa), e_a = actual vapour pressure (kPa), and e_s - e_a = saturation vapour pressure deficit (kPa)

3.7.3 Actual evapotranspiration

To modify the standard evapotranspiration model (Equation (27)) for specific crops, empirically measured crop coefficients (K_c) have been established (Allen et al., 1998).

Actual evapotranspiration may be less than potential evapotranspiration in cases where soil water is not freely available for plants to transpire. If the soil is subject to a period of dry weather, the SMD can increase until the plants can no longer extract the water that they require, and therefore become stressed. The plant transpiration is then reduced, and actual evapotranspiration falls below the potential value.

A model based on CROPWAT (Clarke and Smethurst, 2010) can be used to estimate the actual evapotranspiration. The model uses the concept of readily and total available water in the active root zone, (RAW and TAW, respectively).

Actual evapotranspiration is limited by the total available water within the plant root zone. Some of this water is readily available water, contained in large voids and fissures, but

once this water is removed, soil water stress conditions occur and further evapotranspiration is reduced below the potential rate. It is assumed that there is no upward flow into the root zone from the soil below.

TAW is typically about 18% of the total root zone volume for a clay soil, but it is assumed that only half of this is accessible to plants (i.e. RAW) (Biddle, 1998). Grass and herbs growing on clay soils will typically root to about 0.8–1.0 m depth (Biddle, 1998; Smethurst et al., 2006). In a structured clay soil, the RAW will be the water occupying the larger voids, cracks and fissures, whereas the remainder of the water is harder for the plants to remove (Clarke and Smethurst, 2010).

When the SMD is less than RAW, evapotranspiration is assumed to occur at the potential rate for the crop (Equation (28)). When the SMD exceeds RAW, evapotranspiration is assumed to fall below the potential rate, in proportion to the ratio of non-readily available water (TAW less RAW) which has been extracted (Equation (29)):

For $0 \leq SMD \leq RAW$

$$AET = PET \times K_c \tag{28}$$

Where,

AET is actual evapotranspiration and K_c is the crop factor.

For $SMD \geq RAW$

$$AET = PET \times K_c \times \frac{(TAW - SMD)}{(TAW - RAW)} \tag{29}$$

Should SMD exceed TAW, evapotranspiration is reduced to zero.

3.7.4 Potential evaporation

Evaporation from a soil surface occurs when there is a continual supply of heat to provide energy for the vaporisation of water, the vapour pressure in the air above the soil is lower than the vapour pressure at the soil surface, and there is a continual supply of water which is available for evaporation. The first two of these conditions are controlled by atmospheric conditions and the last is controlled by soil moisture conditions.

Potential evaporation can be calculated using the Penman equation (Penman, 1948), or when the soil is unsaturated and suctions limit the evaporation rate, from PET using the Penman-Wilson formulation (Wilson, 1990):

$$E = PET \left[\frac{h_r - \frac{P_{v.sat.air}}{P_{v.sat.soil}} h_a}{1 - \frac{P_{v.sat.air}}{P_{v.sat.soil}} h_a} \right] \quad (30)$$

Where,

PET is the potential evapotranspiration (Equation (27) (mm/day), h_r is the relative humidity at the soil surface (%), h_a is the relative humidity of the air above the soil surface (%), $P_{v.sat.soil}$ is the saturated vapour pressure at the soil surface (kPa), and $P_{v.sat.air}$ is the saturated vapour pressure of the air above the soil surface (kPa).

3.7.5 Potential transpiration

It is difficult to measure transpiration directly because it can be problematic to determine the proportion of solar energy which is received by the plant and the proportion which reaches the soil (Blight, 2003). Therefore evaporation and transpiration are commonly treated as one term. However, transpiration occurs from within the root zone whereas evaporation occurs at the surface. Therefore treating them as one process during modelling can lead to unrealistic estimates of pore water pressure variation with depth within a soil profile (Briggs et al., 2016). The depth over which transpiration occurs varies depending on the type of vegetation, for large trees this can be considerably deeper than for smaller vegetation such as grass and shrubs (Briggs and Smethurst, 2013).

To overcome the difficulty in separating evaporation and transpiration, Ritchie (1972) and Feddes et al. (1978) proposed that the proportion of potential transpiration within total evapotranspiration depends on the degree of vegetation cover. This degree of cover can be estimated using the Leaf Area Index (LAI), which represents the total one-sided area of photosynthetic tissue per unit area of ground surface (Monteith and Unsworth, 1990). It can be used to divide available solar energy between that available for direct evaporation from the soil surface and that available to the plant for transpiration.

Ritchie (1972) proposed that potential transpiration (PT) could be calculated with LAI using:

$$PT = E \left[-0.21 + 0.7\sqrt{LAI} \right] \quad (31)$$

Where,

LAI = Leaf area index ($0.1 \leq LAI \leq 2.7$) and E is the potential evaporation (mm/day) (Equation (30))

There is no standard technique to measure LAI and it can be achieved using direct collection methods or indirect methods such as satellite measurement (Morisette et al., 2006). This, in conjunction with the seasonal variation associated with LAI, mean that there is a very large variation in published LAI values.

Ritchie (1972) describes three degrees of vegetation cover, surface evaporation only (bare soil), combined evaporation and transpiration (partial cover) or solely transpiration (full leaf cover). When there is full leaf cover, all solar energy is assigned to transpiration, while for the bare soil condition all solar energy would be assigned to surface evaporation only. Ritchie (1972) defines the LAI for full leaf cover as 2.7 when transpiration is the main component of evapotranspiration and as 0.1 for a bare soil where transpiration is negligible.

3.7.6 Actual transpiration

Root water uptake describes the rate and spatial distribution of water removal from the soil by plant roots in response to transpiration. Feddes et al. (1978) proposed that the maximum extraction rate for a well-watered soil (S_{max}) can be obtained from:

$$S_{max} = \frac{PT}{D_r} \tag{32}$$

Where,

PT is the potential transpiration (Equation (31)) and Dr is total depth of root zone,

However, lack of available plant water or high evaporative demands will cause most plants to biologically react by closing stoma and reducing transpiration (Saxton, 1982). Under continued and increasing stress the plant will reach its 'wilting point' which results in leaf drop and tissue death (Saxton, 1982). This process can be described using a Plant Moisture Limiting (PML) function which determines the percentage decrease in the plants ability to draw water as suction increases within an unsaturated soil. The concept of a plant limiting function has been experimentally confirmed by (Kutilek and Nielsen, 1994) and adopted in subsequent root water uptake models (e.g. (Tratch et al., 1995; Nyambayo and Potts, 2010)). A typical PML function for grass with a wilting point of 1500 kPa is shown in Figure 3.2.

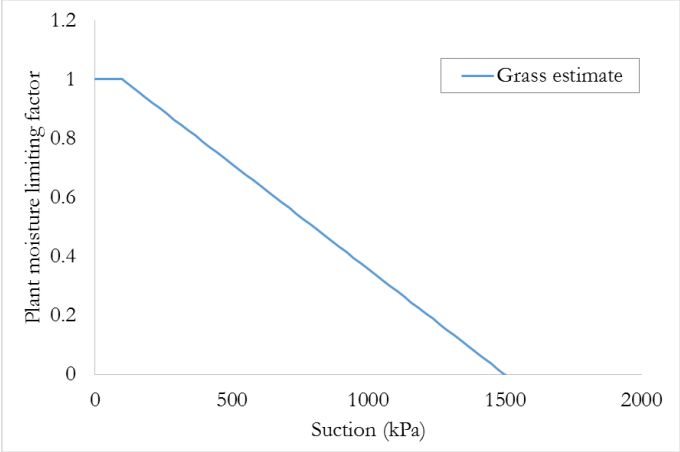

Figure 3.2 - Estimation of a plant moisture limiting function for grass (Feddes et al., 1978)

If the soil is partially saturated, then the actual transpiration value is reduced according to the plant moisture limiting function (GEO-SLOPE, 2008):

$$AT = PRU \times PML \tag{33}$$

Where,

AT = Actual nodal transpiration, and PRU the plant root uptake is given by:

$$PRU = \frac{2PT}{D_R}\left(1 - \frac{D_n}{D_R}\right)A_n \tag{34}$$

D_r is total depth of root zone, D_n is the nodal depth, A_n is the nodal contributing area of the node in question, PT is the potential transpiration (Equation (31)), and PML is the value of the plant moisture limiting function at the current nodal soil negative pore water pressure (Figure 3.2).

3.7.7 Actual evaporation

When water is not readily available for evaporation the actual rate of evaporation decreases below its potential rate (Hillel, 1998). Ritchie (1972) proposed that actual evaporation (AE) could be calculated with LAI using:

$$AE = E\left[1 - (-0.21 + 0.7\sqrt{LAI})\right] \tag{35}$$

Where, LAI = Leaf area index ($0.1 \leq LAI \leq 2.7$) and E is the potential evaporation ((30)

3.8 Preferential flow at a slope scale

Using the relationships described above, in conjunction with the flow equations described in Chapter 2, it is possible to model the hydrological conditions within a slope. However, as discussed in Chapter 2, flow in macropores can bypass the soil matrix and lead to preferential flow. Many observations of preferential flow in field soils have been reported (e.g. Flury et al., 1994). As well as macropore flow, other types of preferential flow have also been observed; for example in the form of unstable infiltrating 'fingers' in highly uniform soils (Hillel, 1998) or large-scale flow through fissures (Bouma, 1991).

The potential for non-equilibrium macropore flow at any site depends on the nature of the macropore network, which is determined by many factors including the abundance and activity of earthworms, the soil properties (e.g. clay content), and site specific factors (e.g. slope position, drying intensity, vegetation) (Jarvis et al., 2016). Preferential flow in macropores has been shown to strongly influence infiltration in some soils (Weiler and Naef, 2003). However, macropore flow processes are often not considered in hydrological models, where soils are usually treated as a continuous porous medium and flow modelled using Darcy-Richards theory (which depends on the representative elementary volume concept).

Continued inadequacy in addressing preferential flow remains a challenge in hydrology and soil science (Weiler, 2017). Many studies have demonstrated that preferential flow severely limits the applicability of standard models for flow and transport that are mostly based on homogenous domain theory (Lin, 2010). Some models take into account macropore flow by defining a higher conductivity for the soil, particularly in near-surface regions. However, this can lead to an unrealistic parameterization of soil properties in hydrological models in order to compensate for the influence of macropore flow. Other models use dual-permeability 'add-ons' to the Richards' equation which lack rigorous physical underpinning (Beven and Germann, 2013). Therefore a new conceptualisation is needed to develop the next generation of hydrological models that can explicitly consider dynamic flow pathways and flow configuration evolution over time (Vereecken et al., 2016).

Some researchers have suggested that a complete rejection of the Richards theory is not the solution, as the theory works well when describing flow in the soil matrix (Weiler, 2017). However, as the approach frequently fails to predict infiltration into soils containing macropores, cracks or other structural features, particularly during high intensity rainfall, new models are needed (Beven and Germann, 2013). These models should be based on experimental data and should take into account the specific soil structures and macropore

properties relevant to flow within individual macropores and their interaction with the soil matrix (Weiler, 2017).

Desiccation cracking results in macropores at the surface of slopes (Figure 3.1) and has been a topic which has presented considerable trouble to researchers for decades (Kodikara and Costa, 2013). The presence of desiccation cracks strongly affects the hydraulic and mechanical properties of a soil and can therefore pose a problem across a wide range of geotechnical structures (Stirling et al., 2015). Desiccation cracking can have a significant impact on slope hydrology, as it provides rainfall with preferential flow paths, enabling deeper infiltration (Flury et al., 1994; Drumm et al., 1997). Cracking is particularly a problem in clays, where it has been shown to increase hydraulic conductivity by between 12 - 34 times, depending on the plasticity of the soil (Rayhani et al., 2007).

The formation and propagation of cracks is highly complex due to coupling between the hydraulic and mechanical behaviour of soils. Water loss during evaporation induces a rise in capillary forces and the soil tends to contract under increasing suction (Rodríguez et al., 2007). During shrinkage, the changes in the stress state tend to lead to movement of the soil particles and, at a certain point of the drying process, crack generation begins (Sanchez et al., 2013).

The influence of desiccation cracking on geotechnical structures can be large. For instance, there is evidence that cracking at the crest area of slopes can trigger the initiation of slope failure (e.g. (Take, 2003)). In embankments, cracking reduces strength and increases the infiltration capacity of the soil, mobilizing the shrinkage/swelling potential of deeper soils which can lead to progressive failure (Sanchez et al. 2013).

3.9 Critical discussion

This chapter has shown the key role of pore water pressures and the influence of climate and the hydrological cycle on the stability of infrastructure slopes. Pore water pressures within earthworks vary seasonally in response to climatic events and the effects of vegetation, which results in effective stress cycles. This can lead to a degradation of strength over time. Field monitoring of PWPs is often limited by the quality of the equipment used.

Estimations of water content within soils can be made using water balance equations and soil moisture deficit. Evaporation and transpiration can be considered separately or as a lumped term within models. Actual evaporation and transpiration vary from potential rate when soil water is not freely available. Penmen-Monteith based soil-atmosphere boundary conditions are based largely on a notional reference crop, however, they do provide useful estimations of potential evaporation. That said, these definitions do appear to lack adequate definition of the dynamic site-specific wind, shade, and leaf coverage conditions which are often present on real world slopes.

A root water uptake term may be used to model water removal at depth by deep rooted vegetation. However, the role of vegetation in slope hydrology is still poorly understood and integrated into models. This is explored further in the Appendix.

Vegetation and desiccation cracking can lead to changes in the structure of the soil and the presence of macropores which, in turn, can result in preferential flow which does not obey Darcy-Richards type flow equations. The presence of cracking and macropores resulting from other hydrological and dynamic natural processes within infrastructure slopes is likely to result in variation of measured hydraulic conductivity throughout the near-surface region. The impact of such changes on the hydrology of slopes is investigated further in Chapter 5. Modelling can help to further identify the key uncertainties in the slope hydrological system, particularly, concerning the variation of hydraulic conductivity with depth and saturation, and the validity of continuum assumptions at a slope scale.

Many types of preferential flow have been observed in the field, implying that different macropore structures affect infiltration into slopes in different ways, therefore any link established between soil structure and preferential flow may be specific to that soil.

The connection between macropore structure and increases in hydraulic conductivity must be explored further with research based on direct measurement of the macropore structure within the samples. The relationship between macropore properties (e.g. size and

connectivity) and the hydraulic conductivity within infrastructure slopes is still underexplored and is investigated further in Chapter 8.

Direct visualisation of macropores and quantification of pore size and connectivity has the potential to help improve our understanding of the relationship between macropore size properties and hydraulic conductivity. The following Chapter explores the use of computed tomography, a new technique which has the potential to be adapted from other fields and modified for the non-invasive quantification of soil pore architecture within large clay fill samples.

4 Computed tomography in the geosciences

4.1 Introduction

Chapter 3 discussed the significant influence macropores can play on the hydrology and stability of slopes. Flow within soils is strongly dependent on a soil's physical structure and pore space architecture and is therefore affected by the presence and interconnectivity of macropores (Perret et al., 1999). As a result, it is essential that the pore networks present within soils can be visualised and quantified accurately in order to help improve our understanding of the role of macropores. However, this has historically been hard to achieve, particularly in a non-destructive manner.

Recently, X-ray computed tomography has developed as a means for non-destructive observation and analyses of the internal pore space architecture of soil samples in three dimensions (Cnudde and Boone, 2013). This chapter introduces the X-ray computed tomography technique and its suitability for geotechnical research. The chapter is intended to provide an overview of the fundamental concepts involved within the CT scanning and image analysis processes, as well as some of the drawbacks of the technique. Previous research within the literature specifically related to the scanning of soils is also reviewed and discussed.

4.2 Introduction to X-ray computed tomography

X-ray computerized transverse axial tomography, commonly known as computed tomography (abbreviated to CAT or CT), is a 3D imaging process that was first developed as a tool for diagnostic medicine in the 1970's because of its capacity to produce non-destructive, high-contrast, cross-sectional images quickly (Ambrose, 1973; Hounsfield, 1973; Ommaya et al., 1976). The earliest X-ray CT scans of soft tissue and bone took only 35 minutes to acquire (Hounsfield, 1973).

Researchers quickly realised the potential of CT for use in a wide range of academic disciplines. For instance, Petrovic et al. (1982) demonstrated the potential for studies involving soil by observing a relationship between the bulk density and the X-ray attenuation coefficient. However, it is only within the last decade that technological advances including the development of smaller, less expensive, 'microCT' scanners have allowed research using CT within the geoscience field to progress rapidly.

In general, X-ray computed tomography can be split into three different subsections depending on the type and power of the CT scanner used. These are medical, synchrotron, and laboratory.

Medical CT machines are capable of very fast scans of human patients at spatial resolutions down to several hundred microns (> 200 μm) (du Plessis et al., 2016). Synchrotrons are the most powerful CT machines available and can provide extremely high quality, sub-micron resolution images (Peyrin et al., 2012). Access to synchrotron facilities is extremely limited however, and the operational costs are very high (Smith, 2015). Laboratory scanners (or microCT machines) span a wide range of spatial resolutions between the synchrotron and medical extremes, depending on the requirements of the research (Cnudde and Boone, 2013). Apart from the size and cost of the machines, a difference between medical CT and microCT is that in medical CT, the object (i.e. the patient) remains stationary, whilst the X-ray source and detector system rotates around it, whereas in most microCT systems, it is the object that rotates whilst the source and detector remain static.

4.3 MicroCT principles and theory

Figure 4.1 shows a typical microCT scanner machine set up. In essence, microCT scanners comprise three main elements, an X-ray source (tube), a rotating sample mount, and a detector (either an X-ray detector or a scintillator screen followed by a charge coupled device (CCD) camera focussed via a lens).

Computed tomography is based on the principle of electromagnetic wave attenuation. X-rays emitted from the source pass through the sample and are attenuated by absorption and scattering as the scanned object itself becomes a secondary source of X-rays and electrons through atomic interactions (Mooney et al., 2012). The detector subsequently produces a 2D grey-scale image of the sample showing the degree of attenuation of the X-rays which have passed through the sample. This grey-scale is related to the linear attenuation coefficient for each pixel (μ) which depends on the bulk density of the material scanned as well as X-ray energy and intensity.

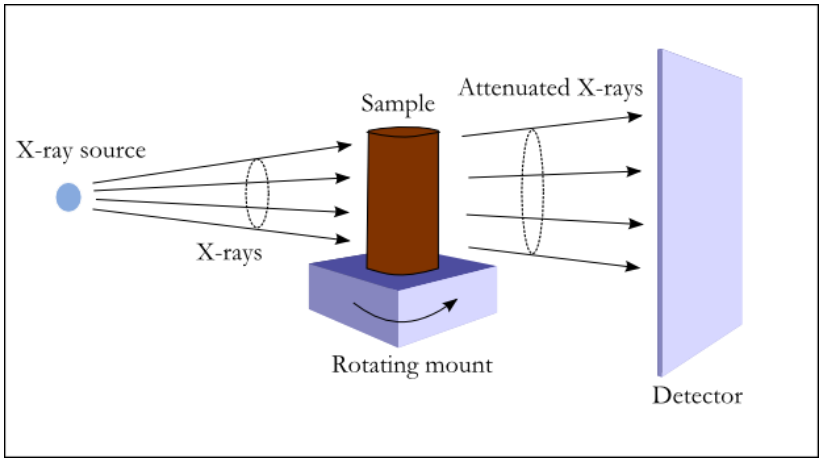

Figure 4.1 – A diagram of a typical Micro X-ray CT system

As they pass through an object, the attenuation of X-rays follows Lambert–Beer's law:

$$I = I_0 e^{-\mu x} \tag{36}$$

Where,

I is the attenuated intensity after the X-rays have passed through an object of thickness x, I_0 is the incident radiation intensity, and μ is the linear attenuation coefficient.

From Equation (36) it can be seen that the attenuated intensity is a decreasing function of the distance x and the attenuation coefficient, therefore materials with a high attenuation coefficient will only allow X-rays to penetrate a relatively short distance, whereas materials with a low attenuation coefficient are more easily penetrated.

A typical scan involves rotating the sample in small increments to acquire a series of radiograph (projections) images over 360°, which can be used to mathematically reconstruct the 3D sample via integration of the linear attenuation coefficient values (Taina et al., 2008). This process is known as back-projection and converts the series of 2D X-ray absorption images into a series of 2D greyscale 'slices' in the x-z plane from which a 3D representation of the sample can be generated which provides an indication of the density at any point within the sample. Each slice consists of discrete units known as voxels which are the 3D equivalent of pixels, the size of which reflects the spatial resolution of the scan. The reconstructed 3D image data from the scanned sample can subsequently be used for visualisation and quantitative analysis.

An X-ray source (tube) generates a beam of electrons directed at a target which, when hit, decelerates the electrons and generates X-rays which are shaped into a cone as they exit the tube (Figure 4.1). The usefulness of the resulting beam of X-rays is dependent on the energy spectrum produced, the focal spot size, and X-ray intensity (number of X-rays) (Helliwell et al., 2013).

The energy spectrum produced affects the level of detail achieved when imaging samples with varying density. Higher energy X-rays penetrate more effectively through a material, enabling the scanning of more dense samples, however they are less sensitive to differences in material density which may make areas of differing density harder to identify.

The focal spot size defines the possible source-detector paths that can intersect at any given point within the sample (Smith, 2015). A smaller spot size leads to less blurring and the ability to detect smaller features.

The X-ray intensity affects the amount of noise which is found within sample images (the consequences of noise are discussed later in Section 4.6.4). Higher intensities can help improve the image quality (less noise) however they often require larger spot sizes which can increase blurring of images.

4.4 Image quality

The image quality comprises two factors, these are the contrast between sample constituents and the spatial resolution.

The image contrast is largely dependent on X-ray energy and the range of densities in the sample. The energy of the X-rays relative to the average density of the sample determines the quantity of X-rays penetrating the scanned object. If X-ray energies are too low, insufficient X-rays will pass through the object for acceptable counting statistics (Helliwell et al., 2013). However if the X-ray energies are too high then the sample will appear transparent to the X-rays and no definition between different density material constituents will be possible (Ahmed, 2014).

The spatial resolution is largely dependent on the focal spot size, the detector capabilities, and the distance between the source, the sample, and the detector within the system. Therefore there is often a trade-off between sample size and the highest resolution achievable (smaller samples allow the distance between the source and the sample to be reduced, resulting in higher resolution) (Dhondt et al., 2010). This is of relevance to CT

research within the geoscience field as large samples may be required for the result to be representative but high resolutions are also required for the scientifically relevant detail of water storage pores or fine root distributions (Young et al., 2001). As a consequence of this many microCT studies have often been limited to small sample sizes (< 5 cm) to achieve the required resolution. This is discussed further later in this Chapter.

4.5 Image data processing

After reconstruction, the image data can be visualised as a 3D volume (composed of 2D slices) based on the local linear attenuation coefficient where the intensity or brightness of each voxel is directly related with the density of the material or phase it represents. An example of this is presented in Figure 4.2, which shows a slice through a scanned foam sample and the difference in greyscale corresponding to the two phases present. Although visual inspection itself is an extremely valuable qualitative tool, quantitative results are often required. The image data can be analysed and quantified in dedicated software packages for visualising and analysing CT data such as Avizo (FEI, 2014) or Fiji (Schindelin et al., 2012).

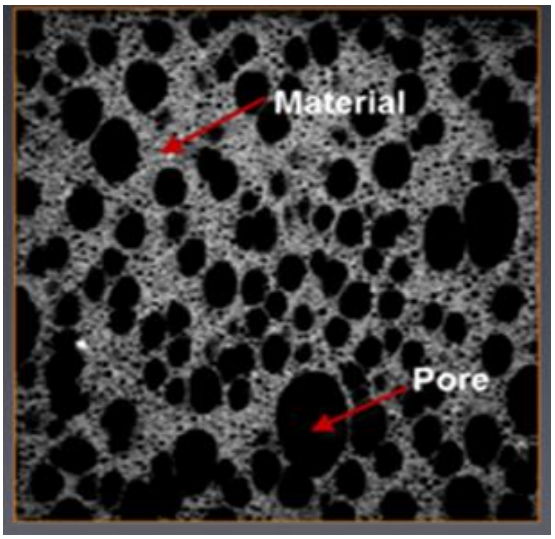

Figure 4.2 – An example of a slice of greyscale CT image data showing the different phases present within the sample (foam) (lowest density constituents appear darkest)(FEI, 2014)

In the geosciences, quantitative results from 3D analysis can include data on the texture, volume fractions, particle sizes and morphology, porosity and pore properties, classification of pores into matrix and macropores, etc. The porosity of a material can be estimated by simply counting the number of voxels assigned to each phase after segmentation, which is the process of separating the phases within the sample.

In practice, quantitative 3D analysis is often not straightforward and can be prone to several systematic errors caused by artefacts within the image data and other difficulties involved in image processing which are described within this Chapter. As noted by Cnudde and Boone (2013), it is essential that microCT users are aware of the limitations and pitfalls while recording or analysing data.

In order to improve the quality of scan image data and obtain accurate quantitative results, a variety of image data analysis procedures have been developed by researchers using X-ray computed tomography (see Helliwell et al. (2013) and Wildenschild & Sheppard (2013). Three key stages which are involved in almost all such methods are explored within this Chapter:

- The extraction of subvolumes
- Segmentation and thresholding of the image data
- Filtering and image enhancement of the image data

4.5.1 Subvolume extraction

CT scans can generate very large data sets which can prohibit effective analysis and quantification of the data. It is often necessary to reduce the file size prior to analysis in order to obtain useful results from the extremely large amounts of data. It is therefore common practice within CT image analysis procedures to extract a subvolume of the total scanned sample for analysis, in order to reduce the computational load of the process (Luo et al., 2010). Image data can also be converted to a smaller quantity of bits to reduce file size. However, as the file size determines the relationship between the greyscale range and the densities represented within the voxels of the image data, it is important to ensure that no greyscale detail is lost as the file size is reduced (Ahmed, 2014).

In studies which involve the microCT scanning of soils, the aim is not usually to visualise the network of macropores in large samples. As a consequence, the choice of subsampling technique and how representative the results obtained are, is not explicitly investigated. This is explored further in Chapter 7.

4.5.2 Segmentation of sample phases

The segmentation of image data refers to the identification and separation of the discrete materials or phases within a sample in order to allow for quantification and analysis of the properties of these constituents.

The greyscale value associated with each individual voxel after reconstruction is proportional to its X-ray attenuation coefficient, which is a function of material density. Therefore the intensity, or brightness, of each voxel is directly related with the density of the phase it represents. The densest sample constituents are represented by bright voxels (high attenuation) and the less dense pore spaces by darker voxels (low attenuation). An idealised example of a greyscale intensity histogram for a CT scan of soil can be seen in Figure 4.3. Different peaks within the greyscale histogram correspond to different material phases (densities) within the scanned sample (for Figure 4.3, these are air filled pores, organic material, and the solid soil matrix). Therefore a greyscale histogram can be used to distinguish between material phases and segment the data.

The most commonly used approach to segment image data is 'global thresholding' which uses an estimate from the intensity histogram of the image to define a threshold greyscale value between phases or constituents (Wildenschild and Sheppard, 2013). Many approaches to thresholding exist, a simple method being to use the lowest points in the valleys of the histogram. However, even after filtering (see Section 4.5.3.), finding the minimum point between two peaks can be difficult, as the intensity corresponding to each phase can overlap considerably (Figure 4.3).

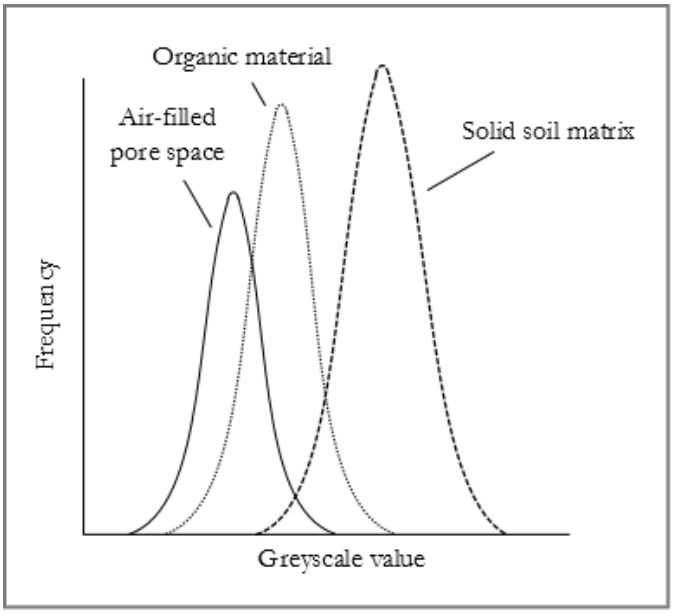

Figure 4.3 – Idealised greyscale (intensity) histogram showing three constituents/phases frequently present in X-ray CT scans. The cross-over in greyscale values between the phases makes segmentation a challenging task (Helliwell et al., 2013)

The difficulty associated with assigning an appropriate threshold value for segmentation can be further exacerbated by poor image quality (for example due to use of high energy X-rays on very dense samples, or a large focal spot size due to large samples, or due to acquisition time constraints (less exposure)). Figure 4.4 shows an example of the effect of poor image quality on the greyscale histogram achieved through scanning of a sand. It can be seen that poor image quality makes establishing accurate threshold values considerably more difficult.

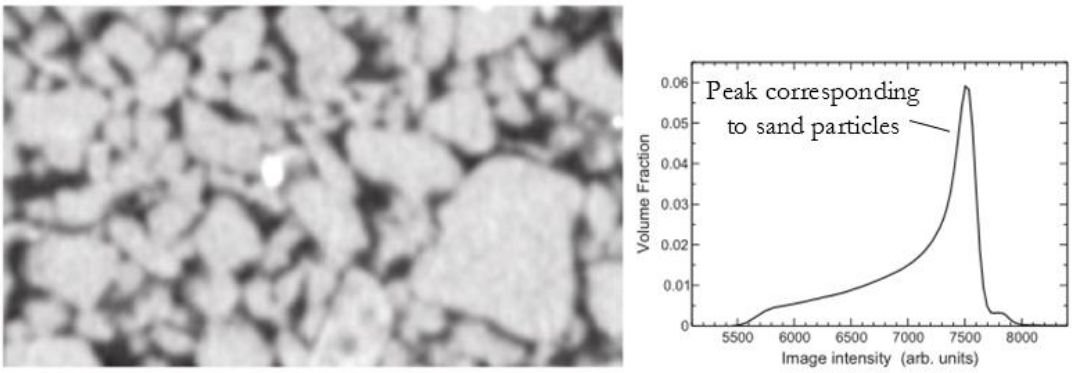

(a)

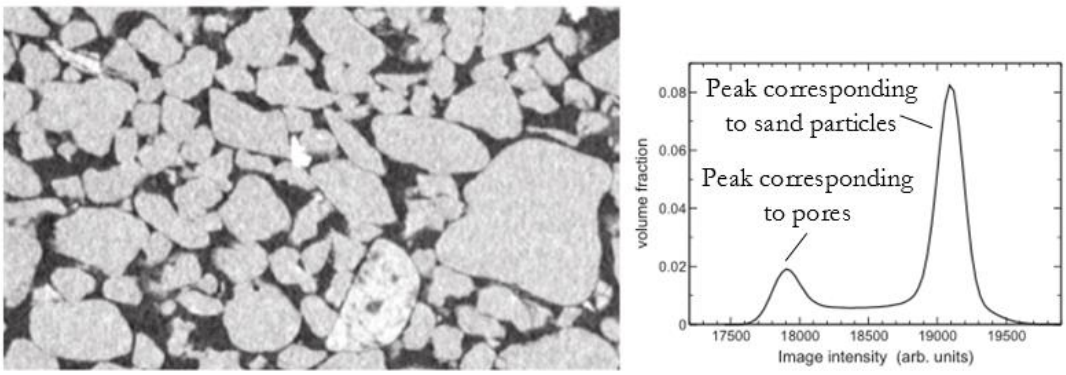

(b)

Figure 4.4 - An example of the effect of poor image quality on the greyscale histogram achieved through scanning showing (a) A slice of scan data histogram (unconsolidated sand) with poor resolution compared to the geometrical features (28μm) and corresponding single-peaked histogram. (b) An image of the same region with sufficient resolution for this sample (10μm) showing the corresponding clear double peaked histogram (Varslot et al., 2010)

The choice of threshold value has an important influence on the final results gained from the analysis programme, as a small variation can make a large difference in the volume and properties of the phases identified (Taina et al., 2008). Several manual or automated (either partially or fully) methods exist in order to determine the best value for the threshold used

for segmentation (e.g. manual thresholding or automated watershed-transform based methods).

Manual methods have been shown to produce differing results when compared. For instance, Baveye et al. (2010) showed that when thirteen CT experts were asked to manually threshold image data from the same scan, results of porosities varied by between 13 % and 73 %. For this reason, it is desirable to keep operator input or bias to a minimum during the analysis procedure. It is true however, that as long as the same analysis procedure is used on all the samples within a study, the quantitative results can be legitimately compared and meaningful conclusions made (Cnudde & Boone, 2013). Ideally, the reconstruction and analysis procedures would be completely automated or standardised to remove any operator bias so as to enable direct comparison between results from various researchers.

The effectiveness of segmentation methods is difficult to evaluate as there is no "right answer" when it comes to segmentation of microCT image data (Helliwell et al., 2013). Often only a visual comparison can be made between different methods to indicate which provides the most realistic segmentation of the sample image data. Additionally, the optimal segmentation method for a particular sample type and microCT setup will almost certainly not be optimal for other systems.

There is a clear consensus amongst the CT research community that automated methods are preferable in theory, since they both reduce the demands on operator time and eliminate operator bias (Sharma and Aggarwal, 2010). Recent advances in imaging hardware mean that for simple materials (i.e. with uniform densities), the grayscale image can be sufficiently clean that automated thresholding can be used. For instance Porter and Wildenschild (2010) showed that automated segmentation can work very well on high quality images of glass beads obtained using a synchrotron. Contrastingly, Iassonov et al. (2009) found that, for more complex materials, some fully automated methods give inconsistent results and that 'unsupervised' automated schemes cannot yet be used with any confidence. The use of automated methods on complex samples (e.g. clay fill) and large sample sizes (> 5 cm) remains underexplored and is investigated further in Chapter 7.

4.5.3 Image enhancement and filtering

When CT scans result in poor image quality, it can be difficult to segment the sample constituents using the greyscale intensity histogram. This can be due to inadequate image contrast, as shown in Figure 4.4, or image artefacts such as noise (see Section 4.6.) present within the image data. As a result, images acquired which contain significant amounts of image noise (e.g. scans of complex materials, using older systems, or with acquisition time constraints) can often result in a poor quality segmentation.

Corrections for noise and poor contrast can be carried out on the greyscale data prior to segmentation and many methods for performing edge-preserving noise reduction have been published (e.g. Sheppard et al., 2004). These methods can be very computationally intensive to apply to very large 3D image sets and the memory requirements for applying 3D image filters can lead to post-processing software becoming very unstable (Smith, 2015). It is therefore necessary to balance the benefits of image enhancement against the computational restraints involved in analysis of microCT image data during post scan processing.

Many filtering methods work by smoothing image data in order to remove noise. They modify the greyscale value of a selected voxel by comparing it to some measure of the greyscale value of its neighbouring voxels. Figure 4.5 shows the result of using one type of filter (median) on the resulting greyscale histogram of the image data from a scan of glass beads. The correct application of filters can lead to increased definition between the peaks corresponding to material constituents within a greyscale histogram and therefore allow for more precise thresholding and segmentation (FEI, 2014).

Commonly, smoothing of image data using filtering can reduce the contrast at the boundaries between phases (Chen et al., 2006). Some filters therefore include a sharpening process in order to correct for this and to reduce the partial volume effects often present within image data (See section 4.6.1).

Whilst image enhancement methods such as filtering and sharpening can assist in segmentation and therefore quantification of image data, they will always result in the total information content of an image being reduced, usually resulting in the loss or distortion of very small features within the image data (Smith, 2015).

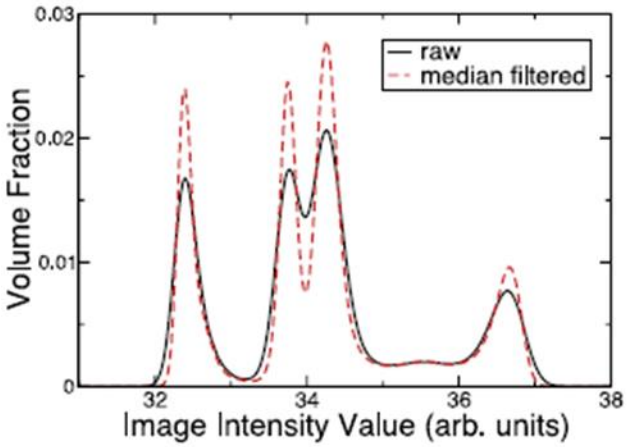

Figure 4.5 – The effect of median filtering on a greyscale histogram of showing sharpening of the peaks corresponding to each phase. (Scan of partially saturated glass beads – the two overlapping peaks of similar attenuation are from two different types of glass) (Porter and Wildenschild, 2010)

4.6 Artefacts within CT image data

The microCT technique can result in poor quality images as a result of insufficient image contrast, resolution, or from the presence of imaging artefacts within the data. The most common artefacts found within microCT image data are briefly discussed here.

4.6.1 The partial volume effect

When image data is reconstructed it is composed of 3D voxels arranged in a grid throughout the image. As a consequence, at the boundaries between the material constituents of a sample some voxels will contain more than one material. The greyscale value attributed to these voxels are therefore average values of the phases present. This is known as the partial volume effect (PVE) and is reflected in the blurring of edges between two different materials within a sample. Thus material boundaries, rather than being sharp, will often extend across 2-4 voxel widths featuring a gradual greyscale transition (Ahmed, 2014). Figure 4.6 shows an illustration of the partial volume effect on the greyscale values of voxels at the phase boundaries. Whilst filters to sharpen edges in an image can be applied during the image-processing stage, the blurring of material boundaries can never be completely avoided.

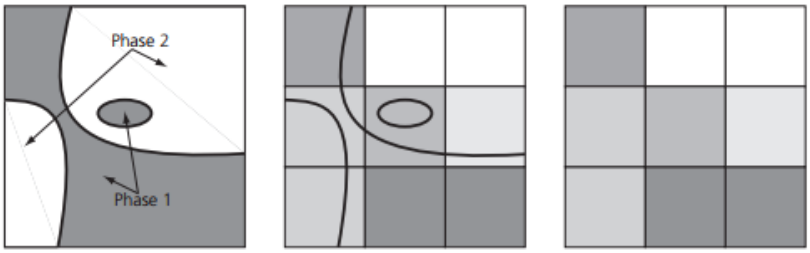

Figure 4.6 - Schematic of a sample with two phases and the corresponding greyscale of voxels within the image data, showing the partial volume effect on the voxels containing phases boundaries (Kato et al., 2013)

As a result of the PVE a number of voxels will have indeterminate greyscale values which will impact on segmentation of the image data. The degree to which the PVE influences the quality of segmentation and the measured properties obtained depends on the properties of the sample scanned (e.g. the size and distribution of pores present when scanning a soil).

A PVE correction involves the removal of small objects within the image data which cannot definitely be determined to lie within one phase or another. However the quantitative impact of this type of correction is another aspect of post scan image processing which is overlooked in the published literature discussing microCT work involving soils. This is examined in more detail in Chapter 7.

4.6.2 Beam hardening

All microCT machine X-ray sources generate a polychromatic beam (i.e. one that contains a spectrum of X-ray energies and wavelengths) (Wildenschild and Sheppard, 2013). Beam hardening occurs when there is an increase in the mean X-ray beam energy as it passes through a sample due to the energy dependence of the linear attenuation coefficient. Lower-energy (soft) x-rays are more readily attenuated than higher-energy (hard) X-rays and therefore have less penetrating power and will be absorbed more easily. This results in a beam relatively depleted in lower energies with reduced overall intensity but greater mean energy. The beam is therefore said to have become harder. The effects of beam hardening are typically shown by the outer edges of an object appearing brighter (i.e. denser with a larger grey value/attenuation coefficient) than identical material at the centre of the object. An example of this beam hardening artefact is shown in Figure 4.7.

Beam hardening, even when minor, makes segmentation more difficult since it is a large-scale, gradual inhomogeneity. It can be difficult to correct for the artefact because different elements within the scanned sample harden the beam in different ways, so each

path through a heterogeneous sample will diverge from Lambert–Beer's law in a different manner (Dewulf et al., 2012). The effect can be diminished by using beam hardening filters (thin sheets of copper or tin), which remove the lower energy soft X-rays before they reach the sample, ensuring only the high energy X-rays pass through (Mees and London, 2003). However, as discussed in Section 4.4., higher energy X-ray flux may make it harder to segment the data between phases. Beam hardening effects can also be corrected to some degree in post-processing, when software-based correction algorithms can be used to manually reduce common X-ray CT data artefacts (Boas and Fleischmann, 2012).

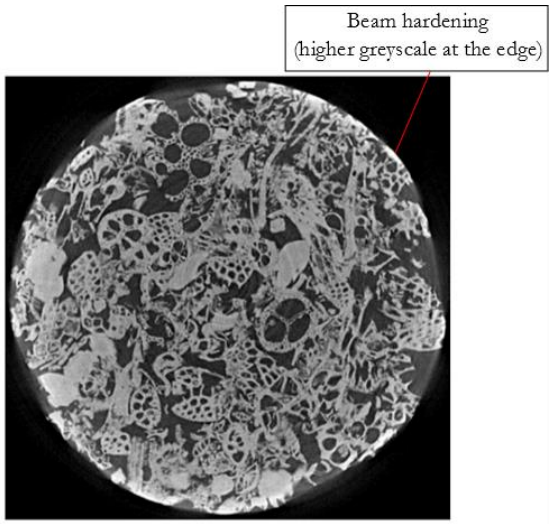

Figure 4.7 – An example of microCT scan image data exhibiting beam hardening (an apparent increase in attenuation near the sample edge (5 mm diameter calcite limestone) (Wildenschild and Sheppard, 2013)

4.6.3 Penumbra effect

As the X-ray source within a microCT scanner is a focal spot as opposed to a point source, when X-rays pass through the object some edge blurring can sometimes be observed (Kueh et al., 2016). Blurring specifically at the edges of a reconstructed volume is known as a penumbra effect.

When the focal spot size is small this effect is minimal and the boundary of images are very sharp. When the focal spot size is large, an X-ray's path depends on the location within the spot from which it originates. This can create a poorly defined image. The focal spot size is dependent on the distance of the sample from the source, the size of the sample and the power used for scanning. Increased power increases the focal spot size which generates a greater penumbra effect. Therefore it is desirable to minimise the X-ray power, in order to minimise penumbra artefacts. However, this may prevent enough X-rays

penetrating the sample within the specified exposure time and the effects of penumbra are further exacerbated by the partial volume effects described above (Ketcham and Carlson, 2001).

4.6.4 Other artefacts

As well as the major image artefacts discussed previously, several other types of artefact can occur within scan image data. These include noise, ring artefacts, star artefacts, and artefacts caused by sample movement or mechanical instability (Cnudde and Boone, 2013).

As with all experimental imaging techniques, CT image data is subject to noise (Poisson noise due to random variations in detected X-ray intensity). CT image noise is associated with the number of X-rays contributing to each detector measurement and therefore affected by all the CT settings used (e.g. voltage, current, scan time, and slice thickness) and the sample properties (Goldman, 2007).

Figure 4.8 shows an example of noise within scan image data. Ring artefacts are caused by the failure of one or more pixels in a pixelated detector or by the non-linearity of different pixels and result in sharp contrasting rings concentric to the centre of rotation within the image data (Sijbers and Postnov, 2004). Star artefacts appear as star shaped distortions around high density objects and are caused by inaccurate measurement of the X-ray attenuation of high density regions within a lower density material.

The degree of artefacts present within the scan images depends largely on the type of sample scanned. The use of optimal scan settings for a particular sample (e.g. power and exposure) can produce images of high quality with minimal artefacts and this is examined in detail in Chapter 6.

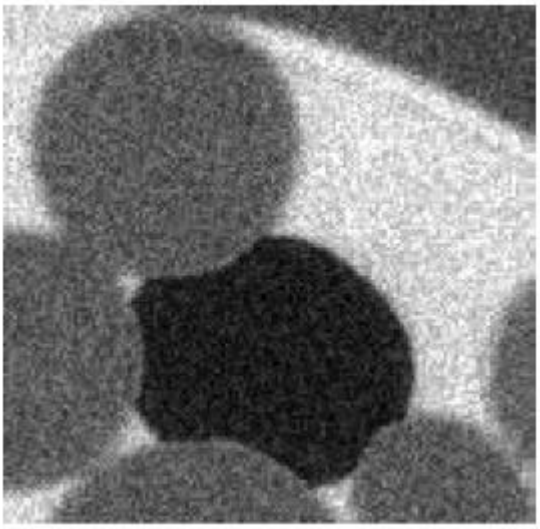

Figure 4.8 – An example of noise with the scan data of a partially saturated glass bead pack (Wildenschild and Sheppard, 2013)

4.7 MicroCT scanning of soils

Computed tomography has been used to scan soil samples for various purposes over the past decade or so (e.g. Perret et al., 1999; Vogel, 2000; Mooney, 2002; Mees and London, 2003; Sněhota et al., 2007; Luo et al., 2008; Anderson et al., 2010; Peth et al., 2010; Mooney et al., 2012; Geistlinger, 2013; Naveed et al., 2013; Shin et al., 2013; Lamorski et al., 2014; Larsbo et al., 2014; Katuwal et al., 2015; Eck et al., 2016).

The microCT technique is continuously growing in popularity as a research tool within geoscience due to the rapid technological and computational progress being made. Indeed, Cnudde and Boone (2013) predict that the number of research projects using microCT will continue to rise, and that microCT will become an indispensable technique in the field of geosciences.

The following key conclusions can be drawn from a review of the published literature regarding CT in the field of geosciences in terms of the materials and sample sizes that have been researched and the scanning procedure used.

Materials and sample size – The majority of microCT soil research has involved samples consisting of narrowly-graded materials with particle sizes between 0.1 mm and 2 mm (i.e. sands) (Smith, 2015). In general, scanning of clay materials has been avoided, although Naveed et al. (2013) and Larsbo et al. (2014) have measured the macroporosity of clay soils.

Scanned samples have almost always tended to be reformed or reconstituted samples and there is a lack of data for natural undisturbed samples. This is probably because

reconstituted samples tend to have a more uniform range of densities and can therefore lead to better quality images (with easier segmentation).

Most published microCT literature within the geosciences uses cylindrical samples with diameters of less than 15 mm, with sample sizes generally ranging from 1 mm to 5 cm (Wildenschild and Sheppard, 2013). The sample sizes scanned are often limited by the type of microCT scanner used, or most commonly, the desire to achieve very high resolution images so that very small objects within the image data can be identified. Visualising the network of macropores in undisturbed clay fill samples therefore requires scanning of larger samples than are commonly scanned.

It is also worth noting that a significant number of papers using CT have not published any quantitative results (e.g. measurements of material or pore properties) from their scans. Although visualisation and qualitative analysis is, in itself, a very valuable tool, this does not take full advantage of the potential of the CT technique.

Scanning procedures – Due to the large variation in uses of the microCT technique, covering a range of sample sizes, shapes, and materials, there are no generally accepted protocols which exist regarding microCT scanning procedures. Therefore a great number of parameters involved in these processes which influence the final results of the scan (e.g. tube voltage, number of projections, total exposure time, etc.) can vary from scan-to-scan. Many published papers contain little to no information on the specific scanning procedures used by researchers to perform their scans. As Smith (2015) stated, this has led to CT being presented as a 'black-box analysis technique' which can provide perfect information about any given sample rather than as a key stage within the experimental procedure, the limitations of which should be critically analysed. This approach has potentially limited development of the technique, as researchers cannot build from a large knowledge base to further advance the technique and to develop new methods specific to the geosciences.

One of the main potential advantages of the microCT technique in relation to soil science is that it is a non-destructive characterization technique which allows observation of temporal internal structural changes at high resolutions.

With the exception of Peth et al. (2010) researchers have yet to fully take advantage of the non-destructive nature of the CT technique in order to repeatedly scan samples under altered conditions (e.g. after changes in saturation) and to analyse quantitatively the evolution of the pore structure (Helliwell et al., 2013). Peth et al. (2010) used CT to observe structural

changes and crack formation during wetting and drying of 5 cm and 5 mm loess samples. It was observed that wetting produced a rearrangement of particles accompanied by a restructuring of the pore space. This was a result of swelling and the formation of new coarse pores due to entrapped air.

No research has explored the evolution of pore structure with saturation within clay fill samples.

4.8 Critical discussion

Within microCT literature, many of the variables it is necessary to define to perform a scan often appear hidden when researchers come to publish results. MicroCT in the geosciences has tended to focus on small samples with idealised constant density (e.g. glass beads) which makes scanning easier and enables higher image quality to be achieved in order to observe the smallest object possible within the scan.

However, MicroCT has the potential to allow for the three-dimensional visualisation of large heterogeneous soil samples in a non-intrusive manner, provided that scanning and image analysis procedures are developed which can overcome the issues involved with the technique.

A scanning procedure is needed which uses suitable power settings for the size and type of sample investigated in order to achieve sufficient image quality (contrast and resolution) with minimal imaging artefacts. Currently within the geosciences, microCT scanning of soil has been primarily concerned with small samples (< 5 cm) and tended to focus on uniform remoulded samples. Chapter 6 investigates the capabilities of microCT and the development of a scanning procedure for larger clay fill samples.

A consistent image analysis procedure is needed to allow for comparison of results from different scans. However, more understanding is needed regarding the effects of subsampling method, the most efficient image enhancement method, the viability of automated segmentation, and the impact of a PVE correction for a large clay fill sample. This is discussed further in Chapter 7.

MicroCT also provides the potential of scanning samples in different saturation states to examine the evolution of the internal macropore structure of samples and this aspect is explored in Chapter 8.

5 Hydrological modelling of Newbury cutting

5.1 Introduction

This chapter presents details of a finite element modelling exercise in which the hydrological conditions within a case study cutting slope were explored using site-specific climate and soil input parameters.

The modelling undertaken investigates slope hydrology in response to real climate conditions and examines the key influences and uncertainties affecting flow in the system. This chapter informs the direction of the laboratory work carried out to subsequently understand the complex role of macropores within infrastructure slopes.

Climate data collected from an instrumented section of a highway cutting was used within a hydrological finite element model (Vadose/W (GEO-SLOPE, 2008)) to calculate pore water pressure and volumetric water contents throughout the slope over a three year period. A model domain and soil parameters were established using an initial sensitivity analysis and validated with field data. A comprehensive sensitivity analysis was then conducted using this 'field representative model', in which the results of the model with varying input parameters were compared to site-measured pore water pressure and volumetric water content distributions. This was used to investigate the modelling process and the hydrological relationships involved, particularly, the influence of factors controlling water transfer at the surface of the slope.

5.1.1 Modelling aims and objectives

This chapter aims to examine the primary controls on water transfer into and out of slopes using a field representative model and sensitivity analysis. The influence of anisotropy of hydraulic conductivity, unsaturated soil behaviour characteristics and hydraulic conductivity variation at the surface and at depth within the model were explored.

The specific objectives of this modelling exercise were:

- To take input data from Newbury cutting and compare simulated pore water pressures and volumetric water contents with field measured data, in order to explore the implications of soil heterogeneity in slopes in relation to the continuum assumptions made within hydrological models (See Chapter 2). Specifically, does the field representative model (using Darcy-Richards type flow equations) capture the hydrological behaviour of the slope and do the definitions of unsaturated soil

behaviour (e.g. SWRCs) enable accurate simulation of in-situ conditions in both wet and dry conditions.

- Learn from sensitivity analyses to determine the key model parameters which affect slope hydrology and pore water pressures within models. Particularly, to use understanding from the modelling process to comment on anisotropic flow within slopes and the influence of variation of both the near-surface and underlying hydraulic conductivity of the slope.

5.1.2 Key facets of modelling

Before commencing a discussion of the modelling carried as part of this investigation, it is perhaps worthwhile to briefly note the general purpose of modelling within geotechnics and some important aspects of good modelling practice.

In the geotechnical engineering field, the physical systems which engineers deal with on a daily basis are extremely complex. So in order to convert a complex physical reality into a mathematical system which can be used to understand risk and uncertainty, it is necessary to simplify the system and reduce it to its most important components. Perhaps contrary to popular belief, the main goal of numerical modelling is not to predict future performance. Rather, the main goal is to enter into a process in which it is possible to improve engineering judgements and understanding of the system (Fredlund et al., 2012).

As Wood (2003) notes, it is good practice that any commercial software used is verified prior to model development either using a simpler problem or an initially simpler conceptualisation. This process has two benefits, namely, it confirms that the modelling software is working correctly in appropriate scenarios, whilst also allowing the user to become familiar with the software and the intricacies associated with using it. The ultimate aim of this initial process is the development of knowledge and confidence in the limits of the modelling software, theory, and results (GEO-SLOPE, 2008).

Vadose/W was benchmarked (validated) against other FE software and an analytical method using a simple 1D caisson problem. For further discussion of this preliminary modelling exercise please see the Appendix.

It is also good practice to begin modelling using the simplest model possible and then gradually add complexity (Vaughan, 1994). After development of a model, a sensitivity analysis can be conducted in order to gain understanding of the engineering processes and model parameters. This analysis involves running a series of simulations in which only one

parameter is varied at a time. Results of these simulations are then compared to an indicator of performance, for example, water content in a particular region. The aim of a sensitivity study is to aid understanding with regards to which elements of the conceptual and theoretical models are of most importance. As noted by Barbour and Krahn (2004), one of the key reasons for creating complicated numerical models is to enable us to explore and eliminate aspects of complexity from the physical system until it is possible to identify one or two central ideas.

5.2 Newbury site description

The modelled cutting, which is adjacent to the A34 Newbury bypass in southern England (Figure 5.1) was constructed in 1997 and is entirely within a region of London Clay. The clay at the site is about 20 m thick, highly weathered in places to a depth of about 2.5 m below original ground level, and underlain by Lambeth Group deposits and Upper Chalk. After the cutting was excavated, around 0.4 m of topsoil was placed over the cut London Clay surface to facilitate the planting of vegetation on the slope. A gravel fin drain approximately 0.6 m deep was installed at the roadside approximately 4 m from the toe of the slope (Smethurst et al., 2006).

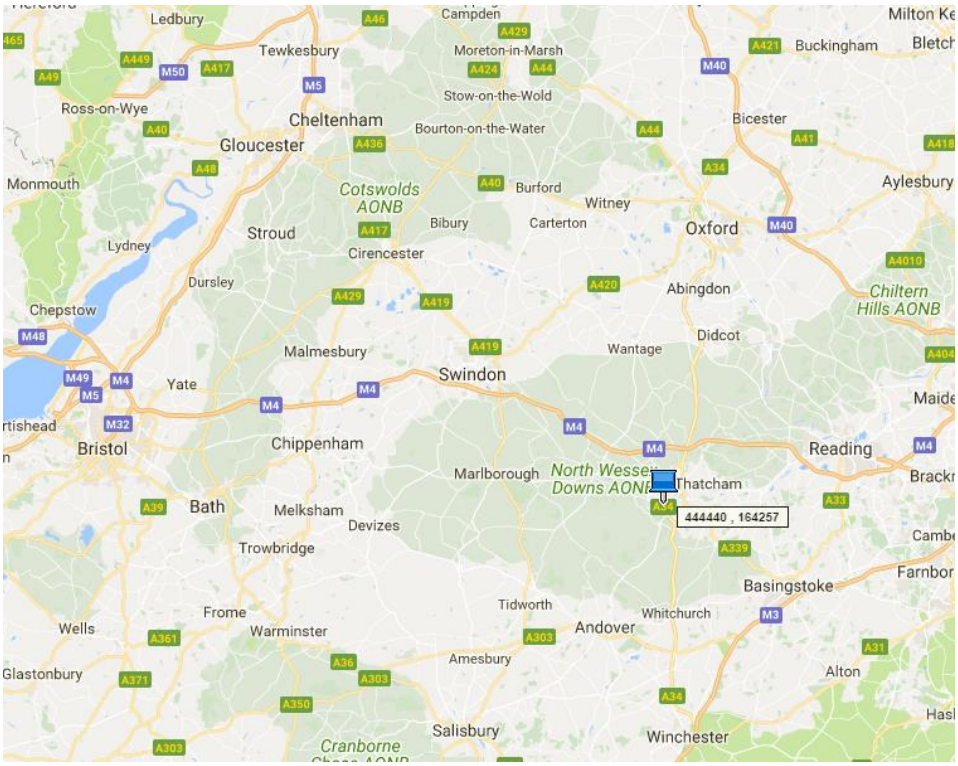

Figure 5.1 - Map showing the location of the instrumented site (Google maps (2016))

The cutting is east facing, 8 m high and 28 m long. A cross-section through the slope is shown in Figure 5.2. Instruments were first installed on the site by researchers from the University of Southampton in 2003 in order to monitor soil water content (VWC), pore water pressure (PWP), rainfall, runoff, and the climate data required to estimate evapotranspiration (Smethurst et al., 2006). Monitoring of the site has continued since installation in 2003 (Smethurst et al., (2006), Smethurst et al., (2012)).

The equipment installed on-site includes arrays of time domain reflectometry (TDR) probes, flushable wire piezometers, water-filled tensiometers and equitensiometers in four groups spaced along the slope at depths of between 0.3 and 2.5 m. (Figure 5.2). A climate station was placed on the slope to record air temperature, humidity, wind speed, and solar radiation, whilst rainfall and surface runoff were measured using a rain gauge and an interceptor drain. A calibrated neutron probe was also used to measure soil water profiles at approximately two-monthly intervals. For further information on sensors installed on the site see Smethurst et al. (2012).

All the field data shown in this Chapter from the Newbury site has been collected by Smethurst et al. (2006) and Smethurst et al. (2012) although it may be presented in new forms.

Due to the nature of the field measurements at the site and their respective collection methods, it was observed that the years 2006-2009 were the years with the best combination of reliable weather, pore water pressure and water content measurements (as explained below - see Section 5.3.). For this reason and to prevent overly long computational times, it was decided that these three years would serve as the modelling duration.

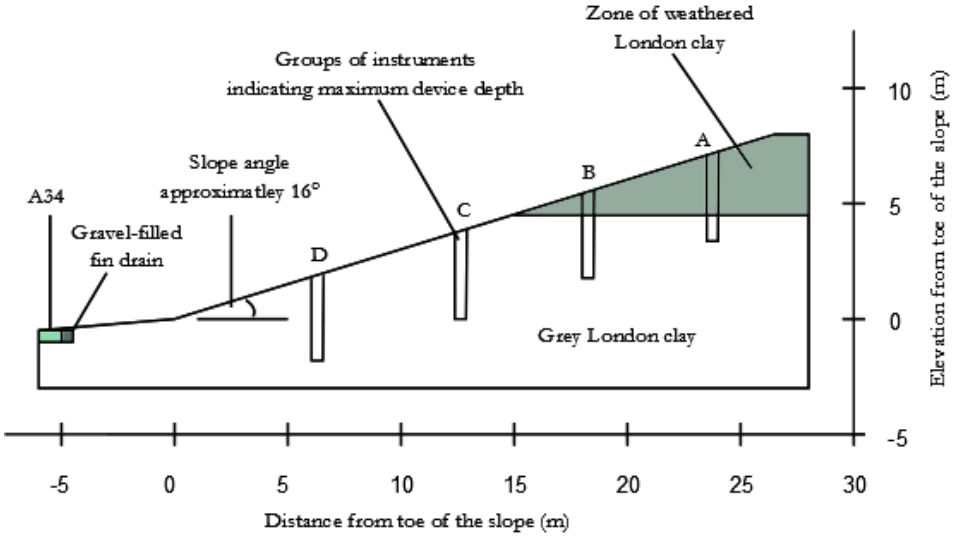

Figure 5.2 – A cross-section of Newbury cutting showing the location of instrument groups (redrawn from Smethurst et al. (2006))

Vegetation at the site is shown in Figure 5.3. The slope was covered in medium length grass with some small shrubs, however, the very top of the slope was fringed by fully mature trees. The vegetation change at the site throughout the study period was not measured.

Figure 5.3 - Picture of the modelled cutting and the vegetation present (from the top of the slope)

5.2.1 Site weather and monitoring data summary

Cumulative annual rainfall and soil moisture deficit (calculated from a 1D water balance concept as described earlier in Chapter 3) for the years 2003-2013 are shown in Figure 5.4, along with cumulative estimated potential and actual evapotranspiration (See Appendix for a table of evapotranspiration parameters).

Figure 5.4 shows that in the relatively dry summers of 2003, 2005, 2006 and 2010, actual evapotranspiration is significantly less than potential evapotranspiration. This is due

to a reduction of transpiration caused by plant stress during prolonged dry periods when SMD exceeded the readily available water within the soil (see Chapter 3).

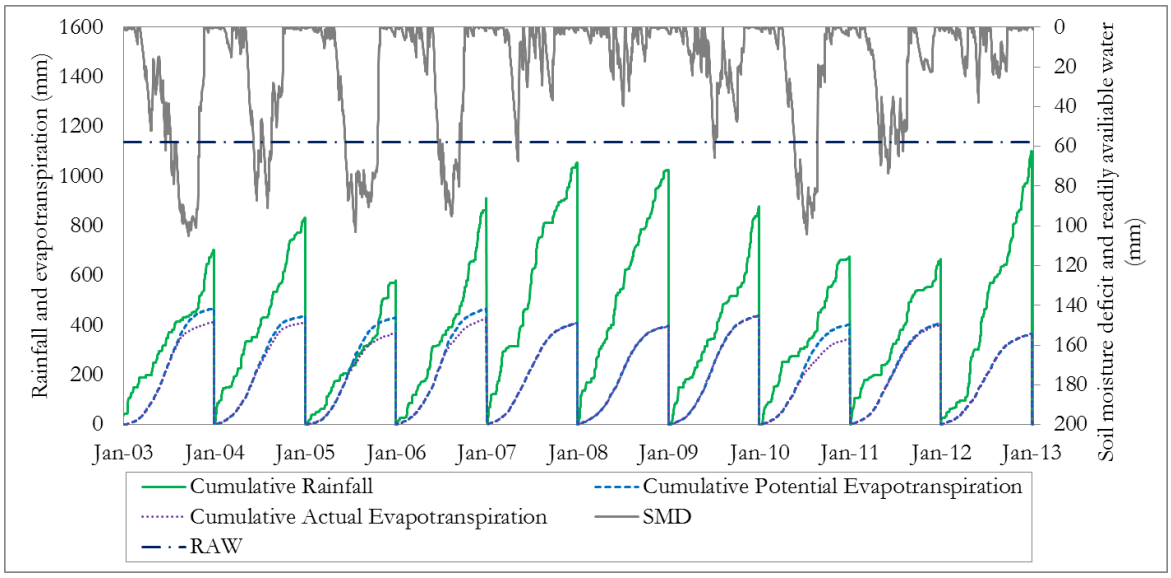

Figure 5.4 – Cumulative annual rainfall, soil moisture deficit and estimated evapotranspiration at Newbury 2003-2013 (data from (Smethurst et al., 2012))

Figure 5.5 which presents cumulative monthly rainfall at the site, shows that the winter of October 2006 until March 2007 was continuously above the long term average rainfall (LTA) for the site. Similarly, the summer months of 2008 were wetter than the LTA, whilst, during the summer months of 2007 the site was subject to almost twice the average rainfall.

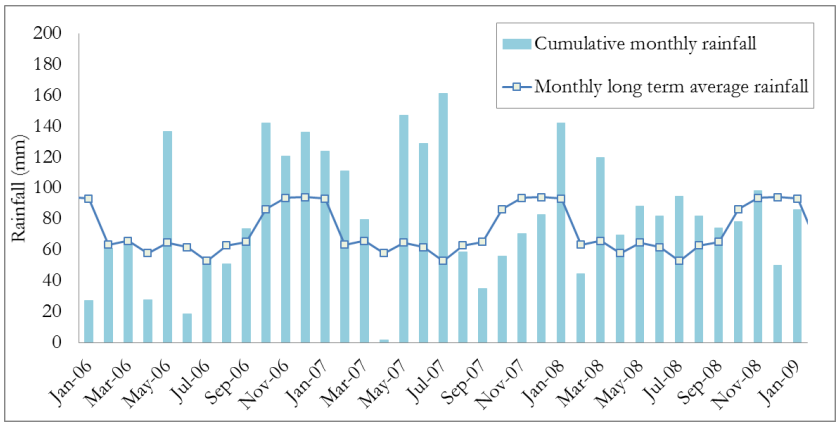

Figure 5.5 - Cumulative monthly rainfall at Newbury 2006-2009 and long term average monthly rainfall (1970-2013) (data from (Smethurst et al., 2012))

Figure 5.6 shows that 2007 and 2008 had the highest cumulative rainfall since 1970, making them representative of extremely wet years.

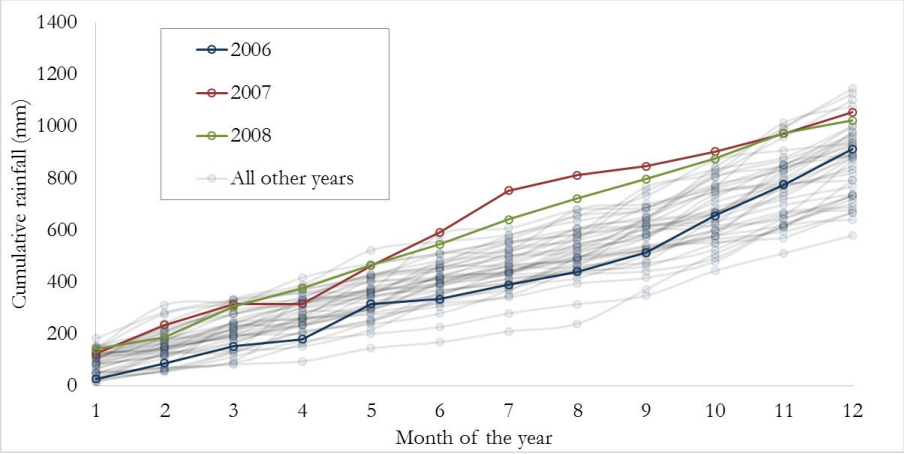

Figure 5.6 - Cumulative annual rainfall at Newbury every year since 1970 (data from (Smethurst et al., 2012))

The extremes captured during this period are highlighted by examining the return periods for the modelled years (Figure 5.7). These return periods were calculated from the relative frequency of the total annual rainfall at Newbury for every year since 1970 (data from (Smethurst et al., 2012)). More information on these calculations can be found in the Appendix.

In terms of total annual rainfall (Figure 5.7 (a)), all three years were wetter than the long term average. 2006 has a relative frequency of 1 in every 2.5 years, 2007 of approximately 1 in 10 years, and 2008 of around a 1 in 8 years.

If rainfall during the summer months of June, July, and August of each year are examined (Figure 5.7(b)) it can be seen that the summer of 2006 was well below average with a cumulative probability of exceedance of 72.1%, indicating that this was a particularly dry period compared to other years. However, the summer of 2007 was the most extreme within the dataset with respect to summer rainfall and the summer of 2008 has a return period of approximately 1 in 10 years indicating that this was also an exceptionally wet summer.

For the winter months December, January and February, 2006 was very wet, having an approximately 1 in 14 years return period. The year 2007 was wetter than average with a 1 in 3 years return period and 2008 was significantly drier than average (Figure 5.7 (c)).

The modelled period (2006-2009) therefore contains both periods of below average and moderately extreme rainfall and provides a good opportunity to explore a wide range of potential hydrological conditions within the cutting.

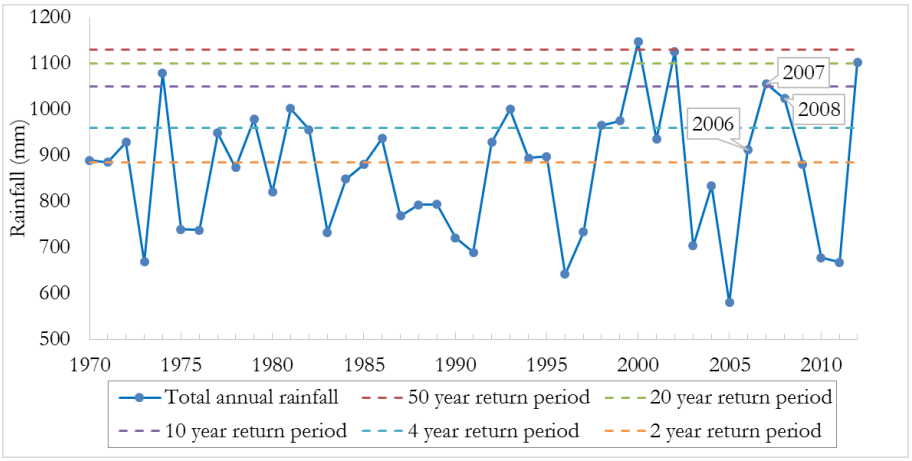

(a)

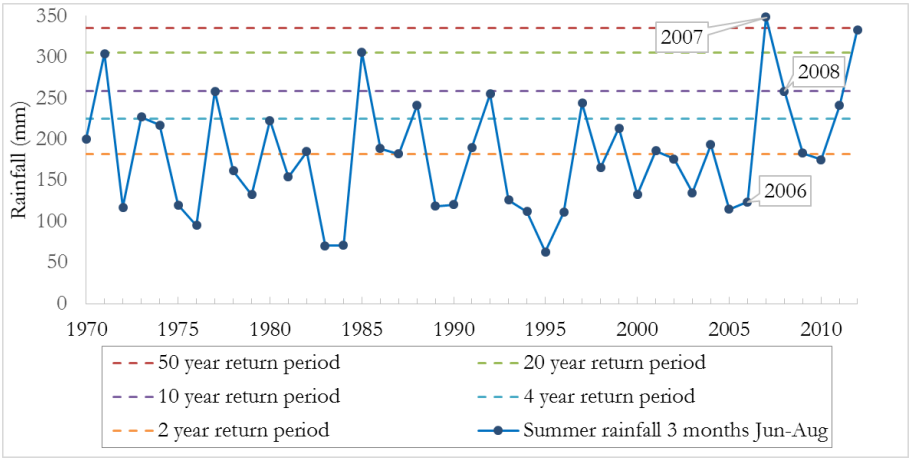

(b)

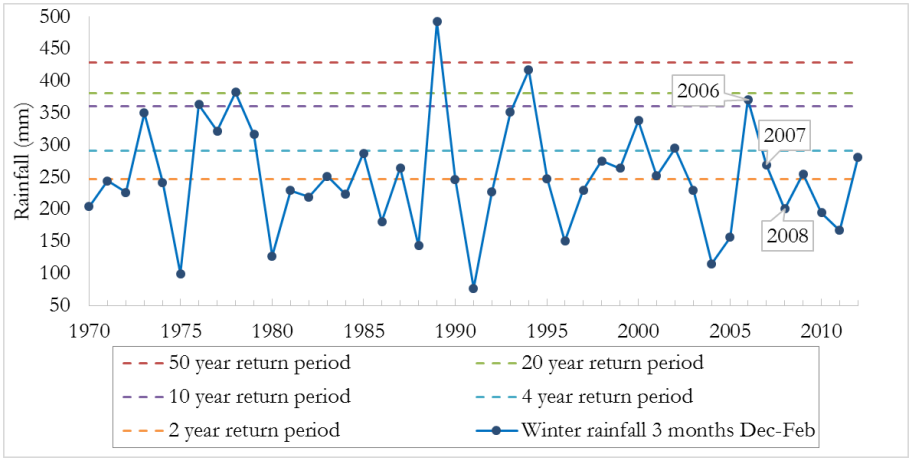

(c)

Figure 5.7 - Return periods for all years since 1970 based on (a) Total annual rainfall (b) Total summer rainfall (June-August) (c) Total winter rainfall (December-February) (data from (Smethurst et al., 2012))

Despite the fairly extreme variation in rainfall throughout the modelling period, site-measured solar radiation and temperature (Figure 5.8) was consistent each year, with only slightly higher temperatures and radiation measurements during the driest summer of 2006.

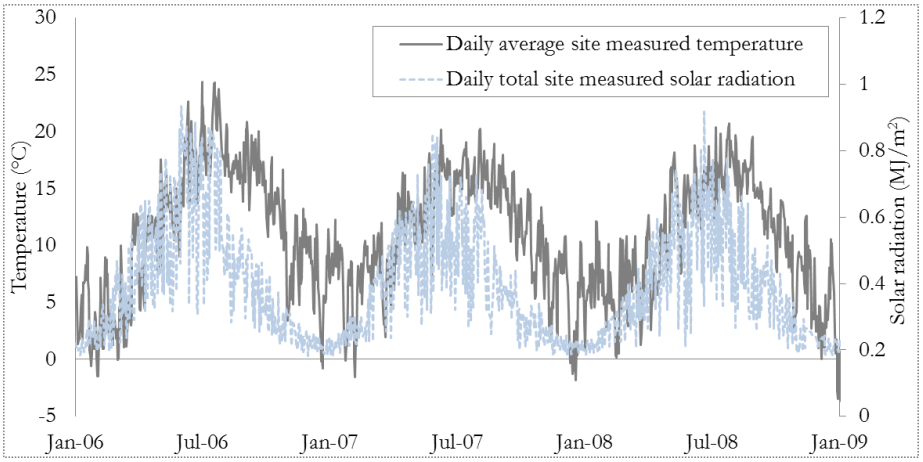

Figure 5.8 - Daily average temperature and solar radiation measured at Newbury (data from (Smethurst et al., 2012))

Instrument locations A and C (Figure 5.2) were deemed the most reliable of the four instrument groups on the slope (due to instrument reliability) and are therefore the primary field results used for comparison with the results of the simulation. Figure 5.9 & Figure 5.10 illustrate the pore water pressure variation at location C between 2006 and 2009. There are noticeably higher suctions during the dry summer of 2006 compared to the other years. The magnitude of the response of PWP to changing weather conditions decreased with increased measurement depth, as the influence of vegetation and evapotranspiration decrease with depth. However, a suction was still present at a depth of 2.5 m during the summer of 2006. The positive PWPs recorded at this depth (2.5 m) throughout 2007 and 2008 imply that this point usually lies below the groundwater table at this location on the slope.

It is important to note that the tensiometers installed in the slope here are limited to a maximum suction of around 100kPa, as at greater suctions they become desaturated (See Chapter 3). Therefore it is possible that higher suctions were present during the summer of 2006 than were measured by the tensiometers.

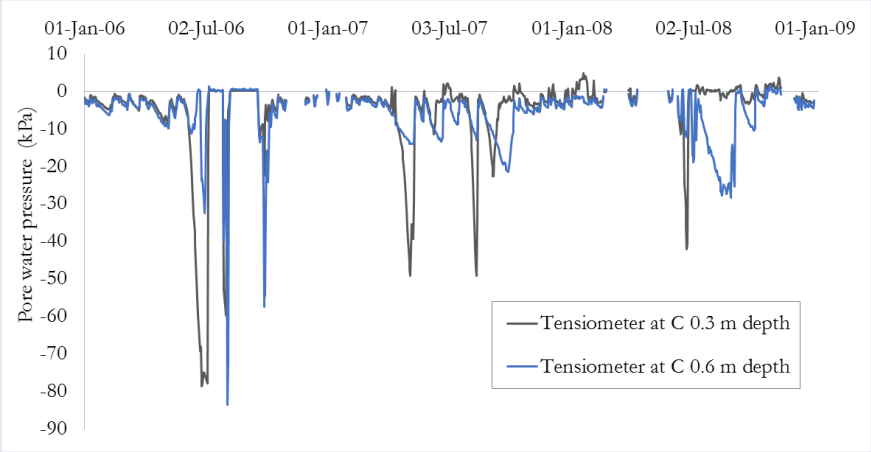

Figure 5.9 - Pore water pressures from tensiometers at C (data from (Smethurst et al., 2012))

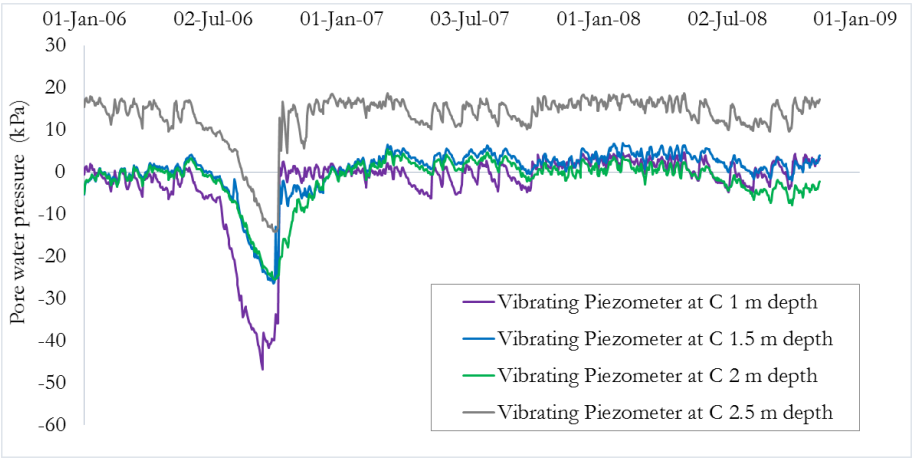

Figure 5.10 - Pore water pressures from vibrating piezometers at C (data from (Smethurst et al., 2012))

The variation of pore water pressure change with depth can be explored by plotting the maximum and minimum depth profile envelopes of PWP at the different instrument locations (Figure 5.11). These envelopes are the maximum and minimum values of pore water pressure recorded at all instrumented depths throughout the profile at location C between 2006 and 2009. The narrowing of each of the yearly envelopes with depth (Figure 5.11) indicate that there was a greater range of pore water pressure at the near-surface than at depth. This reflects the diminishing role of surface effects throughout the soil profile.

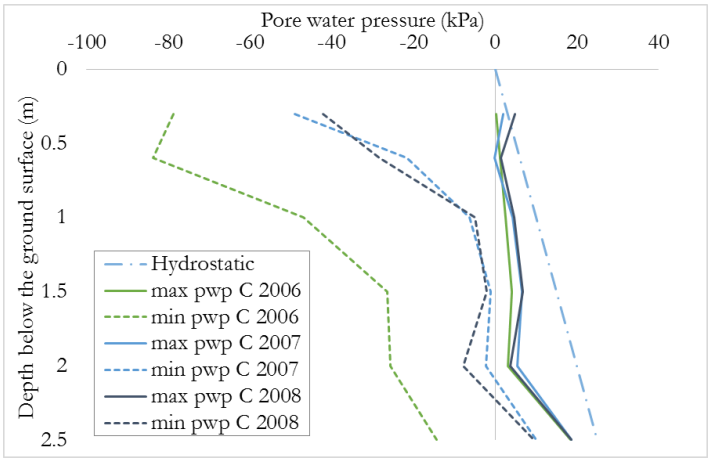

Figure 5.11 – Maximum and minimum depth profile envelopes of pore water pressure from tensiometers and vibrating piezometers at C (data from (Smethurst et al., 2012))

Volumetric water content (VWC) was recorded at Newbury and the results from TDR probes at A are shown in Figure 5.12. Below a depth of about 1 m the profile shows minimal VWC change due to changing climate conditions, with the exception of the very dry summer of 2006.

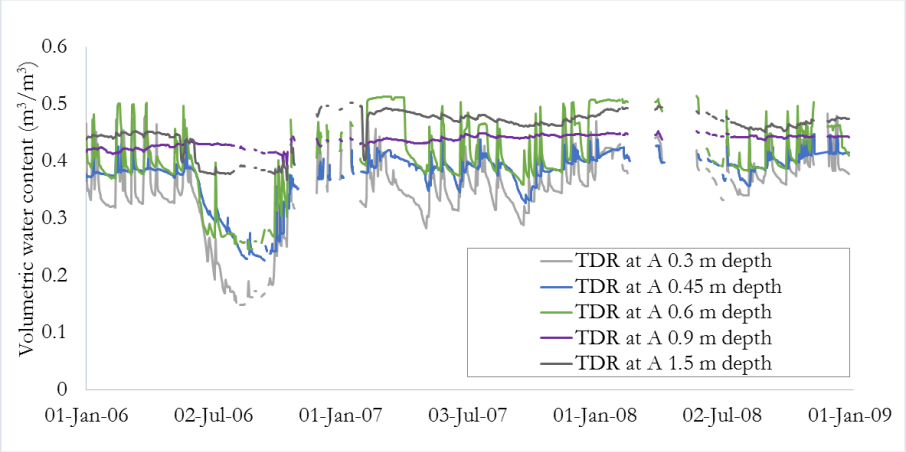

Figure 5.12 - Volumetric water content from TDR probes at A (data from (Smethurst et al., 2012))

Water contents at the instrumented locations were measured periodically using a neutron probe by Smethurst et al. (2012). Figure 5.13 presents profiles measured using the neutron probe over the summer of 2006 and shows that a change in water content occurs above a depth of about 0.7 m, with little difference below this depth throughout the summer.

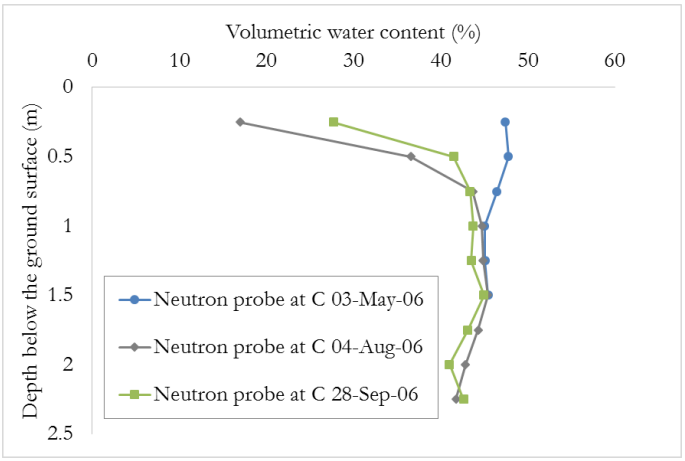

Figure 5.13 - Volumetric water content profiles across the summer of 2006 using a neutron probe (data from (Smethurst et al., 2012))

As discussed in Chapter 3, Soil moisture deficit (SMD) can be a useful tool for assessing the amount of water within the near-surface zone. As well as being calculated from a one dimensional water balance (Chapter 3 - Equation 25), SMD can also be inferred from the TDR array and neutron probe measurements at the site using Equation (37) (Smethurst et al., 2012). By subtracting the daily depth profiles from the field capacity profile, a deficit within the instrumented zone can be calculated.

$$SMD = \sum_{i=1}^{n} \Delta w_{vol(i)} \times h_{(i)} \qquad (37)$$

Where,

n is the number of measurement depths within the root zone, Δw_{vol} is the change in volumetric water content, and h is the depth of profile over which the measurement of change in water content is taken. (Total root zone depth was taken to be 800 mm to correspond with the 1D balance method (see appendix) and the wettest profile measured throughout the study period was assumed to correspond to SMD = 0).

The three estimated soil moisture deficits (from a 1D water balance, from the neutron probe measurements, and from the TDR array measurements) are presented in Figure 5.14. There appears to be good agreement between the SMD estimations, although only three suitable neutron probe measurements were taken during the modelled period (2006 - 2009) and some of the TDR data is incomplete. However, the overall magnitude of estimated SMD and pattern of response to wetting is similar.

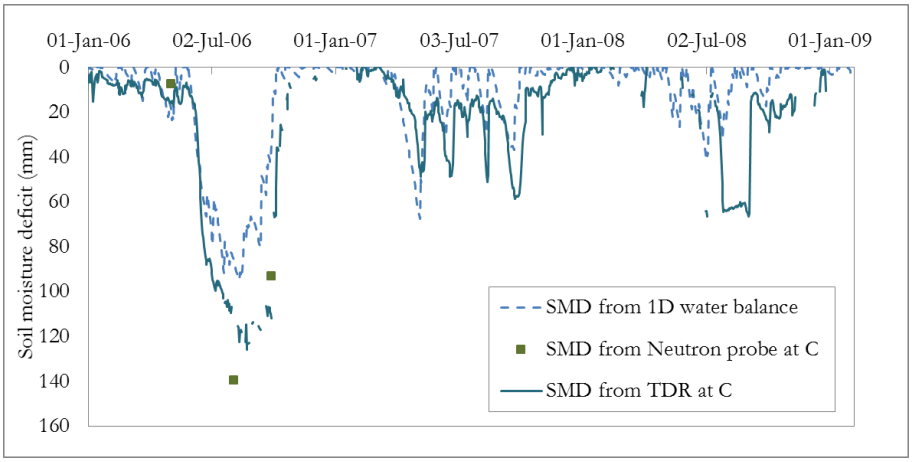

Figure 5.14 - Soil moisture deficit derived from a 1D water balance, neutron probe measurements, and TDR measurements at C (neutron and TDR probe data from (Smethurst et al., 2012))

5.3 Modelling

5.3.1 Vadose/W description

The finite element software Vadose/W was used to model hydraulic conditions within the cutting at Newbury (GEO-SLOPE, 2008). The software was used to calculate changes in pore water pressure in response to a boundary condition informed by real historical climate data. The effects of vegetation on slope hydrology were also explored and this is discussed further in the Appendix.

Vadose/W calculates saturated and unsaturated water, heat and vapour flow in response to applied boundary conditions using Wilson's form of Richard's equation (Wilson, 1990)(Equations (13) and (14) in Chapter 2). Vadose/W includes the provision to specify a climate boundary condition which uses daily climate data to calculate water infiltration and removal from the surface of the soil and the rooting zone (see Section 3.7.). This allows for the investigation of changes in pore water pressure and volumetric water content in response to variations in weather conditions, soil properties, or vegetation cover.

Vadose/W was used for this investigation as opposed to alternative commercial software (e.g. Hydrus (Šimůnek et al., 2013), Shetran (Ewen et al., 2000), etc.) for a number of reasons. The most important was that this software uses the equations and descriptions discussed in Chapters 2 and 3 which are the most commonly used modelling approaches (e.g. Darcy-Richard's) in the geotechnical industry and it was therefore possible to investigate the impact of the assumptions and theory previously discussed.

For clarity, any results obtained from numerical analysis in this Chapter are described here as 'calculated', whereas any results presented from site instruments are described as 'measured'.

5.3.2 Interpreting field conditions and creating a field representative model

To create a model of Newbury which could be used to aid understanding of the site, it was first necessary to establish model inputs which are an accurate representation of the site material properties, initial model conditions, and boundary conditions. Using site-specific field data wherever possible in combination within an initial sensitivity study a 'best field representation of Newbury' model was created. This model was assessed in comparison with site instrumentation data and used as a 'field representative model' or 'base model' for all subsequent sensitivity analyses. Construction of this field representative model is explored here.

5.3.3 The model domain

The domain was derived from a cross-section of the cutting (see Figure 5.2). However, as shown in Figure 5.15, the domain is extended at the sides and below what would usually be defined as the cutting. This was to ensure that edge effects of the boundary conditions other than the soil surface did not overly influence hydrology within the slope as discussed in Powrie (2013).

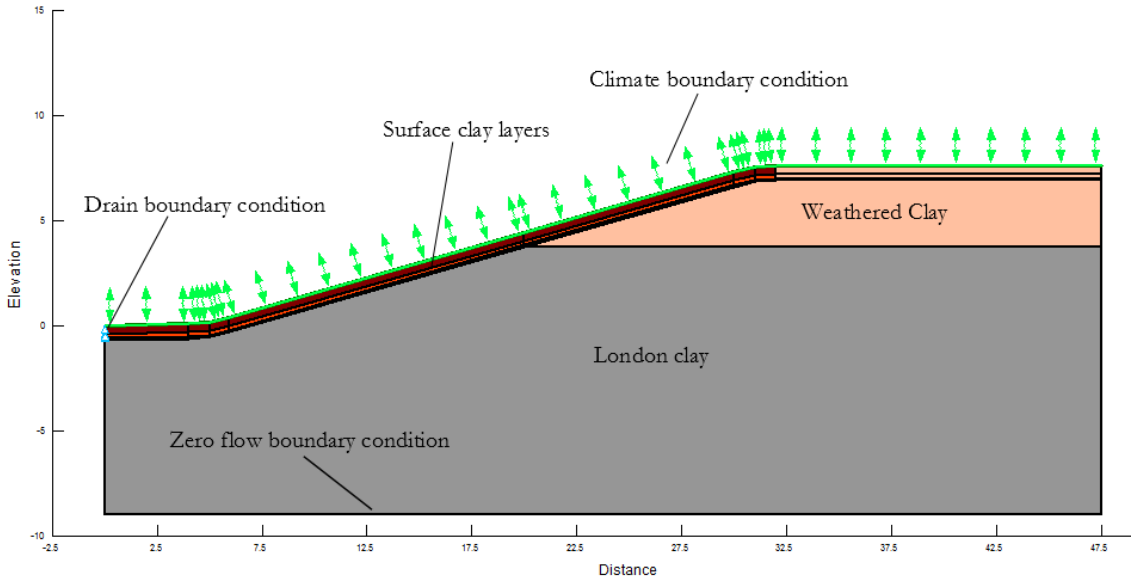

Figure 5.15 - A cross-section of the field representative model domain used with Vadose/W

A mesh which varied in size was discretised within the model domain. The mesh was very fine within the surface layers (0.1 m elements) to ensure accurate calculations but coarser at depth to avoid overly long computational times (0.5 m elements). The mesh was also made finer at any boundaries between materials to prevent unconverged nodes developing (GEO-SLOPE, 2008). Correspondingly, although results are output in daily time steps, adaptive time stepping was used within the solver to ensure convergence.

5.3.4 Material properties

Values from permeability measurements for Newbury from literature are shown in Table 5.1. Borehole bail-out tests were carried out in May 2003 by Smethurst et al. (2006), in unlined boreholes extending to depths of 2.0 m below ground level. Double ring infiltrometer tests were carried out at the site at a later date (Briggs et al., 2012).

It can be seen that in-situ measurements from borehole bail-out tests for the site are typically one or two orders of magnitude larger than laboratory measured values. This is likely a result of the scale of the laboratory measurements failing to fully capture the effects of anisotropy and the soil fabric (e.g. bands of silt/sand or clay fissures).

Measurements from infrastructure slopes show that saturated hydraulic conductivity (k_{sat}) can vary by up to five orders of magnitude in the top 0.5 m of infrastructure slopes. At greater depths the k_{sat} generally reduces and is less variable (Dixon et al., in review).

The field representative model was established using averages of the laboratory and site-measured values and by defining four distinct regions in the domain which are seemingly present within the cutting (London clay, weathered clay, sub surface, and surface). The influence of the number and permeability of the surface layers is discussed in more detail later in this chapter.

Table 5.1 - In-situ and laboratory saturated hydraulic conductivity (k_{sat}) measurements on samples from Newbury Cutting

Depth (m)	Material	Measurement type	k_{sat} (m/s)	Average k_{sat} (m/s)	Researchers
0.1	-	DRI*[1]	3×10^{-8} to 2.4×10^{-7}	9.2×10^{-8}	Briggs et al. (2012)
0.6	-	DRI	2.45×10^{-8} to 9.6×10^{-7}	9.3×10^{-8}	Briggs et al. (2012)
0.5-3	London clay	Triaxial	3.9×10^{-11} to 6.6×10^{-10}	2.3×10^{-10}	Smethurst et al. (2006)
3	London clay	BBO*[2]	2.3×10^{-9} to 4.4×10^{-9}	3.7×10^{-9}	Smethurst et al. (2006)
0.5-3	Weathered clay	Triaxial	5.0×10^{-10} to 1.6×10^{-9}	8.7×10^{-10}	Smethurst et al. (2006)
3	Weathered clay	BBO	3.6×10^{-8} to 5.8×10^{-8}	4.3×10^{-8}	Smethurst et al. (2006)

*[1]DRI is a double ring infiltrometer

*[2]BBO is a borehole bailout test

The makeup of the domain in shown in Figure 5.16, where it can be seen that at this particular point in the slope the four material regions overlay each other. Table 5.2 gives the absolute values of saturated hydraulic conductivity used within the field representative model.

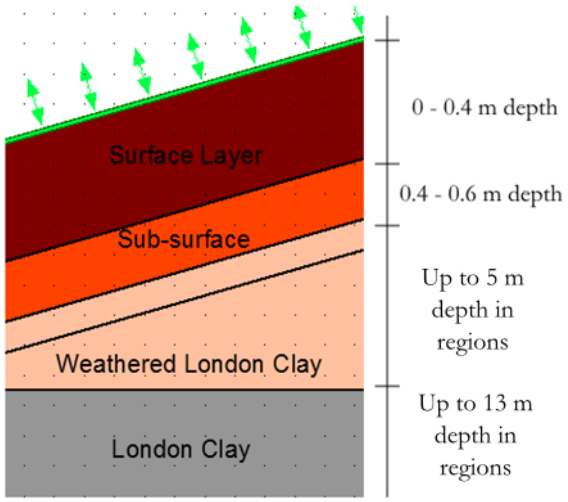

Figure 5.16 - Material regions within the model domain

Table 5.2 – Values of saturated hydraulic conductivity used for the four material regions within the field representative model

Material region	Saturated hydraulic conductivity (m/s)
Surface (0 – 0.4 m depth)	2.4×10^{-7}
Sub-surface (0.4 – 0.6 m depth)	9.3×10^{-8}
Weathered London Clay	5.8×10^{-8}
London Clay	3.7×10^{-9}

As discussed in Chapter 2, the unsaturated behaviour of a soil can be described using a soil water retention curve (SWRC) and a hydraulic conductivity function (HCF). Vadose/W requires an estimate of these functions in order to solve the governing equations. As determining SWRCs from undisturbed samples is a very difficult and time consuming process (Fredlund et al., 2012), it was decided to use the established values from literature for the field representative model and then assess the influence of these parameters within the sensitivity study.

Croney (1977) conducted a series of SWRC tests on undisturbed London clay samples and the values established are shown in Figure 5.17(a) up to a typical plant wilting point of 1500 kPa (Kabat & Beekma, 1994). The rate of suction increase can be seen to rapidly increase the more the soil dries. Both wetting and drying curves (Croney, 1977) are shown as the bounding behaviour for the soil although it should be noted that Vadose/W does not allow for hysteresis.

Croney obtained this data by using a suction plate (for suctions below 90 kPa) and a pressure plate apparatus (for higher suctions) on small samples of intact clay. Due to the size of the samples, the curves presented may not necessarily be representative of the wider fabric of the soil, including the effects of macropores, fissures and cracks and could correspond more to the behaviour in intact peds (Fredlund et al., 2011).

Figure 5.17(b) shows the Croney data plotted on a log-suction scale where differences between the two curves at low suctions (< 5kPa) are minimal, however at higher suctions a given water content can correspond to very different levels of suctions.

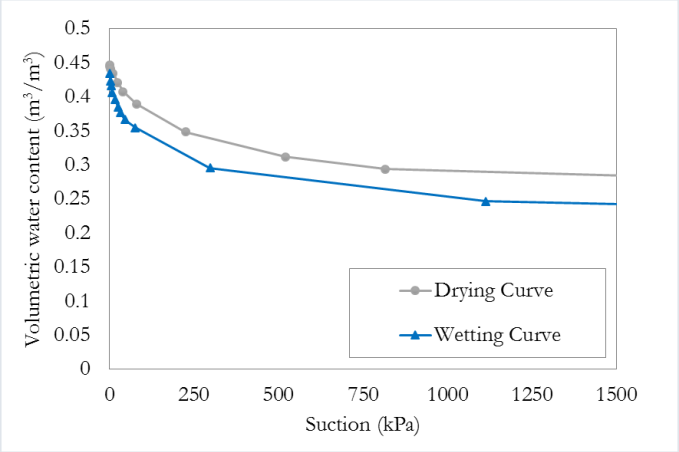

(a)

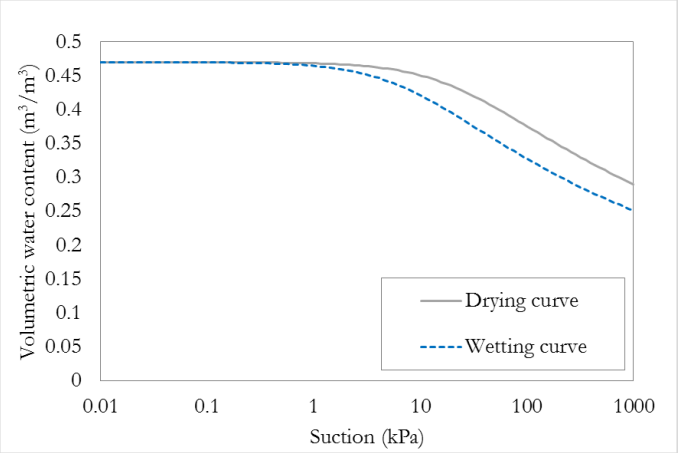

(b)

Figure 5.17 - Graphs of volumetric water content against suction for undisturbed samples of London Clay, (a) plotted up to a typical plant wilting point of 1500 kPa and (b) on a log-suction axis (redrawn from Croney (1977))

Differences in SWRCs can evidently have a large effect on the magnitude of suctions and volumetric water contents simulated within the model. To compare SWRCs from literature with measurements obtained from the cutting, estimates of unsaturated behaviour using data from the field instruments were made. Figure 5.18 compares VWC and PWP measurements from instruments installed at locations A and C on the cutting slope (Figure 5.2). Volumetric water content values from neutron probe measurements are plotted with corresponding pore water pressure values from adjacent piezometers installed at the same depth below the ground surface. Behaviour at both A and C is very similar to the Croney laboratory drying curve although the saturated water content appears to vary slightly depending on location within the cutting.

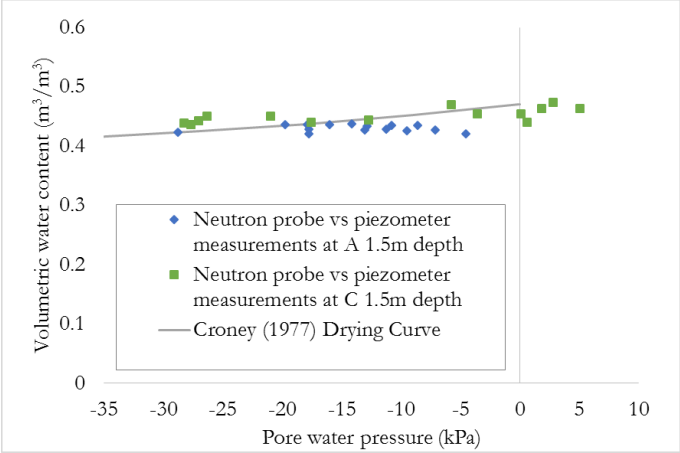

Figure 5.18 - Neutron probe volumetric water content measurements with corresponding piezometer measured pore water pressure measurements from instrumented sections A and C (Figure 5.2) compared to the Croney (1977) drying curve for London Clay (data from Smethurst et al. (2012))

If the volumetric water contents measured using the TDRs (Smethurst et al., 2012) are plotted against corresponding PWP values in a similar fashion (Figure 5.19), this pattern of behaviour can be seen even more clearly. The majority of data points show good agreement with the Croney (1977) drying curve, however a significant number of data points appear to follow the drying curve behaviour at a lower saturated water content. It was decided that all materials within the field representative model would initially use the Croney (1977) drying curve and a sensitivity study would be used to explore the influence of differing saturated water contents and the wetting curve on simulated PWPs and VWCs. Figure 5.19 also shows that there are limited measurements with which to characterise the behaviour of in-situ suctions greater than around 30 kPa.

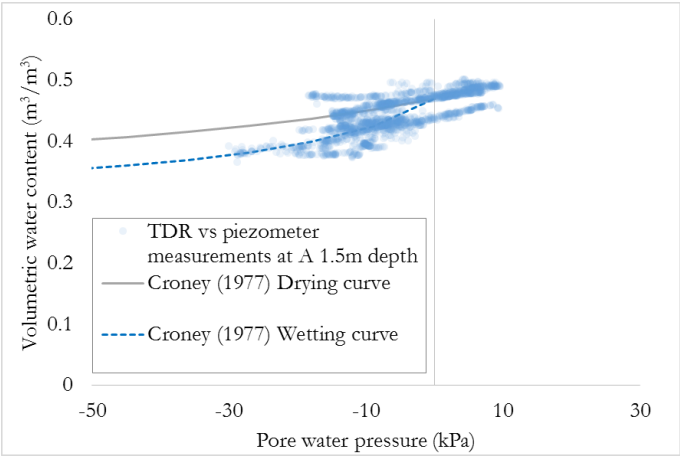

Figure 5.19 – TDR volumetric water content measurements and corresponding piezometer measured pore water pressure values for all instrumented days, compared to wetting and drying soil water retention curves (Croney, 1977)

The corresponding HCFs for the field representative model were estimated from the drying curve SWRC using a van Genuchten approximation (see Section 2.10.) (van Genuchten, 1980) (Figure 5.20). The effects of altering these approximation parameter values were further explored during the sensitivity studies (Section 5.4.9.).

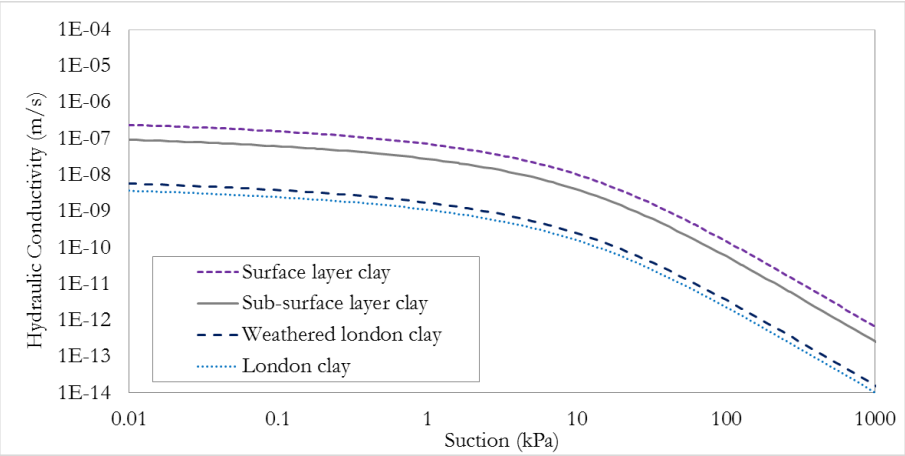

Figure 5.20 – Hydraulic conductivity functions for material layers within the field representative model (All curves use van Genuchten approximation for Croney (1977) drying curve. k_{sat} is informed by an interpretation of field and laboratory measurements (Table 5.2))

5.3.5 Initial conditions

The initial conditions for the field representative model were derived from field monitoring data at the beginning of the study period (2006 – 2009). At both locations A and C on the slope, the water table was found to vary between close to the ground surface (most winters) and a maximum depth of between 2 - 3.5 m (depending on the level of summer precipitation) (Figure 5.21). An initial zero pressure line was set to correspond to the piezometer measurements at the start of 2006, with suction limited at a certain height above this to prevent high initial suctions (greater than 25 kPa) at the near surface. Further information on the impact of the initial conditions on simulated hydrology can the found in the Appendix.

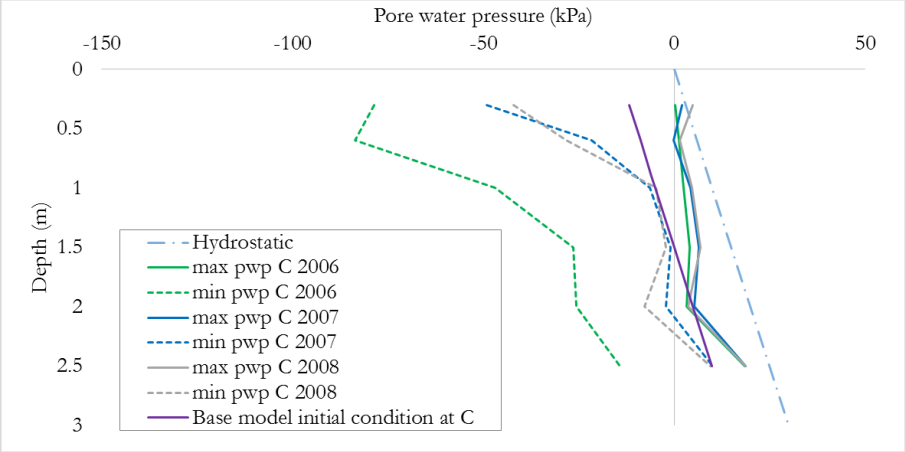

Figure 5.21 – Maximum and minimum pore water pressure depth profile envelopes from the instruments at C (Smethurst et al., 2012) and initial field representative (base) model conditions

5.3.6 Boundary conditions

Daily weather data was inputted as the hydrological boundary condition at the surface of the slope, whilst an open flow boundary was applied near the toe of the slope to replicate the road side drain. The effects of this drain on the hydrology on the slope was one of the parameters investigated during the preliminary sensitivity study in order to develop a field representative base model. However, it was found to have little effect on pore water pressures within the slope at the instrumented positions.

When modelling any site, it is essential that the outer edges of the domain, which are specified as no flow boundaries, do not affect conditions within the most important areas of the model (Powrie, 2013). The domain was therefore established so that it was large enough to prevent edge effects from influencing the results in the key parts of the slope. This was checked by assessing the contours of flow through the slope and ensuring that they were not distorted. The full specified domain is shown in Figure 5.15, where the surface and drain boundary conditions can be seen.

The climate boundary condition within Vadose/w applies a net moisture flux to the soil surface in daily time steps, according to the water balance equation:

$$NF = R - AE - RO \quad (38)$$

Where,

NF is the net moisture flux into the soil surface (mm/m²) AE is the actual evaporation (mm/m²)(see chapter 3), R is the rainfall (mm/m²) and RO is the runoff (mm/m²).

Water is also transpired by removing the actual transpiration (AT) from within the root zone via a root water uptake function (see Chapter 3).

5.3.7 Vegetation properties

Sensitivity analyses were conducted by varying vegetation parameters discussed in Chapter 3 (Leaf area index, root depth and the plant moisture limiting function) and the results are explored in the Appendix, however the values included in the field representative base model are given here.

In Vadose/W, transpiration is allocated over a specified root depth (See Section 3.7.). Initially within the field representative model, root depth was assumed to remain constant year round at 0.5 m, to agree with observations from the site (Smethurst et al., 2006; Briggs et al., 2012).

Another Vadose/W vegetation input parameter is Leaf Area Index (LAI) (see Section 3.7.) which specifies the proportion of energy allocated to transpiration and evaporation out of the total available for evapotranspiration. The initial field representative model LAI was set as a constant 2.7 to be consistent with values from literature (Scott et al., 2007; Briggs et al., 2016) in effect assuming a summer condition year-round, where evaporation would be low compared to transpiration. Vadose/W also includes in-built estimates of this function which depend on the quality of grass present on the slope. Use of these estimates is discussed later in this chapter.

The last major vegetation input parameter into the surface boundary condition is the plant moisture limiting function (Section 3.7.) which determines the rate at which plants become stressed and can no longer transpire effectively, therefore reducing actual evapotranspiration from potential evapotranspiration. For the Field representative base model Feddes et al., (1978) estimate for grass was used after site observations of the slope vegetation.

Other model input parameters not discussed here are given in the Appendix.

5.4 Results and analysis

A numerical modelling analysis of hydrological conditions within Newbury cutting over a 3 year period from Jan 2006 to Jan 2009 (1097 days) was conducted using site-measured climate data (Figure 5.4 and Figure 5.8) and material properties (Table 5.1). The results of this modelling exercise are presented in four forms:

i. **Pore water pressure and volumetric water content variation** shows variation with time at a single location. This provides a continuous record of simulated pore water pressures or volumetric water contents at an instrumented location over the course of the modelling period to compare to field measured results.

ii. **Pore water pressure variation with depth** displays depth profiles of PWP at a single section of the slope for individual time steps. Profiles are plotted at instrumented locations in the slope for the wettest and driest days, as well as maximum and minimum envelopes for longer time periods. These profiles allow comparison of the magnitude and variation of pore water pressures across all instrumented depths and have the advantage that they can be used to compare pressures throughout the whole root zone and not just at one single point.

iii. **Model derived soil moisture deficit (SMD_{FRM})** provides an assessment of the total water content within the root zone. Model derived soil moisture deficit is determined from the model results by establishing the average volume of water in the top 0.8 m of the domain and determining the difference between this volume and the maximum volume at any time. An advantage of using SMD as opposed to individual TDR results is that it gives an indication of the VWC state of the whole root zone rather than at just one depth. SMD_{FRM} can be compared to the 1D water balance derived SMD (see chapter 3) - SMD_{1D}, and to the field instrument (TDR array) derived SMD (See section 5.2.1.) - SMD_{TDR}.

iv. **Spatial variation of pore water pressure** uses two dimensional contour plots of PWP over the entire model domain for a specific time step and therefore shows the distribution of pore water pressures throughout the entire cutting at a given point in time.

For direct comparison of model and field results at individual time steps, the 'wettest' and 'driest' days according to the cumulative mesh water balance of the field representative model were selected (Figure 5.22). The cumulative mesh water balance is a water balance equation (see Chapter 3) for the whole model domain and therefore provides a good indication of

periods of extremes with regards to soil moisture. Behaviour described during 'wetting' and 'drying' periods refers to a time period between a maximum and minimum of this graph or vice versa.

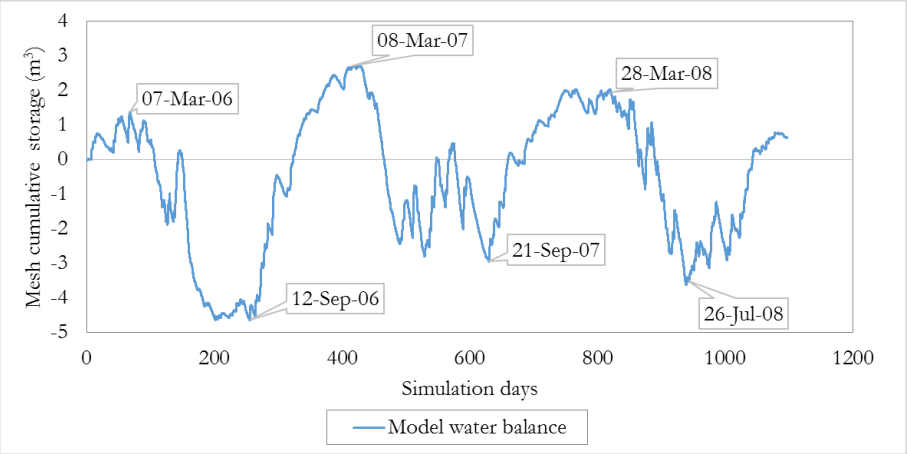

Figure 5.22 - Field representative base model calculated water balance throughout modelling period

5.4.1 A comparison of field representative model calculated PWPs and VWCs to field measurements

Over the course of the three year simulation period (2006-2009), field representative model calculated volumetric water contents generally showed good agreement with TDR measured values (Figure 5.23). However during the exceptionally dry summer of 2006, the degree of change of water content within the domain appears to be underestimated by the model. This is the case at both locations A and C and at both 0.3 m and 1.5 m depths.

The calculated VWC compares well with the field data, in that location A (Figure 5.23 (a)) appears more responsive to rainfall events than location C (Figure 5.23 (b)). This is perhaps expected as location A lies further up the slope than location C and within the weathered clay material layer which has a higher hydraulic conductivity (Figure 5.20). Rainfall is therefore likely to infiltrate further and deeper into the domain at this point. At location C the simulation appears to overestimate saturated water content compared to the field data at 1.5 m depth. Nonetheless, during the wetter years of 2007 and 2008 the overall response of the model to the rainfall events matches the field data very well. The reduced response of VWC to the climate boundary condition with increasing depth within the field measurements is also reflected in the model.

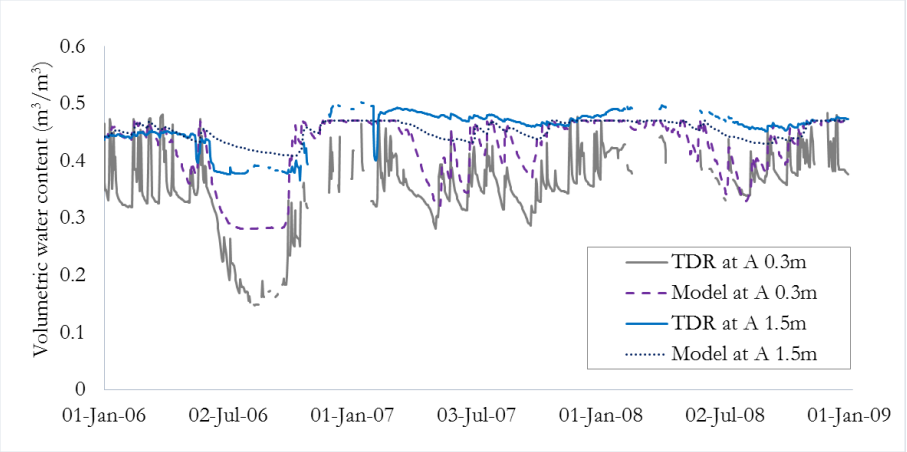

(a)

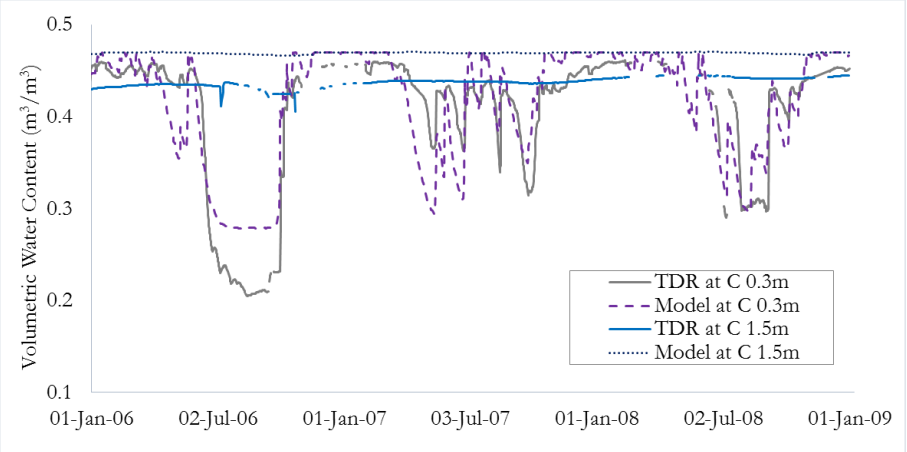

(b)

Figure 5.23 – Calculated field representative model volumetric water content, with site-measured TDR data (Smethurst et al., 2012) over the simulation duration at location A (a) and location C (b)

Figure 5.24 compares simulated and measured PWP variation over the simulated period (2006-2009). At very shallow depths the model overestimates the suctions generated during dry periods such as the summer of 2006. This is likely to be a result of the idealised model assumptions associated with the reduction of hydraulic conductivity at high suctions (from the HCF, see Section 2.9.). The hydraulic conductivity may not decrease to such an extent in the field during dry periods because of desiccation cracking (Chapter 3) which alters the soil structure results in larger infiltration and hence lower suctions.

It is also worth noting that the tensiometers installed at the site are limited in the suctions they can measure, as they can become desaturated above 90 kPa. This is illustrated by the difference between equitensiometers and tensiometer measurements at the same shallow depth. The equitensiometers recorded suctions around three times higher than the tensiometers during the summer of 2006. Unfortunately the rest of the data from these equitensiometers is largely incomplete. Despite the difference in magnitudes of calculated

and measured pore water pressures, the pattern of response (i.e. the time at which wetting and drying occur) between the model and the field data is good.

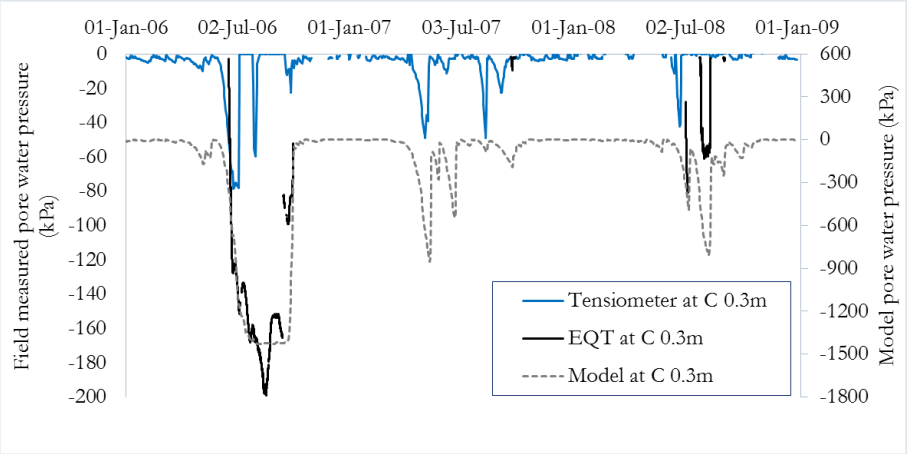

Figure 5.24 – Field measured (Smethurst et al., 2012) and simulated field representative base model pore water pressures at shallow depth (0.3 m) at instrumented location A (Figure 5.2)

At greater depth below the surface (2 m), the magnitude of calculated PWPs is much closer to measured values, as can be seen from Figure 5.25. At 2 m depth the model actually slightly underestimates the suctions generated during the summer of 2006 and rewets during the winter much faster than the field data. Overall responsiveness of the model PWPs appears to be less than the measured PWP values. This is a result of higher suctions being generated at the surface within the model leading to reduced infiltration and depth of infiltration. Nonetheless, the overall periods of wetting and drying over the three years within the simulation show general agreement with the field measured data.

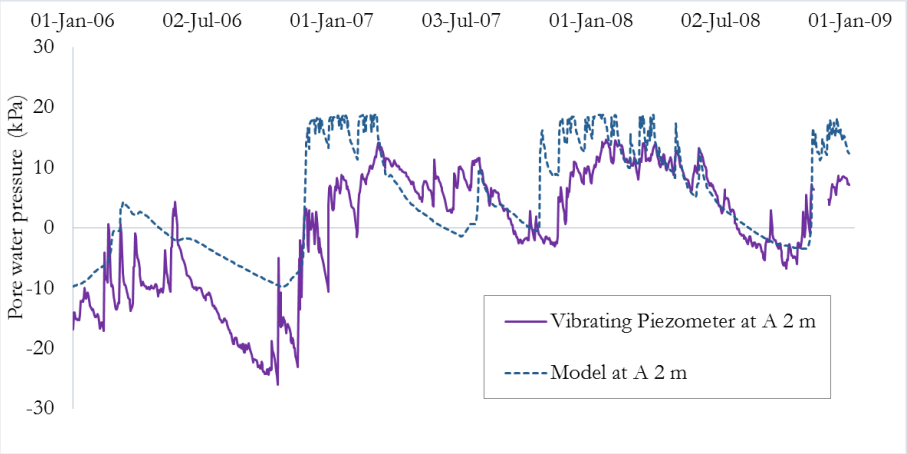

Figure 5.25 – Calculated field representative base model and field measured pore water pressures at instrumented location A (Figure 5.2), 2 m depth (Smethurst et al., 2012)

5.4.2 Shallow vs deep pore water pressure behaviour

Generally, simulated PWPs are more comparable to the field data at depths below the root zone (0.8 m). This is illustrated by Figure 5.26, which shows the maximum and minimum PWP depth profile envelopes of the model and the field data in the period 2006-2009. The differences arising above 0.8 m are due to both the development of high suctions in the model and the limited suction measurement capabilities of the tensiometers in the field. The overall size of the PWP envelope throughout the depth of the profile (i.e. the difference between maximum and minimum values) is quite similar for the model and for the field, with the tensiometers measuring slightly greater suctions than the model at depth, as noted earlier in Figure 5.25.

Rajeev et al. (2012), modelled ground-atmosphere interaction using Vadose/W for two instrumented sites in Australia, they also found that model outputs showed closer agreement with field results at depths below the root zone, than near the soil surface.

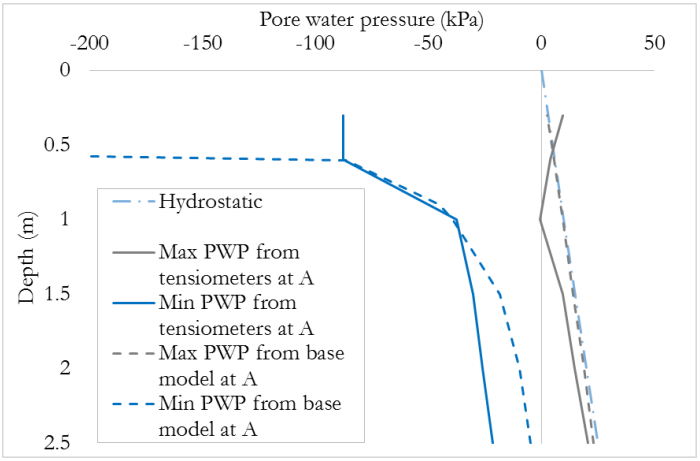

Figure 5.26 – Pore water pressure depth profile envelopes for 2006-2009 calculated for the field representative model and measured from the tensiometers (Smethurst et al., 2012) at A

5.4.3 Summer vs winter pore water pressure behaviour

Pore water pressure depth profiles from the model at the wettest and driest points of the simulation (Figure 5.27) indicate that the model is generally in closer agreement with the field measurements when the domain is at its wettest. However, below 1 m depth the model also compares well with field PWP when the domain is at its driest, with the exception of the very dry summer of 2006.

In combination with Section 5.4.2. these results indicate that the behaviour of the model when it is unsaturated (i.e. in dry periods and at shallow depths) matches field data less well than when saturated. This was explored further during sensitivity analyses (Section

5.4.9.) by altering hydraulic conductivity definitions and unsaturated (SWRC and HCF) characteristics.

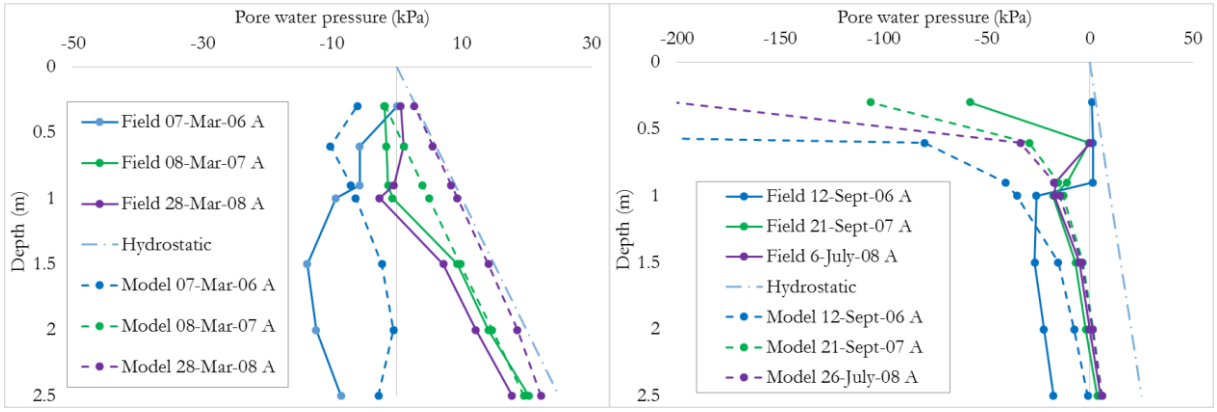

(a)

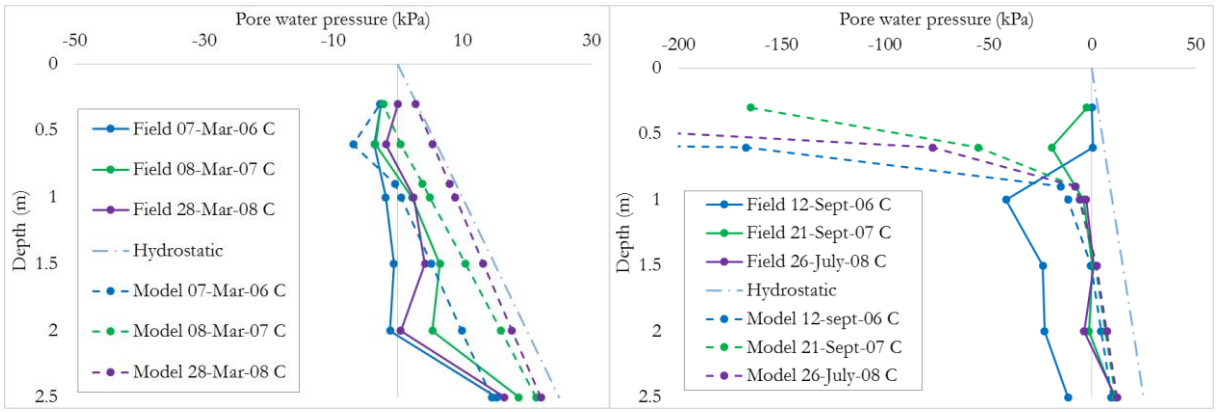

(b)

Figure 5.27 – Pore water pressure depth profiles calculated for the field representative model and measured from the tensiometers and piezometers at location A (a) and location C (b) (Smethurst et al., 2012) on the wettest and driest days of the simulation period

5.4.4 Wetting vs drying behaviour

Figure 5.28 compares the calculated and measured PWP response to heavy rainfall events. As an example of this behaviour, it was observed that heavy rainfall occurred on the night on 19/20th of October 2006. Figure 5.28 shows the measured and simulated PWP depth profiles during this time and the days immediately after. It can be seen that a wetting front progressively moves through the model domain after the rainfall event, reducing suctions down to the zero pressure line at around 1.5 m depth. This behaviour is also shown by the field measurements which show a minor decrease in suctions being observed after the event. However, the magnitude of the measured decrease in PWP is much less than that calculated within the model and the progression of the wetting front is not as well defined.

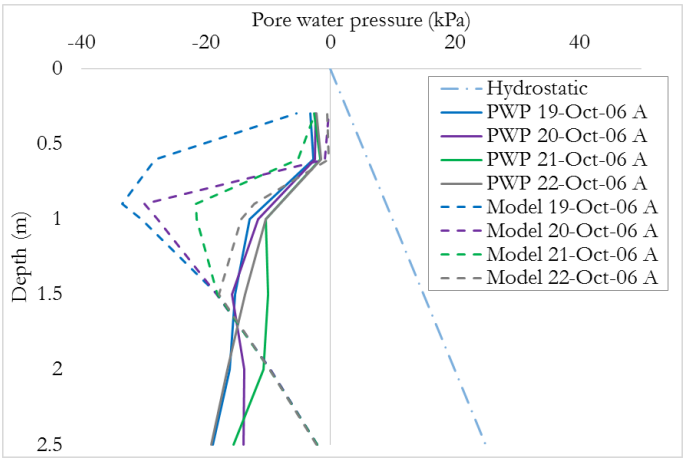

Figure 5.28 – Pore water pressure depth profiles calculated for the field representative model and measured from the instruments at location A (Smethurst et al., 2012) following heavy rainfall on the 19th/20th of October 2006

During prolonged wet weather, or a 'wetting period', the model behaves differently than during a 'drying period'. Figure 5.29 shows the decrease in model calculated soil moisture deficit (SMD_{FRM}), TDR derived SMD (SMD_{TDR}), and SMD estimated using a 1D water balance (SMD_{1D}) following the summer of 2006. It can be seen that the model rewets more slowly than SMD_{1D} but at a similar rate to SMD_{TDR}. However, the opposite is apparent during a drying period (Figure 5.30), when SMD_{FRM} increases at a much faster rate than SMD_{1D}.

It is possible that this discrepancy in behaviour is due to the 2D nature of the Vadose/W model as opposed to the SMD_{1D}. When the domain is dry, it is possible to think of the slope as a series of 1D 'slices' which behave in a similar fashion to SMD_{1D}, however, when the domain is wet, the water in the slope may be flowing down towards the toe or 'cascading' from one theoretical slice to another. The behaviour of the slope during wetting is therefore likely to be more accurately represented by the two dimensional model (SMD_{FRM}), whereas the one dimensional SMD_{1D} model might be more representative of drying behaviour. This is somewhat confirmed by comparing SMD_{1D} with the incomplete SMD_{TDR} and observing that the field measured TDR data is closer to SMD_{1D} during drying than wetting (Figure 5.29 and Figure 5.30). Additionally, the overall responsiveness of water content in the Vadose/W field representative model agrees more with the 1D water balance model during the drying period than the wetting period.

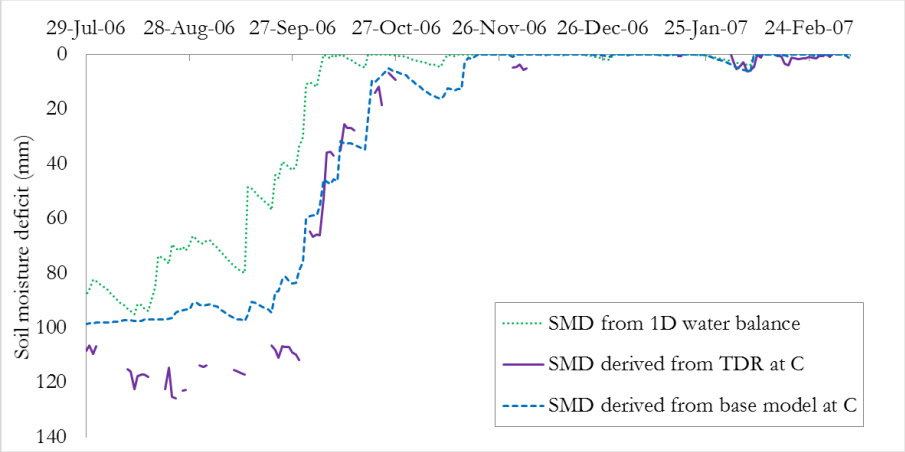

Figure 5.29 – Soil moisture deficit during a wetting period calculated from the field representative base model, from a 1D water balance equation and from TDR measurements from the field data.

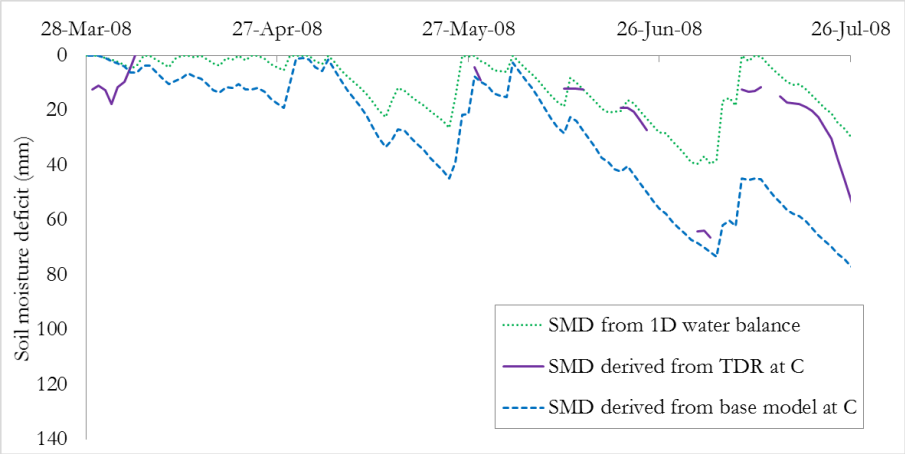

Figure 5.30 - Soil moisture deficit during a drying period calculated from the field representative base model, from a 1D water balance equation and from TDR measurements from the field data.

The SMD data shown in Figure 5.29 and Figure 5.30 indicates that the Vadose/W model agrees better with field measurements during wetting than drying periods. However, this is only the case within the root zone. At depth below this, the opposite is true, as reflected by Figure 5.31 & Figure 5.32, which present the PWP change with time at 2 m depth during the same wetting and drying periods. At 2 m depth the Vadose/W model matches the field results more closely during drying periods than wetting periods.

The Vadose/W model is continuum based (Wilson's equation see Section 2.7) and makes no allowance for any preferential flow which may occur in the field. As discussed earlier in Chapter 3 preferential flow could lead to the faster rewetting of the soil profile after rainfall events and this could be a cause of disparity between model calculated results and field measured values during wetting periods. However, at depth below the root zone, the model general matches the field results well (also shown in Section 5.4.2.) which indicates that flow at these depths is following the continuum assumptions (Darcy-Richards flow).

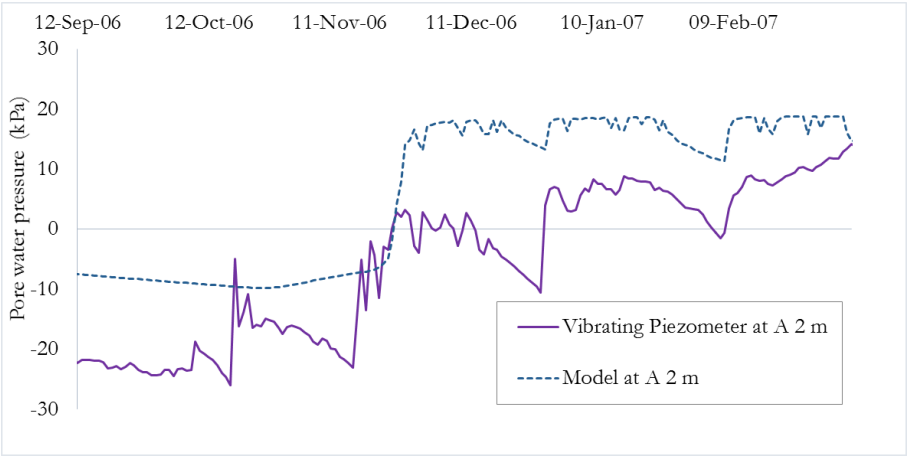

Figure 5.31 – Pore water pressure calculated for the field representative base model and measured from a piezometer at location A (Smethurst et al., 2012) during a wetting period

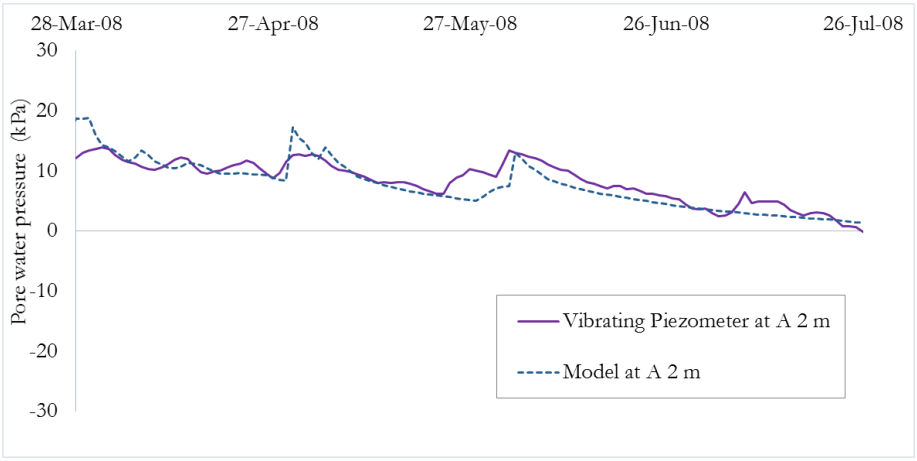

Figure 5.32 – Pore water pressure calculated for the field representative base model and measured from a piezometer at location A (Smethurst et al., 2012) during a drying period

5.4.5 Sensitivity studies

Sensitivity analyses were used to explore the relative impact of input parameters on the simulated pore water pressures and moisture contents within the finite element model. The sensitivity analyses were used to identify the key influences and uncertainties related to understanding the effects of climate on slope hydrology.

The influence of hydraulic conductivity variation at the surface and at depth, anisotropy, and unsaturated properties (SWRC characteristics) were investigated and are discussed here. Further detail on other sensitivity analyses including the effects of vegetation can be found in the Appendix.

5.4.6 The influence of surface layers of increased hydraulic conductivity

As a result of laboratory and in-situ permeability measurements within the field, two surface layers (with higher saturated hydraulic conductivity (see Table 5.1)) were defined within the field representative base model reflecting the spatial change in measured hydraulic conductivity with depth observed at the site (Section 5.3.2). To investigate the effects of removing or altering this model definition, three additional Vadose/W models were constructed containing no surface layers, one surface layer (0.4 m deep), and one surface layer (0.6 m deep) respectively (Figure 5.33).

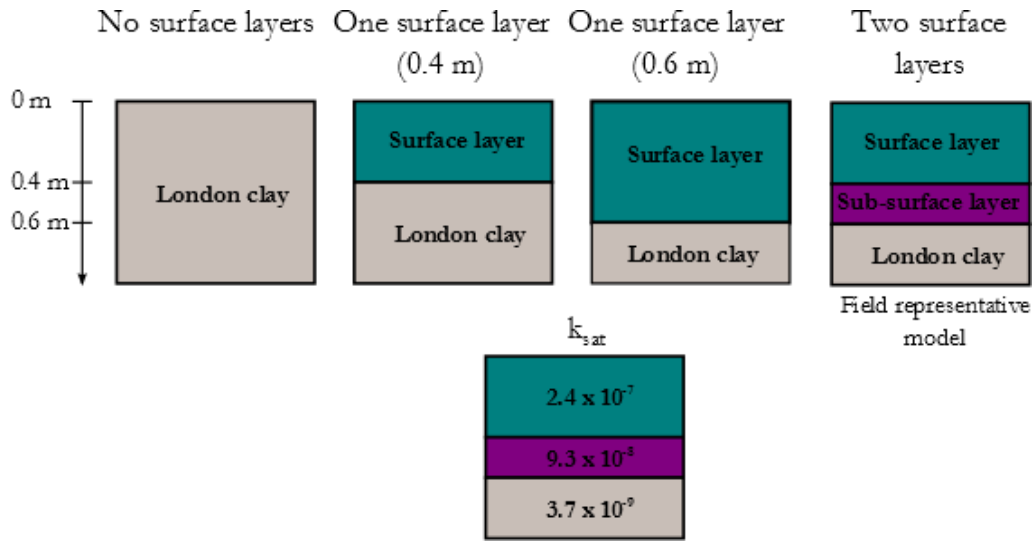

Figure 5.33 - Diagram of the four different Vadose/W model material set ups used to investigate the influence of the number of surface layers within the Newbury model

Figure 5.34 shows the temporal variation of PWP at 1 m depth for the four Vadose/W models. There is little difference between the one and two surface layer models, with only the extremely dry summer of 2006 resulting in a large difference in calculated PWP. However, the size of the layer is important to note when comparing to field measurements from one depth, as although the higher permeability layer of 0.6 m produced higher suctions at 1 m depth, the no surface layer and 0.4 m layer models generate very high suctions at shallower depths. Having no surface layer results in high suctions at shallow depths every summer, with long rewet times. This is due to the lower hydraulic conductivity of the no surface layer model when the soil is dry allowing less infiltration. PWPs at depth seem less responsive in the models with two surface layers and are closer to field measurements. This likely reflects that most of the change of moisture content is occurring within the near-surface zone of the

slope (0 – 0.6 m) and the higher conductivity of the two-surface layer model better captures this behaviour.

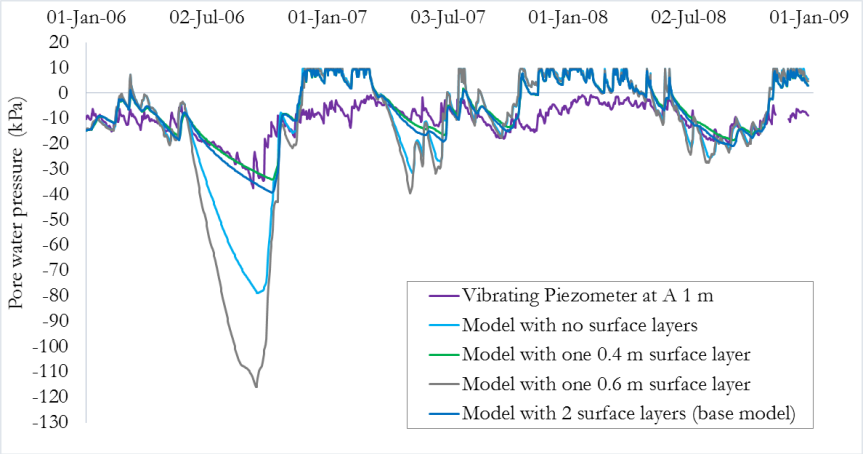

Figure 5.34 – Pore water pressure at A 1 m depth calculated for four Vadose/W models each with a different surface layer configuration and pore water pressure measured from a piezometer (Smethurst et al., 2012)

Figure 5.35 shows the simulated temporal variation of VWC over the models duration for the four models with different surface layer configurations. It is noticeable that the model with no surface layers rapidly produces lower water contents during the summer months of all three years (2006-2009) which are then maintained for a greater duration than the other models in the winter months. There is little apparent difference between the other models (0.4 m, 0.6 m, and 2 surface layers).

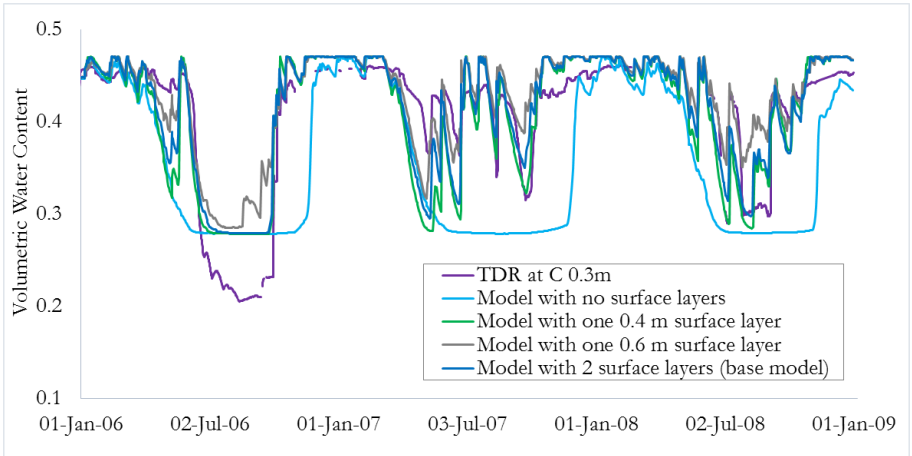

Figure 5.35 – Volumetric water content at 0.3 m depth at location C for four Vadose/W models each with a different surface layer configuration and pore water pressure measured from a piezometer (Smethurst et al., 2012)

It is clear that including two surface layers of higher hydraulic conductivity than the London clay (as indicated by field measurements) within a model of the site is necessary to better capture in-situ behaviour. These layers prevent extremely high suctions being simulated in

the very near-surface zone during dry summers and better reflect the shallow depth over which the majority of change of moisture within the slope occurs.

5.4.7 The relative influence of altering underlying hydraulic conductivity as opposed to surface layer hydraulic conductivity

The sensitivity of the model to the saturated hydraulic conductivity (k_{sat}) of the clay below the near-surface (below 0.6 m) was explored and compared to the effects of changing only near-surface saturated hydraulic conductivity. Near surface hydraulic conductivity influences infiltration into the slope whereas deeper hydraulic conductivity governs water storage within the model (Briggs, 2011).

Section (5.4.6.) showed that increasing near-surface layer k_{sat} results in lower suctions generated at the near-surface. This is likely due to more infiltration in the dry summer months. Increasing near-surface k_{sat} also reduces the depth at which changes in pore water pressure can be observed throughout the year. This is a result of more transpiration occurring due to less plant stress and increased rates of evaporation from the surface, meaning that infiltration does not percolate as deep.

In addition to the field representative model (Section 5.3.2), two Vadose/W models were set up with altered k_{sat} below the near-surface of the slope (i.e. The London clay) but with an unchanged surface layer k_{sat}. One with a London clay k_{sat} greater by an order of magnitude and one with a London clay k_{sat} reduced by one order of magnitude.

Figure 5.36 shows the effect of altering the saturated hydraulic conductivity of the underlying London clay layer, which comprises the majority of the domain, on pore water pressure variation with depth in the model.

Increasing the k_{sat} of the underlying clay layer results in a decrease in the minimum pore water pressures calculated in the root zone throughout 2007 and an increase in the depth at which suctions are observed, implying that the model is responsive to the climate boundary condition at greater depths as a result. Conversely, decreasing the London clay k_{sat} has the effect of increasing suctions in the near-surface region and reducing the depth within the model at which pore water pressure changes can be observed.

These results indicate that when the underlying k_{sat} is reduced, less percolation into the London clay layer occurs and therefore the majority of PWP (and VWC) change occurs

in the surface layers, reducing the depth of the model influenced by the surface boundary condition.

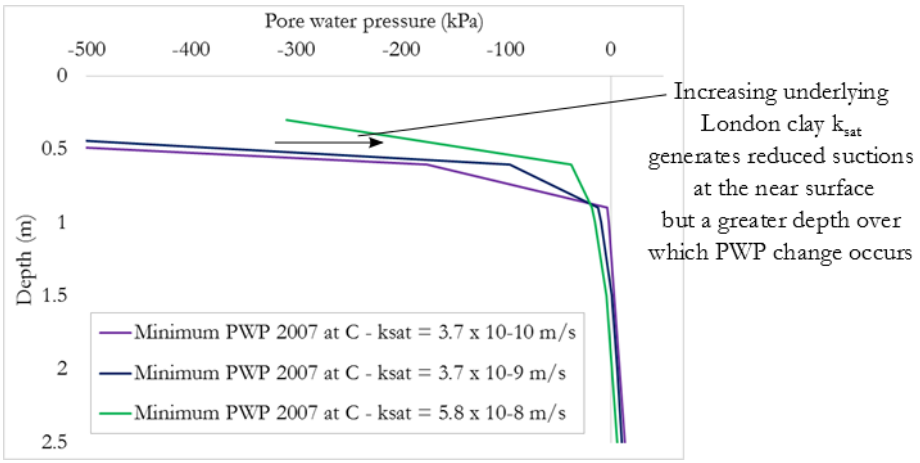

Figure 5.36 - Minimum pore water pressure depth profile envelopes for 2007 calculated from three Vadose/W models each with a different London clay saturated hydraulic conductivity value.

5.4.8 The influence of hydraulic conductivity anisotropy on horizontal and vertical flow in the slope

Due to the internal structure and history of the cutting, it is highly likely that permeability at the site varies depending on the direction of water flow (Smethurst et al., 2006). Horizontal layers of sand or silt may result in a larger horizontal than vertical permeability in some regions, whilst loading history at the site and the formation of vertical cracks may mean that the vertical permeability is increased in others.

The effects of k_{sat} anisotropy were investigated by varying the K-ratio parameter ($k_y = R \times k_x$, where R is the K-ratio, k_y is the vertical saturated hydraulic conductivity (m/s), and k_x is the specified horizontal saturated hydraulic conductivity of the material (m/s)). Figure 5.37 shows soil moisture deficit for models with K-ratio values of 0.5, 1, 2 and 10 respectively (the K-ratio assumed constant throughout the whole model domain).

Increasing the K-ratio appears to lower the change in SMD within the root zone, whilst decreasing the ratio appears to result in a higher SMD during the summer months. This is likely a result of the reduced vertical permeability in the low K-ratio models delaying the model response during wetting periods. This difference is reflected by Figure 5.38, which presents a plot of PWP at 1 m depth for all four models (K-ratios of 0.5, 1, 2, and 10). Increasing the K-ratio results in higher suctions being generated in the summer months, whilst models with lower K-ratios show less responsiveness to the changing climate boundary condition.

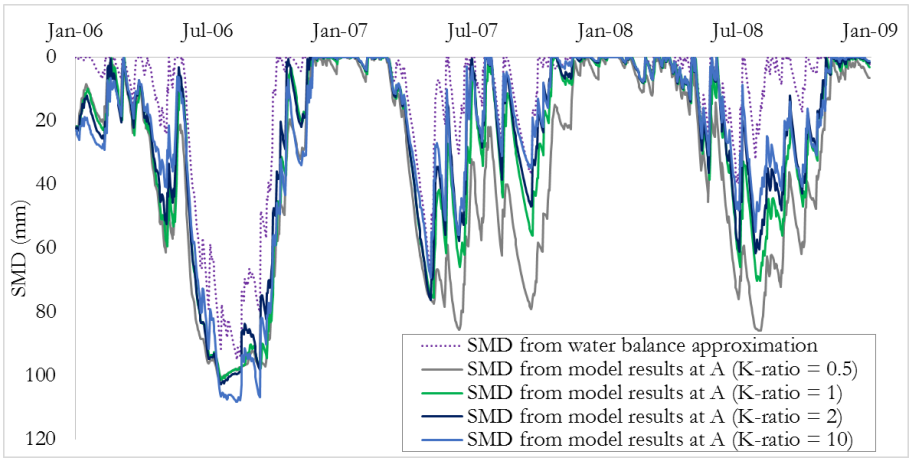

Figure 5.37 – Soil moisture deficit calculated from four Vadose/W models each with a different ratio vertical to horizontal permeability throughout the domain and from a water balance equation

The behaviour of the models might also be explained with regards to the 1D vs 2D behaviour discussed earlier in Section (5.4.4.). When the K-ratio = 0.5, horizontal flow has a large impact, meaning that a considerable amount of 2D flow from one theoretical 'slice' to another takes place. It would therefore be expected to be least comparable to the SMD_{1D}. Likewise, in the K-ratio = 10 model horizontal flow is reduced, as are 2D effects, meaning that it is likely to be closer to the SMD_{1D}, as shown in Figure 5.37.

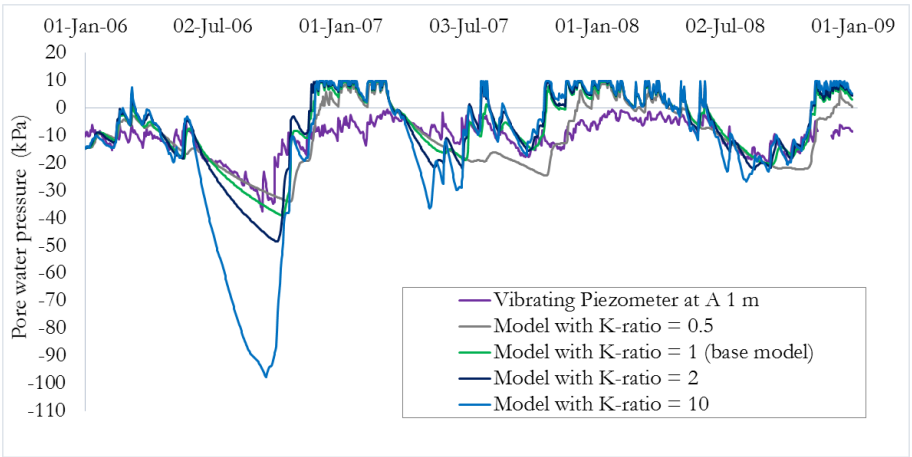

Figure 5.38 – Pore water pressure at 1 m depth for models calculated from four Vadose/W models each with a different ratio vertical to horizontal permeability throughout the domain and measured from a piezometer in the field (Smethurst et al., 2012)

5.4.9 The influence of soil water retention characteristics within the model

To investigate the effects of altering the soil water retention characteristics on the hydrology of the modelled slope, the drying SWRC (Croney, 1977) in the model was replaced by the wetting curve also derived by Croney (1977). The two functions are shown in Figure 5.17

and the specific van Genuchten parameters associated with each are given in Table 5.3. The difference between the two theoretical curves of behaviour is largely reflected in a reduced air entry point. The drying curve has a higher air entry valve as the surface tension of the smallest pores can keep water within the largest pores when drying and sustain higher suctions than when wetting. More detail of the physical significance of these parameters can be found in Chapter 2. Since the hydraulic conductivity function is directly calculated from the SWRC (Section 2.9.) the corresponding HCFs of all materials in the domain were also altered as a result of this change to the model SWRC.

Table 5.3 - Van Genuchten parameters derived for wetting and drying soil water retention curves from Croney (1977) (shown in Figure 5.17)

	AEV (kPa)	θ_s	θ_r	m	n	m_v (kPa)
Drying curve	20	0.47	0.1	0.14	1.17	$1x10^{-5}$
Wetting curve	7	0.47	0.1	0.15	1.18	$1x10^{-5}$

Figure 5.39 shows the depth profile envelopes of pore water pressure for two Vadose/W models with the wetting and drying SWRCs. It can be observed that the model using the wetting curve has a much shallower PWP response to climate, with PWP largely unaffected below 1.5 m depth. This is emphasised by Figure 5.40 which shows the temporal PWP change at 1 m depth. In the wetting curve model there is a very uniform response to wetting and drying periods despite the varying extremes of the simulated years (2006-2009). In contrast, the PWPs calculated within the drying curve model are much more responsive to rainfall events.

Briggs (2011) and GEO-SLOPE (2008) have also shown more responsiveness within Vadose/W models as a result of reducing the AEV.

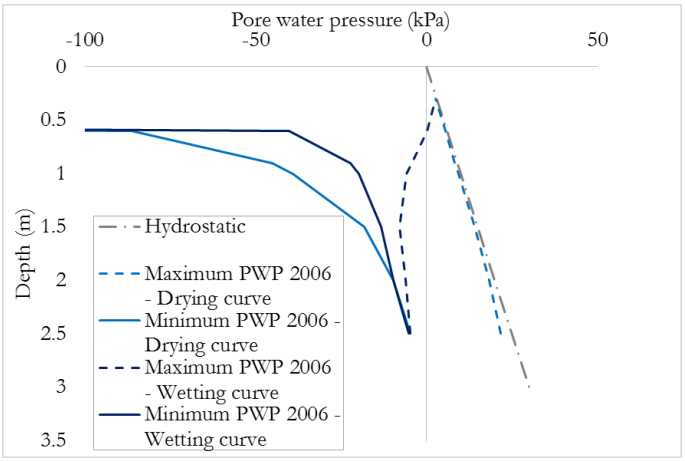

Figure 5.39 – Pore water pressure depth profile envelopes for the year 2006 calculated from two Vadose/W models, one using a wetting soil water retention curve and one using a drying soil water retention curve (Croney, 1977)

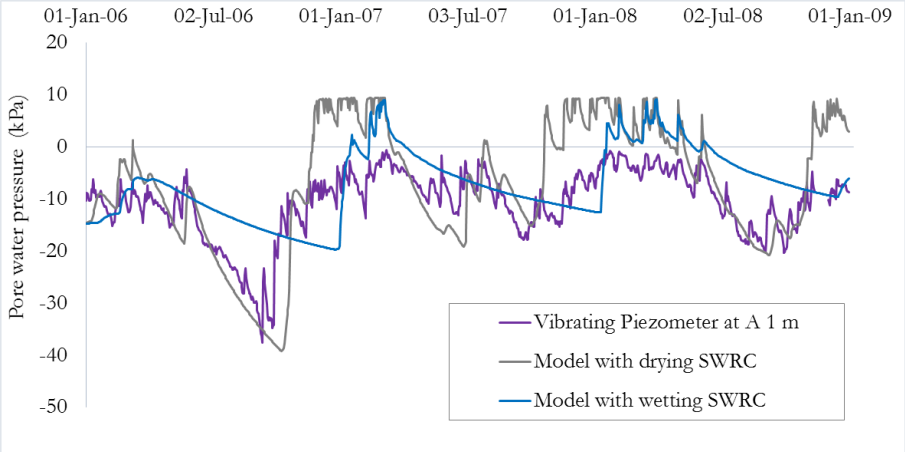

Figure 5.40 – Pore water pressure at 1 m depth calculated from two Vadose/W models, one using a wetting soil water retention curve and one using a drying soil water retention curve (Croney, 1977), and pore water pressure measured in the field using a piezometer (Smethurst et al., 2012)

At shallower depths the suctions generated during the summer months are considerably greater and more prolonged in the wetting curve model than in the drying curve model. This is reflected in terms of VWC as Figure 5.41 shows. It is apparent that within the root zone (0 - 0.8 m), substantially higher and more prolonged soil moisture deficits are generated in all three years of the simulation by the wetting curve model than the drying curve model. During the initial drying stages there is little difference between the two models, only once a large SMD (> 50 mm) is established do the differences become apparent, with the wetting curve model generating maximum SMDs more than 30 mm larger than the drying curve model in the summer months. Toll et al. (2014) observed similar behaviour when modelling tropical soils with Vadose/W.

From Figure 5.18 and Figure 5.19 it was shown that the Croney (1977) London clay drying curve better reflected the site behaviour as measured using field instruments than the Croney (1977) London clay wetting curve. This is replicated in the results of the models shown here in Figure 5.40 and Figure 5.41 where the drying curve model results appear to capture the changes in PWP and VWC in response to climate conditions in a manner more reflective of field observations.

The impact of altering the SWRC implies that the definition of a SWRC is very influential in modelling the hydrology of this slope. This is likely to be because the many of the important hydrological processes within this slope occur in the unsaturated zone. However, it also shows the limitations of the modelling assumptions involving SWRCs. As discussed in Chapter 2, SWRCs are curves approximately fitted to laboratory data (see figure 2.6) and are not true reflections of the soil behaviour which follows scanning curves between wetting and drying SWRCs. Therefore these results indicate that better relationships describing unsaturated behaviour based on true measurements of pore connectivity are needed.

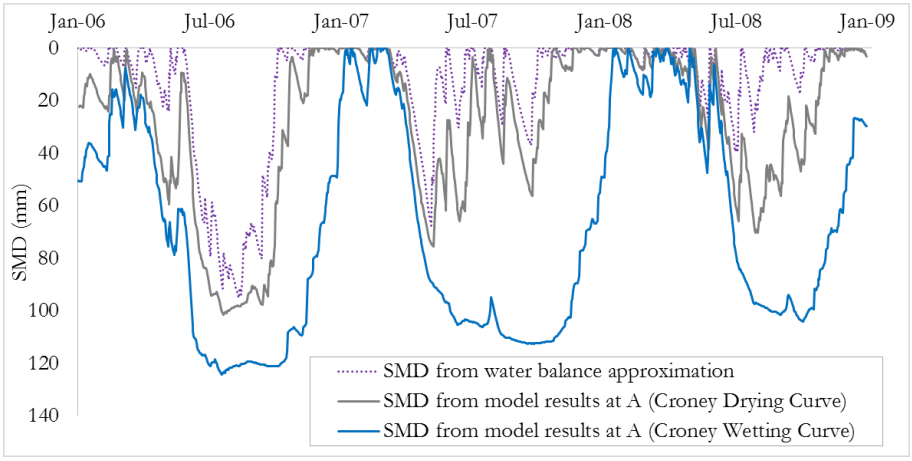

Figure 5.41 – Soil moisture deficit calculated from two Vadose/W models, one using a wetting soil water retention curve and one using a drying soil water retention curve (Croney, 1977), and from a water balance equation

5.5 Conclusions

Vadose/W was used to model a roadside cutting near Newbury in order to assess hydrological modelling with regards to estimating pore water pressures and volumetric water contents and to examine slope hydrology in response to real climate data. The model was used to explore key uncertainties and their impact on slope hydrology. The following conclusions can be drawn from the findings presented here and have informed the rest of the work carried out as part of this thesis:

- Generally, the pattern of response of the field representative model pore water pressures in the root zone and the field measurements is good. However, the field representative model generates large suctions at the near-surface during dry periods which are not measured within field observations. The model makes no allowance for preferential flow due to cracking or the presence of macropores, which could result in higher hydraulic conductivity and lead to lower suctions occurring in the field. The magnitude of calculated PWP values is much closer to field measurements at depths below the root zone (0.8 m). At these depths, the soil behaviour is described better by the continuum assumptions and Richard's equation type flow within the model.

- The behaviour of the slope during wetting periods is more accurately represented by the Vadose/W field representative model than the SMD_{1D} water balance model due to the two-dimensional nature of flow within the slope during these periods. Flow within the slope during drying periods is shown to be a more one-dimensional process. This was emphasised using a sensitivity analysis of hydraulic conductivity anisotropy.

- The field representative model generated pore water pressures are closer to field measured pore water pressures when the domain is close to saturation as opposed to dry. The results indicate that the assumptions of unsaturated soil behaviour (SWRC and HCF parameters) used within the model do not reflect the true behaviour of the slope in dry conditions. A sensitivity analysis which explored altering soil water retention characteristics showed that these parameters have a large impact on slope hydrology and exposed the limitations of the use of SWRCs to characterise unsaturated soil behaviour. Therefore better relationships describing unsaturated

behaviour based on true measurements of pore connectivity and structure are needed.

- Including surface layers within the model to represent the spatial variation of hydraulic conductivity in near-surface region (0 – 0.6 m) was shown to be important in order to better reflect the shallow depth over which the majority of moisture change occurs and to better model field behaviour. During sensitivity analyses, altering saturated hydraulic conductivity of the underlying clay within the slope was also shown to affect the magnitude of simulated suctions in the near-surface zone and the depth over which PWP changes occur.

The results of this investigation reinforce the importance of determining how the hydraulic conductivity of clay soils varies with depth and saturation within earthworks, in order to be able to correctly model the hydrological response of these slopes to climate conditions. It has been shown in Chapter 2 that macropores and the pore structure of a soil plays a role in the hydraulic conductivity. Determining the degree to which this pore architecture and its evolution with changes in saturation and depth influence hydraulic conductivity is therefore of great importance. This is explored further in Chapter 8 after Chapters 6 and 7 first investigate the use of microCT to visualise and quantify the internal macropore structure of earthwork samples.

6 Investigation into microCT capabilities and development of a scanning procedure for large scale clay fill samples

6.1 Introduction

Chapter 5 showed the importance of accurately describing the variation of hydraulic conductivity with depth and with changes in saturation, when modelling the hydrological conditions of infrastructure slopes. However, it has historically been difficult to precisely observe the effects of soil macroporosity on soil hydraulic conductivity due to the difficulty in quantifying the internal macropore structure of representative natural samples in a non-destructive manner. Computed tomography is a potential new tool for overcoming this problem.

Over the past decade or so, CT scanning has become a more widely used experimental technique in disciplines outside of medicine, including hydrology and soil science (See Chapter 4). This technique allows high resolution, 3D, non-destructive imaging of soil structure and macropore networks. This imaging data can then be used to provide quantitative estimates of many properties associated with the pore architecture including macroporosity, pore connectivity, and tortuosity. It therefore offers the potential to link soil structure and pore architecture to flow and hydraulic conductivity. This is discussed further in Chapter 8.

Although quantitative measures of the macropore network calculated from X-ray tomography images can provide useful information on soil structure, they are dependent on the sample size, scanning procedure, image quality, and image processing methods used (Chapter 4).

This chapter investigates the capabilities of a microCT scanner with regards to scanning large clay fill samples within the scan acquisition time constraints imposed by a working day. Subsequently Chapter 7 develops a suitable image analysis procedure using the data obtained using the scanning procedure developed here.

Within the geosciences, the definition of what constitutes a macro or micro pore can vary widely (Perret et al., 1999). For clarity, throughout this chapter and any subsequent

descriptions of CT derived pore parameters, the term 'macropore' is used to describe any pore that is visible within the CT image data. As the samples scanned are clay, this will exclude a significant amount of smaller 'micropores', which are pores not visible in the CT data and constitute the majority of the total porosity of the scanned samples.

6.2 Objectives

This chapter presents an investigation into the use of microCT to scan a large scale clay fill block sample, as well as two smaller 100 mm diameter clay fill samples (which are still large by microCT standards), assessing the limits of microCT scanner capabilities with regards to sample size and image quality.

The objective of this work was to scan a large clay fill sample (either a block sample or 100 mm diameter cylindrical sample) at an image quality (i.e. resolution and contrast) which allows for the visualisation and quantification of the macropore structure inside the samples (pores > 63 microns in size) within the acquisition time restraints of a working day.

This investigation can then be used to explore the effects of sample size and to determine appropriate scan settings (e.g. X-ray energy, number of projections etc.) that will be used to scan undisturbed clay fill samples in Chapter 8.

6.3 Background

As discussed in Chapter 4, the quality of image data (contrast and spatial resolution) obtained from CT scanning is usually relative to the size of the sample being scanned.

The spatial resolution is dependent on the distance between the source, sample, and detector, as the focal spot size is altered according to the field of view required to scan the entire sample (a larger sample requires a larger focal spot size). The best resolution achievable is reduced as power and field of view increase. This is due to focal spot defocusing at high powers which results in edge blurring or penumbra (see Chapter 4).

Contrast depends on the difference in X-ray attenuation by the respective materials which comprise the sample. It therefore depends on the power of X-rays fired through the sample, with high powers resulting in a lower contrast (Helliwell et al., 2013). Higher contrast means that internal features of the specimens become more visible and results in an easier segmentation process between material phases.

However, if sample size (or density) is increased, then higher powers need to be used in order to enable the X-rays to penetrate through to the detector. As a result, there is commonly a trade-off between contrast and the size and density of the samples being scanned (Cnudde and Boone, 2013). This is one of the reasons that, historically, researchers exploring the use of CT in the geosciences have tended to focus on very small sample sizes (< 5 cm) (see Chapter 4).

6.4 Method

6.4.1 The microCT machine used

The scans presented within this thesis were undertaken using a Nikon X-Trek XTH225ST microCT machine installed at the Department of Mechanical Engineering at the University of Bath (Figure 6.1). It has a 225 kV micro-focus X-ray source with minimum 3 μm focal spot size. Other specifications are given in Table 6.1.

Figure 6.1 - Manufacturer image of the microCT scanner used for all scans (Nikon X-Trek XTH225ST)

Table 6.1 - Specifications for the Nikon X-Trek XTH225ST

Micro-focus X-ray source	Max. kV	Max. power	Focal spot size*	Focal spot size at max power*
225 kV Reflection target	225 kV	225 W	3 μm up to 7 W	225 μm at 225 W

*Focal spot size depends on the power used (i.e. the size and density of the sample)

6. Investigation into microCT capabilities and development of a scanning procedure for large scale clay fill samples

6.4.2 Materials

Three scans were used in this investigation to explore microCT capabilities and establish a suitable scanning procedure. The scans explored sample size, achievable image quality, sample consistency and imaging artefacts.

Three different samples were used for the respective scans. Details of the samples are shown in Table 6.2. All the samples were derived from clay fill from Laverton Embankment in Gloucestershire. This embankment forms part of the Gloucestershire-Warwickshire historic railway line which has suffered slope failures in the past and was originally part of the Honeybourne line (Cheltenham–Stratford-upon-Avon–Birmingham) built between 1900 and 1906. The embankment is around 6 m high and is believed to have been constructed by end tipping of local Charmouth Mudstone (see Chapter 8 for more details on the site and sampling methods).

The first sample (Figure 6.2) was a large block sample of clay fill (approximately 30 cm x 30 cm x 30 cm) obtained from the near-surface (0.5 m depth) within Laverton Embankment which was the largest sample that could be realistically inserted into the microCT machine.

The second sample was a 100 mm diameter core trimmed from within the block sample (Figure 6.3). The third sample was a 100 mm diameter core manufactured from reconstituted clay fill obtained from within the embankment (3.5 m depth) (Figure 6.4). The reconstituted sample was prepared using wet compaction to a bulk density of 1.91 g/cm^3 in line with the most dense of the core samples scanned later in Chapter 8 (Table 8.1) and the mean bulk density associated with samples from Laverton embankment measured by Gunn et al. (2016).

Particle size distributions for the clay fill block sample and for the reconstituted sample are shown in Figure 6.5, as well as the particle size distribution from a clay fill core sample taken from 4.5 m depth (5C bot, scanned in Chapter 8). One novel aspect of this work is that the block and trimmed samples are both near-surface (0.5 – 0.8 m depth) samples which contain small rocks, and in contrast to many previous studies involving CT, no sieving or grading was conducted prior to scanning. This is shown by the large particles sizes present within the block sample particle size distribution (Figure 6.5).

Figure 6.2 - The clay fill block sample (0.5 - 0.8 m depth) excavated from Laverton embankment (approx. 30 cm diameter)

Figure 6.3 - The 100 mm diameter trimmed core (from a clay block sample) from Laverton embankment (80 mm height))

Figure 6.4 - The reconstituted sample prepared from a clay fill from Laverton embankment (3.5 m depth) (80 mm height)

Table 6.2 – Details of the three clay fill samples used in the investigation into microCT capabilities and scanning procedure

Sample	Dimensions	Parent material	Origin	Sampling procedure	Scanning and saturation procedure
Block sample	Height ≈ 30 cm Width ≈ 30 cm Length ≈ 30 cm	Charmouth Mudstone	Laverton embankment fill 0.5 - 0.8 m depth	Block sampled using an excavator by the British Geological Survey	Scanned at sampled (field) conditions.
Trimmed 100 mm diameter cylindrical sample	Height: 79 mm Diameter: 98 mm	Charmouth Mudstone	Laverton embankment fill 0.5 - 0.8 m depth	Trimmed from the block sample to a cylindrical sample with a diameter of approximately 100 mm	Scanned fully saturated (submerged).
Reconstituted 100 mm diameter cylindrical sample	Height: 87 mm Diameter: 100 mm	Charmouth Mudstone	Laverton embankment fill 3.5 m depth	After crushing sample was prepared using wet compaction with a hydraulic ram to a bulk density of 1.91 g/cm^3 in line with cores from Laverton (Chapter 8)	Stored refrigerated at 3ºC. Scanned after saturated hydraulic conductivity testing within a triaxial cell.

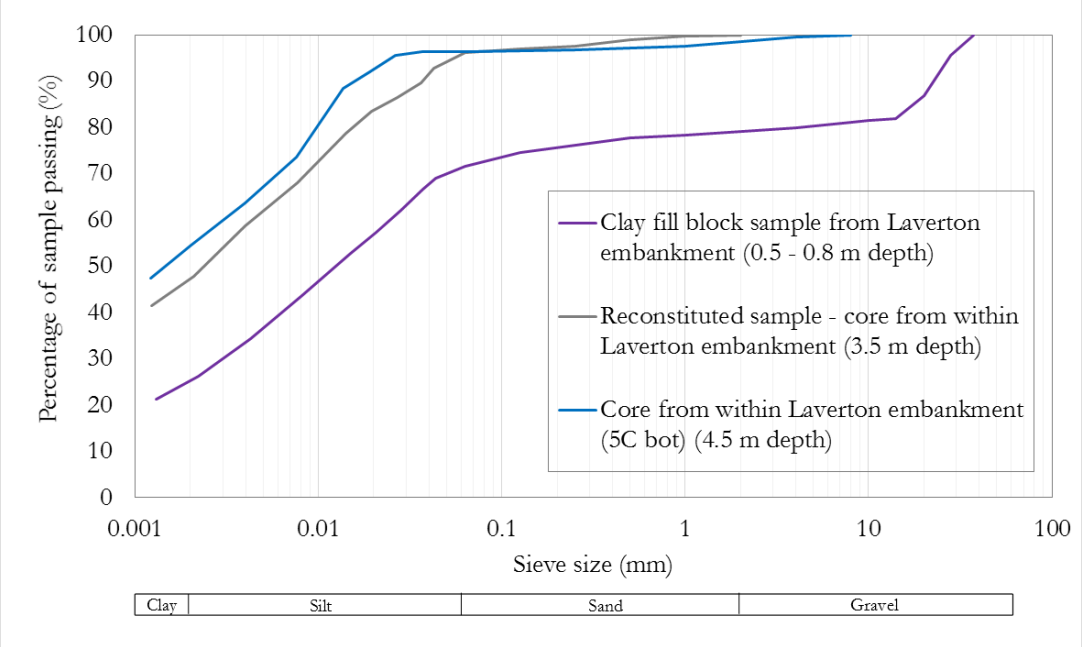

Figure 6.5 – Particle size distributions for a near-surface clay block sample, a reconstituted sample made from a clay fill core (3.5 m depth), and a clay fill core from 4.5 m depth, obtained from wet sieving and hydrometer tests (BS 1377-2:1990)

X-Ray diffraction analysis of the clay fill was undertaken using a Bruker D8 Advance X-ray powder diffractometer. This showed that the clay fraction of the fill (< 63 μm) consisted of quartz, calcite, kaolinite, illite and sodium magnesium aluminium silicate.

Table 6.3 shows the plasticity, moisture content, density and porosity properties determined from samples from Laverton embankment both from Gunn et al. (2016) and from the samples investigated later in Chapter 8.

Table 6.3 - Material properties determined from samples from Laverton embankment both from (Gunn et al., 2016) and from the samples investigated later in Chapter 8 (including the reconstituted sample).

Sample type and source	Properties
Properties from Laverton embankment samples (see Chapter 8) as well as results from (Gunn et al., 2016)(6 additional samples (12 total))	Liquid limit range : 61 – 77% Plastic limit range 27 – 37% Moisture content (gravimetric) range: 21 – 33% Bulk density range: 1.76 – 1.97 g/cm^3 Dry density range: 1.33 – 1.64 g/cm^3 Particle density: 2.66 g/cm^3
Reconstituted 100 mm diameter cylindrical sample	Bulk density: 1.91 g/cm^3 Dry density: 1.45 g/cm^3 Void ratio: 0.98 Porosity: 0.49

6. Investigation into microCT capabilities and development of a scanning procedure for large scale clay fill samples

6.4.3 MicroCT Scanning Method

The microCT scanning method used within this investigation can by summarised by the following procedural steps:

1) Firstly, a scan was conducted on the largest possible sample that could be placed within the Nikon X-trek machine (the block sample) using the maximum power possible in order to determine the image quality achievable for this size of clay fill sample within the acquisition time restraints of a working day (4 hour scan).
2) To obtain images containing less artefacts and better contrast between phases (pores and matrix) the block sample was trimmed to a 100 mm diameter cylinder and scanned using lower microCT power settings (inferred from Step 1)(still achieving high resolution images).
3) A reconstituted 100 mm diameter sample (which was denser and more representative of core samples from depth within the embankment) was prepared and subsequently scanned using the same power and scanner settings as the trimmed sample (Step 2).
4) The image quality (resolution, contrast, artefacts) of the trimmed and reconstituted sample scans was compared to determine the scan settings to be used for all embankment core samples (Chapter 8).
5) The image data from the trimmed and reconstituted sample scans was also compared to assess differences in the structure and consistency of the samples to determine the optimum sample to use in order to develop a suitable image analysis procedure (Chapter 7).

The microCT power and scan parameters for all three scans are shown in Table 6.4.

Table 6.4 – MicroCT scan properties for three scans

Sample	Scanner power settings		Scan parameters			Other
	Voltage (kV)	Current (mA)	Exposure (ms)	Projections	Vertical slices	
Block sample	225	395	4000	1800	1998	copper filter (0.5 mm thick)*
Trimmed 100 mm diameter cylindrical sample	195	105	2000	1800	1998	-
Reconstituted 100 mm diameter cylindrical sample	195	105	2000	1800	1998	copper filter (0.5 mm thick)*

* A copper filter was used to remove low powered X-rays and reduce beam hardening image artefacts

The duration of microCT scans depends on two scan parameters, namely, the number of projections (rotations) of the sample and the exposure time used. The number of projections is usually a function of detector size although it can be optimised for particular samples if desired. The exposure time is the amount of time that the detector measures photons to create an image. Increasing exposure time allows the use of lower scan powers which can lead to increased contrast and image quality of large specimens (see Chapter 4). However, long exposure times increase the duration of scans significantly which can be problematic due to several limitations imposed on the length of scan time.

The scan acquisition time (i.e. the duration of the scans) in this investigation was influenced by the following factors:

- The nature of the samples – The samples could not be left to overly dry out during the scanning process as new macropores may develop due to cracking.
- The saturation procedure – Due to the desire to keep the saturated samples as close to saturation as possible during scanning, the experimental programme dictated that the scans had to occur at certain times of day to allow for pre and post scanning sample preparation.

- Access to the CT scanner facilities - The machine is heavily used by researchers and an operator is need to set up and end any scans so scan duration was limited to 4 hrs

The block sample was scanned using the maximum power and the longest exposure time possible within 4 hours. A 0.5 mm copper filter was also used to reduce the effects of beam hardening (see Chapter 4).

After the results of this scan had been analysed, the X-ray power was lowered to improve image quality (discussed later) in order to scan the trimmed sample. Having achieved sufficient image resolution and contrast, the same settings were then used to scan the reconstituted sample in order to investigate if the image quality was preserved when scanning denser samples (e.g. embankment cores from depth).

6.4.4 Scan output

Prior to analysis and quantification of image data, the raw attenuation data must first be reconstructed into a 3D image. Image data from scans is reconstructed by building a 3D image from 2D slices (see Chapter 4). All the scan images were reconstructed using proprietary software supplied by Nikon with the scanner. The software contains inbuilt correction algorithms to reduce ring artefacts, beam hardening and noise (see Chapter 4). These were used during the reconstruction process along with a shading correction, which takes into account any error in greyscale caused by ageing of the microCT detector. These reconstruction settings were kept constant for all subsequent scans to aid comparison of sample data and repeatability of the tests. Reduction of noise and artefacts can also subsequently be carried out during analysis of the image data as discussed later.

An example of how image quality is assessed is shown in Figure 6.6, which shows the trimmed sample reconstructed within Avizo Fire (FEI, 2014), a commercial software tool for visualisation and analysis of microCT scans. Figure 6.6 shows a clear contrast between phases (pores and soil matrix) which indicates good image quality and the potential to segment the data. Image contrast can also be examined using the greyscale intensity histogram of an image (see Chapter 4) where more pronounced peaks corresponding to different material phases increase the ease with which a sample can be segmented. The spatial resolution of an image is determined from the voxel size achieved during the scanning process.

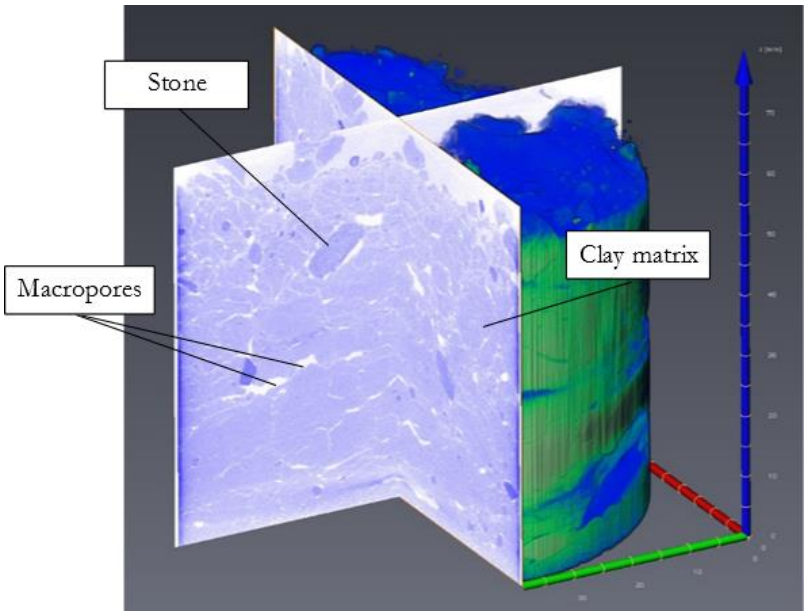

Figure 6.6 – An example of how microCT image data can be visualised - A reconstruction of the trimmed 100 mm diameter sample (79 mm height) within Avizo Fire showing a cross-section of the sample with clear contrast between material phases (pores, soil matrix, and higher density stones) (greyscale is inverted in this image (pores appear lighter)).

6.5 Results and discussion

Figure 6.7 shows two vertical slices from the reconstructed microCT image data of the clay fill block sample. Table 6.5 shows the spatial resolution achieved within scans of all three samples within this investigation).

Figure 6.7 shows that there is not enough contrast between the phases within the sample in order to segment the images. The figure also shows several image artefacts present within the image data, including a significant amount of noise (shown as the white speckle), beam hardening (higher greyscale at edges of sample), and penumbra (blurring at sample edges). As well as the poor contrast, these artefacts prevent the image data from being segmented and therefore quantified reliably. However, as Table 6.5 shows, the scan of the block sample did achieve good spatial resolution for a large sample (37 μm sized voxels).

Both these results indicate that the high X-ray power used in order to achieve good resolution mean that the image contrast has suffered severely. This problem has been exacerbated by beam hardening and noise due to the high density of the sample absorbing low energy X-rays. The presence of penumbra is a result of the large focal spot size needed to scan a sample of this size.

It can also be seen from Figure 6.7 that the image data does not allow the presence of stones within the sample (Figure 6.3 and Figure 6.5) to be distinguished. If acquisition

time had not been limited to four hours, exposure time could have been increased therefore allowing a lower X-ray power to have been used in the scan. This may have resulted in better image contrast, however the large number of image artefacts present in the sample mean that this would not have improved the image quality enough for the data to be quantifiable. Therefore this size of sample (30cm x 30cm x 30cm) is too large in order to achieve usable data with the microCT scanner used here in a 4 hour scan.

Table 6.5 – The spatial resolution achieved within the three scans investigation microCT capabilities

Sample	Voxel resolution (mm^3)
Block sample	0.037475
Trimmed 100 mm diameter cylindrical sample	0.038775
Reconstituted 100 mm diameter cylindrical sample	0.062784

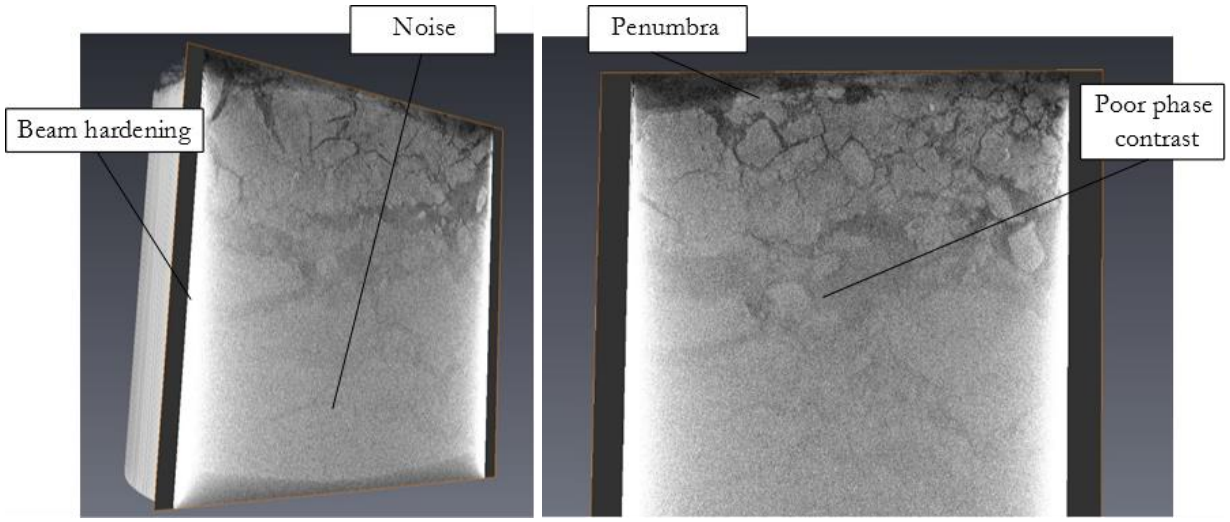

Figure 6.7 – Two vertical slices from a microCT scan of a clay fill block sample showing poor contrast between phases, noise (white speckle), beam hardening (lighter/higher greyscale at edges), and penumbra (blurring at the top and bottom of the image)

Figure 6.8 shows a vertical slice from the trimmed (100 mm diameter) sample and a vertical slice from the 100 mm diameter reconstituted sample. Figure 6.8 shows that both of these scans achieve a clear contrast between phases and that sharp boundaries are present between these phases, which allows for accurate segmentation. It can also be seen that any image artefacts present (e.g. beam hardening) are not significant. Table 6.5 shows that the spatial resolution for the trimmed sample remains approximately the same as for the block sample despite the lowering of X-ray power and the change in sample size. This is because the power

settings used for the trimmed sample scan were chosen to achieve a similar resolution. The change in sample size allows a lower exposure time and X-ray power to be used as these two changes, in effect, counteract one another. The reduction of the diameter of the sample allows enough X-rays to penetrate the samples at these lower power settings, leading to acceptable image quality.

Table 6.5 shows that although the contrast for the 100 mm diameter reconstituted sample data was improved relative to the large block sample (Figure 6.8(b)), the spatial resolution achieved in that scan was less than the previous two (62 μm). This is because the same X-ray power settings were used for both the trimmed and reconstituted sample scan. The reconstituted scan is considerably denser than the trimmed sample, which is composed of near-surface clay fill and can be seen to contain larger macropores and stones (Figure 6.8(a)). As a result of this difference in density, the X-rays are less effective at penetrating the reconstituted sample at these power settings. However these settings were chosen in order to assess if the power settings used for the trimmed sample provide useful data when used to examine the embankment cores in Chapter 8. The resolution and contrast achieved using these X-ray power settings within the acquisition time restrictions was deemed acceptable for the study of macropores presented within this thesis, as it allows for the visualisation and quantification of individual macropores above (a maximum of) 62 microns in size.

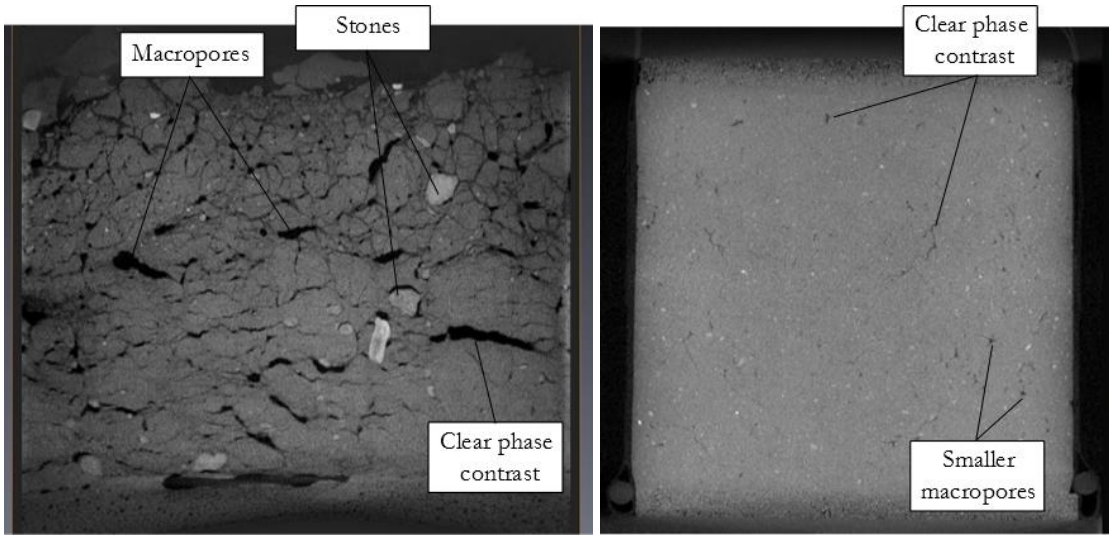

Figure 6.8 – A vertical slice (80 mm height) from the reconstructed microCT image data of (a) the 100 mm diameter trimmed sample and (b) the 100 mm diameter reconstituted sample. Showing clear phase contrast (between pores and other constituents) and no significant imaging artefacts

The image quality of all three scans can be further assessed by viewing the greyscale intensity histogram corresponding to each scan. These are shown in Figure 6.9. It can be seen that the intensity histogram corresponding to the block sample (Figure 6.9(a)) shows only one clear peak within the data. This is due to noise and beam hardening and the data is therefore impossible to segment (As illustrated by Figure 6.7). The block sample histogram also has a much larger range of greyscale than the histograms corresponding to the other scanned samples (Figure 6.9(b) and Figure 6.9(c)). This is due to the presence of a significant amount of high density stones within the sample (Figure 6.5).

The greyscale histograms from the trimmed sample and the reconstituted sample scans (Figure 6.9(b) and Figure 6.9(c)) show a clearer indication of the overlap between the material phases and therefore the threshold value which could be used to segment the data. However, the maxima and minima within the data are not totally apparent due to some noise within the samples. This indicates that 100 mm diameter samples of this density (clay fill) are at the limit of the scanner capabilities in terms of generating scan image data with good image quality. Despite this, the scans conducted here (with these power settings and acquisition time) have provided image data which is of sufficient quality in order for the segmentation and quantification process to be carried out after image enhancement (Chapter 7) (as illustrated by the clear contrast shown in Figure 6.8 and the resolutions shown in Table 6.5). It can also be noted from Figure 6.9 that the reconstituted sample histogram (c) has a lower greyscale range than trimmed sample (b). This is due to the presence of stones in the trimmed sample (Figure 6.8).

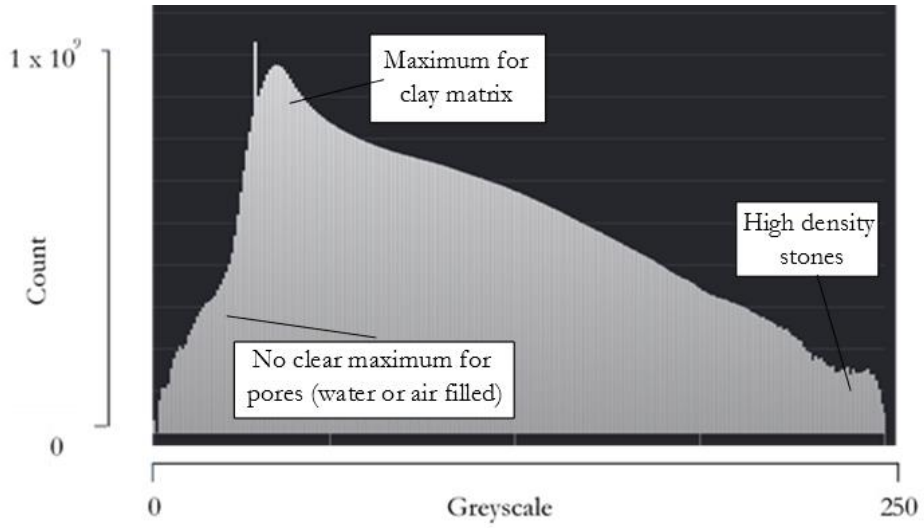

(a)

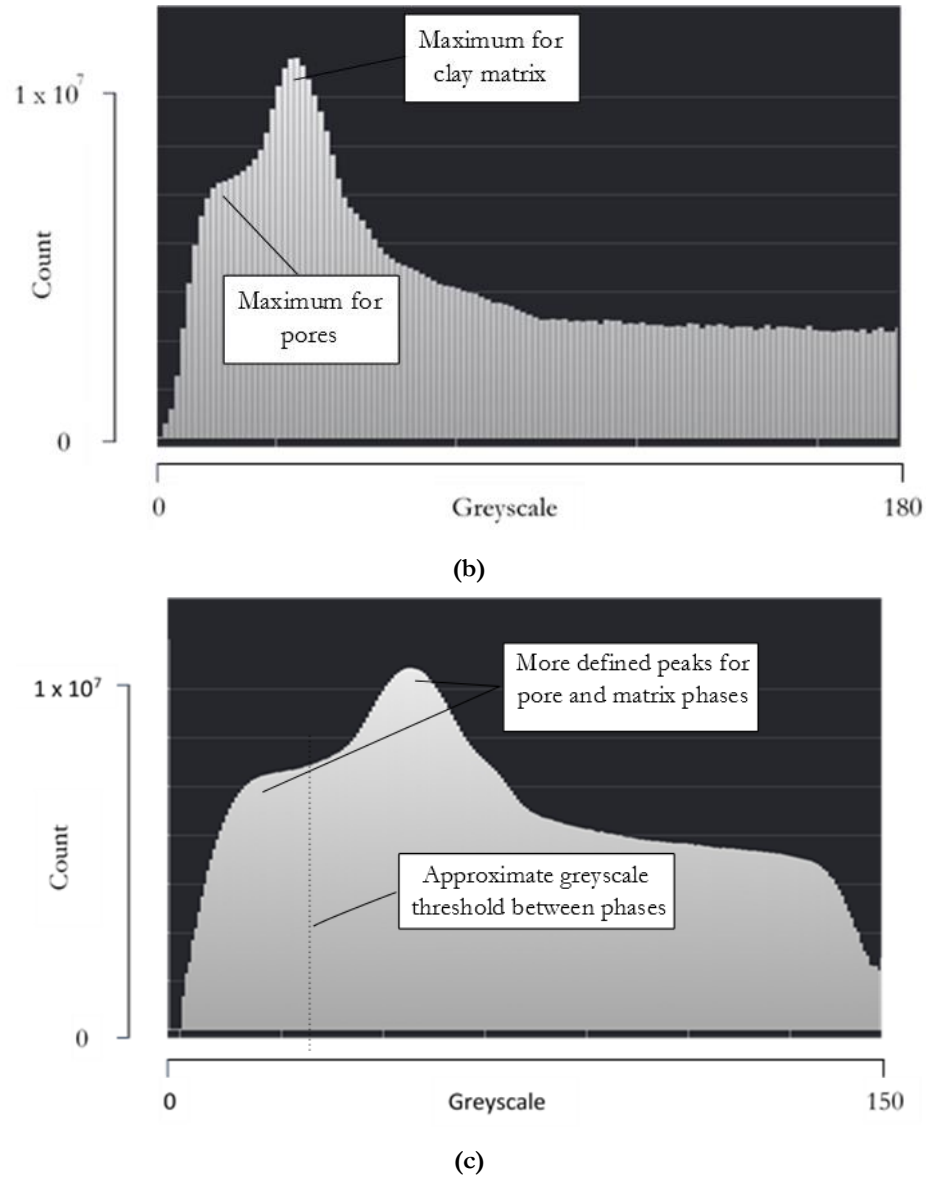

Figure 6.9 – Greyscale intensity histograms for (a) the large block sample, (b) the trimmed 100 mm diameter core, and (c) the reconstituted 100 mm diameter sample. Showing more defined peaks corresponding to the pores in the 100 mm diameter samples

Figure 6.10 shows a series of horizontal slices from three heights (20, 40, and 60 mm from the base of the sample) within trimmed and reconstituted samples. The figure shows the consistency of the samples throughout their height. It can be seen that the trimmed sample has a much greater degree of macroporosity (both larger and more numerous macropores) and is much more variable throughout the entire height of sample, whereas the reconstituted sample is very consistent in terms of macroporosity and structure. Figure 6.10 also shows the difference in edge disturbance between the trimmed and reconstituted samples. The figure shows that the trimmed sample has a much greater degree of heterogeneity along the edges of the sample (large macropores) due to the trimming process during sample preparation.

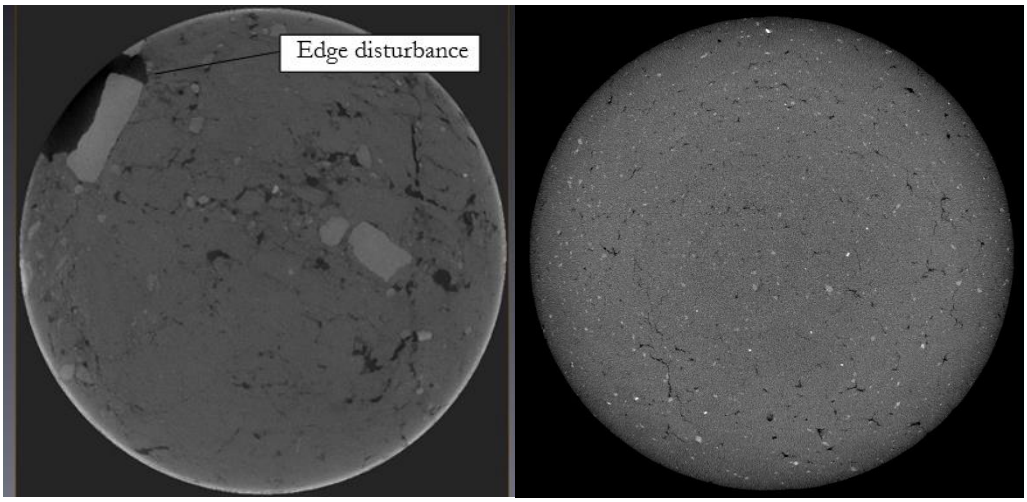

(a)

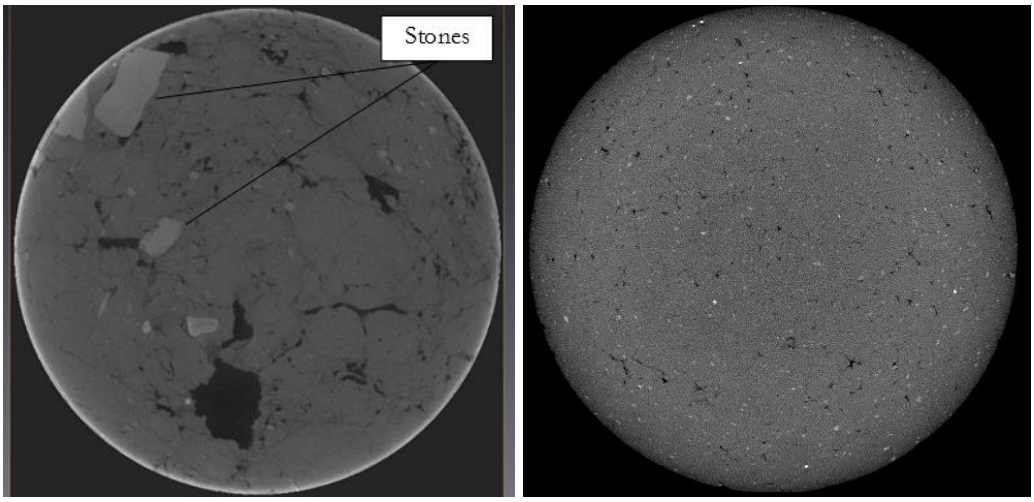

(b)

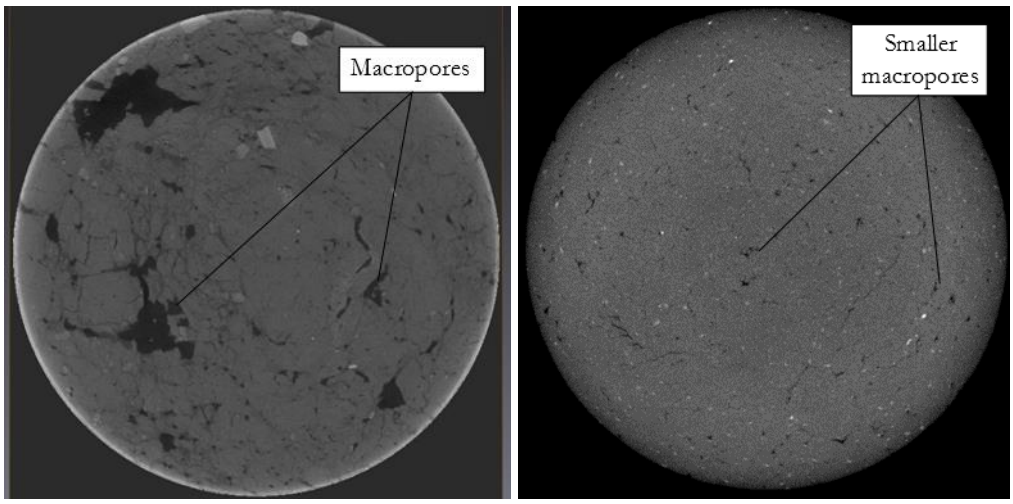

(c)

Figure 6.10 – Horizontal (x-y) slices throughout the height of the samples showing (a) 20 mm height (b) 40 mm height and (c) 60 mm height for the trimmed 100 mm diameter sample (left) and the reconstituted 100 mm diameter sample (right). Showing that the trimmed sample contains much larger macropores and is less consistent than the reconstituted sample.

The reconstituted samples shows less edge disturbance, a more uniform distribution of macropores, and a more consistent structure (more uniform particle sizes) than the trimmed sample (which is near-surface clay fill). Figure 6.5, Figure 6.10, and Table 8.1 (Chapter 8) show that the embankment cores taken from depth within the embankment are similar in particle size, density and edge disturbance to the reconstituted sample. This indicates that the reconstituted sample is a suitable sample to use in order to develop a consistent image analysis procedure which allows for the quantification of macropores within the embankment cores (Chapter 7).

6.6 Conclusions

This chapter presented an investigation into the capabilities of a microCT machine with regards to scanning large clay fill samples within the scan acquisition time constraints imposed by a working day. Several key conclusions were drawn from this investigation and were subsequently used within the scanning methodology for the embankment cores discussed later in this thesis.

- It was not possible to scan a large clay fill block sample (30 cm) using a microCT scanner and obtain sufficient image quality to quantify macropores within the time restraints imposed by a working day (4 hours). This was due to the very dense nature of the clay fill sample requiring very high X-ray powers in order to achieve good resolution and the subsequent loss of phase contrast. The large sample size and density also resulted in excessive amounts of imaging artefacts (such as beam hardening) which further hinder accurate image segmentation.

- A 100 mm diameter sample of near surface clay fill was scanned using a microCT scanner within a working day at sufficient image quality to distinguish material phases (pores and soil matrix) and to allow for segmentation. The reduced diameter of the sample (compared to the large block sample) enabled X-rays to penetrate the sample at a lower intensity without generating excessive imaging artefacts. This size of sample is much larger than commonly scanned using microCT (< 5 cm), especially so for a clay soil.

  The power settings used to scan the 100 mm diameter trimmed sample also achieved acceptable image quality to identify macropores (> 63 microns) and distinguish phases for segmentation when used on a denser 100 mm diameter

reconstituted clay fill sample. Therefore, in order to maintain consistency in all subsequent scans (to allow for comparison between results) the microCT power settings determined for these scans should remain constant (Voltage: 195 kV, current: 105 mA, exposure time: 2 seconds, projections: 1800, and 1998 slices).

- Differences in soil structure between the reconstituted sample (clay fill from 3.5 m depth) and the near-surface (0.5 m) clay fill samples are identifiable from scan image data. Scans of the reconstituted clay fill sample show that the structure, macropore size, and macropore distribution are consistent throughout the sample. This indicates that the reconstituted sample is a suitable sample to use in order to develop an image analysis procedure which allows for the quantification of macropores within other cores extracted from Laverton embankment (Chapter 7).

  Scans of the near-surface clay fill sample show more complexity (including edge disturbance due to sampling), spatial changes in macropore size and distribution, and particle sizes (containing higher density stones). This sample is therefore less suitable for exploring image analysis techniques (Chapter 7) and relationships between macropore properties (e.g. pore size distribution, macroporosity, macropore length, and macropore surface area) with measurements of saturated hydraulic conductivity (Chapter 8).

7 Development of a microCT image analysis procedure for large scale clay fill samples

7.1 Introduction

This chapter presents a microCT image analysis procedure for a reconstituted 100 mm diameter clay fill sample which allows for visualisation and quantification of the internal macropore architecture. This procedure provides a technique to consistently image and measure macropore properties including size, structure, and distribution. A consistent image analysis procedure is necessary to compare results obtained from different microCT scans. The procedure developed here allows embankment core samples to be reliably measured and compared (including at different states of saturation) in Chapter 8.

This chapter explores subsampling as a technique to allow for quantification (identification and measurement of individual macropores) within a data set from a large scale microCT scan taking into account computational demands. The image procedure developed also seeks to limit the effects of operator input/bias into the analysis and establish a consistent method of improving and segmenting scan image data, as these are common sources of error when processing microCT scan image data (see Chapter 4). Additionally, this chapter investigates the impact of a partial volume effect correction on measured pore property metrics (e.g. number, and volume of macropores).

7.2 Objectives

The aim of this investigation was to develop a consistent and repeatable image analysis procedure for 100 mm diameter clay fill cores which can be subsequently used on scan data obtained from the sample cores in Chapter 8. This procedure was developed by achieving the following specific objectives:

1) To explore three types of subsampling (A maximum cuboid subvolume, 25 mm layers, and a 40 mm central cube) as a method to reduce computational demand in order to allow for the quantification of scan image data from a large clay fill sample (100 mm diameter).
2) To determine suitable image improvement and segmentation methods which allow for an accurate definition of the macropores (> 60 μm) within a 100 mm diameter clay fill sample.
3) To assess the impact of the partial volume effect on measured macropore properties (e.g. number, volume, and distribution of macropores) within a 100 mm diameter clay fill sample.

7.3 Methodology

7.3.1 Materials and microCT scanning procedure

An investigation was carried out to determine the optimal image analysis procedure to use for a clay fill 100 mm diameter sample. A reconstituted specimen (100 mm diameter, 87 mm height) (Figure 7.1) was prepared and scanned using the settings described previously (Section 6.4.3.). These settings are shown in Table 7.1. It has been shown in Chapter 6 that this scan is of acceptable image quality (resolution and contrast) to allow for segmentation between the pores and soil matrix and represents the densest sample found within the embankment samples.

Figure 7.1 - The reconstituted sample prepared from a clay fill from Laverton embankment (3.5 m depth) (80 mm height)

Table 7.1 – The microCT scan settings used in order to scan the 100 mm diameter reconstituted clay fill sample at sufficiently image quality (see Chapter 6).

Sample	Voltage (kV)	Current (mA)	Exposure (ms)	Projections	Vertical slices	Other
Reconstituted 100 mm diameter cylindrical sample	195	105	2000	1800	1998	Copper* filter (0.5 mm thick)

*copper filter used to reduce beam hardening

Image data from the scan of the reconstituted sample was reconstructed in Avizo fire (FEI, 2014) as shown in Figure 7.2. The image data was used to compare various analysis techniques and procedural steps and comment on peculiarities and limitations of the experimental method. Figure 7.3 shows a flowchart of the analysis procedure investigated. The following four key steps in this process were explored and are discussed in this Chapter:

- Extraction of sub volumes from within the sample image data in order to reduce computational demands and enable the quantification of macropore size properties (Section 4.5.1).
- Filtering and image enhancement to remove any image artefacts and increase definition between pore and matrix phases to enable more accurate segmentation (Section 4.5.3.).

- Segmentation and thresholding methods to effectively assign voxels within the image data to material phases in an accurate manner, (ideally with limited operator bias) (Section 4.5.2.).
- Establishing the impact of a partial volume effect correction on the pore property metrics (e.g. number of pores) obtained from sample scan data (Section 4.6.1).

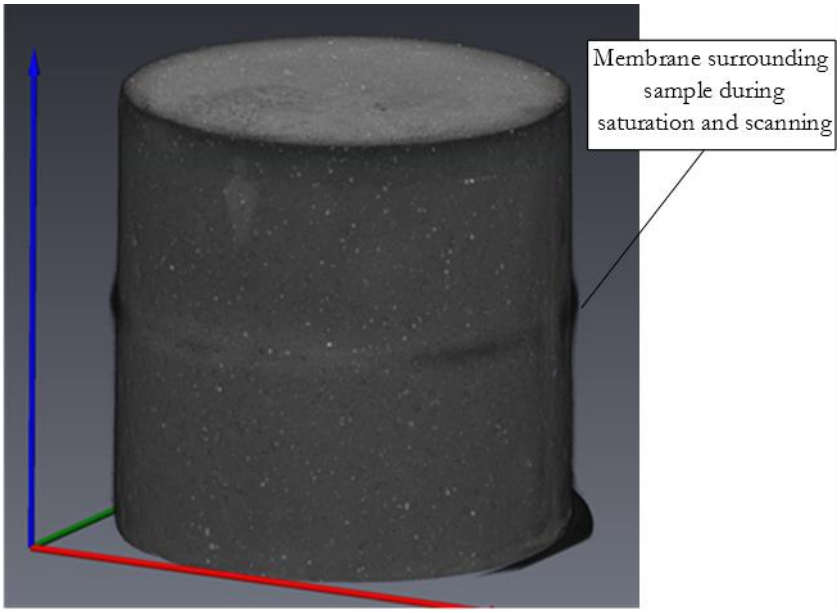

Figure 7.2 – Reconstruction of the 100 mm diameter reconstituted sample visualised within Avizo fire (FEI, 2014)

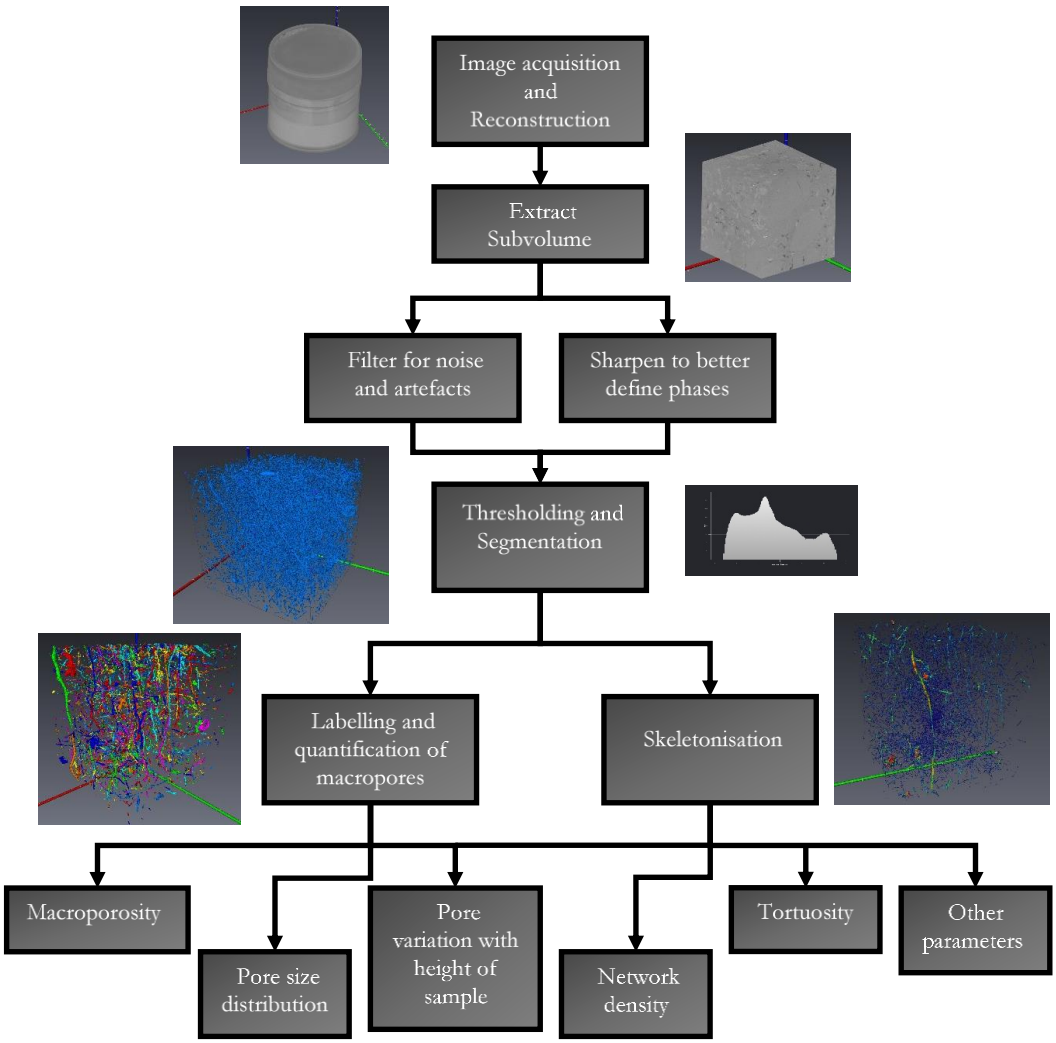

Figure 7.3 – A flowchart of the key steps involved in a microCT scan image analysis procedure in order to visualise and quantify the internal macropore structure of clay fill samples

7.3.2 Subsampling

As discussed in Chapter 4, extraction of a subvolume for analysis is a method which can be used within microCT image analysis procedures in order to remove edge effects and/or reduce the sometimes prohibitive size of the image files generated. It is often necessary to reduce file size prior to analysis in order to output useful results from the extremely large amounts of data (32 Gb) generated during the scans, even on a computer with significant processing power (all samples were analysed in a specifically designed CT visualisation suite on a computer with 2 x 2.5 GHz processors and 176 Gb of RAM).

As the aim of the image analysis procedure is to quantify the macropore structure within the samples, extraction of a subvolume has the limitation that almost all subvolumes

will contain truncated pores at their edges. Quantitative results from one subvolume within a sample will therefore differ from the results of another, due to this truncation of pores as well as the inherent variation of soil parameters throughout the sample.

The use of the three subsampling methods with respect to quantification and truncation of pores was measured by examining pore size distributions, pore property metrics (macroporosity, macropore volume, length, surface area etc.), and the variation of volume of macropores with depth throughout the sample. These three types of subsample are shown in Table 7.2 and visualised in Figure 7.4. The impact of both the size and location of the subvolumes were examined. The computational implications in terms of time and what results could be generated from the subsamples was also explored.

The first method investigated was the extraction of the maximum possible cuboid volume from the centre of the sample (Figure 7.4). This volume was chosen to see if it was possible to visualise and quantify almost the entire volume of macropores within the sample. This volume also results in removing some, but not all, edge effects caused by sampling disturbance. These edge effects are important as they can result in incorrectly quantified pores along the edges of the subvolume.

The second method involved splitting the core into three volumes (or layers) (top, middle and bottom) so that the maximum volume could be analysed in smaller, less computationally demanding, sections (Figure 7.4).

The last method involved the extraction of a 4 cm cube from the centre of the sample (Figure 7.4). This has the advantage of removing the effects of sampling disturbance around the edge of the sample whilst the smaller volume means that the analysis is potentially less computationally costly.

Table 7.2 – The dimensions and location of the different subsampling methods used in the investigation into the impact and importance of subsampling with microCT image data

Subvolume method	Number of subvolumes	Height (mm)	Width (mm)	Location
Max cuboid	1	80	70	Centre of sample
Layers	3	25	70	Top (1), middle (2), and bottom (3) of sample
4 cm cube	1	40	40	Centre of sample

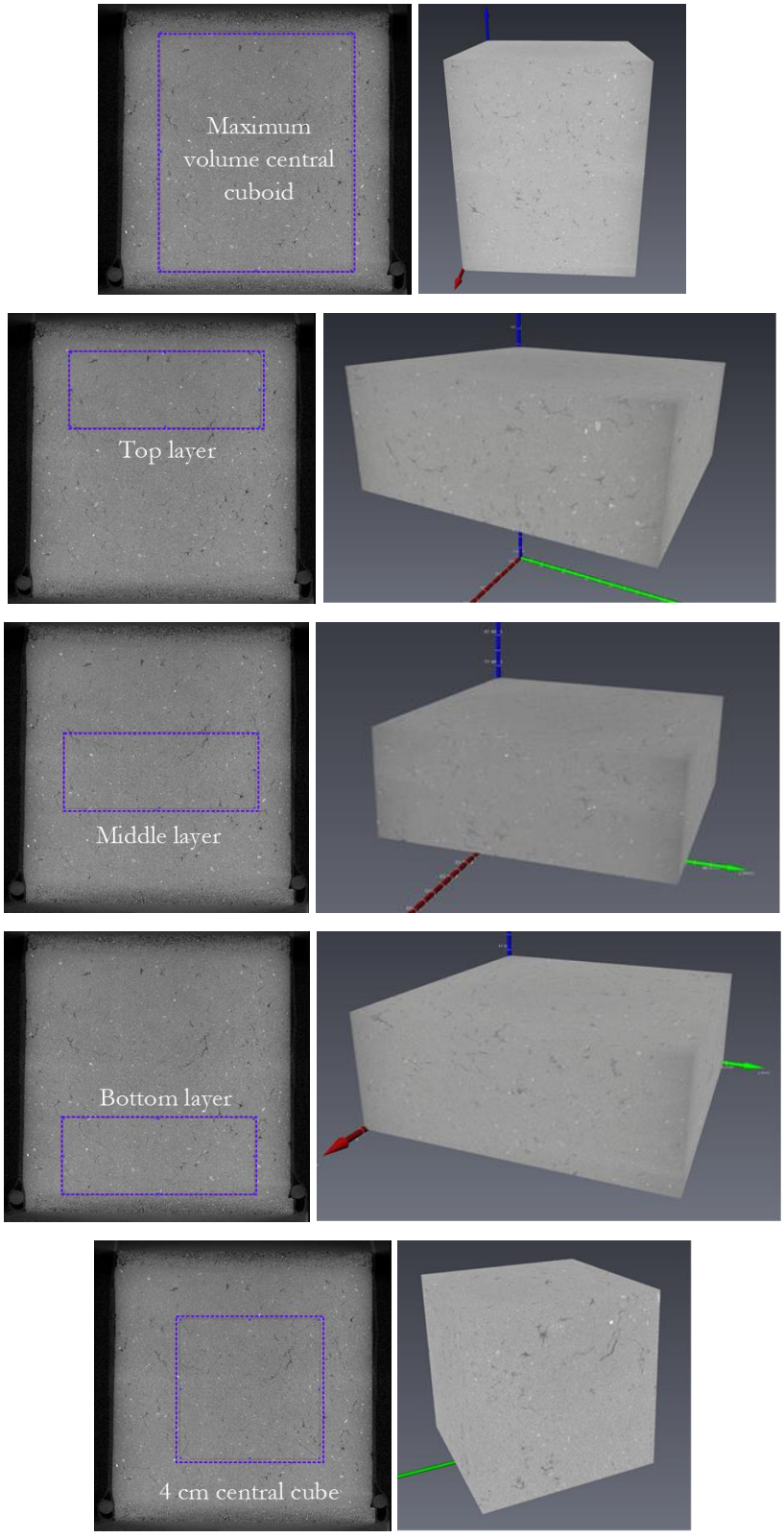

Figure 7.4 – Visualisations of the five subsample locations within the reconstituted sample image data (dimensions in Table 7.2)

7.3.3 Filtering and image enhancement

All microCT scans contain imaging artefacts to some degree or other (e.g. noise or beam hardening) due to the nature of the scanning process (see Chapter 4 and Chapter 6). The effect of these imaging artefacts on the quality of the image data and the ability to segment and quantify the macropore size properties of the sample accurately can be alleviated to some extent during the image analysis process (See Chapter 4 Section 4.5.3.).

In this investigation four different methods of image enhancement were explored (a median filter, a sharpened median filter, a non-local means filter, and a Gaussian filter). The methods investigated were all types of image filter, commonly used within microCT research to improve the quality of the image data by removing noise and other imaging artefacts, allowing the pores to be more clearly identified and segmented. The effectiveness of these methods was measured by comparing the degree of contrast (from image slices and greyscale histograms) achieved using each technique whilst balancing against the computational cost of each respective method. These methods were investigated using a 4 cm cube subsample due to the computational requirements necessary for image improvement.

This process was used to determine the most appropriate image enhancement procedure to achieve sufficient image contrast to analyse embankment core samples (Chapter 8) at the minimum computational cost. Therefore, only available filters thought to provide clear noise reduction and increased phase contrast (between pores and matrix) within computational limits were explored. It is possible that different types of noise removing filters which were not investigated may have been more effective than those discussed here. However, there is no published standard for filtering image data such as this. Indeed, very few published microCT studies in the geosciences discuss the use of image enhancement filters in detail, often choosing filters seemingly arbitrarily.

The four methods explored were:

1) A median filter is commonly used to remove noise and smooth images, particularly in cases where the preservation of edges and phase boundaries is a priority (see Chapter 4). The principle of a median filter is that voxel greyscale values are related to the values of neighbouring voxels and by examining the surrounding cells of each voxel, greyscale values can be better smoothed. A median filter has the effect of smoothing the image data and removing noise, however this can lead to a loss of contrast between phases.

2) A sharpened median filter applies a subsequent deburring filter as well as a median filter to the image data in order to sharpen the edge boundaries between phases.

3) A non-local means filter works in a similar manner to a median filter, although it only considers the mean value of voxels in the vicinity which are similar in greyscale to a particular voxel when smoothing. In other words, this filter only takes into account the neighbouring voxels which are in the same phase as a voxel and look similar. It is therefore considered useful for maintaining edge sharpness and increasing the contrast between phases.

4) A Gaussian filter smooths the image data and reduces noise by applying a transformation to each voxel in the image using a Gaussian distribution. Values from this distribution are used to build a convolution matrix which is applied to the original image (FEI, 2013). In a similar manner to the median filter, each voxel's new value is set to a weighted average of that voxel's neighbourhood.

7.3.4 Segmentation and thresholding

As discussed in Chapter 4 Section 4.5.2, segmentation is the process by which individual voxels can be classified as the different phases or materials present within the sample according to their greyscale (X-ray attenuation) values. Segmentation is a key step within the microCT image analysis procedure, as different methods and operators can achieve very wide ranging end results (e.g. estimates of total macroporosity ranged between 13 and 73 % in one study (Baveye et al., 2010)). The most commonly used approach is global thresholding which uses an estimate from the greyscale histogram of the image data to determine a threshold between phases (e.g. between macropores and the soil matrix). This has historically been done manually, however researchers have noted the need to implement more automated segmentation processes in order to reduce the impact of operator bias (see Chapter 4 Section 4.5.2).

Therefore within this investigation, the use of both an automated and a manual method for determining a threshold value were explored and compared. The automated method used was watershed segmentation which simulates the flooding of the image data from a series of seed points using a greyscale gradient image (FEI, 2014). The effectiveness of this segmentation method to fully ascertain the pore phase within the reconstituted sample was assessed against manual (interactive) segmentation of the image data and visual

verification of a section of segmented slices. The total macroporosity measured using the respective segmentation techniques was also compared.

7.3.5 The influence of a partial volume effect correction

Partial volume effect, as discussed earlier in Chapter 4 (Section 4.6.1), is a consequence of the fact that many voxels contain more than one material or phase and that the greyscale value attributed to that voxel will therefore be an average of the constituents of the voxel. This often leads to the boundaries between phases being blurred and occurring over the width of several voxels.

To counteract this limitation of the CT image data, it is common practice to remove all of the objects within the scan data which are below the width of either one or two voxels in equivalent diameter (Helliwell et al., 2013). The partial volume correction therefore effectively results in reducing the resolution of the scan images up to twice the original voxel resolution. However, without this correction it is possible that the smallest objects within the data set identified as pores are not actually pores.

The quantitative impact of correcting for PVE was measured by calculating the differences in pore property metrics between image data with no correction applied and image data with a two voxel PVE correction applied. The influence of a two voxel PVE correction on the measured pore size distribution and the variation of macropores throughout the height of subsample was also established.

7.4 Results and discussion

7.4.1 Presentation of results

Within the results of this investigation, two visualisations of pore size distributions are used:
1) *Pore volume as a percentage of total sample volume* – This displays the total macroporosity present within the sample in relation to the volume of the whole sample (in terms of pore size).

2) *Pore volume as a percentage of total pore volume* – Displays the proportion each pore size contributes to the total macroporosity within a sample.

The variation of macroporosity throughout the samples is presented by examining profiles of the *total pore volume per slice.* Which is a measure of the pore volume within each vertical slice of the sample as a percentage of the total volume of that slice.

Calculating the *volume of the top ten largest pores* identified allows for the effects of subsampling and pore truncation to be examined.

Some researchers have shown that it is possible to represent the macropore structure of a soil sample using a process known as *skeletonisation* (Luo et al., 2008). A skeleton of a macropore is its centre line. Skeletons can be generated by determining the nearest distance to the border voxels of a pore and thinning so that the pores can be represented by lines (or tubes) and nodes. The process is extremely computational heavy and can only be carried out on small subsamples. The following pore property metrics are also used to describe quantitative results in this study:

- *Macropore density* is the number of macropore networks per unit volume.
- *Mean macropore length* is the average length of each individual macropore.
- *Length density* is the total actual length of macropores per unit volume.
- *Surface area density* is the total surface area of macropores per unit volume.
- *Mean tortuosity* is the ratio of the total actual macropore length to total straight-line (skeletonised) distance of all the macropores within the sample.
- *Computational cost* is also noted.

7.4.2 Subsampling

Figure 7.5 shows the pore size distributions corresponding to the five different subvolumes extracted from within the reconstituted scan image data (Figure 7.4) in terms of total sample volume. The figure shows that the 4 cm cube subsample has a similar total macroporosity to the maximum cuboid subsample. This is confimed by Table 7.3 which shows the quantitative pore property metrics calculated for the five different subvolumes. The macroporosity of the 4 cm central cube subsample was 0.40 % compared to 0.39 % for the maximum cuboid sample. The individual layer subsamples varied in total macroporosity between 0.27 % and 0.48 %. This indicates that the smaller 4 cm central cube subsample captures the overall average macroporosity within the reconstituted sample better than the individual layer subsamples.

Figure 7.5 shows that the macroporosity varies considerably between the top and bottom layer subsamples. This is likely a result of the increasing macroporosity present throughout the height of the sample due to the compaction technique used when manufacturing the reconstituted sample (i.e. it is denser at the bottom than the top). This is shown in Table 7.3 as the other quantifiable pore property metrics for the subsamples are also less in the bottom layer subsample than the top layer subsample. For instance, the macropore surface area density within the bottom subsample is significantly less than the

surface area density calculated for the top subsample (45.87 m^2/m^3 compared to 74.76 m^2/m^3).

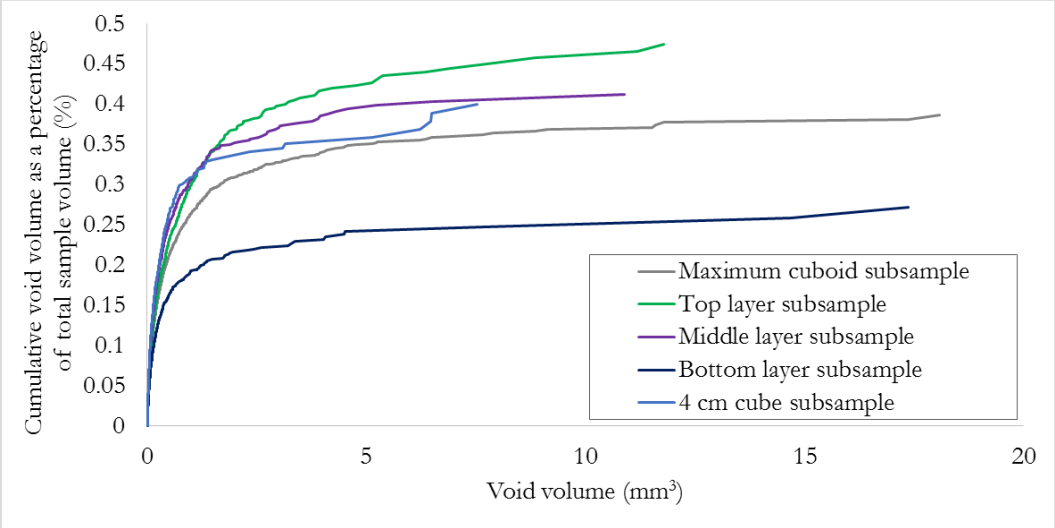

Figure 7.5 – Pore size distributions (as a % of total sample volume) quantified using five different subvolumes within the reconstituted sample.

Table 7.3 – Pore property metrics quantified using five different sub volumes within the reconstituted sample (see Figure 7.4)

	Maximum cuboid subsample	Top layer subsample	Middle layer subsample	Bottom layer subsample	4 cm central cube subsample
Macroporosity (with 2 voxel PVE correction) (%)	0.386	0.475	0.412	0.272	0.400
Macropore density ($x10^6$) (no/m^3)	42.079	45.452	48.766	33.170	51.697
Mean macro pore length (mm)	1.007	1.033	0.999	0.981	0.979
Length density (km/m^3)	42.391	46.945	48.761	32.536	50.607
Surface area density (m^2/m^3)	63.003	74.76	68.612	45.867	69.153
Mean tortuosity*	-	-	-	-	1.241

* Tortuosity could not be computed for the larger subvolumes due to the number of macropores present.

These results show that the location of the subsample defined within the scan image data influences the macropore property metrics achieved within the quantitative analysis due to the variability of these properties within the sample.

As well as the location of the subsample influencing the quantified results, it is evident that the size of the subsample also impacts the size (volume, length, and surface area) and number of pores identified in the analysis. Figure 7.6 shows the pore size distributions of the five subvolumes in terms of total pore volume. It shows that the total macroporosity within the 4 cm cube subsample is comprised of smaller voids than the other three samples, with 100 % of the macroporosity consisting of pores under 7.5 mm^3 in volume. Table 7.4 shows the maximum, minimum and average volume of the ten largest pores within each subvolume. The table shows that the average volume of the ten largest pores is lower for the three layer subsamples and the 4 cm cube subsample than it is for the maximum cuboid subsample. This indicates that the layer and 4 cm cube subsamples do not fully capture the largest pores present within the sample and some truncation of pores occurs at the edges of these subvolumes. Despite this, Table 7.3 shows that the mean macropore length within the subsamples is fairly consistent. This contradiction is an indication that the majority of macropores identified are very small in terms of volume and length, and that it is mostly the largest macropores which are affected by the subsample choice. Figure 7.6 shows that the total macroporosity appears to be mainly comprised of smaller macropores (for all samples around 80 % of total pore volume is made up of pores less than 2 mm^3 in volume). These sizes of pores appear to be captured in all the subvolumes and the subvolume choice therefore has less impact. It should be noted however that this is the case for the reconstituted sample and, as discussed in Chapter 6, this is quite a uniform clay fill sample. So the choice of subsample methods is likely to generate greater discrepancies when examining less homogenous samples.

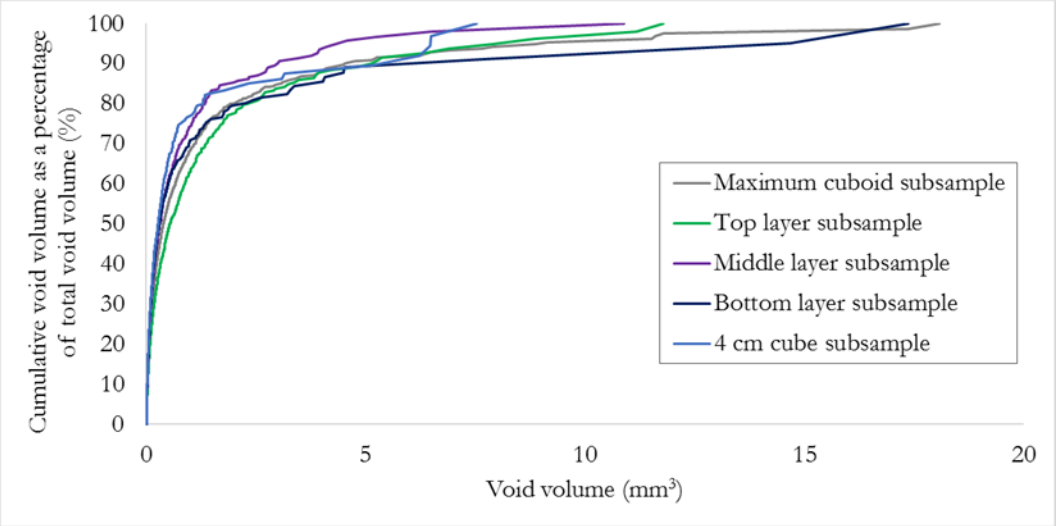

Figure 7.6 - Pore size distributions (as a % of total pore volume) quantified using five different subvolumes within the reconstituted sample.

Table 7.4 – The properties of the ten largest pores measured within five different subvolumes within the reconstituted sample

10 largest pores	Maximum cuboid subsample	Top layer subsample	Middle layer subsample	Bottom layer subsample	4 cm central cube subsample
Mean volume (mm^3)	10.080	7.346	5.068	6.664	4.422
Max volume (mm^3)	18.081	11.787	10.888	17.362	7.527
Min volume (mm^3)	6.902	4.764	3.438	3.204	1.764

The computational cost for the subsample methods is shown is Table 7.5. The Maximum cuboid subvolume is considerably more computational demanding than the other subsampling methods. Table 7.5 shows that only the 4 cm cube subvolume allows for skeletonisation of the pores and image improvement (filtering) due to the number of pores present within each subvolume (the maximum cuboid and layer subvolumes contain a greater total number of pores). This is because skeletonisation and image enhancement of microCT data for samples with so many pores requires more computational power than was available for the analysis carried out here.

In addition to the differences in computational cost, the 4 cm cube subvolume appears to capture overall sample macroporosity and other property metrics well. This subvolume is therefore suitable to use within the image analysis procedure of subsequent scans of clay fill samples.

Table 7.5 – The computational cost of the different methods of subsampling investigated

Subvolume method	Computational cost
Max cuboid	Extremely heavy - does not allow for complete quantification/ skeletonisation due to the quantity of pores present. Image improvement is difficult.
Layers	Moderate - does not allow for skeletonisation. Image improvement is difficult.
4 cm central cube	Moderate but allows for skeletonisation. Image improvement possible.

7.4.3 Image improvement

The effects of the applying image filters to the reconstituted scan data in order to improve image quality were explored by examining greyscale intensity histograms and by visual assessment of slices throughout the height of the subsample (4 cm central cube). An example of one such slice from the midsection of the subsample is shown in Figure 7.7.

Figure 7.8 shows this midsection slice subject to no filter, a 3D median filter, a 3D sharpened median filter, a non-local means filter, and a Gaussian filter. It can be seen that all of the filters used reduce the level of noise present within the scan image data. The sharpened median filter and the non-local mean filter appear to give the sharpest contrast between phases with the most defined pore edges. However, the Gaussian filter and the median filter result in blurring of the pore boundaries due to the smoothing process which reduces noise. Using any of the filters results in the loss of some very small pores, however these pores are likely to be below the value of pores affected by the partial volume effect (volume < 0.0082 mm^3) so would not be included in quantitative results anyway.

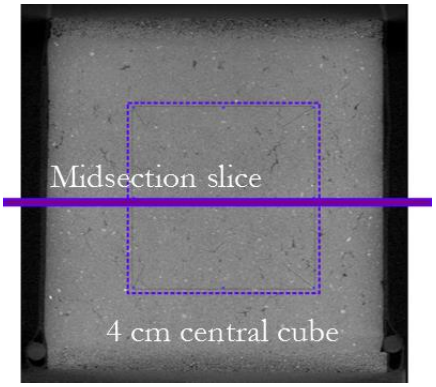

Figure 7.7 – The location of an example slice used to explore the effectiveness of image filters used in order to improve the image quality of the reconstituted sample

The visual inspection of the effectiveness of these image filters was supplemented by examining the greyscale intensity histograms before and after application of the image filters (Figure 7.9). Figure 7.9 shows that the median and Gaussian filters do not make a significant improvement on the definition of the material phase peaks within the greyscale histograms whereas the sharpened median filter and non-local means filter result in improved image quality and definition of peaks. These filters will therefore make the process of segmentation easier and more reliable.

The effectiveness of image enhancement methods has to be balanced against the computation cost required in order to achieve higher quality image data. Table 7.6 shows the computational cost of all the enhancement methods investigated. The non-local means filter is considerably more computationally costly than the sharpened median filter, taking twice as long to complete. It is also worth noting that applying the median filter and sharpened median filter in three dimensions, as opposed to two, causes a significant increase in the time need for computation.

The sharpened median filter and the non-local means filter both have a similar effect in terms of reducing noise and improving phase contrast when applied to the image data Therefore due to the very significant difference in computational time needed for each respective method, the 3D median filter with sharpening represents the most effective and useful image enhancement process to include within the analysis procedure for all subsequent scans.

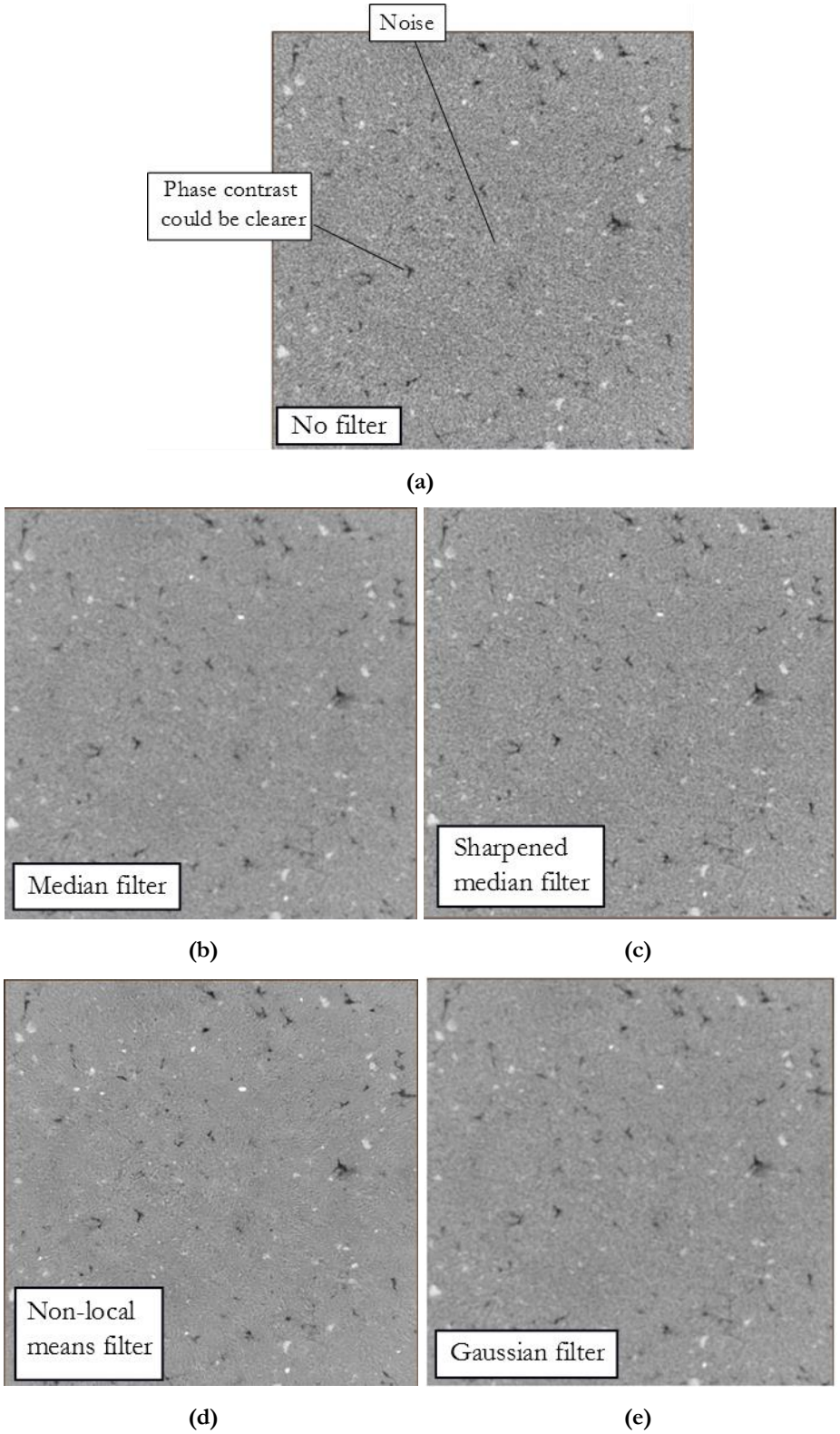

Figure 7.8 – A midsection slice from the reconstituted scan image data (4 cm cube subsample) subjected to (a) no filter, (b) a 3D median filter, (C) a 3D sharpened median filter, (d) a non-local means filter, and (e) a Gaussian filter.

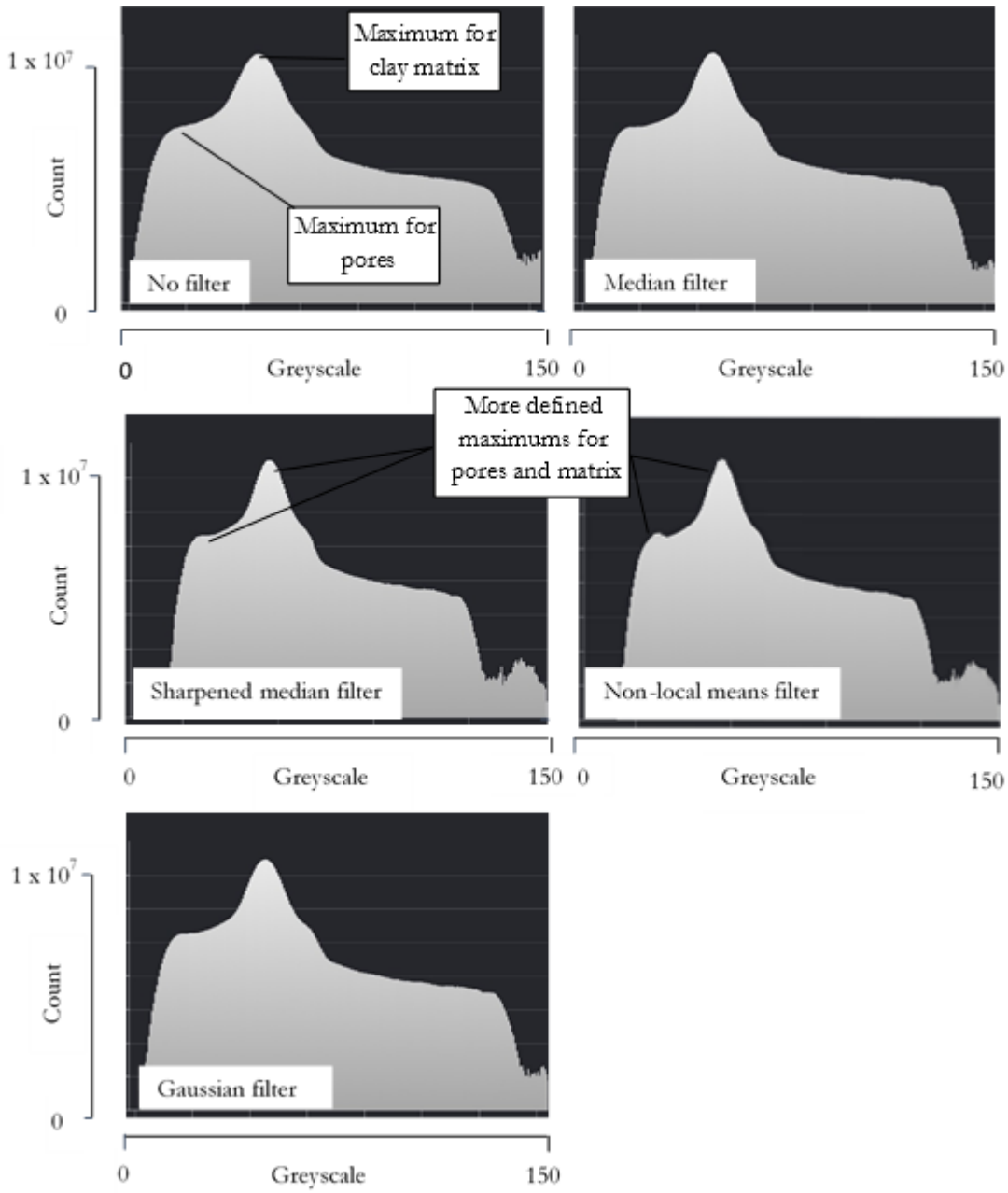

Figure 7.9 – Greyscale intensity histograms corresponding to the reconstitute sample before and after application of four different image enhancement filtering techniques (no filter, a 3D median filter, a 3D sharpened median filter, a non-local means filter, and a Gaussian filter).

Table 7.6 – The computation cost of the four image enhancement filtering techniques investigated

Type of image enhancement	Computational cost
No filter	None
Median filter	Moderate
Sharpened median filter	Moderate (completion time 1.5 times longer than median filter)
Non-local means filter	Heavy (completion time more than three times longer than median filter)
Gaussian filter	Light (completion time half as long as median filter)

7.4.4 Thresholding and segmentation of the image data

The effectiveness of automated watershed thresholding in relation to interactive manual thresholding was compared by visual assessment of a set of slices throughout the height of the reconstituted sample (4 cm central cube subsample).

Figure 7.10 shows a midsection slice throughout the 4 cm subsample prior to segmentation (after application of a sharpened median filter) (see Figure 7.7(c)). Figure 7.11 shows the same slice after application of the watershed flooding algorithm within Avizo fire (FEI). Using the fully automated method on this sample results in many unsegmented pores compared to the manual method (Figure 7.12). This indicates that the automated method does not provide a reliable measurement of sample macroporosity. This suggests that the automated watershed thresholding method is more suited to scan image data containing more pronounced peaks within the greyscale histogram. Because the reconstituted sample is a large clay fill sample, the peaks corresponding to different phases within the greyscale histogram are not as distinct as they would be within a smaller scan of a more homogenous material of consistent density (e.g. glass beads) (see Chapter 4 Figure 4.3 for an idealised greyscale histogram with clear peaks).

Figure 7.12 shows the midsection sample slice after segmentation using the manual interactive thresholding method. It can be seen that the image data does not contain a significant amount of unsegmented pores. The manual method, although more labour intensive, does allow for a more reliable segmentation method than the automated method for a sample of this type (dense clay with intensity histograms lacking complete definition).

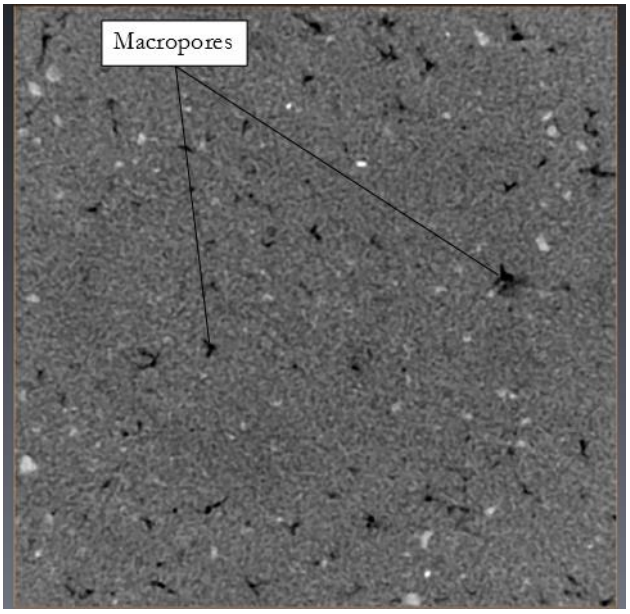

Figure 7.10 – A midsection slice through the reconstituted sample (4 cm central cube subsample) prior to segmentation (pores shown in black)

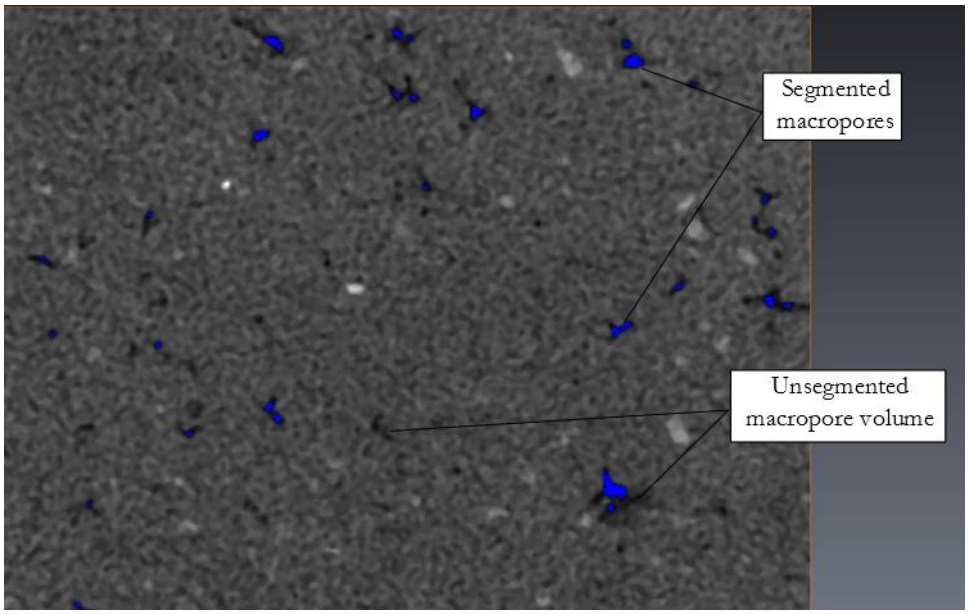

Figure 7.11 – The midsection slice of the reconstituted sample (4 cm central cube subsample) after thresholding using the fully automated 'watershed' method. Showing the pores segmented using the method in blue.

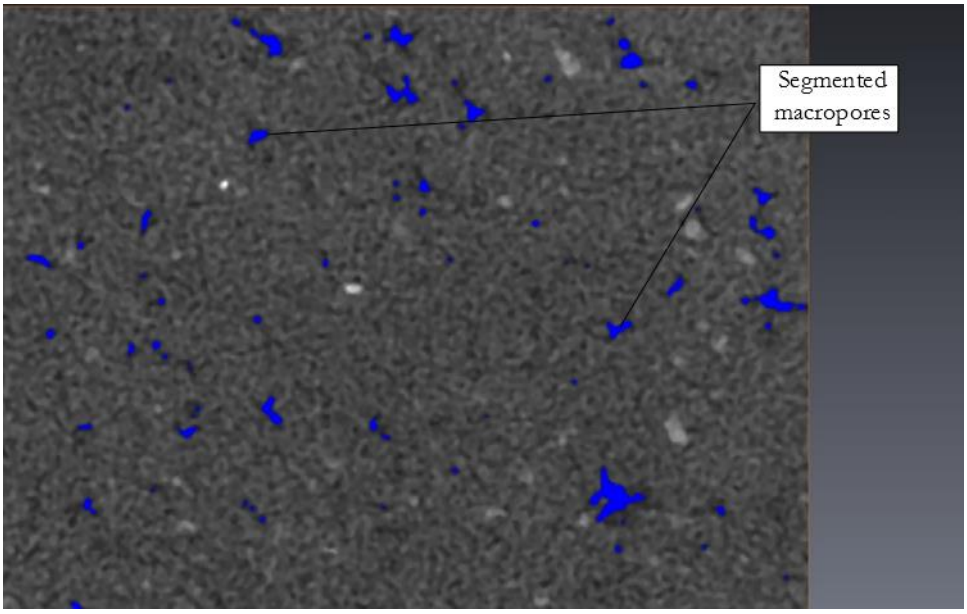

Figure 7.12 - The midsection slice of the reconstituted sample (4 cm central cube subsample) after manual thresholding using the interactive method. Showing the pores segmented using the method in blue.

The impact of using the different segmentation methods on the measured macroporosity is compared in Table 7.7 which shows the total macroporosity calculated using the threshold values defined by the automated and manual segmentation techniques. The difference in the calculated macroporosity is very significant, particularly as overall sample macroporosity is low, so the relative difference between the two segmentation methods is substantial (46 % of total macroporosity).

Table 7.7 – Total macroporosity within the reconstituted sample (4 cm central cube subsample) calculated from pores segmented using the automated segmentation method and using manual interactive thresholding

Threshold greyscale value	Macroporosity (2 voxel partial volume correction) (%)
Automated threshold (30)	0.216
Manual threshold (35)	0.400

7.4.5 Partial volume effect correction

In order to remove the uncertainty associated with the small objects within the scan image data caused by the partial volume effect, all objects with an equivalent diameter less than two voxels (volume < 0.0082 mm^3) wide were removed from the image data prior to quantification of macropore property metrics.

Table 7.8 shows the impact of this partial volume correction on the pore property metrics derived through the image analysis procedure by comparing the results of an

uncorrected and corrected analysis of the reconstituted scan image data. It can be seen that this correction leads to removal of a large number of objects from within the image data.

This is because the reconstituted sample is quite uniform in terms of pore size and distribution and contains few large macropores compared to the number of smaller macropores. However it is noticeable that although the number of pores removed is large, particularly in the largest subvolume, that the volume of pores removed is actually quite small. Therefore the effect of a two voxel partial effect correction on total calculated macroporosity is small (between 0.02 and 0.04 % of sample volume depending on the size of the subsample).

Table 7.8 – The quantitiative impact of partial volume correction (2 voxels) on pore properties derived from the five different subvolumes throughout the reconstituted sample image data

	Maximum cuboid subsample	Top layer subsample	Middle layer subsample	Bottom layer subsample	4 cm central cube subsample
Number of pores with no partial volume correction	79295	31164	29393	19108	16840
Number of pores with a correction	16885	6084	6513	4440	3307
Total volume of macropores with no partial volume correction (mm^3)	1663.21	679.22	592.19	391.81	279.62
Total volume of macropores with a correction (mm^3)	1550.02	635.57	550.04	363.89	256.17
No PVE correction macroporosity (%)	0.41	0.51	0.44	0.29	0.44
Corrected Macroporosity (%)	0.39	0.48	0.41	0.27	0.40

Figure 7.13 shows the result of the partial volume correction on the pore size distribution obtained from the segmented images (in terms of total sample volume). It shows that the PVE correction translates the pore size distribution downwards by the volume of pores removed, whilst keeping the shape of the distribution the same. This is to be expected as the PVE correction only affects the smallest objects within the image data and not the pores which comprise the majority of the pore size distribution.

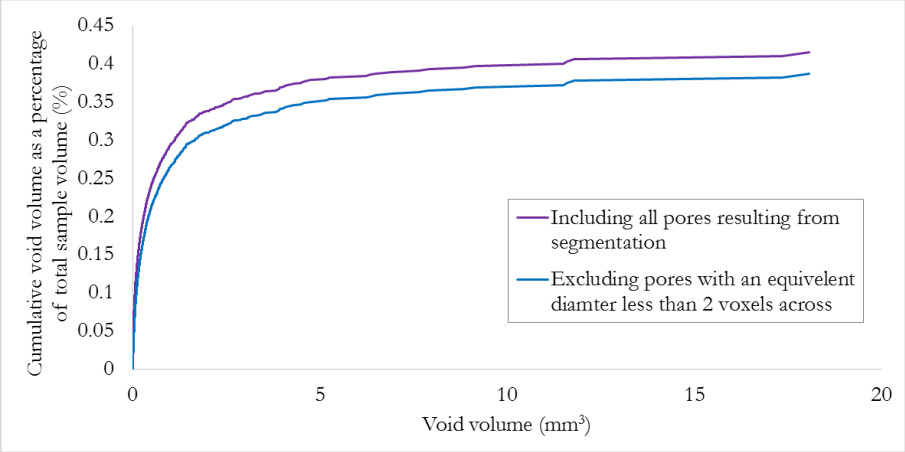

Figure 7.13 – The impact of partial volume correction (2 voxels) on pore size distributions calculated from the reconstituted sample (maximum cuboid subsample)

Figure 7.14 shows the impact of the PVE correction on the profile of volume of pores per slice throughout the height of the reconstituted sample. The correction does not seem to have a great impact on the profiles with the exception of one small section at the centre of the subsample, which has a higher macroporosity. This difference would indicate that the increase in macroporosity in these middle slices is due to lots of individual small macropores as opposed to a few larger macropores, as these are the size of pores which are removed from the scan data in the correction because they cannot definitely be determined to be pores. This increase in macroporosity is likely a consequence of sample preparation of the reconstituted sample. The effect of the PVE correction therefore depends on the nature of the sample scanned and the distribution of macropore sizes present as opposed to the total level of macroporosity.

Overall, the partial volume effect correction allows for more reliable pore property metrics from the scan image data due to the removal of uncertainty related to the smallest objects in the data, whilst only altering calculated macroporosity by a small amount. A two voxel correction (equivalent diameter < two voxel widths) is therefore included within the image analysis procedure of clay fill embankment samples in Chapter 8. Within samples scanned at different states of saturation the correction was standardised to aid comparison of calculated pore property metrics.

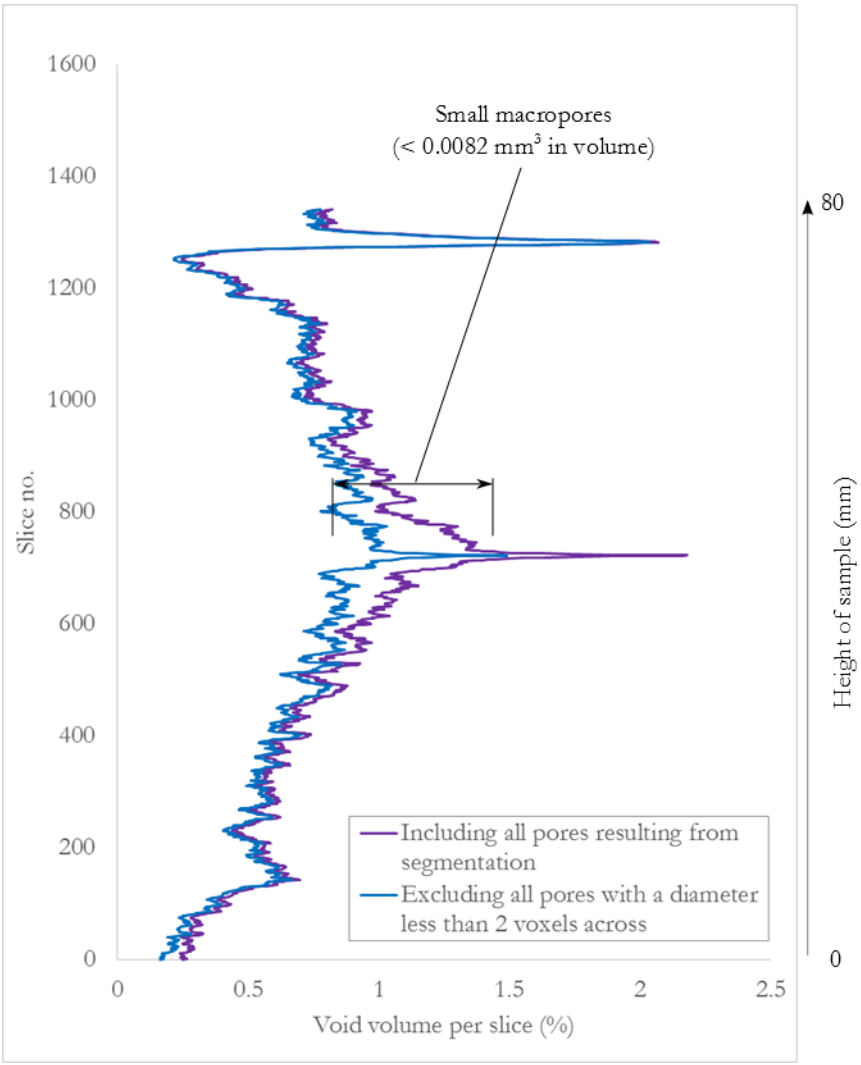

Figure 7.14 - The impact of partial volume correction (2 voxels) on pore variation with depth throughout the reconstituted sample (maximum cuboid subsample)

7.4.6 Labelling and quantification of pores

After the key image analysis steps of subsampling, image enhancement, and segmentation, the pores within the sample can be extracted from the soil matrix in order to be quantified.

Figure 7.15 shows all the segmented pores extracted from within the reconstituted sample (4 cm central cube subsample). Each individual pore must then be labelled in order to be quantified as shown in Figure 7.16. The labelling process involves automatically assigning each macropore a unique label and colour. These labels subsequently enable calculations of pore property metrics (e.g., surface area, volume, length, etc.) to be carried out for each pore within the segmented image data (see Table 7.3).

Figure 7.17 shows a visualisation of the top 10 largest pores within the reconstituted sample by volume. It can be seen that these are very irregular in shape and representations

by circular or cylindrical shapes are likely to be a simplification of the true macropore geometry. Being able to measure and visualise the shape of such internal macropores in a non-intrusive manner shows one of the key advantages of using the microCT technique within the geoscience field, as this would simply not be possible using many other techniques.

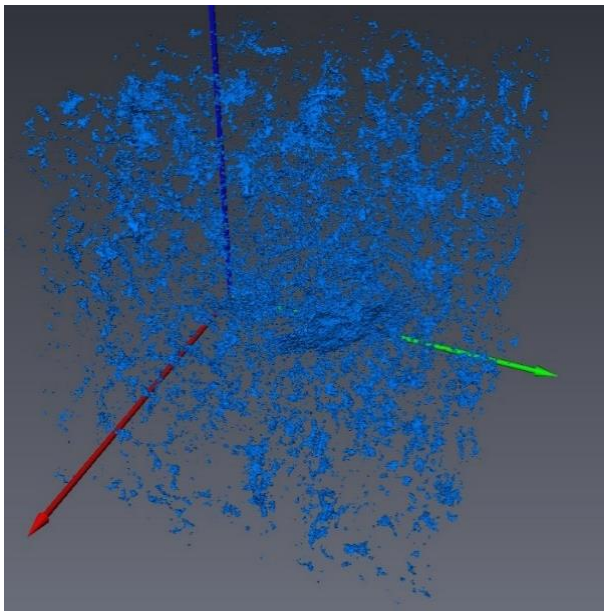

Figure 7.15 – The result of segmentation, showing only the thresholded pores (>63 μm) without the soil matrix, from the reconstituted sample (4 cm cental cube subsample)

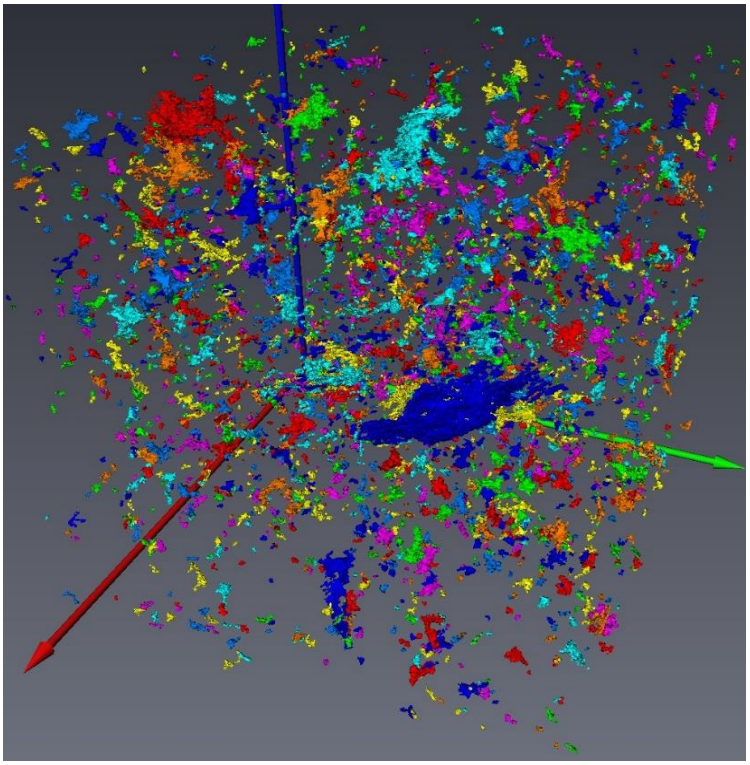

Figure 7.16 - Individual labelling applied to each segmented pore within the reconstitttuted sample (4 cm central cube subsample)

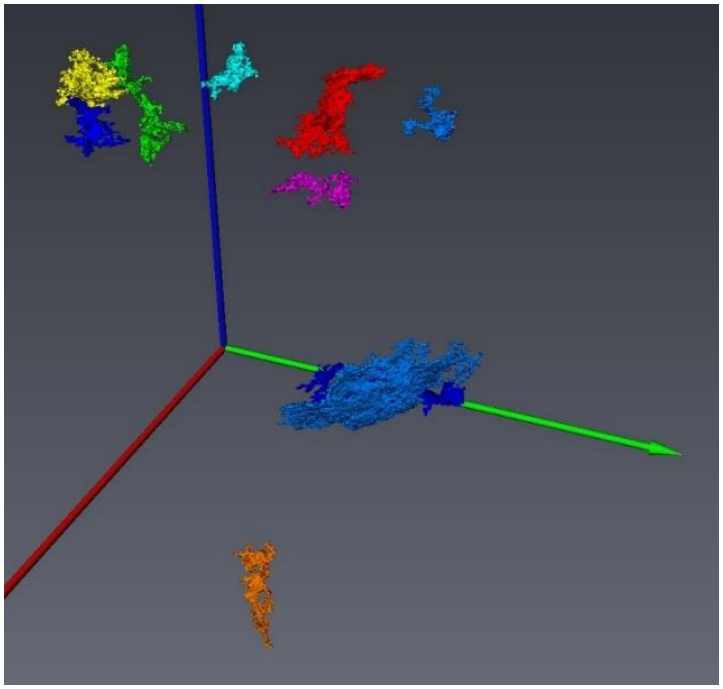

Figure 7.17 – The ten largest pores by volume within the reconstituted sample (4 cm central cube subsample) quantified using labellling of the segmented image data.

After labelling of pores, if the subsample is small enough to allow for the computational process necessary, then a pore skeleton within the sample can be generated (Figure 7.18). As shown in Table 7.5, it was only possible to skeletonisation the reconstituted sample image data within the 4 cm central cube subsample due to computational difficulties associated with the other subsamples.

Figure 7.19 shows this skeleton with the pores represented by cylindrical tubes, the 'thickest' of which are coloured in red. Some researchers have shown that these pores may represent key pores for flow (Luo et al., 2010). However the majority of the pores within clay fill samples are extremely irregular in nature and the pore property metrics (Table 7.3) appear to represent a more reliable indication of macropore architecture than the skeletonisation technique. For this reason, skeletonisation was not included within the image analysis procedure for the embankment samples in Chapter 8.

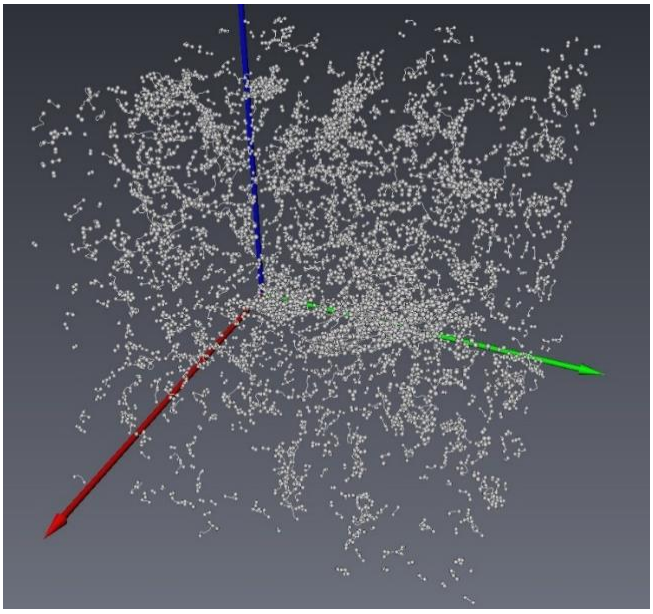

Figure 7.18 – The pore structure within the reconstituted sample (4 cm central cube subsample) after skeletonisation of the segmented image data

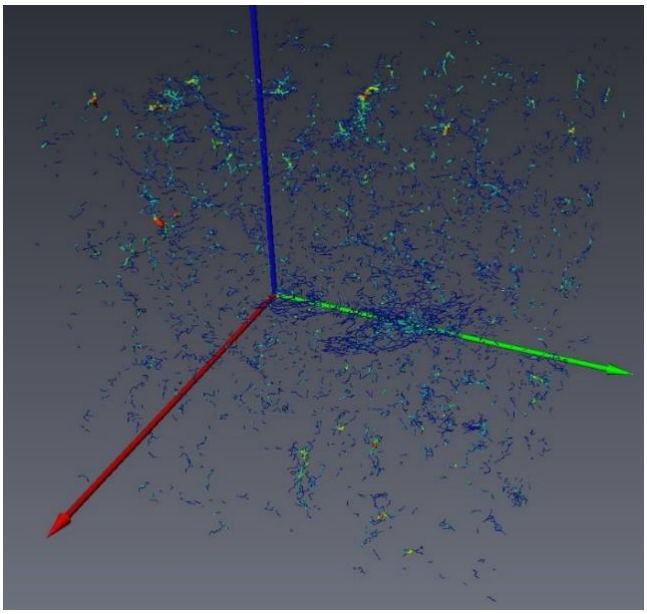

Figure 7.19 – The pore skeleton within the reconstituted sample (4 cm central cube subsample) showing the 'thickest' tubes correspning to pores in red.

7.5 Conclusions

This chapter explored the development of a microCT image analysis procedure which allows for visualisation and quantification of the internal macropore architecture within 100 mm diameter clay fill samples. Several key conclusions were drawn from this investigation:

- Subsampling was used to reduce computational cost, to enable image improvement and to allow for quantification of macropore property metrics. Different subsampling methods were investigated and compared. It was found that both the size and location of the subsample used affects the pore property metrics achieved from analysis of the image data (total macroporosity, macropore density, length, volume and surface area). Smaller subsamples result in truncation of pores and more location specific pore properties, although they are less computationally costly. A 4 cm central cube subsample represents a good balance between reducing file size in order to allow for quantification of macropores whilst providing pore property metrics which are representative of the sample as a whole.

- Four different methods of image enhancement were explored to improve the contrast between phases and to reduce imaging artefacts (noise). A 3D sharpened median filter and a non-local means filter were both found to smooth image data, eliminating noise whilst also preserving pore edge boundaries and contrast between phases. A non-local means filter was found to take twice as long as a 3D sharpened median filter to complete the image improvement process. Therefore a 3D sharpened median filter is the most effective and efficient image enhancement process, of those trialled, to include within the analysis procedure for all subsequent scans.

- The use of fully automated watershed thresholding was explored in order to keep operator input to a minimum during segmentation of scan image data. The effectiveness of this method was compared with the manual interactive thresholding technique of segmentation. The difference in calculated macroporosity was found to be very significant (46 %), particularly as the overall macroporosity within the sample is low. The automated method was found to define a threshold which leaves voxels which appear to correspond to pores unsegmented. It is therefore not suitable for use on scan image data from a sample of this type (dense clay with intensity

histograms lacking complete definition). The manual method, although more labour intensive, appears to allow for more reliable segmentation of a sample of this type.

- A partial volume effect correction which excludes objects less than two voxels in equivalent diameter allows for more reliable pore property metrics from the scan image data due to the removal of uncertainty related to the smallest objects in the data. The correction, whilst removing a large number of objects, only alters calculated macroporosity by a small amount (less than 0.04% within the subsample types investigated here). A two voxel correction is therefore included within the image analysis procedure of clay fill embankment samples in Chapter 8.

This chapter has established suitable subsampling, filtering, segmentation, and PVE correction procedures to achieve the image quality required to measure the pore architecture within a 100 mm diameter reconstituted sample of clay fill. This allows the more complex structure of clay fill samples to be explored in Chapter 8. The repeatable and consistent nature of these developed procedures allow for the comparison of macropore structure variation with depth, evolution with saturation, and the relationship of these microCT derived pore properties to the hydraulic conductivity within the samples.

8. Examining the internal macropore structure of large scale clay fill samples using microCT

8 Examining the internal macropore structure of large scale clay fill samples using microCT

8.1 Introduction

This chapter explores the use of microCT as a means to visualise and quantify the macropore networks present within large (100 mm diameter) clay fill cores extracted from within an embankment. For the first time, clay fill cores of this size were scanned repeatedly at different water contents using the non-destructive nature of the microCT technique to investigate the evolution of macropore structure with increases in saturation.

The work presented within this chapter also explores the variation in macroporosity with depth throughout the embankment and examines the influence of macropores on the saturated hydraulic conductivity of the samples using triaxial and oedometer permeability tests. The pore property metrics (total macroporosity, macropore density, mean macropore length, macropore surface area density, and mean volume of the largest pores) derived from the microCT image data which have the strongest relationship to saturated hydraulic conductivity are investigated. Additionally, the differences in porosity observed using microCT in relation to other techniques (e.g. mercury intrusion porosimetery) are discussed.

8.2 Objectives

The objectives of the work presented within this chapter were as follows:

- To visualise and quantify the macropore architecture of 100 mm dimeter samples of undisturbed clay fill.
- To comment on the pore structure observable with the microCT technique in comparison to other experimental techniques, such as mercury intrusion porosimetery and phase relationship calculations.
- To assess the change of macroporosity and macropore properties with depth throughout an embankment (between 1.5 - 6.5 m) and to comment on the heterogeneity of the macropores.
- To assess the evolution of the macropore structure within samples due to changes in saturation.
- To investigate the influence of the internal macropore structure (measured using microCT derived macropore property metrics) on the measured saturated hydraulic conductivity of samples.

8. Examining the internal macropore structure of large scale clay fill samples using microCT

8.3 Background

Chapter 3 discussed the role that macropores can play in influencing the hydraulic properties of soil if they can act as high conductivity preferential flow conduits for infiltrating water. Some researchers have shown that saturated conductivity is particularly sensitivity to the abundance and size of macropores, as demonstrated by the considerable decrease (often across several orders of magnitude) in hydraulic conductivity when macropores are excluded from measurements by the application of slightly negative potentials (Jarvis, 2007). Although only a small fraction of total soil porosity, macropores may dominate near-saturated flow and lead to infiltration by bypassing the soil matrix (Beven and Germann, 2013).

However, classical morphological descriptions have not allowed the direct 3D visualisation of the pore and solid space geometry within samples which determine the hydraulic conductivity (Vervoort and Cattle, 2003). Additionally these descriptions do not tend to investigate the large sample sizes required to evaluate a representative sample of macropores due to the low spatial density of macropores (Lauren et al., 1988). Chapter 6 showed that microCT can be used to scan larger samples to investigate macropore structure.

Classical morphological descriptions are also usually conducted under dry soil conditions (Vogel and Roth, 2001). As a result, the metrics of visible soil pores are not representative of those pores under saturated conditions for soils with moderate or large potential for swelling (McKenzie and Jacquier, 1997).

As discussed in Chapter 4, microCT scanning can be used to determine soil properties in a non-destructive manner, which allows repeated scans of the same sample under different conditions. These scans at different moisture contents provide a direct assessment of any spatial modifications of the soil pore architecture caused by dynamic processes continuously re-arranging pore networks and therefore altering hydraulic properties as a result of wetting the sample.

8. Examining the internal macropore structure of large scale clay fill samples using microCT

8.4 Methodology

8.4.1 Materials

Six clay fill cores (102 mm diameter (two deepest samples 87 mm diameter), 160 mm height) extracted from bore holes within Laverton embankment in Gloucestershire (Figure 8.1) by the British Geological Survey were used for this investigation. The embankment, shown in Figure 8.2, forms part of the Gloucestershire-Warwickshire historic railway line which has suffered slope failures in the past. Originally part of the Honeybourne line (Cheltenham–Stratford-upon-Avon–Birmingham) built between 1900 and 1906, Laverton embankment is around 6 m high and is believed to have been constructed by end tipping of local Charmouth Mudstone. The centre of the embankment contains a variable 0.9 m thick upper layer of ballast fouled with fines, ash, and soil (rich in humus) which is generally underlain by clay fill of reworked Charmouth Mudstone (Gunn et al., 2016).

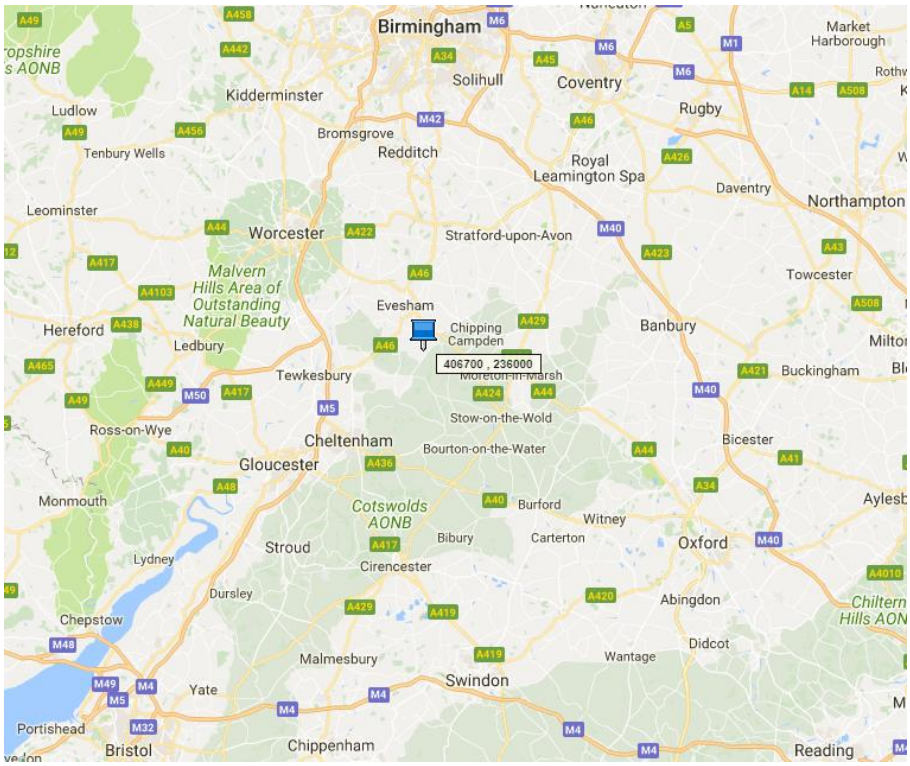

Figure 8.1 - Map showing the location of Laverton embankment where the samples were collected (Google maps (2016))

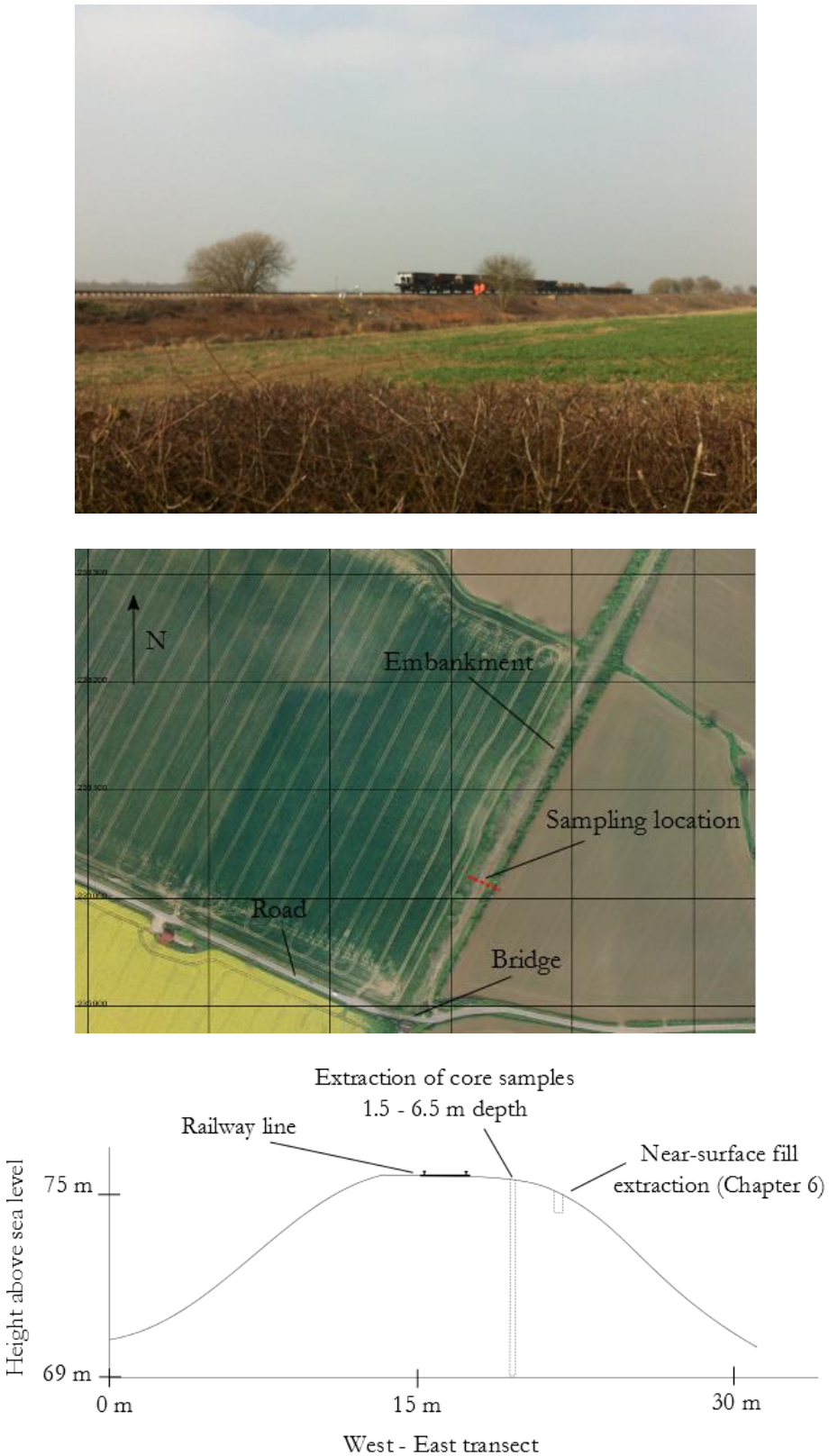

Figure 8.2 – A photograph of Laverton embankment, a map showing the location of sampling within Laverton embankment, and a cross-section through the embankment at that location

The six samples were taken from approximately 1 m intervals between 1.5 - 6.5 m depth. Figure 8.3 shows an example of one of the cores after sampling. Due to the trade-off between

sample size and achievable scan resolution (due to focal spot size), discussed in Chapter 6, these cores were halved, and only the top half of each of the cores was scanned. One exception to this was sample 5C, which was scanned three times across its full height (top, middle and bottom focussed scans) to assess macroporosity variation and the ability to link microCT data from multiple scans. It is worth noting that the samples scanned within this study still represent very large samples in comparison to other conducted microCT literature (See Chapter 4). The literature shows that sample sizes above 5 cm are extremely rare and that scanning of clay samples of this size (in order to quantify macropore properties) has not yet been achieved. Furthermore, no scans reported in the literature have investigated the change in macroporosity with depth throughout an embankment or the change in macropore structure due to saturation within samples of this size.

Table 8.1 shows the properties of the samples scanned within this study. After scanning in their sampled conditions, the samples were scanned again after saturation and hydraulic conductivity testing. A reconstituted clay fill sample was formed from a core (3.5 m depth) within the embankment and was also scanned for inclusion in the analysis (see Chapter 6) (Table 8.1).

Figure 8.3 – An example of one of the cores extracted from Laverton embankment prior to being cut in half and saturated (sample shown is 2C)

The cores were collected using a Dando Terrier 2002 rig and were driven using cable-percussion which allows recovery of continuous 1 m long samples captured in polyvinyl

chloride (PVC) liners. Figure 8.4 shows the rig used during extraction of the cores. The diameter of the two deepest cores, 6C and 7C (5.5 m and 6.5 m depth) was reduced from 102 mm to 87 mm due to resistance issues associated with collecting the wider core at these depths.

Disturbance occurs at several different stages during the acquisition of a lab test specimen and can change the structure and properties of the specimens. Samples were obtained by using a drill rig, thus displacing soil which causes disturbance at the edges of the sample. Extrusion, storage and preparation for testing can also result in disturbance. The relative importance of the disturbance caused during each of these stages cannot be prejudged because bad practice at any stage can have a very significant effect on the quality of the specimen (Clayton and Siddique, 2001).

Therefore while it is impossible to obtain a 'perfectly' undisturbed sample from the field for testing, it was attempted to keep disturbance minimalised in every part of the process. After trimming, the samples were contained within PVC tubes with secure end caps to prevent mechanical disturbance and evaporation. Before and after scanning in their sampled state, the samples were stored in a refrigerator at 3°C until the start of the saturation and hydraulic conductivity testing experimental stages.

Figure 8.4 – A photograph of the Dando Terrier 2002 rig used to extract the core samples (1.5 - 6.5 m depth) from within Laverton embankment

Table 8.1 – Details of all the samples from Laverton embankment which were microCT scanned (both in field and saturated conditions).

	2C	2C saturated	3C	3C saturated	4C	4C saturated	5C-top	5C-top saturated	5C-mid	5C-bot	5C-bot saturated	6C	6C saturated	7C*	Reconstituted
Height (mm)	98	86	87	80	92	78	92	83	107	94	75	91	78	92	87
Diameter (mm)	102	102	102	102	102	102	102	102	102	102	102	87	87	87	100
Bulk density (g/cm^3)	1.75	1.73	1.79	1.79	1.85	1.91	1.80	1.79	1.84	1.84	1.89	1.81	1.85	1.87	1.91
Origin - depth of centre of sample from the surface (mm)	1507	1507	2511	2511	3506	3506	4501	4501	4539	4579	4579	5507	5507	6510	3580
Water content (gravimetric)	0.25	0.31	0.26	0.34	0.26	0.29	0.26	0.29	0.26	0.26	0.30	0.25	0.33	0.24	0.33

* Sample 7C could not be saturated and rescanned due to the fragmented nature of the sample

8. Examining the internal macropore structure of large scale clay fill samples using microCT

8.4.2 MicroCT scanning and analysis procedure

The samples were scanned using the microCT scan settings determined in Chapter 6 in order to obtain image data with good spatial resolution, a sharp contrast between material constituents of the samples, and with minimal imaging artefacts (see Chapter 4). Image data with sufficient quality can subsequently be segmented, visualised and quantified in an accurate manner. Table 8.2 shows the microCT scan settings used to achieve this image quality within the image acquisition time restraints of a working day.

Table 8.2 – The microCT scanning procedure/settings used to scan the cores from Laverton embankment (determined in Chapter 6)

Sample	Voltage (kV)	Current (mA)	Exposure (ms)	Projections	Vertical slices	Other
102 or 87 mm diameter cylindrical sample	195	105	2000	1800	1998	Copper* filter (0.5 mm thick)

* Copper filter used to reduce beam hardening

After scanning, the image data obtained from the samples was processed using the rigorous and repeatable image analysis method determined in Chapter 7. Figure 8.5 presents a flow diagram of the method used. The goal of the analysis process was to improve image quality and allow for segmentation and quantification of the image data of all the samples in a reliable fashion. As discussed in Chapter 7, it was vital that this process was kept consistent to allow for comparison of results between scans of different samples, particularly, the repeated scans of samples in different states of saturation.

Due to the inherent variability of the samples in this study, the scans were performed at a range of voxel sizes. Table 8.3 shows the voxel sizes achieved from each scan. To keep the resolution constant between repeated scans of the same sample and to allow for comparison of the evolution of the macropore structure with saturation, the partial volume effect correction was matched between corresponding samples.

The quantitative results presented in this chapter use the pore property metrics discussed in Chapter 7. Macropore size is classically sorted by equivalent pore diameter however macropores with greater volume are likely to be more active in flow at near-saturated conditions (Luo et al., 2010). For this reason macropore size was sorted by volume as opposed to equivalent pore diameter in the results presented within this chapter.

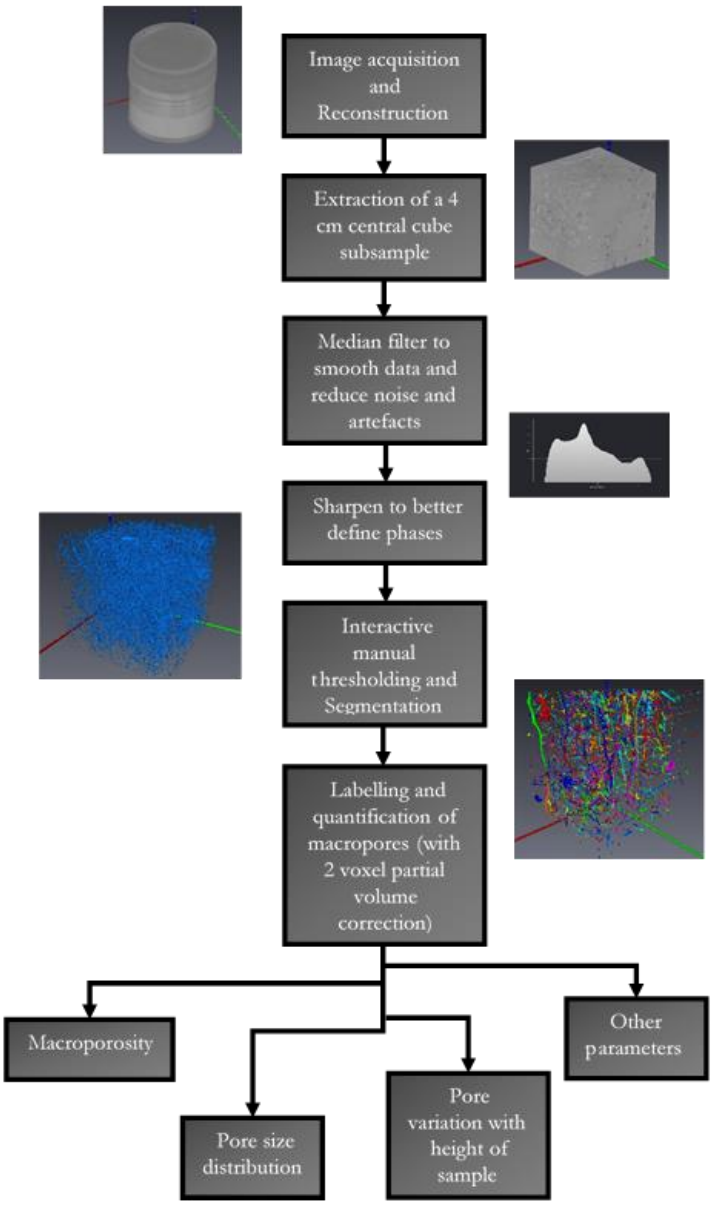

Figure 8.5 – The microCT image analysis procedure used for all samples (determined in Chapter 7)

A 4 cm cental subsample was used for all image anaylsis processing of the samples as this allowed for the greatest range of image improvement and quanitifcation by reducing file size (see Chapter 7).

Since the sample surfaces were slighlty uneven, the soil surface of the samples was demmed to be located where the soil matrix filled 50 % of the horizontal column cross-sectional area as determined from the microCT image data.

Table 8.3 – The voxel resolution achieved from microCT scans of the clay fill cores from Laverton embankment

Sample	Voxel resolution (mm)	Sample	Voxel resolution (mm)	Sample	Voxel resolution (mm)
2C	0.0582	5C-top*2	0.0573	6C	0.0534
2C saturated*1	0.0611	5C-top saturated*1	0.0615	6C saturated*1	0.0529
3C	0.0548	5C-mid*2	0.0537	7C	0.0544
3C saturated*1	0.0604	5C-bot*2	0.0547	Recon	0.0627
4C	0.0555	5C-bot saturated*1	0.0597		
4C saturated*1	0.0582				

*1 Saturated and unsaturated sample resolutions were matched using the PVE correction to allow for comparison.

*2 The resolutions of the three samples within 5C were matched using the PVE correction to allow for porosity throughout the height of the sample to be compared.

The consistency of the image analysis procedure was explored by examining the results of the three scans over the height of sample 5C (at the top, middle, and bottom of the sample). Data from three individual scans was processed independently, however there is some crossover (overlap) in the height of sample measured, so this allows for a comparison of the quantitative results obtained between the scans. This process also reveals macroporosity throughout the sample over 12 cm as opposed to the 4 cm subvolume giving an insight into the variation over the full height of samples which is not observed within the analysis procedure.

The spatial distribution of macropores and macropore geometry with depth influences the potential for non-equilibrium flow within soils (Luo et al., 2010). Therefore the variation in macroporosity with depth within the embankment was assessed by comparing the microCT measured macropore properties from all of the samples (in their sampled conditions), each corresponding to a different depth (1.5 – 6.5 m).

8. Examining the internal macropore structure of large scale clay fill samples using microCT

8.4.3 Saturated hydraulic conductivity testing

The samples were saturated within a triaxial cell and, after saturation was achieved, constant head permeability tests were carried out on the samples before they were scanned in a saturated condition.

The goal of these tests was not to determine in-situ hydraulic conductivity of the embankment, as the samples would not be fully representative of the embankment due to fissuring and other large discontinuities which may be present which are not captured within 100 mm diameter samples (i.e. the size limited by the microCT technique). Rather, the goal was to determine if macroporosities and macropore property metrics measurable using microCT had an observable impact on hydraulic conductivity.

The constant head permeability tests were carried out according to BS 1377:1990, using the experimental set up described in Chapter 2 (Figure 2.5).

After installation in the triaxial cells, the samples were saturated using back pressure saturation (B-ratio > 95%). CO_2 flushing was explored to achieve better saturation, although this was found to be ineffective. The effective stresses on the sample were set to replicate field conditions at the depth from which the sample originated (Table 8.1). A hydraulic gradient of 125 was applied over the height of the samples and measurements were taken to record the flow rate. The saturated hydraulic conductivity was calculated for the samples using Darcy's Equation (Equation 7 in Chapter 2).

The saturated conductivity testing stage is likely to have resulted in some soil structure changes in addition to those caused by saturation due to the changes in effective stress to which the samples were subjected. During testing the samples were returned to their in-situ pressures which had previously been reduced after extraction from the embankment. This pressure was subsequently reduced again prior to scanning the samples in their saturated state as the samples could not be scanned within a triaxial cell.

After microCT scanning in a saturated state, the samples were subsequently divided into three layers and subjected to three one-dimensional oedometer consolidation tests according to BS 1377-6:1990. Using Terzaghi's (1943) theory (Equation 11 in Chapter 2) values for the saturated hydraulic conductivity of the three layers within the samples were calculated.

8. Examining the internal macropore structure of large scale clay fill samples using microCT

8.4.4 Mercury intrusion porosimetery testing

To investigate the degree of porosity in the samples which was not captured by the microCT technique, two mercury porosimetery tests were carried out (on the reconstituted and 5C-bot samples). The aim of these tests was to examine the difference in porosity identified using laboratory measurements of void ratio (phase relationships) and microCT image data.

Mercury intrusion porosimetery, as discussed in Chapter 2, has the ability to estimate porosity to a much finer resolution than microCT (between 4 nm and 0.4 mm). The technique's upper bounds in terms of pore size overlap with the point at which microCT can capture pores (i.e. > 0.05 mm). This is shown in Figure 8.6 which presents typical ranges of pore size measured using different experimental techniques including MIP, microCT, and phase relationship (total) measured porosity.

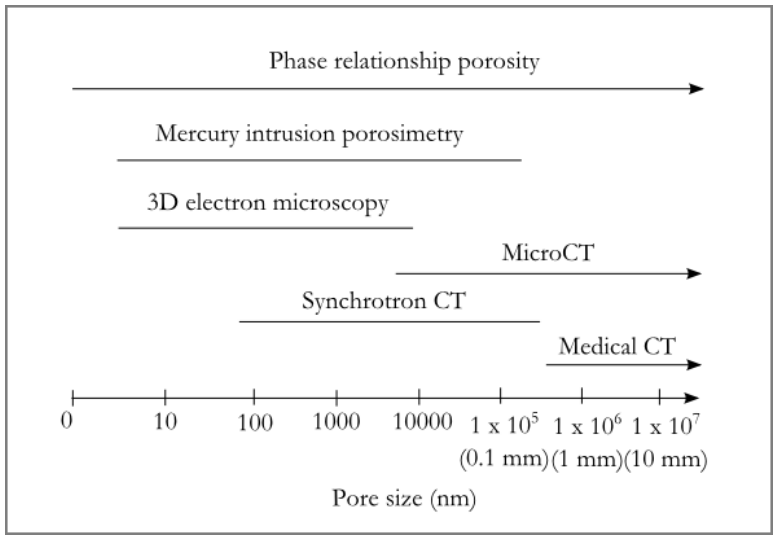

Figure 8.6 – Typical ranges of pore size measured using different experimental techniques

MIP therefore represents a useful tool for exploring the range of pore sizes within the samples further. However, as noted in Chapter 2, MIP does not measure pore volume directly but rather the entrance diameter associated with the pores (and the pressure required for mercury to enter them). It therefore has several limitations and sources of error which were discussed in more detail in Chapter 3.

As is common practice, the surface tension of mercury was taken to be equal to 0.484 N/m at 25°C (Smith, 2015). The contact angle is usually taken between 139° and 147° for clays (Diamond, 1970) and 140° was used in these tests.

8. Examining the internal macropore structure of large scale clay fill samples using microCT

8.4.5 Method to compare the strength of association between results obtained from microCT and from conventional measurement techniques

Conventional measurements of porosity were calculated using the phase relationships discussed in Chapter 2 (Equation 2).

The correlation between the microCT derived property metrics and the measurements of porosity, density, and saturated hydraulic conductivity, were examined using Spearman's correlation coefficient (r_s)

$$r_s = 1 - \frac{6 \sum D^2}{N^3 - N} \tag{39}$$

Where, D is the difference between the two ranks of each observation and N is the number of observations.

Spearman's correlation coefficient is a non-parametric test used to measure the strength of association between two variables, where $r_s = 1$ means a perfect positive correlation and the $r_s = -1$ means a perfect negative correlation.

8.5 Results

8.5.1 Visualisation and quantification of macropores within the samples from microCT image data

Table 8.4 shows the macropore property metrics calculated using the image analysis for the samples. It can be seen that total macroporosity within the samples (after PVE correction) ranged from 0.12 % to 4.12 % and that the mean macropore length varied between 0.80 and 2.03 mm. These values are similar in magnitude to macroporosities derived from CT scans of various soils reported in the literature (Luo et al., 2010 (silt loam samples); Naveed et al., 2013 (clay and sandy clay samples); Shin et al., 2013 (artificial clay samples); Larsbo et al., 2014 (clay loam samples)).

Figure 8.7, shows the visualisation of all the internal macropores within the samples after segmentation and labelling. Figure 8.7 shows that the macropore structure within each of the samples is extremely wide ranging, with some samples containing more biological type pores running throughout the subvolume (e.g. 5C top), some samples containing several very large macropores (e.g. 3C), and some samples containing a more uniform size and spatial

distribution of macropores (e.g. the reconstituted sample). From Figure 8.7 it can be seen that sample 7C was extremely fractured in nature, and as a result, the sample could not be saturated and scanned using the same procedure as the other samples.

This visualisation of clay fill samples shows that the size and distribution of macropores within the samples is heterogeneous. An accurate quantitative description of these internal macropore structures is difficult to achieve using conventional morphological techniques (e.g. method of sections). Therefore the results from these microCT scans emphasise the clear benefits of microCT as a non-destructive 3D visualisation and analysis tool for soil research.

8.5.2 Effects of saturation procedure on sample macroporosity

Table 8.4 shows that for all the samples the saturation procedure reduced the total calculated macroporosity within the samples. This is confirmed by Figure 8.7 which shows that the quantity of visible macropores within the subvolumes was reduced after saturation.

The pore property changes reflected here as a result of saturation are associated both with the experimental procedure used to test the samples and the changes caused by saturation. The samples were saturated under effective stress equal to their in-situ effective stress, which the samples had not been under for some time after extraction from the embankment. Additionally, as the samples could not be scanned whilst within the triaxial cell, they had to be removed prior to scanning in their saturated condition. To remove the sample from the cell, the pore pressure within the sample must first be lowered whilst the cell pressure is still relatively high. Therefore some consolidation could have occurred at this stage as the effective stresses in the sample increased. Unloading from the triaxial cell for scanning also has the consequence that the samples were no longer completely saturated as they contained some air which was driven into solution by back pressure saturation prior to the saturated hydraulic conductivity test.

Table 8.4 shows that the saturation procedure reduced the macropore density and the macropore surface area density within the scanned samples. This suggests that the saturation procedure reduces both the quantity and size of macropores within the samples. Saturation also appeared to reduce the mean macropore length within the samples, except in samples 4C and 6C which had the lowest initial macroporosity. This may be because, within these samples, the reduction in the number of small macropores (reflected in the reduced

macropore density) after saturation has a greater relative effect on the mean length than the reduction in the size of the largest macropores.

Figure 8.8(a-f) shows pore size distributions (as a % of total pore volume) for all the samples scanned in both partially saturated and saturated conditions. Figure 8.8 therefore shows the proportion of pore volume within each sample made up of pores of a certain size. It is clear that in all samples the saturation procedure reduces the size of the largest macropore present. For all samples except 3C and 4C (Figure 8.8b and Figure 8.8c) it appears that the total macropore volume within samples is composed of a greater proportion of small pores after saturation than at field conditions. These results suggest that it is the largest macropores within samples which are most affected by the saturation procedure and are likely to suffer changes in volume as a result.

Figure 8.9(a-f) shows profiles of pore volume per vertical slice throughout the subvolumes within the scan image data for each sample. The figure shows that the saturation procedure tended to decrease the volume of pores per slice throughout the subvolumes and tended to result in less variation in total macroporosity throughout the height of the subvolume. For example compare the changes shown in Figure 8.9a and Figure 8.9f as a result of saturation. It can be seen that after saturation the range of variation between the minimum and maximum macroporosity measured throughout the subvolume is less than prior to saturation. This implies that the saturation procedure resulted in the samples becoming more uniform in structure, this can also be observed in Figure 8.7.

Table 8.4 – The pore property metrics calculated from analysis of the microCT image data from scans of the clay fill samples (4 cm central cube subvolumes)

	2C	2C saturated	3C	3C saturated	4C	4C saturated	5C-top	5C-top saturated	5C-mid	5C-bot	5C-bot saturated	6C	6C saturated	7C	Reconstituted
Corrected Macroporosity (%)	1.984	0.806	2.030	1.719	0.382	0.155	1.854	1.797	1.301	0.581	0.530	0.180	0.115	4.117	0.400
Macropore density (x10^6) (no/m^3)	66.141	57.765	60.859	35.078	89.625	13.203	142.422	83.453	149.953	74.875	56.453	29.109	25.750	59.844	51.697
Mean macro pore length (mm)	1.094	0.981	1.129	0.965	1.052	1.193	1.594	1.433	1.582	1.570	1.412	0.801	0.815	2.025	0.979
Surface area density (m^2/m^3)	207.870	110.620	198.453	188.523	85.999	19.756	264.183	209.676	203.252	88.807	70.681	34.754	23.764	337.639	69.153
Mean volume of ten largest pores (mm^3)	55.279	13.931	70.570	72.904	6.825	4.469	36.689	21.194	16.156	8.531	6.506	5.679	2.413	203.442	4.422

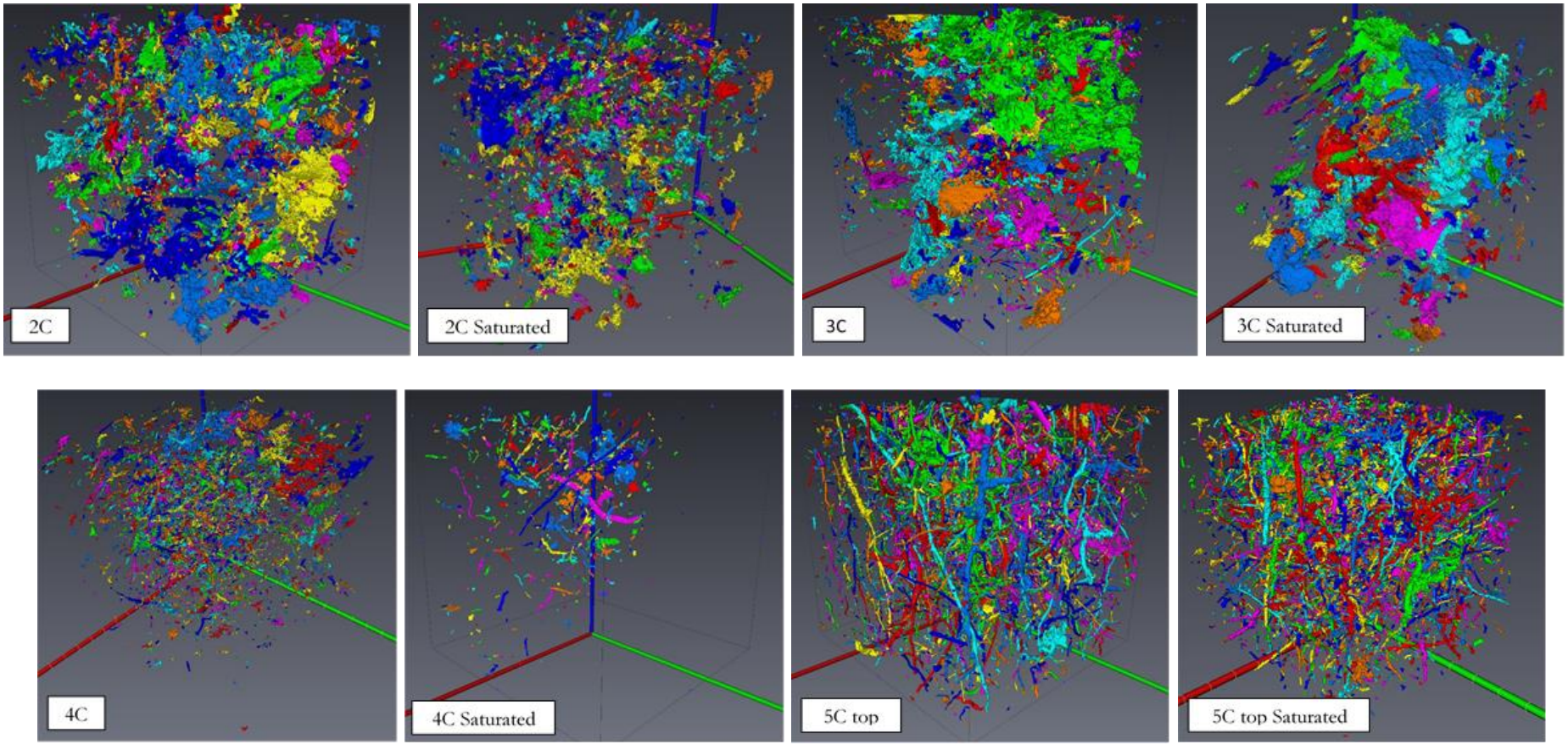

Figure 8.7 – 3D visualisations in Avizo Fire (FEI, 2014) of the macropores present within the clay fill samples from analysis of the microCT scan image data, showing the same samples scanned in different states of saturation (4 cm central cube subvolumes) (continued on next page)

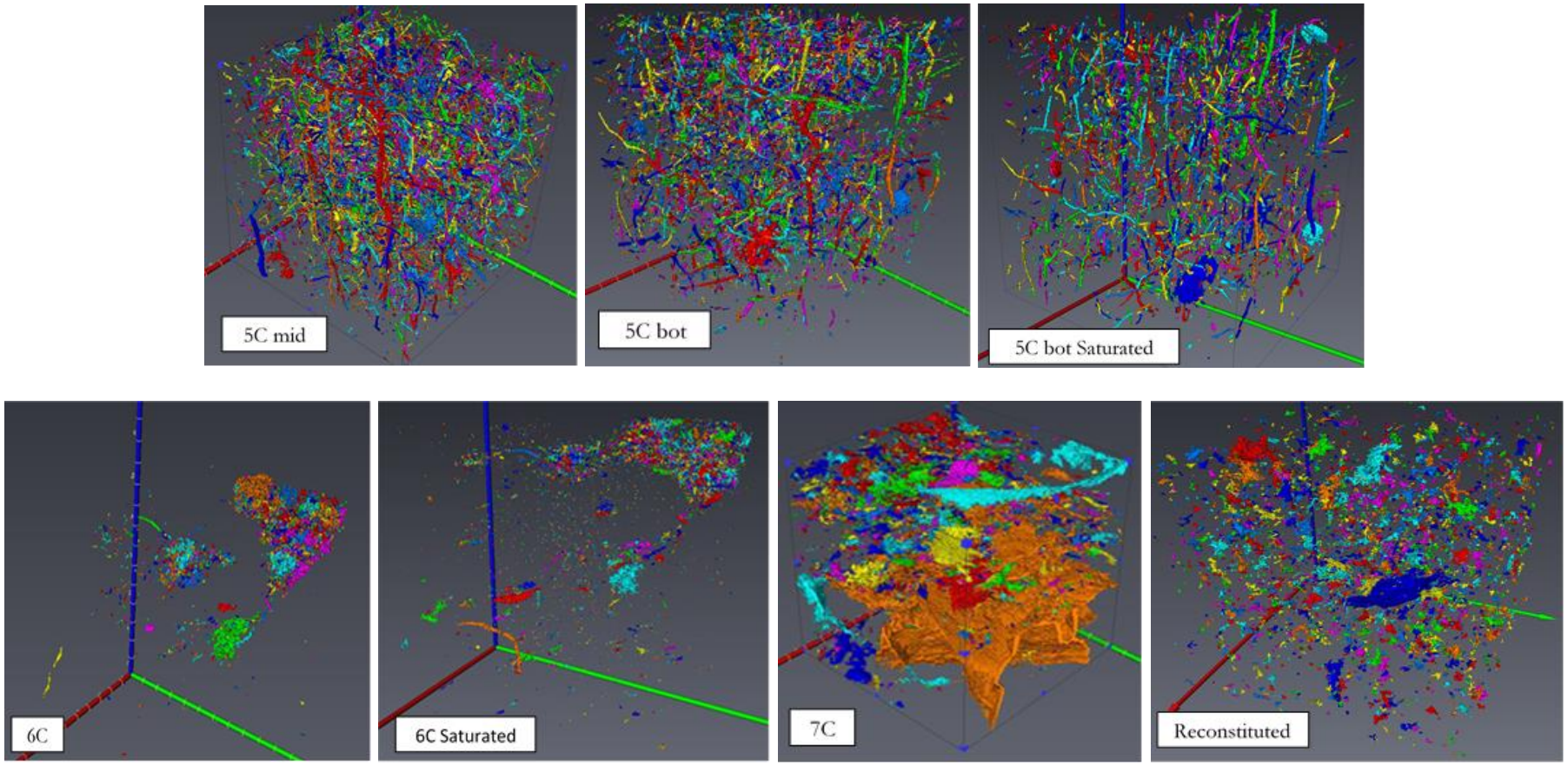

Figure 8.7 - Continued

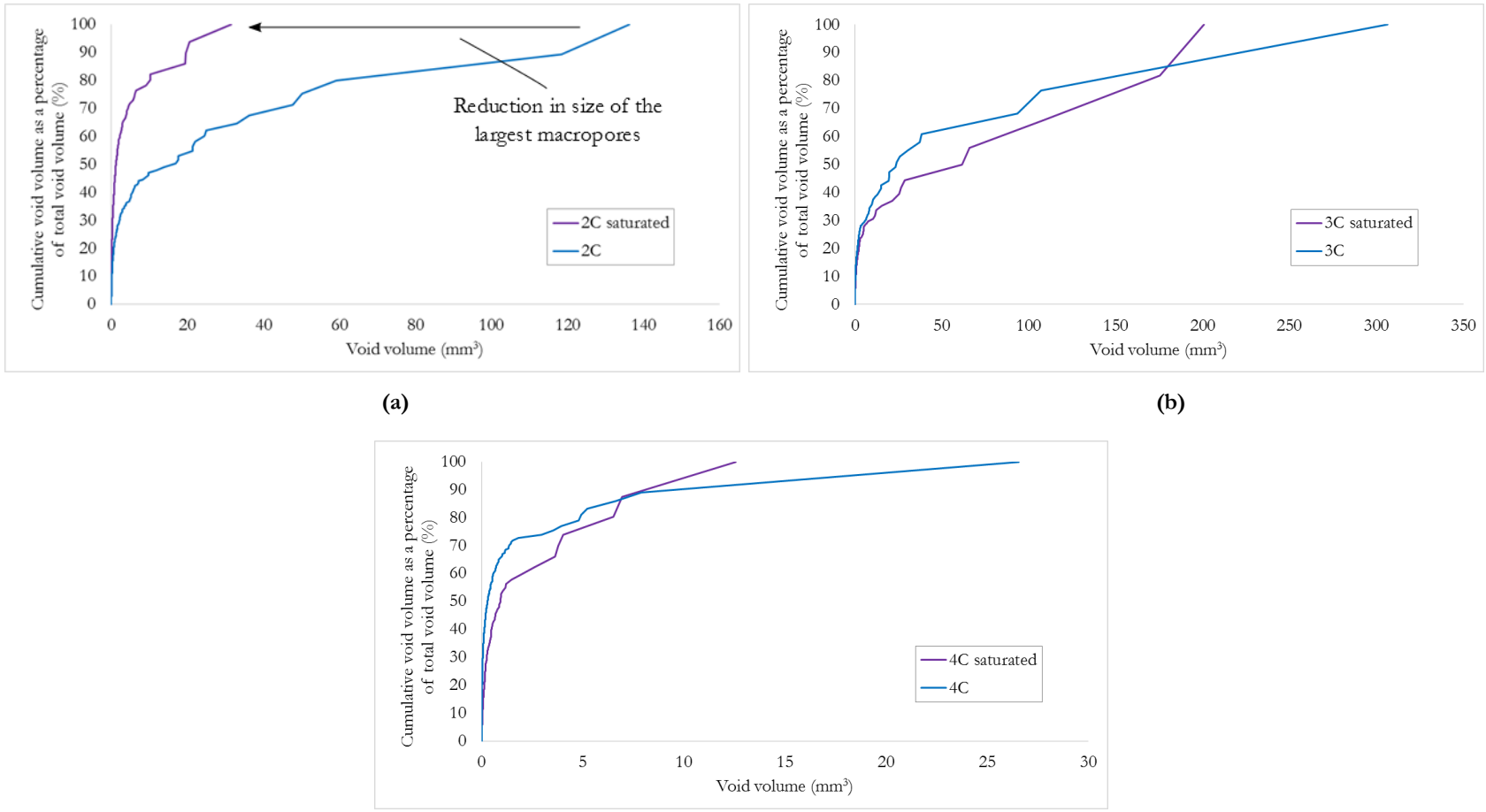

Figure 8.8 – Pore size distributions (in terms of total pore volume) from analysis of the microCT image data from scans of the clay fill samples, showing the change in pore size as a result of saturation (4 cm central cube subvolumes) (continued on next page)

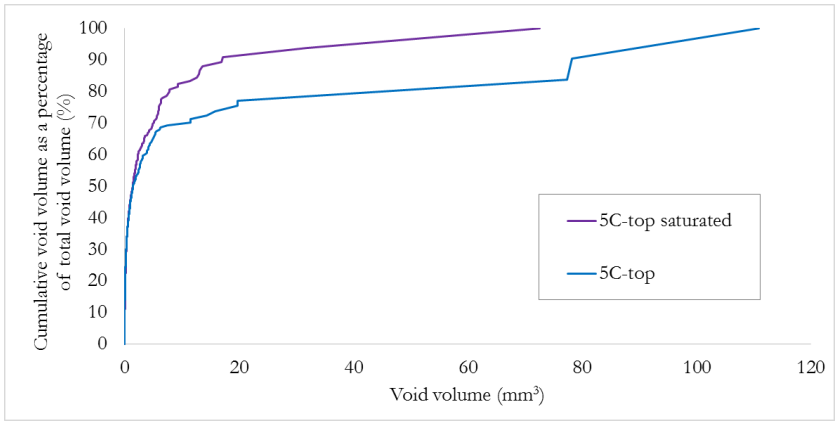

(d)

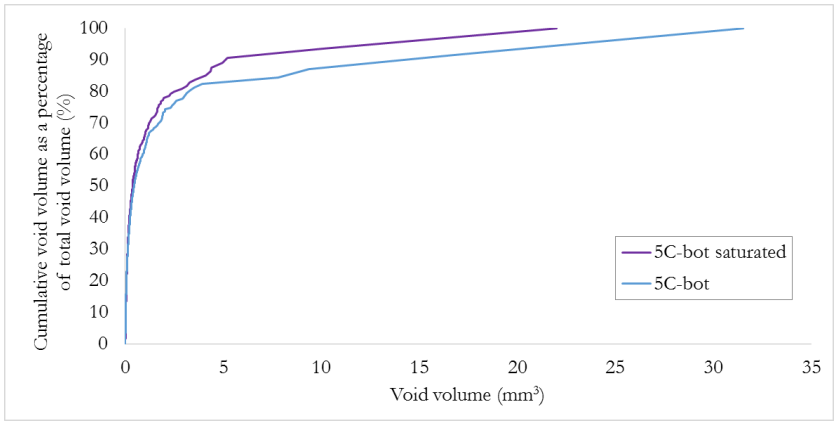

(e)

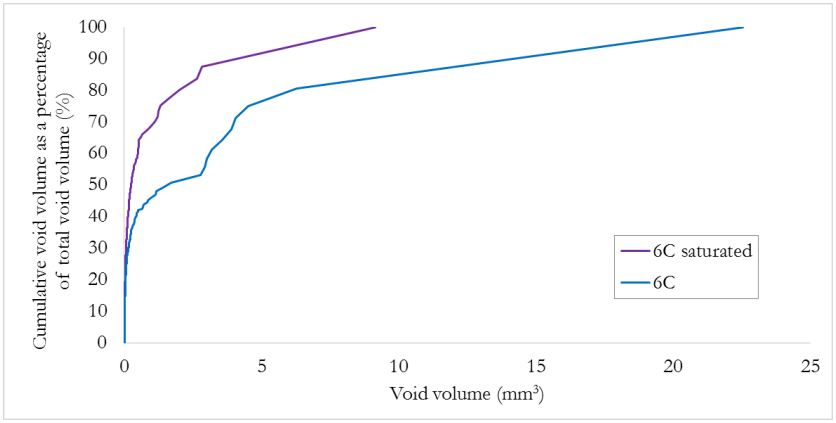

(f)

Figure 8.8 - Continued

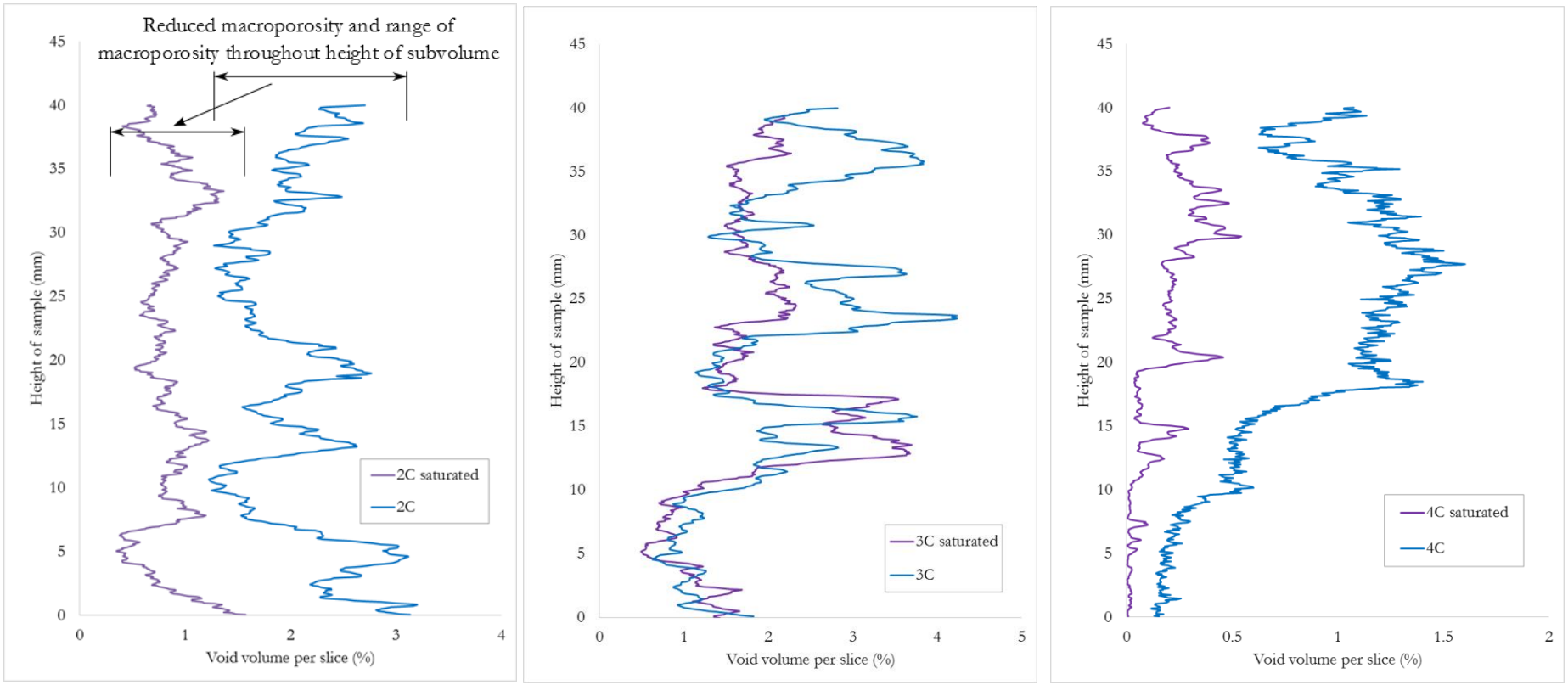

Figure 8.9 – Profiles of the volume of voids calculated within each vertical slice of the microCT image data from scans of the clay fill samples, showing the change in the number of macropores as a result of saturation (4 cm central cube subvolumes) (continued on next page)

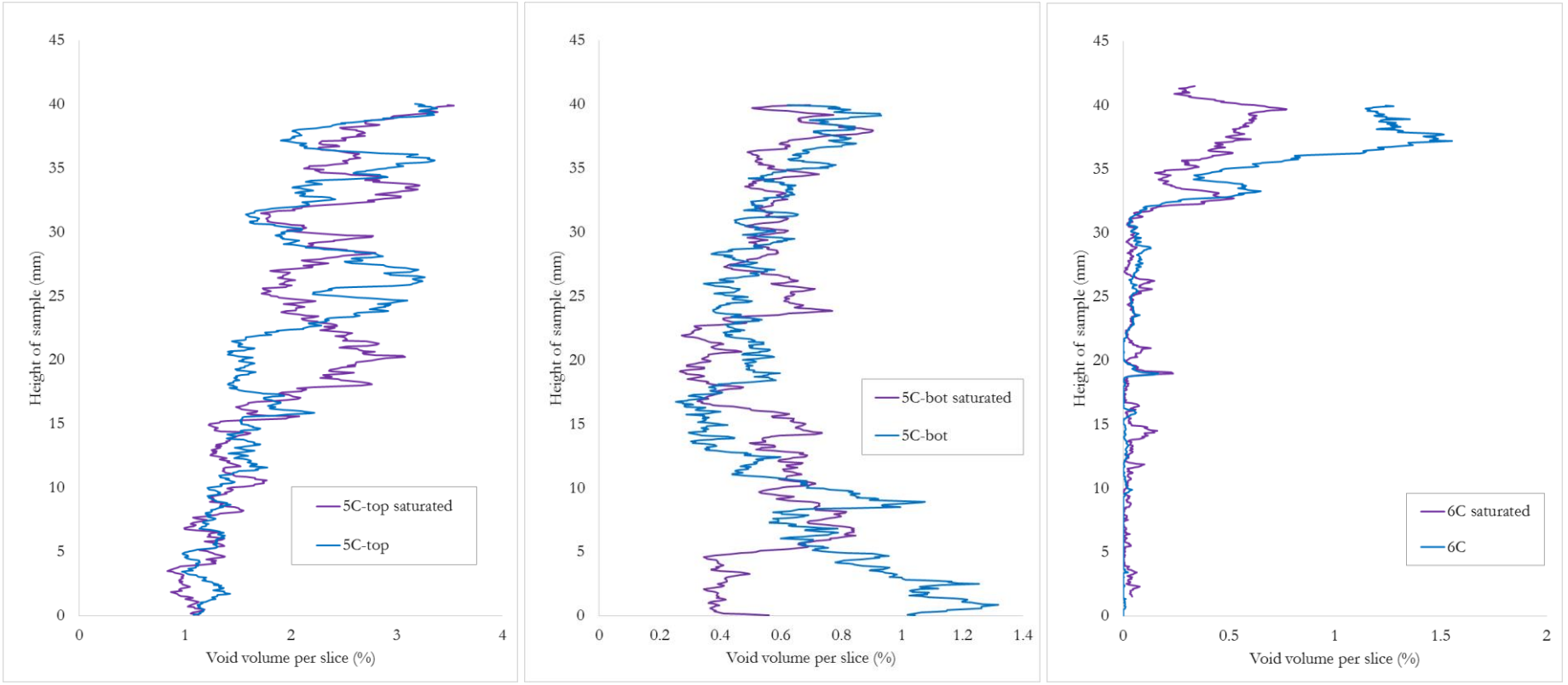

(d) **(e)** **(f)**

Figure 8.9 – Continued

8. Examining the internal macropore structure of large scale clay fill samples using microCT

8.5.3 Linking multiple microCT scans throughout the full height of a sample

The macropore structure within sample 5C was quantified across its entire height using three separate microCT scans. This was used to compare the macroporosity variation within the samples over their full height and to assess the potential of linking image data from multiple adjacent microCT scans. Figure 8.10 shows the profile of volume of pores per slice resulting from image analysis of all three scans on sample 5C. It can be seen that the volume of voids per slice quantified from the three scans align almost exactly at the top and bottom of the middle subvolume. This suggests that the consistent microCT scanning and image analysis procedure developed in Chapter 6 and Chapter 7 can be used to link multiple microCT scans in a reliable manner.

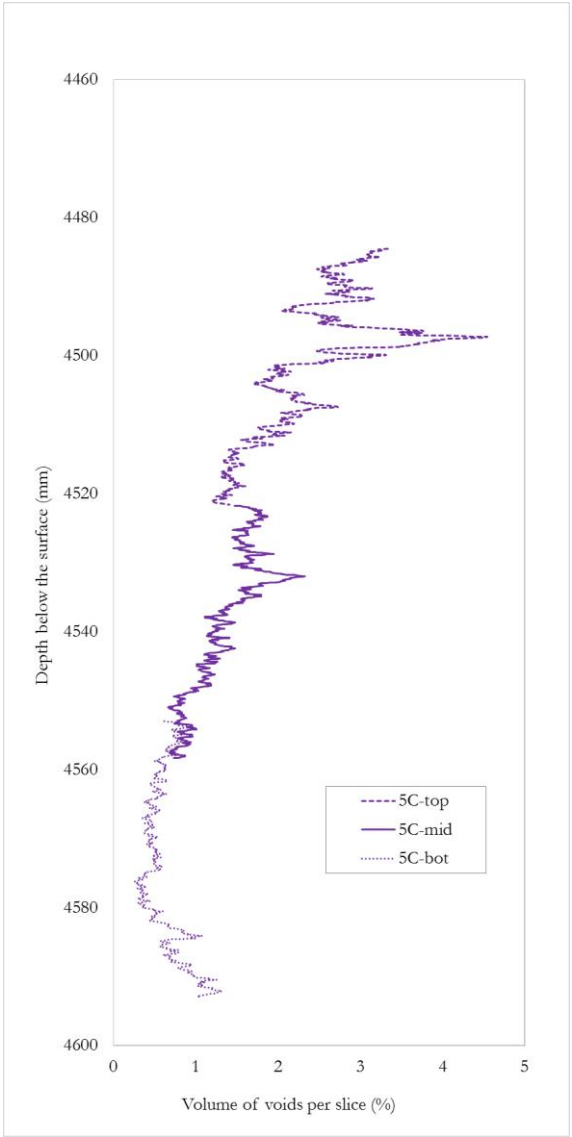

Figure 8.10 – The profile of volume of voids throughout 12 cm of sample 5C, composed of data obtained from analysis of three individual microCT scans of 5C (one at the top, one in the middle, and one at the bottom)(each a 4 cm central cube subvolume).

Figure 8.10 is an important validation of the microCT scanning methods used in this thesis. The ability to compare results obtained from different scans of variable density material has proven difficult in the past due to the scanning complications and necessary operator input discussed in Chapter 4.

Figure 8.10 also shows that the sample macroporosity decreases slightly with depth throughout the full height of the sample. The figure shows that the maximum and minimum macroporosity within the full sample are not captured by the middle scan subvolume. This is a consequence of using a smaller subvolume to reduce computational demand and to enable quantification of the macropores within large microCT scanned samples (see Chapter 7).

From Figure 8.7 it can be seen that some macropores extend throughout the height of the subvolumes from top to bottom and may therefore prove influential to flow through the sample. Although the volume of pores throughout the height of the subvolumes obtained from the three different scans of 5C can be linked (Figure 8.10), the individual macropores within the data sets and their corresponding pore property metrics cannot due to truncation of pores during analysis (See Section 7.3.2). To overcome this, visual assessment was used to examine if individual macropores connected throughout the entire height of 5C. It was observed that no individual macropores apparently extended throughout the entire height of the triaxial-scale combined sample.

Assessing the scan data from different heights within 5C before and after saturation also allows for an assessment of the impact of consolidation during the saturated hydraulic conductivity testing stage of the experimental procedure. Figure 8.8 shows that the largest pores within the 5C-top are reduced to a greater extent as a result of saturation than those within 5C-bot. This may be an indication of increased consolidation within 5C-top due to the gradient over the sample during conductivity testing (i.e. effective stress is higher at the top of the triaxial sample). However, Table 8.4 shows that the impact of the saturation procedure on total macroporosity was similar throughout the height of 5C (0.057 % reduction after saturation for 5C-top as opposed to 0.051 % for 5C-bot).

8. Examining the internal macropore structure of large scale clay fill samples using microCT

8.5.4 Variation in microCT measured macroporosity with depth throughout the embankment

Figure 8.11 shows profiles of volume of pores per slice for all of the samples shown throughout the depth of the embankment (between 1.5 – 6.5 m depth). It can be seen that no clear pattern of macropore distribution exists (for instance decreasing macroporosity with depth). Figure 8.11 reflects the inherent variability of the macropore structures within the clay fill forming the embankment. This was also evident from the visualisation of the wide range of internal macroporosity within the samples presented in Figure 8.7. No other studies exist showing the quantitative variation of macroporosity throughout the depth of an embankment for comparison of the results given here. It is therefore difficult to comment on the significance of the variation shown in Figure 8.11.

As visualised in Figure 8.7, Figure 8.11 shows that sample 7C was particularly fractured in nature. This could be a result of increased disturbance of the samples during extraction due to resistance encountered at this depth (diameter had to be reduced for samples from 5.5 m and 6.5 m depth). This could also reflect the changing nature of the clay at the foundation of the embankment or the inherent heterogeneity present within clay fill.

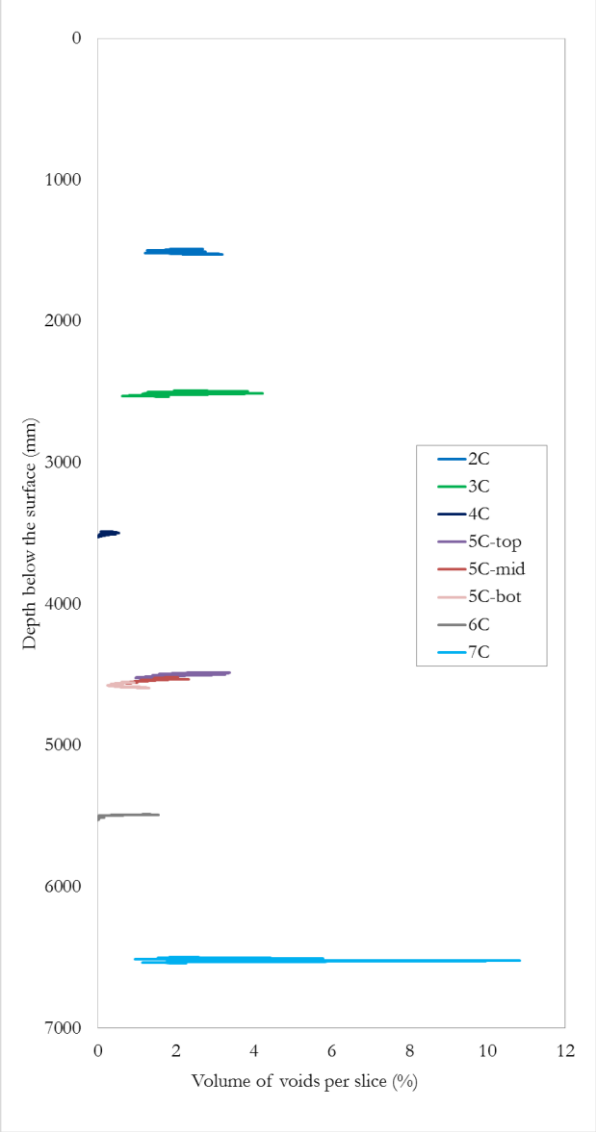

Figure 8.11 – The profiles of volume of voids per slice for all the samples (between 1.5 – 6.5 m depth within the embankment) showing the variability of microCT measured macroporosity within the embankment

8.5.5 A comparison of porosity measured at different scales

Measured pore characteristics (e.g. connectivity) depend on the spatial resolution of the experimental technique used, as pores which exist in the sample below this size will also be connected but not included in the results. As a result, the connectivity of the pore structure within the samples will change with resolution because more connections or more isolated features appear and are measured. Figure 8.6 showed the range of pore size measured by various experimental techniques including microCT and mercury intrusion porosimetery.

Table 8.5 shows the results of the mercury intrusion porosimetery tests carried out on the reconstituted and 5C-bot samples, as well as total porosity for the samples calculated

using phase relationships from the oedometer samples. The porosity determined using the MIP technique is found to be significantly smaller than the values measured on the oedometer size samples (0.27 as opposed to 0.45 for the 5C-bot sample). This difference likely arises due to the scales of pores measured using the MIP technique. MIP does not measure non-intruded porosity with pore entrance diameters less than 4 nm and non-detectable porosity for pore sizes larger than 110 μm. Also the other limitations of MIP discussed in Chapter 2 will cause a discrepancy between the two values.

Table 8.5 – Mercury intrusion porosimetery properties and results for two samples (5C-bot and the reconstituted sample)

	5C-bot sample	Reconstituted sample
Mass of sample (g)	0.49	1.39
Density (g/cm^3)	1.78	1.91
Volume of sample (mm^3)	275.83	730.05
Total specific volume of pores (mm^3/g)	152.34	134.73
Total pore volume (mm^3)	74.62	187.72
Max pore entrance diameter (μm)	109.52	110.01
Min pore entrance diameter (μm)	0.0037	0.0037
Average pore entrance diameter (μm)	0.023	0.024
Modal pore entrance diameter (μm)	0.051	0.052
Median pore entrance diameter (μm)	0.042	0.043
MIP Porosity (%)	27	26
Total porosity (phase relationship) (%)	45	50

A typical MIP output is a graph of log differential intrusion curve vs pore entrance diameter (pore size density function) which aids the visual detection of the dominant pore modes. Figure 8.12 shows this relationship for the two MIP tested samples. This function is not necessarily a true reflection of the pore size distribution, as MIP measures pore entrance diameter as opposed to pore volume, but rather provides a useful quantitative description of the sample pore structure.

Figure 8.12 shows that both samples contain a peak pore size of around 0.05 microns which is a thousand times smaller than can be observed within the microCT images, hence the difference in estimated porosity between the MIP and microCT (microCT macroporosity for 5Cbot is 0.58 % and 0.40 % or the reconstituted sample (Table 8.4)). It is difficult to link MIP derived pore size density functions with microCT derived pore size distributions as the

volume of intruded mercury does not necessarily correspond to the volume of individual pores and the overlap between the techniques is small (60 – 110 μm).

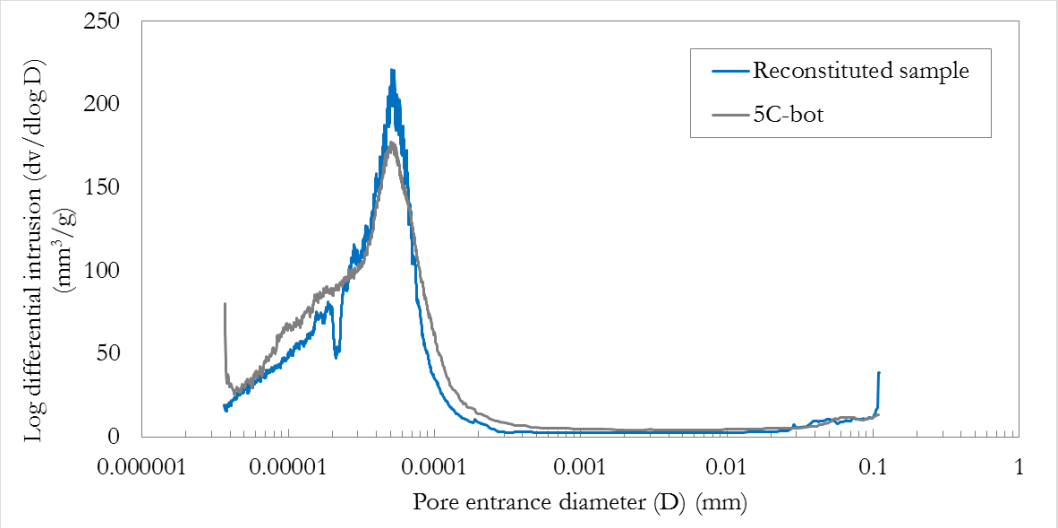

Figure 8.12 – Mercury intrusion porosimetery measurement of pore entrance diameter within the reconstituted and 5C-bot samples

8.5.6 The relationship between saturated hydraulic conductivity and microCT measured pore property metrics of the samples

Table 8.6 shows the saturated hydraulic conductivity measurements from triaxial permeability tests and one-dimensional consolidation tests for all the samples along with the phase relationship measured total sample porosity. Table 8.6 shows that the saturated hydraulic conductivity determined on triaxial size samples is consistently less than the hydraulic conductivity measured on the oedometer sized samples. The triaxial k_{sat} is lower by a factor of between 3.6 and 17. This is likely a result of the height of the samples (20 mm oedometer, 80 mm triaxial) and the relative influence of macropores within them.

Figure 8.13 shows the spearman correlation coefficients calculated for the microCT derived macropore property metrics and the measurements of porosity, density and saturated hydraulic conductivity (at the triaxial scale and the oedometer scale).

Table 8.6 – Porosity and saturated hydraulic conductivity measurements from triaxial permeability tests and one-dimensional consolidation test for the saturated samples

	2C saturated	3C saturated	4C saturated	5C-top saturated	5C-bot saturated	6C saturated	Reconstituted sample
Total porosity	0.50	0.49	0.44	0.48	0.45	0.48	0.50
Oedometer (3 x 70 mm diameter, 20 mm height) - average saturated hydraulic conductivity (first loading step) (m/s)	1.77 x 10^{-9}	6.24 x 10^{-10}	7.35 x 10^{-10}	3.75 x 10^{-9}	1.65 x 10^{-9}	2.26 x 10^{-10}	2.95 x 10^{-10}
Triaxial (100 mm diameter, 80 mm height) - saturated hydraulic conductivity (m/s)	1.04 x 10^{-10}	5.32 x 10^{-11}	1.67 x 10^{-10}	8.03 x 10^{-10}	1.08 x 10^{-10}	1.76 x 10^{-11}	8.15 x 10^{-11}
Factor of difference between oedometer and triaxial measured saturated hydraulic conductivity	17.0	11.7	4.4	4.7	15.3	12.8	3.6

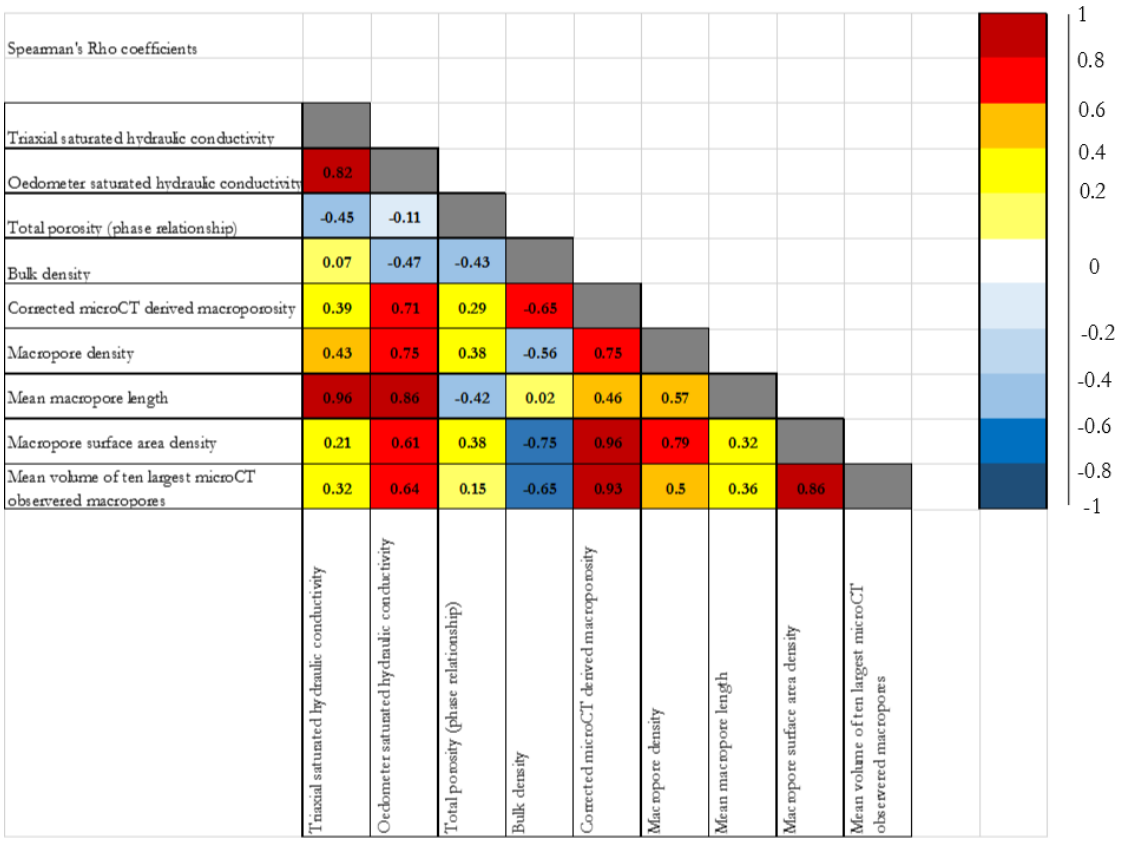

Figure 8.13 – Spearman's correlation coefficients for all the microCT calculated pore property metrics from saturated samples as well as the lab measurements of saturated hydraulic conductivity, porosity, and bulk density

Figure 8.13 shows that total porosity has a slight negative correlation to both forms of the saturated hydraulic conductivity measurement (oedometer and triaxial samples). This indicates that the hydraulic conductivity cannot be related to the overall porosity. The correlation between the triaxial measured hydraulic conductivity and microCT derived total macroporosity is mild ($r_s = 0.39$) suggesting that the macroporosity has less of an influence on the hydraulic conductivity than the connectivity of the soil matrix (at a scale below that visible with microCT).

The microCT measured mean macropore length shows a strong positive correlation with both the triaxial hydraulic conductivity ($r_s = 0.96$) and oedometer hydraulic conductivity ($r_s = 0.86$), indicating that the length of the macropores is more influential than the quantity of macropores (total macroporosity) within a sample. This could be a result of preferential flow only being influential in pores which are connected throughout the length of the samples as opposed to 'dead end' pores. From Table 8.4, Table 8.6, and Figure 8.7, it can be seen that the samples with the most connected pores (from top to bottom of subsample) have the highest saturated hydraulic conductivity and the highest mean macropore length. MicroCT derived mean macropore length therefore appears to represent a measure of the connectivity of macropores within the samples which is strongly related to their influence on flow.

These results are consistent with some researchers who have shown that highly continuous macropores are potentially active in hydrological processes at near-saturated conditions (Perret et al., 1999; Luo et al., 2010).

In general, correlations between the oedometer measured hydraulic conductivity and microCT derived pore property metrics are more significant than between the triaxial measured saturated hydraulic conductivity and the microCT pore property metrics. Indeed, the oedometer measured saturated hydraulic conductivity shows good correlation with all of the microCT derived pore property metrics. These correlations could be a result of the size of subsamples used for analysis of the microCT images being more representative of the oedometer samples. It is possible that the macropores quantified within the microCT 4 cm subvolumes correspond to the macroporosity (and other metrics) within the oedometer samples more closely than within the triaxial samples, where macroporosity can vary across the entire sample height (see Figure 8.10). Munkholm et al (2012) showed similar results on

scans of agricultural soils, in that the strongest correlations were found between parameters assessed at similar levels of observation.

However, as discussed earlier, macropores can be seen to extend throughout the height of the oedometer samples but were not observed to connect throughout the height of a triaxial sample. Therefore the correlation between the oedometer measured hydraulic conductivity and microCT derived pore property metrics may be due to the macropores having a much greater influence on the conductivity within the smaller oedometer samples than the triaxial samples due to their increased relative size (i.e. long macropores connect throughout the height of the oedometer samples and affect flow but not within the triaxial samples). This result explains the difference in triaxial and oedometer measured saturated hydraulic conductivity shown in Table 8.6.

8.6 Conclusions

MicroCT was used to visualise and quantify the pores within 100 mm diameter clay fill embankment samples at a resolution which enables quantification of macropores (> 60 microns). The samples were scanned in both partially saturated and saturated conditions to investigate the evolution of internal macropore structure with saturation. Additionally, microCT derived pore property metrics were compared to saturated hydraulic conductivity measurements to assess the influence of macroporosity on flow. The following conclusions can be drawn from the work presented here:

- Visualisation of the samples, obtained from between 1.5 – 6.5 m depth within the embankment, showed that the size and distribution of macropores present within the samples varied considerably. Total microCT measured macroporosity ranged between 0.12 % and 4.12 % although this is a small proportion of the total porosity of the samples, which depends on the scale of measurement technique used (MIP porosity varied between 0.26 - 0.27 and total porosity between 0.44 - 0.5).

  Historically, visualising and achieving an accurate description of the internal macropore structure of soil has proven difficult. The results from these microCT scans emphasise the clear benefits of microCT as a non-destructive 3D visualisation and analysis tool for soil research, even on large undisturbed clay samples which have not been previously scanned using the technique. This is only possible if a consistent microCT scanning and image analysis procedure is developed and followed within the experimental program. The procedures developed in Chapters 6 and 7 allow for

direct comparison of the macropores within these large samples in different states of saturation and enable multiple microCT scans of the same sample to be linked.

- It was found that the saturation procedure of the clay fill samples reduced the overall total macroporosity and the number/density of macropores within the samples. The saturation procedure was observed to decrease other macropore properties (mean macropore length and surface area) as well as the size of the largest macropores within the samples. After saturation the majority of the samples were composed of a greater proportion of smaller pores than at sampled conditions, indicating that it is the largest macropores within samples which are most affected by the saturation procedure. Saturation was also shown to make the samples more uniform in structure throughout their height, with less variation in total macroporosity throughout the subvolume than prior to saturation.

- Saturated hydraulic conductivity of the clay fill samples measured within an oedometer cell was found to correlate well with all microCT derived pore property metrics (better than triaxial measured k_{sat}). Macropores within oedometer samples can be seen to extend throughout the height of the samples whereas macropores were not observed to connect throughout the height of a triaxial sample. This suggests that macropores have a much greater influence on the hydraulic conductivity of oedometer samples than triaxial samples due to their increased relative size.

- MicroCT derived mean macropore length has a strong positive correlation with the hydraulic conductivity measured using triaxial or oedometer size samples (r_s = 0.96 and r_s = 0.86 respectively) and appears to represent a measure of the connectivity of macropores within the samples. The results indicate that the length of the macropores is more closely related to flow within the samples than the quantity of macropores (total macroporosity) which was not found to correlate significantly with measures of hydraulic conductivity. Therefore, the length and connectivity of macropores rather than the total volume of pores is the key influence on saturated hydraulic conductivity.

9 Overall discussion

The work presented within this thesis has analysed definitions of flow and unsaturated behaviour and developed the capabilities of microCT to help improve our knowledge of the influence of macropores on the hydrology of infrastructure slopes.

In Chapter 5, a field representative finite element model was used to calculate the pore water pressure and volumetric water content response of a cutting slope to the effects of climate and the results were compared to field measurements. It was found that the continuum assumptions (Richard's equation flow) and characterisation of unsaturated soil behaviour (SWRC parameters) used within the model do not reflect the true behaviour of the slope at shallow depths or in dry conditions. In other words, the practice most commonly used within geotechnics does not fully capture the real world behaviour of the slope. The lack of understanding of macropore influence hinders our ability to accurately estimate slope hydrology and to upscale models of slope hydrology across transport networks.

These results reinforce the importance of determining how the hydraulic conductivity of clay soils varies with depth and with saturation within earthworks, in order to be able to correctly model the hydrological response of these slopes to climate conditions. Macropores and the pore structure of a soil plays a role in the hydraulic conductivity of the soil both when saturated and unsaturated. Determining the relationship between macropore properties (e.g. size and connectivity) and saturated hydraulic conductivity is therefore of great importance. As is the degree to which this pore architecture evolves with changes in saturation and depth within a slope.

The need for new flow descriptions based on the real physical structure of soils is clear. This must take into account the interaction of the macropores and soil matrix as well as the properties of the macropores present (e.g. size, density, and connectivity).

To enable such descriptions to be formulated it is necessary to advance current experimental techniques in order to accurately measure the pore structure present within samples without destroying the samples.

This thesis has shown that after development of suitable scanning and image analysis procedures, microCT can be adapted to help overcome the difficulties associated with traditional laboratory methods. The microCT technique is not without its own difficulties however, Chapter 6 showed the trade-off encountered between image quality and the size of sample scanned due to the power needed to scan such dense samples. Chapter 7 also showed

the advancements necessary to ensure that image analysis is consistent and allows for comparison between scans of different samples (by using consistent and suitable subsampling, segmentation, image enhancement, and PVE correction methods etc.). This thesis has shown that following investigation into these issues, microCT enables non-destructive visualisation and quantification of the macropores (> 63 microns in size) within 100 mm diameter clay fill samples in the time restraints imposed by a working day. However, this size of sample is currently at the limit of microCT scanner capabilities in terms of achieving good image quality (resolution and phase contrast) from scans.

Chapter 8 showed that the macropore structure within relatively undisturbed clay fill samples could be observed due to the non-destructive nature of the technique. This visualisation of clay fill samples shows that the size and distribution of macropores within the samples is heterogeneous. An accurate quantitative description of these internal macropore structures is difficult to achieve using conventional morphological techniques (e.g. method of sections). Therefore the results from these microCT scans emphasise the clear benefits of microCT as a non-destructive 3D visualisation and analysis tool for soil research.

Chapter 8 also built on this method to show how microCT can be used in a repeatable fashion to scan samples at different water contents and throughout the depth of an embankment. This enables the dynamic nature of macropore structure to be investigated. MicroCT was used to investigate the evolution of macropore structure with saturation within 100 mm diameter clay fill samples at high resolution for the first time. It was found that the saturation procedure of the clay fill samples reduced the overall total macroporosity and the number/density of macropores within the samples. The saturation procedure was observed to decrease other macropore properties (mean macropore length and surface area) as well as the size of the largest macropores within the samples. After saturation, the majority of the samples were composed of a greater proportion of smaller pores than at sampled conditions, indicating that it is the largest macropores within samples which are most affected by the saturation procedure. Saturation was also shown to make the samples more uniform in structure throughout their height, with less variation in total macroporosity throughout the subvolume than prior to saturation.

To improve understanding of macropore influence on the saturated hydraulic conductivity of clay fill, microCT quantified macropore characteristics were compared to saturated hydraulic conductivity tests. It was found that microCT derived mean macropore

length has a strong positive correlation with the hydraulic conductivity measured using both triaxial and oedometer sized samples and appears to represent a measure of the connectivity of macropores within the samples. The results indicate that the length of the macropores is more closely related to flow within the samples than the quantity of macropores (total macroporosity) which was not found to correlate significantly with measures of hydraulic conductivity. Therefore, the length and connectivity of macropores rather than the total volume of macropores is the key influence on saturated hydraulic conductivity.

The fundamental aim of the work presented within this thesis is to help progress research towards achieving a complete picture of transient water movement within infrastructure slopes, based on a fundamental understanding of earthwork material and system behaviour. Improving our knowledge of macropore influence on flow within soils and infrastructure slope hydrology can enable us to advance our modelling of slope behaviour and develop a more resilient transport network.

It terms of achieving this aim, the development of the microCT technique and the 'proof of concept' studies presented here are significant progress to help build up the knowledge surrounding macropores. However, the techniques discussed here are some way away from directly affecting the modelling of geotechnical practitioners. Despite this, it is clear that microCT provides the potential to improve models of flow and make modelling assumptions more physically based in the future if research into the technique is continued. The technique allows the real world complexity present in infrastructure slopes to be captured at a scale larger than possible before. Provided the difficulties surrounding scanning fully saturated samples and issues with operator bias can be overcome then use of the technique within this field will surely increase.

10 Conclusions

This thesis used detailed numerical modelling of a case study infrastructure slope in conjunction with field data to assess the key influences on flow within infrastructure slopes. The results of this investigation reinforce the importance of determining how the hydraulic conductivity of clay soils varies with depth and with saturation, in order to be able to correctly model the hydrological response of earthworks to climate conditions. Determining the extent to which pore structure and connectivity influence hydraulic conductivity and the evolution of this pore architecture with changes in saturation and depth is therefore of great importance.

This thesis builds on recent developments in X-ray computed tomography (CT) in order to progress the technique as a means of visualising and quantifying macropore characteristics in a non-intrusive manner. A microCT scanning technique which allows for the scanning of large undisturbed clay fill samples was developed, as well as an image analysis procedure that allows for the quantification of internal macropore architecture. It was shown that 100 mm diameter clay cores are at the limit of microCT capabilities as a result of achievable spatial resolution and phase contrast. The use of subsampling and image improvement techniques allows for the pores above 63 microns in size present within the samples to be visualized and quantified.

Macropore influence on governing flow has traditionally been hard to define within laboratory experiments, particularly on representative and undisturbed samples. Additionally, quantitative descriptions of the dynamic nature of soil pore architecture and the effects of saturation on altering internal pore networks have proven elusive.

This thesis assessed the evolution of the internal macropore structure of undisturbed clay fill samples with saturation. Scans were conducted on 100 mm diameter clay fill samples at different states of saturation at microCT resolution for the first time. It was found that the saturation procedure reduced overall measured total macroporosity as well as the number of macropores within the samples. Additionally, the saturation procedure was observed to decrease the size of largest macropores within the samples and to make the samples more uniform in structure throughout their height.

MicroCT determined macropore property metrics of the clay fill samples were compared to saturated hydraulic conductivity tests of the samples. Saturated hydraulic conductivity was found to correlate strongly with microCT derived mean macropore length,

which represents the connectivity of the macropores within the samples. The results also indicate that the length of the macropores within a sample has more influence on the saturated hydraulic conductivity than the quantity of macropores (total macroporosity).

Overall, the developed microCT technique allows the real world complexity present in infrastructure slopes to be captured at a scale not possible before. As shown, if the difficulties surrounding use of the technique can be overcome, then it represents a new tool with which to develop more realistic flow and unsaturated behaviour theories and develop current modelling practice to better take account of the effects of macropores.

11 Future Research

The literature review and research presented within this thesis show that are still many areas of research in relation to slope hydrology (across several different scales) of which we require a better understanding. A few key topics which could be explored to further knowledge within this field are presented here:

- In order for microCT to be further adopted as a research tool for 3D non-invasive quantification within the geosciences, it is important that automated image processing techniques are developed which remove the influence of the operator and allow comparison between scans using different experimental methods. This is particularly important for segmentation of image data between material constituents, where significant operator input is currently necessary for inhomogeneous samples.

- The novel work presented within this thesis used the non-destructive nature of microCT to conduct repeated scanning of samples in different states of saturation. The microCT technique offers further potential yet to be fully taken advantage of by researchers. For instance, scans could be carried over a wide range of water contents in order to better understand macropore evolution with drying and potentially develop more realistic unsaturated behaviour descriptions. Additionally, development of microCT scanners which could house the experimental set up needed for real-time flow and conductivity measurements could lead to the development of new models of flow within soils where preferential flow occurs.

12 References

Ahmed, S. I. (2014) *An investigation of fabric and of particle shape in railway ballast using X-ray CT and the discrete element method*. University of Southampton.

Allen, R. et al. (1998) *Crop evapotranspiration - Guidelines for computing crop water requirements - FAO Irrigation and drainage paper 56*. Rome.

Ambrose, J. (1973) 'Computerized Transverse Axial Scanning (Tomography): Part 2: Clinical Application', *British Journal of Radiology*, 46, p. 1023.

Anderson, S. et al. (2010) 'CT-measured macropore parameters for estimating saturated hydraulic conductivity at four study sites', *2010 19th World Congress of Soil Science, Soil …*, (August), pp. 13–16.

Asch, T. W. J. Van, Buma, J. and Beek, L. P. H. Van (1999) 'A view on some hydrological triggering systems in landslides', (June 1997), pp. 25–32.

Aubertin, M., Mbonimpa, M. and Chapuis, R. P. (2003) 'A physically-based model to predict the water retention curve from basic geotechnical properties', *Canadian Geotechnical Journal*, 40(February), pp. 1104–1120.

Barbour, S. L. and Krahn, J. (2004) 'Numerical modeling-prediction or process?', *Geotechnical News*, 22(December), pp. 44–52.

Barnes, G. (2010) *Soil mechanics : principles and practice*. Third. Basingstoke: Palgrave Macmillan.

Baveye, P. C. et al. (2010) 'Observer-dependent variability of the thresholding step in the quantitative analysis of soil images and X-ray microtomography data', *Geoderma*, 157(1–2), pp. 51–63. doi: 10.1016/j.geoderma.2010.03.015.

Beven, K. and Germann, P. (1982) 'Macropores and water flow in soils', *Water Resources Research*, 18(5), pp. 1311–1325. doi: 10.1029/WR018i005p01311.

Beven, K. and Germann, P. (2013) 'Macropores and water flow in soils revisited', *Water Resources Research*, 49(6), pp. 3071–3092. doi: 10.1002/wrcr.20156.

Biddle, P. G. (1998) *Tree Root Damage to Buildings*. Wantage, England: Willowmead Publishing.

Birch, G. and Dewar, A. (2002) 'Earthwork failures in response to extreme weather', in Forde, M. (ed.) *Proceedings of the international conference of railway engineering*. London: Engineering technics press CD-ROM.

Bishop, A. (1960) 'The principle of effective stress', *Norwegian Geotechnical Institute*, 32, pp. 1–5.

Blaney, H. F. and Criddle, W. D. (1962) 'Determining consumptive use and irrigation water requirements', *United States Department of Agriculture*, Technical, pp. 1–59. doi: USDA Technical Bulletin 1275.

Blight, G. (2003) 'The vadose zone soil-water balance and transpiration rates of vegetation', *Geotechnique*, (1), pp. 55–64.

Boas, F. E. and Fleischmann, D. (2012) 'CT artifacts: causes and reduction techniques', *Imaging in Medicine*, 4(2), pp. 229–240. doi: 10.2217/iim.12.13.

Bouma, J. (1991) 'Influence of soil macroporosity on environmental quality', *Advances in Agronomy*, 46(C), pp. 1–37. doi: 10.1016/S0065-2113(08)60577-5.

Bouma, J. and Wösten., J. H. M. (1979) 'Flow Patterns During Extended Saturated Flow in Two, Undisturbed Swelling Clay Soils with Different Macrostructures', *Soil Sci. Soc. Am. J.*, 43, pp. 16–22.

Briggs, K. (2011) *Impacts of climate and vegetation on railway embankment hydrology*. University of Southampton.

Briggs, K. M. et al. (2012) *Permeability measurements at Newbury cutting using a double ring infiltrometer (DRI)*.

Briggs, K. M. et al. (2013) 'Managing the extent of tree removal from railway earthwork slopes', *Ecological*

Engineering, 61, pp. 690–696. doi: 10.1016/j.ecoleng.2012.12.076.

Briggs, K. M. et al. (2016) 'The influence of tree root water uptake on the long term hydrology of a clay fill railway embankment", Transportation Geotechnics, 9, pp. 31–48. doi: 10.1016/j.trgeo.', *Transportation Geotechnics*, 9, pp. 31–48. doi: 10.1016/j.trgeo.2016.06.001.

Briggs, K. M., Loveridge, F. A. and Glendinning, S. (2017) 'Failures in transport infrastructure embankments', *Engineering Geology*. Elsevier B.V., 219, pp. 107–117. doi: 10.1016/j.enggeo.2016.07.016.

Briggs, K. and Smethurst, J. (2013) 'Wet winter pore pressures in railway embankments', *Proceedings of the ICE …*, 166(5), pp. 451–465. doi: 10.1680/geng.11.00106.

Chen, T. J. et al. (2006) 'A blurring index for medical images', *Journal of Digital Imaging*, 19(2), pp. 118–125. doi: 10.1007/s10278-005-8736-y.

Clarke, D. and Smethurst, J. a. (2010) 'Effects of climate change on cycles of wetting and drying in engineered clay slopes in England', *Quarterly Journal of Engineering Geology and Hydrogeology*, 43(4), pp. 473–486. doi: 10.1144/1470-9236/08-106.

Clayton, C.R.I., Matthews, M.C. and Simons, N. E. (1995) *Site investigation: A handbook for engineers*. Oxford: Blackwell Science.

Clayton, C. R. I. and Siddique, A. (2001) 'T ube sampling disturbanceöforgotten truths and new perspectives', (3), pp. 127–135.

Clothier, B. E., Green, S. R. and Deurer, M. (2008) 'Preferential flow and transport in soil: progress and prognosis', *European Journal of Soil Science*, 59, pp. 2–13.

Cnudde, V. and Boone, M. N. (2013) 'High-resolution X-ray computed tomography in geosciences: A review of the current technology and applications', *Earth-Science Reviews*. Elsevier B.V., 123, pp. 1–17. doi: 10.1016/j.earscirev.2013.04.003.

Croney, D. (1952) 'The Movement and Distribution of Water in Soils', *Geotechnique*, 3(1), pp. 1–16.

Croney, D. (1977) *The design and performance of road pavements for the Transport and Road Research Laboratory*. First Edit. Edited by T. and R. R. Laboratory. London: H.M.S.O.

Dakshanamurthy, V. and Fredlund, D. G. (1981) 'A mathematical model for predicting moisture flow in an unsaturated soil under hydraulic and temperature gradients', *Water Resources Research*, 17(3), pp. 714–722. doi: 10.1029/WR017i003p00714.

Dewulf, W., Tan, Y. and Kiekens, K. (2012) 'Sense and non-sense of beam hardening correction in CT metrology', *CIRP Annals - Manufacturing Technology*. CIRP, 61(1), pp. 495–498. doi: 10.1016/j.cirp.2012.03.013.

Dhondt, S. et al. (2010) 'Plant structure visualization by high-resolution X-ray computed tomography', *Trends in Plant Science*. Elsevier, 15(8), pp. 419–422. doi: 10.1016/j.tplants.2010.05.002.

Diamond, S. (1970) 'Pore Size Distributions in Clays', *Clays and Clay Minerals*, 18(1), pp. 7–23. doi: 10.1346/CCMN.1970.0180103.

Dijkstra, T. et al. (2014) 'Forecasting infrastructure resilience to climate change', *Proceedings of the Institution of Civil Engineers: Transport*, 167(5), pp. 269–280. doi: 10.1680/tran.13.00089.

Dijkstra, T. and Dixon, N. (2010) 'Climate change and slope stability in the UK: challenges and approaches', *Quarterly Journal of Engineering …*, 43(4), pp. 371–385.

Dixon, N. et al. (2017) 'Near surface saturated hydraulic conductivity in engineered clay slopes', *Quarterly Journal of Engineering Geology and Hydrogeology*, In review.

Domenico, P. A. (1972) *Concepts and Models in Groundwater Hydrology*. New York: McGraw-Hill.

Drumm, E., Boles, D. and Wilson, G. (1997) 'Desiccation cracks result in preferential flow', *Geotech. News*.

Eck, D. V. et al. (2016) 'Relating Quantitative Soil Structure Metrics to Saturated Hydraulic Conductivity', *Vadose Zone Journal*, 15(1), p. 0. doi: 10.2136/vzj2015.05.0083.

Edlefsen, N. E., Anderson, A. B. C. and Station, C. A. E. (1943) *Thermodynamics of Soil Moisture*. University of California.

Ewen, J., Parkin, G. and O'Conell, P. E. (2000) 'SHETRAN : Distributed River Basin Flow Modeling System', *Journal of Hydrologic Engineering*, 5(JULY), pp. 250–258. doi: doi:10.1061/(ASCE)1084-0699(2000)5:3(250).

Feddes, R. A., Kowalik, P. J. and Zaradny, H. (1978) *Simulation of Field Water Use and Crop Yield*. Wiley (A Halsted Press book).

FEI (2014) 'Avizo Fire 3D software'.

Flury, M. et al. (1994) 'Susceptibility of soil to preferential flow of water: a field study', *Water Resouces Research*, 30(7), pp. 1945–1954.

Fredlund, D. et al. (2012) *Unsaturated Soil Mechanics in Engineering Practice*, *… of geotechnical and geoenvironmental engineering*. Wiley.

Fredlund, D. G., Sheng, D. and Zhao, J. (2011) 'Estimation of soil suction from the soil-water characteristic curve', *Canadian Geotechnical Journal*, 48(2), pp. 186–198. doi: 10.1139/T10-060.

Fredlund, D. G. and Xing, A. (1994) 'Equations for the soil-water characteristic curve', *Canadian Geotechnical Journal*. NRC Research Press, 31(4), pp. 521–532. doi: 10.1139/t94-061.

Freeze, R. A. and Cherry, J. A. (1977) *Groundwater*.

Geistlinger, H. (2013) 'Mass transfer processes across the Capillary Fringe: Quantification of gas-water interface and bubble mediated mass transfer', *EGU General Assembly*, 15(i), p. 3343.

Gens, A. (2010) 'Soil-environment interactions in geotechnical engineering', *Géotechnique*, 60(1), pp. 3–74.

van Genuchten, M. T. (1980) 'A closed-form equation for predicting the hydraulic conductivity of unsaturated soils', *Soil Science Society of America Journal*, 44(5), pp. 892–898.

GEO-SLOPE (2008) *Vadose Zone Modeling with VADOSE/W 2007*. Third. Calgary: Canada.

Gili, J. A. and Alonso, E. E. (2002) 'Microstructural deformation mechanisms of unsaturated granular soils', *International Journal for Numerical and Analytical Methods in Geomechanics*. John Wiley & Sons, Ltd., 26(5), pp. 433–468. doi: 10.1002/nag.206.

Glendinning, S. et al. (2009) 'Role of vegetation in sustainability of infrastructure slopes', *Engineering Sustainability - Proceedings of the ICE*, 162(2), pp. 101–110.

Glendinning, S. et al. (2014) 'Construction, management and maintenance of embankments used for road and rail infrastructure: implications of weather induced pore water pressures', *Acta Geotechnica*, 9(5). doi: 10.1016/j.pnsc.2014.06.008.

Glendinning, S. et al. (2015) 'Research-informed design, management and maintenance of infrastructure slopes: development of a multi-scalar approach', *IOP Conference Series: Earth and Environmental Science*, 26(September), p. 12005. doi: 10.1088/1755-1315/26/1/012005.

Goldman, L. W. (2007) 'Principles of CT: radiation dose and image quality.', *Journal of nuclear medicine technology*, 35(4), pp. 213-225-228. doi: 10.2967/jnmt.106.037846.

Gunn, D. et al. (2016) 'Aged embankment imaging and assessment using surface waves', *Proceedings of the Institution of Civil Engineers - Forensic Engineering*, 169(4), pp. 149–165. doi: 10.1680/jfoen.16.00022.

Guzzetti, F. et al. (2007) 'The rainfall intensity–duration control of shallow landslides and debris flows: an

update', *Landslides*, 5(1), pp. 3–17. doi: 10.1007/s10346-007-0112-1.

Harley, R. et al. (2014) 'Progressive deformation of glacial till due to viscoplastic straining and pore pressure variation', *67th Canadian Geotechnical conference*, (October), pp. 1–6. doi: 10.13140/2.1.2112.3846.

Helliwell, J. R. et al. (2013) 'Applications of X-ray computed tomography for examining biophysical interactions and structural development in soil systems: A review', *European Journal of Soil Science*, pp. 279–297. doi: 10.1111/ejss.12028.

Hendrickx, J. M. . and Flury, M. (2001) *Conceptual Models of Flow and Transport in the Fractured Vadose Zone*. National Academies Press.

Hillel, D. (1998) *Environmental Soil Physics - Fundamentals, Applications, and Environmental Considerations*. 1st edn. Academic Press.

Hounsfield, G. . (1973) 'Computerized transverse axial scanning (tomography): part 1. Description of system', *British Journal of Radiology*, 46, pp. 1016–1022.

Hughes, P. N. et al. (2009) 'Full-scale testing to assess climate effects on embankments', *Proceedings of the …*, 162(June), pp. 67–79. doi: 10.1680/ensu.2009.162.

Iassonov, P., Gebrenegus, T. and Tuller, M. (2009) 'Segmentation of X-ray computed tomography images of porous materials: A crucial step for characterization and quantitative analysis of pore structures', *Water Resources Research*, 45(9). doi: 10.1029/2009WR008087.

J. Perry, M. Pedley, K. Brady, and M. R. (2003) 'Briefing: Embankment cuttings: condition appraisal and remedial treatment', *Proceedings of the Institution of Civil Engineers - Geotechnical Engineering*, 156(4), pp. 171–175.

Jarvis, N. J. (2007) 'A review of non-equilibrium water flow and solute transport in soil macropores: Principles, controlling factors and consequences for water quality', *European Journal of Soil Science*, 58(3), pp. 523–546. doi: 10.1111/j.1365-2389.2007.00915.x.

Jarvis, N., Koestel, J. and Larsbo, M. (2016) 'Understanding Preferential Flow in the Vadose Zone: Recent Advances and Future Prospects', *Vadose Zone Journal*, 15(12), p. 0. doi: 10.2136/vzj2016.09.0075.

Joshi, B. et al. (1993) 'A finite element model for the coupled flow of heat and moisture in soils under atmospheric forcing', *Finite Elements in Analysis and Design*, 15, pp. 57–68.

Kabat, P. and Beekma, J. (1994) *Water in the unsaturated zone, in Drainage principles and applications*. ILRI publi. Edited by H. P. Ritzema. Wageningen: International Institute for Land Reclaimation and Improvement.

Kato, M. et al. (2013) 'Segmentation of multi-phase X-ray computed tomography images', (October 2014), pp. 1–14. doi: 10.1680/envgeo.13.00036.

Katuwal, S. et al. (2015) 'Effects of CT Number Derived Matrix Density on Preferential Flow and Transport in a Macroporous Agricultural Soil', *Vadose Zone Journal*, 14(7), p. 0. doi: 10.2136/vzj2015.01.0002.

Ketcham, R. A. and Carlson, W. D. (2001) 'Acquisition, optimization and interpretation of X-ray computed tomographic imagery: applications to the geosciences', *Computers & Geosciences*, 27(4), pp. 381–400. doi: 10.1016/S0098-3004(00)00116-3.

Kodikara, J. and Costa, S. (2013) 'Desiccation Cracking in Clayey Soils: Mechanisms and Modelling', in Laloui, L. and Ferrari, A. (eds) *Multiphysical Testing of Soils and Shales SE - 2*. Springer Berlin Heidelberg (Springer Series in Geomechanics and Geoengineering), pp. 21–32. doi: 10.1007/978-3-642-32492-5_2.

Krstelj, I. (1994) 'Manual of soil laboratory testing', *Soil Dynamics and Earthquake Engineering*, p. 147. doi: 10.1016/0267-7261(94)90007-8.

Kueh, A. et al. (2016) 'Modelling the penumbra in Computed Tomography 1', *Journal of X-Ray Science and*

Technology, 24(4), pp. 583–597. doi: 10.3233/XST-160576.

Kutilek, M. and Nielsen, D. R. (1994) *Soil hydrology: GeoEcology*. Catena-Verlag, Germany.

Lamorski, K., Slawinski, C. and Barna, G. (2014) 'Estimation of water saturated permeability of soils, using 3D soil tomographic images and pore-level transport phenomena modelling', *EGU General Assembly* …, 16, p. 11775.

Lapierre, C., Leroueil, S. and Locat, J. (1990) 'Mercury intrusion and permeability of Louiseville clay', *Canadian Geotechnical Journal*, 27(6), pp. 761–773. doi: 10.1139/t90-090.

Larsbo, M., Koestel, J. and Jarvis, N. (2014) 'Relations between macropore network characteristics and the degree of preferential solute transport', *Hydrology and Earth System Sciences*, 18(12), pp. 5255–5269. doi: 10.5194/hess-18-5255-2014.

Lauren, J. G. et al. (1988) 'Variablity of saturated hydraulic conductivity in a glossaquic hapludalf with macropores', *Soil Science*, 145(1).

Leroueil, S. (2001) 'Natural slopes and cuts: movement and failure mechanisms', *Geotechnique*, (3).

Likos, W. J., Lu, N. and Godt, J. W. (2014) 'Hysteresis and Uncertainty in Soil Water-Retention Curve Parameters', *Journal of Geotechnical and Geoenvironmental Engineering*, 140(4), p. 4013050. doi: 10.1061/(ASCE)GT.1943-5606.0001071.

Lin, H. (2010) 'Linking principles of soil formation and flow regimes', *Journal of Hydrology*, 393, pp. 3–19.

Lourenco, S. D. et al. (2011) 'Cavitation in high suction tensiometers : effect of temperature , time of use , and stone drying Cavitation in high suction tensiometers : effect of temperature , time of use , and stone drying', (1996), pp. 429–435.

Loveridge, F. A. et al. (2010) 'The impact of climate and climate change on infrastructure slopes, with particular reference to southern England', *Quarterly Journal of Engineering Geology and Hydrogeology*, 43(4), p. 461 LP-472.

Luo, L., Lin, H. and Halleck, P. (2008) 'Quantifying Soil Structure and Preferential Flow in Intact Soil Using X-ray Computed Tomography', *Soil Sci. Soc. Am. J.*, 72(4), pp. 1058–1069.

Luo, L., Lin, H. and Li, S. (2010) 'Quantification of 3-D soil macropore networks in different soil types and land uses using computed tomography', *Journal of Hydrology*. Elsevier B.V., 393(1–2), pp. 53–64. doi: 10.1016/j.jhydrol.2010.03.031.

Luo, L., Lin, H. and Schmidt, J. (2010) 'Quantitative Relationships between Soil Macropore Characteristics and Preferential Flow and Transport', *Soil Science Society of America Journal*, 74(6), p. 1929. doi: 10.2136/sssaj2010.0062.

McKenzie, N. J. and Jacquier, D. (1997) 'Improving the field estimation of saturated hydraulic conductivity in soil survey', *Australian Journal of Soil Research*, 35(4).

McMahon, T. A. et al. (2013) 'Estimating actual, potential, reference crop and pan evaporation using standard meteorological data: a pragmatic synthesis', *Hydrology and Earth System Sciences*, 17(4), pp. 1331–1363. doi: 10.5194/hess-17-1331-2013.

Mees, F. and London, G. S. of (2003) *Applications of X-ray Computed Tomography in the Geosciences*. Geological Society (Applications of X-ray Computed Tomography in the Geosciences).

Monteith, J. L. and Unsworth, M. H. (1990) *Principles of environmental physics*. 2nd edn. London: Arnold, Edward.

Mooney, S., Pridmore, T., Helliwell, J. & Bennett, M. (2012) 'Developing X-ray computed tomography to non-invasively image 3-D root systems architecture in soil', *Plant and Soil*, 352, pp. 1–22.

Mooney, S. (2002) 'Three-dimensional visualization and quantification of soil macroporosity and water flow

patterns using computed tomography', *Soil Use and Management*, 18(2), pp. 142–151. doi: 10.1079/SUM2002121.

Mori, Y. et al. (1999) 'Discriminating the Influence of Soil Texture and Management-Induced Changes in Macropore Flow Using Soft X-Rays', *Soil Science*, 164(7), pp. 462–482.

Morisette, J. et al. (2006) 'Validation of Global Moderate-Resolution LAI products: A Framework Proposed Within the CEOS Land Product Validation Subgroup', *44*, 7(7), pp. 1804–1817.

Mualem, Y. (1976) 'A new model for predicting the hydraulic conductivity of unsaturated porous media', *Water Resources Research*, 12(3), pp. 513–522. doi: 10.1029/WR012i003p00513.

Munkholm, L. J., Heck, R. J. and Deen, B. (2012) 'Soil pore characteristics assessed from X-ray micro-CT derived images and correlations to soil friability', *Geoderma*, 181–182, pp. 22–29. doi: 10.1016/j.geoderma.2012.02.024.

Naveed, M. et al. (2013) 'Revealing Soil Structure and Functional Macroporosity along a Clay Gradient Using X-ray Computed Tomography', *Soil Science Society of America Journal*, 77(2), pp. 403–411.

Nitao, J. J. and Bear, J. (1996) 'Potentials and Their Role in Transport in Porous Media', *Water Resources Research*, 32(2), pp. 225–250. doi: 10.1029/95WR02715.

Nyambayo, V. P. and Potts, D. M. (2010) 'Numerical simulation of evapotranspiration using a root water uptake model', *Computers and Geotechnics*, 37(1–2), pp. 175–186. doi: 10.1016/j.compgeo.2009.08.008.

Ommaya, A. K. et al. (1976) 'Computerized Axial Tomography: Estimation of Spatial and Density Resolution Capability', *British Journal of Radiology*, 49, p. 604.

Penman, H. L. (1948) 'Natural Evaporation from Open Water, Bare Soil and Grass', *Proceedings of the Royal Society A: Mathematical, Physical and Engineering Sciences*, 193(1032), pp. 120–145. doi: 10.1098/rspa.1948.0037.

Pennington, C. et al. (2014) 'Antecedent Precipitation as a Potential Proxy for Landslide Incidence in South West United Kingdom', in Sassa, K., Canuti, P., and Yin, Y. (eds) *Landslide Science for a Safer Geoenvironment SE - 34*. Springer International Publishing, pp. 253–259. doi: 10.1007/978-3-319-04999-1_34.

Perret, J. et al. (1999) 'Three-Dimensional Quantification of Macropore Networks in Undisturbed Soil Cores', *Soil Science Society of America Journal*, 63(6), p. 1530. doi: 10.2136/sssaj1999.6361530x.

Peth, S. et al. (2010) 'Dynamics of soil pore space structure investigated by X-ray microtomography', in *19th World Congress of Soil Science, Soil Solutions for a Changing World*, pp. 17–20.

Petrovic, A. M., Siebert, J. E. and Rieke, P. E. (1982) 'Soil bulk density analysis in three dimensions by computed tomographic scanning.', *Soil Sci. Soc. Am. J.*, 46, pp. 445–450.

Peyrin, F. et al. (2012) 'Synchrotron radiation CT from the micro to nanoscale for the investigation of bone tissue', in *Proc. SPIE 8506, Developments in X-Ray Tomography VIII*, p. 12.

Pham, H. Q., Fredlund, D. G. and Barbour, S. L. (2005) 'A study of hysteresis models for soil-water characteristic curves', *Canadian Geotechnical Journal*, 42(6), pp. 1548–1568. doi: 10.1139/t05-071.

du Plessis, A., le Roux, S. G. and Guelpa, A. (2016) 'Comparison of medical and industrial X-ray computed tomography for non-destructive testing', *Case Studies in Nondestructive Testing and Evaluation*. Elsevier Ltd, 6, pp. 17–25. doi: 10.1016/j.csndt.2016.07.001.

Porter, M. L. and Wildenschild, D. (2010) 'Image analysis algorithms for estimating porous media multiphase flow variables from computed microtomography data: A validation study', *Computational Geosciences*, 14(1), pp. 15–30. doi: 10.1007/s10596-009-9130-5.

Potts, D. M., Kovacevic, N. and Vaughan, P. R. (1997) 'Delayed collapse of cut slopes in stiff clay', *Geotechnique*, 47(5), pp. 953–982. doi: 10.1680/geot.2000.50.2.203.

Powrie, W. (2013) *Soil Mechanics: Concepts and Applications*. Third, *Book*. Third.

Rajeev, P., Chan, D. and Kodikara, J. (2012) 'Ground–atmosphere interaction modelling for long-term prediction of soil moisture and temperature', *Can. Geotech. J. Editor's Choice*, 1(1), pp. 1059–1073. doi: 10.1139/t2012-068@cgj-ec.2015.01.issue-1.

Rayhani, M. H., Yanful, E. K. and Fakher, a (2007) 'Desiccation-induced cracking and its effect on the hydraulic conductivity of clayey soils from Iran', *Canadian Geotechnical Journal*, 44(3), pp. 276–283. doi: 10.1139/t06-125.

Richards, L. A. (1931) 'CAPILLARY CONDUCTION OF LIQUIDS THROUGH POROUS MEDIUMS', *Physics*, 1(5), p. 318. doi: 10.1063/1.1745010.

Ridley, A. (2004) 'Role of pore water pressures in embankment stability', *Proceedings of the ICE- …*, (October), pp. 193–198.

Ridley, A., McGinnity, B. and Vaughan, P. (2004) 'Role of pore water pressures in embankment stability', *Proceedings of the ICE - Geotechnical Engineering*, 157(4), pp. 193–198. doi: 10.1680/geng.2004.157.4.193.

Ritchie, J. T. (1972) 'Model for predicting evaporation from a row crop with incomplete cover', *Water Resources Research*, 8(5), pp. 1204–1213. doi: 10.1029/WR008i005p01204.

Rodríguez, R. et al. (2007) 'Experimental and numerical analysis of desiccation of a mining waste', *Canadian Geotechnical Journal*. NRC Research Press, 44(6), pp. 644–658. doi: 10.1139/t07-016.

Romero, E. and Simms, P. (2008) 'Microstructure Investigation in Unsaturated Soils: A Review with Special Attention to Contribution of Mercury Intrusion Porosimetry and Environmental Scanning Electron Microscopy', *Geotechnical and Geological Engineering*, 26(6), pp. 705–727.

Sanchez, M. et al. (2013) 'Exploring desiccation cracks in soils using a 2D profile laser device', *Acta Geotechnica*. Springer Berlin Heidelberg, 8(6), pp. 583–596. doi: 10.1007/s11440-013-0272-1.

Saxton, K. E. (1982) 'Mathematical modelling of evapotranspiration on agricultural watersheds.', *Modeling Components of the Hydrologic Cycle*, (May 18-21), pp. 183–203.

Schaap, M. G. and van Genuchten, M. T. (2006) 'A Modified Mualem–van Genuchten Formulation for Improved Description of the Hydraulic Conductivity Near Saturation', *Vadose Zone Journal*, 5(1), p. 27. doi: 10.2136/vzj2005.0005.

Schindelin, J. et al. (2012) 'Fiji - an Open Source platform for biological image analysis', *Nature methods*, 9(7), p. 10.1038/nmeth.2019. doi: 10.1038/nmeth.2019.

Scott, J. M., Loveridge, F. and O'Brien, A. S. (2007) 'Influence of climate and vegetation on railway embankments', *Geotechnical Engineering in Urban Environments: Proceedings of the 14th European Conference on Soil Mechanics and Geotechnical Engineering*, pp. 659–664.

Sharma, N. and Aggarwal, L. M. (2010) 'Automated medical image segmentation techniques.', *Journal of medical physics / Association of Medical Physicists of India*, 35(1), pp. 3–14. doi: 10.4103/0971-6203.58777.

Sheppard, A. P., Sok, R. M. and Averdunk, H. (2004) 'Techniques for image enhancement and segmentation of tomographic images of porous materials', *Physica A: Statistical Mechanics and its Applications*, 339(1–2), pp. 145–151. doi: 10.1016/j.physa.2004.03.057.

Shin, H. S., Kim, K. Y. and Pande, G. N. (2013) 'Porosity and Pore-Size Distribution of Geomaterials from X-ray CT Scans', in Laloui, L. and Ferrari, A. (eds) *Multiphysical Testing of Soils and Shales SE - 21*. Springer Berlin Heidelberg (Springer Series in Geomechanics and Geoengineering), pp. 177–186. doi: 10.1007/978-3-642-32492-5_21.

Sijbers, J. and Postnov, A. (2004) 'Reduction of ring artefacts in high resolution micro-CT reconstructions.',

Phys Med Biol., 49(14), pp. 247–253.

Šimůnek, J. et al. (2013) 'The HYDRUS-1D Software Package for Simulating the Movement of Water, Heat, and Multiple Solutes in Variably Saturated Media, Version 4.17, HYDRUS Software Series 3', (June), p. 343.

Sivakumar, V. et al. (2015) 'Influence of testing on permeability of compacted fine soils', 168.

Skempton, A. W. (1996) 'Embankments and Cuttings on the early Railways', *Construction History*, Vol. 11, pp. 33–49.

Smethurst, J. et al. (2006) 'Seasonal changes in pore water pressure in a grass-covered cut slope in London Clay', *Geotechnique*, (8), pp. 523–537.

Smethurst, J. et al. (2012) 'Factors controlling the seasonal variation in soil water content and pore water pressures within a lightly vegetated clay slope', *Géotechnique*, (5), pp. 429–446.

Smith, I. (2014) *Smith's Elements of Soil Mechanics*. 9th edn. Wiley-Blackwell.

Smith, J. C. (2015) *Examining Soil Based Construction Materials through X-Ray Computed Tomography*. Durham University. doi: ear.

Sněhota, M. et al. (2007) 'Impact of the biopores morphology on infiltration properties of soil', in *Bioclimatology and natural hazards*. Slovakia.

Stirling, R., Davie, C. T. and Glendinning, S. (2015) 'Multiphase modelling of desiccation cracking in the near-surface of compacted soils / Modélisation multiphasique de fissures ... Multiphase modelling of desiccation cracking in the near-surface of compacted soils Modélisation multiphasique de fissures de ', (September).

Taina, I.A., Heck, R.J. & Elliot, T. R. (2008) 'Application of X-ray computed tomography to soil science: a literature review', *Canadian Journal of Soil Science*, 88, pp. 1–19.

Take, W. A. (2003) *The influence of seasonal moisture cycles on clay slopes*. University of Cambridge.

Take, W. A. and Bolton, M. D. (2011) 'Seasonal ratcheting and softening in clay slopes, leading to first-time failure', *Géotechnique*, 61(9), pp. 757–769. doi: 10.1680/geot.9.P.125.

Terzaghi, K. (1925) 'Principles of Soil Mechanics: I—Phenomena of Cohesion of Clays', *Engineering News-Record*, 95(19), pp. 742–746.

Terzaghi, K. (1943a) *Theoretical soil mechanics*. J. Wiley.

Terzaghi, K. (1943b) 'Theoretical soil mechanics', *Géotechnique*, p. 510. doi: 10.1016/0167-1987(88)90005-0.

Toll, D. G. et al. (2011) 'Soil suction monitoring for landslides and slopes', *Quarterly Journal of Engineering Geology and Hydrogeology*, 44(1), pp. 23–33. doi: 10.1144/1470-9236/09-010.

Toll, D. G. et al. (2014) 'Soil atmosphere interactions for analysing slopes in tropical soils', *The 14th International conference of the International Association of Computer Methods and Advances in Geomechanics*, (2003), pp. 1333–1338.

Tratch, D. J., Wilson, G. W. and Fredlund, D. G. (1995) *An Introduction to Analytical Modelling of Plant Transpiration for geotechnical engineers*, *Proceedings of the 48th Canadian Geotechnical Conference*. Vancouver.

Varslot, T. et al. (2010) 'Fast high-resolution micro-CT with exact reconstruction methods', in, pp. 780410–780413.

Vaughan, P. R. (1994) 'Assumption, prediction and reality in geotechnical engineering', *Géotechnique*, 44(4), pp. 573–609. doi: 10.1680/geot.1994.44.4.573.

Vaughan, P. R., Kovacevic, N. and Potts, D. M. (2004) 'Then and now: some comments on the design and analysis of slopes and embankments', in *Advances in geotechnical engineering: The Skempton conference*, pp. 15–64.

Vereecken, H. et al. (2016) 'Modeling Soil Processes: Review, Key Challenges, and New Perspectives', *Vadose Zone Journal*, 15(5), p. 0. doi: 10.2136/vzj2015.09.0131.

Vervoort, R. W. and Cattle, S. R. (2003) 'Linking hydraulic conductivity and tortuosity parameters to pore space geometry and pore-size distribution', *Journal of Hydrology*, 272(1–4), pp. 36–49. doi: 10.1016/S0022-1694(02)00253-6.

Vogel, H. J. (2000) 'A numerical experiment on pore size, pore connectivity, water retention, permeability, and solute transport using network models', *European Journal of Soil Science*, 51(1), pp. 99–105. doi: 10.1046/j.1365-2389.2000.00275.x.

Vogel, H. J. and Roth, K. (2001) 'Quantitative morphology and network representation of soil pore structure', *Advances in Water Resources*, 24(3–4), pp. 233–242. doi: 10.1016/S0309-1708(00)00055-5.

Weiler, M. (2017) 'Macropores and preferential flow-a love-hate relationship', *Hydrological Processes*, 31(1), pp. 15–19. doi: 10.1002/hyp.11074.

Weiler, M. and Naef, F. (2003) 'An experimental tracer study of the role of macropores in infiltration in grassland soils', *Hydrological Processes*. John Wiley & Sons, Ltd., 17(2), pp. 477–493. doi: 10.1002/hyp.1136.

Wildenschild, D. and Sheppard, A. P. (2013) 'X-ray imaging and analysis techniques for quantifying pore-scale structure and processes in subsurface porous medium systems', *Advances in Water Resources*. Elsevier Ltd, 51, pp. 217–246. doi: 10.1016/j.advwatres.2012.07.018.

Wilson, G. W. (1990) *Soil evaporative fluxes for geotechnical engineering problems*. University of Saskatchewan.

Wood, D. M. (2003) *Geotechnical Modelling*. CRC Press (Applied Geotechnics).

Young, I. M., Crawford, J. W. and Rappoldt, C. (2001) 'New methods and models for characterising structural heterogeneity of soil'. 110, , , 61(1/2), pp. 33–45.

Zotarelli, L. and Dukes, M. (2010) 'Step by step calculation of the Penman-Monteith Evapotranspiration (FAO-56 Method)', *Institute of Food and* …, pp. 1–10.

13 Appendix

13.1 A study of the influence of slope geology on landslide occurrence during extreme rainfall

Landslides are a major natural hazard all over the world and regularly cause severe disruption, damage to infrastructure, and loss of life. In the UK we are fortunate that landslides tend to be on a smaller scale than elsewhere.

By examining historical landslide records and comparing them with climate data it is possible to identify meteorological threshold values for periods of increased slope instability. A common approach is to estimate a meteorological threshold based on rainfall intensity and duration (e.g. Wieczorek, 1987; Guzzetti et al., 2007) However, the rate and quantity of surface water infiltration (causing increased pore water pressures) is influenced by the geological conditions (e.g. soil type, saturation and permeability) and the antecedent weather conditions (Zhang et al., 2011). This can affect the time of landslide occurrence and the type of landslide failure mechanism (Leroueil, 2001).

Soil water balance approaches such as the calculation of soil moisture deficit (SMD) can be used to consider the long term influence of rainfall, runoff and evapotranspiration on surface water infiltration (Blight, 2003) and to assess trends in landslide triggering. For example, Hutchinson (1995, cited Leroueil, 2001) showed that landslides in the London Clay cliffs at Southend-on-Sea occurred when SMD was less than around 10mm between 1967 and 1976. A similar relationship between landslide occurrence and periods of low SMD has been shown by Kovacevic et al. (2001, cited Macdonald et al., 2012), Ridley (2004) and Wilson (2003).

Network Rail has used SMD to predict periods of likely slope instability and identify risk areas within the rail network since 2000 (Birch and Dewar, 2002). The Network Rail threshold considers average monthly rainfall above 175% of the historical long term average during periods of SMD close to zero (Winter et al., 2006). It has proved to be a valuable tool as part of an effective early warning system (Goldfingle, 2010).

An evaluation of existing landslide triggering thresholds and large scale trends requires records of the type, time, and location of landslide events over a range of long term weather conditions including extreme events and from a range of geological areas. With the integration of news and media reports into landslide records, the British Geological Survey

(BGS) has collated a landslide database of over 400 landslide events from across the UK between 2004 and 2014.

The aim of this project was to consider the influence of long term weather, extreme rainfall and the underlying slope geology on the type and time of landslide occurrence, for comparison with existing landslide trigger thresholds. The type, time and location of over 400 landslide events recorded by the BGS over ten years are compared with rainfall data, geological permeability indices and the calculated soil moisture deficit.

13.1.1 Method

Met Office (2014) weather data for England and for Scotland was used to plot daily rainfall and to calculate the long term soil moisture deficit (SMD) for the period 2004 to 2014. This was compared with the type and time of landslide occurrence recorded within the BGS landslide database. Landslide location records were compared with geological maps of the superficial and bedrock geology. This was used to identify geological features such as low permeability soils or the presence of underdrainage by permeable bedrock which might influence groundwater response to extreme weather (Briggs et al., 2013).

Daily SMD was calculated for both central Scotland and central England using daily data from Met Office weather stations at Strathspey and Northampton respectively. SMD was not calculated at individual sites, therefore neglecting the influence of localised weather and vegetation conditions.

13.1.2 BGS Landslide Database

The British Geological Survey first created a landslide database in the 1980's and the current version now contains over 17,000 events (Pennington et al., 2014). However, it is only since 2004 and the gradual integration of media reports into the system, that most events are recorded with accurate temporal data (i.e. a precise date 'stamp' of occurrence). Since 2004, over 400 dated landslide records have been added to the database (coastal landslides have been excluded from the scope of this study). Within the database each event is related to information including the type, time and location of the landslide.

Figure 13.1 shows the distribution of the events within the database according to the BGS landslide type classification described in Foster et al., (2012). Slope failures are the most numerous landslide failure type within the database. This classification contains landslides on man-made slopes affecting transport infrastructure (e.g. road and rail embankments and

cuttings). Many of these records were reported via social media and the exact nature of the landslide failure is not known.

Since 2012, social media has been incorporated into the search system used to populate the database. This has resulted in an increased number of recorded events in the period 2012-2014, as many of the smaller, low impact events which might have previously gone unreported are now detected. The use of media sources does not provide a comprehensive record of all events but it does provide a cost-efficient way to gain an understanding of landslide trends.

Pennington et al. (2014) explored the relationship between antecedent rainfall and landslides in southwest England using the BGS landslide database. Three different types of landslide recorded in the BGS database (falls, slope failures, and translational/planar slides) were examined. Falls were found to correlate with longer term antecedent rainfall (60 days), whereas planar slides and slope failures correlated with shorter-term antecedent rainfall (between 7 and 30 days, and between 1 and 7 days respectively). However, Pennington et al. (2014) noted that these conclusions were based on a limited number of observations in a regional study.

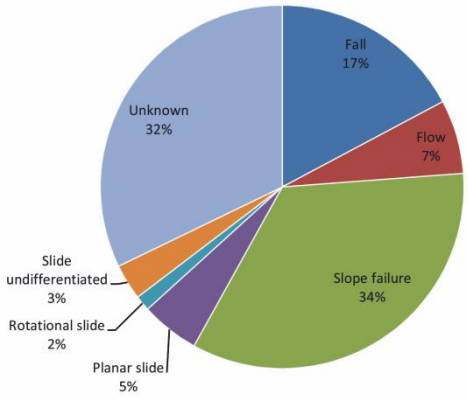

Figure 13.1 - Landslide failure type division of 441 records (2004-2014) within the BGS landslide database

13.1.3 Geological Maps

Landslide records were overlaid on superficial and bedrock geology maps (1:50,000 scale) using ArcGIS software (ESRI, 2014). This associated each landslide record with a bedrock and superficial geology (Figure 13.2), giving an indication of geological features which might influence local hydrogeology in response to weather.

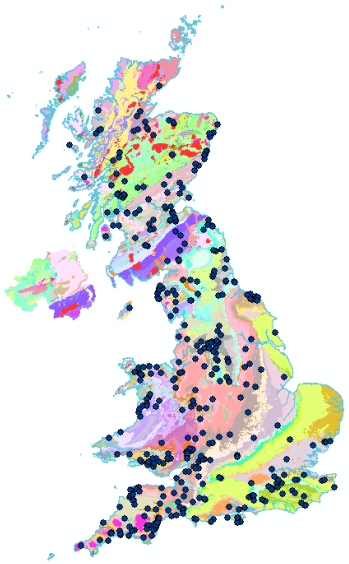

Figure 13.2 - BGS landslide database records (2004-2014) (excluding coastal events) overlaid on a map of UK bedrock geology (© NERC 2014) using ArcGIS software

13.1.4 Permeability Classes

The permeability of the superficial and bedrock geology influences the ability of rainfall to infiltrate and to drain from slopes during periods of extreme rainfall (Briggs and Smethurst, 2013). Broad permeability classes (high, moderate and low) (Table 13.1) were used to indicate the influence of superficial and bedrock geology on local hydrogeology at the landslide locations. The permeability classes were based on the BGS permeability indices (Lewis et al., 2006) categorising every lithology within the Digital Geological Map of Great Britain (DiGMapGB-50). Although this qualitative ranking of soil and rock permeability does not allow a great deal nuance, it allows a simplified examination of its influence on landslide occurrence.

Table 13.1 – BGS landslide database events (2004-2014) categorised by BGS permeability class.

Permeability Class	England/Wales	Scotland
Bedrock Geology		
Low permeability	6	27
Moderate permeability	214	43
High permeability	94	37
Unknown	20	0
Superficial Geology		
Low permeability	6	12
Moderate permeability	82	48
High permeability	26	25
Unknown	220	22

13.1.5 Results and discussion

The rainfall data, soil moisture deficit and permeability classes were used to explore trends within the BGS landslide database. The following questions were considered:

1) Landslides and specifically slope failures are associated with low SMD (Hutchinson (1995), cited Leroueil (2001); Ridley (2004))

Figure 13.3 shows that around 66 % of landslide events occurred when SMD was at, or very close to zero. If the failures are sorted by type, this relationship becomes much more pronounced. Approximately 90 % of slope failures occurred when SMD was less than 1mm. Flow and fall type failures occurred less frequently during periods of low SMD. Cumulative rainfall analysis showed that slope failures are triggered by lesser antecedent rainfall than flow or fall type failures (Pennington et al., 2014). Slope failures are more closely linked to prolonged, low intensity surface water infiltration than fall or flow type failures.

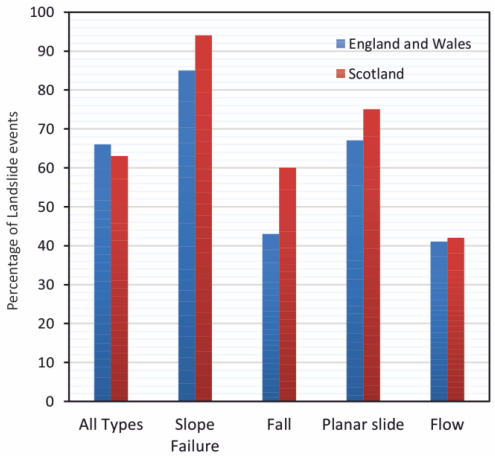

Figure 13.3 - Landslide events by failure type during periods of low (< 1 mm) Soil Moisture Deficit (2004-2014)

2) A rapid reduction in SMD (e.g.. intensive rainfall following a prolonged dry period) is associated with earthwork slope failures (Macdonald et al., 2012)

No correlation was observed between slope failures (or any type of failure) and a large (> 25 mm) reduction in SMD during the week prior to failure.

3) Landslides are associated with intensive rainfall on the day of failure (Wieczorek and Guzzetti, 1999)

The majority of the events were triggered by daily rainfall of less than 10 mm. Daily rainfall alone was not a good indicator of landslide occurrence.

4) Landslides and specifically slope failures are associated with above-average rainfall during periods of low SMD (Birch and Dewar, 2002)

Figure 13.4 shows that slope failures generally occur after longer periods of zero SMD than falls or flows. Figure 13.5 shows that slope failures in England correspond well with periods when both SMD is zero and daily rainfall is above the long term average. This relationship also applied to slope failures in Scotland but was not apparent for other types of failure.

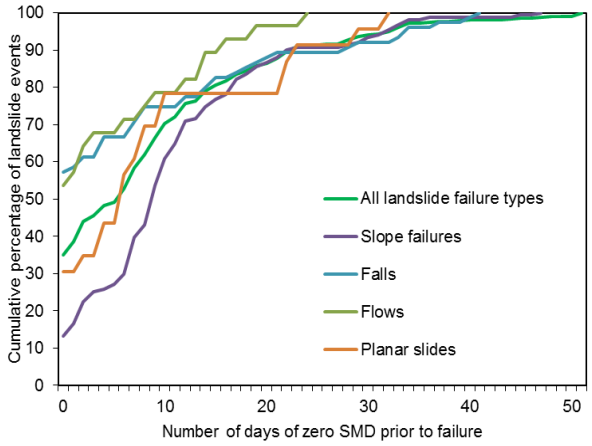

Figure 13.4 - A comparison of the cumulative percentage of landslide events and the number of days of zero SMD prior to failure, sorted by failure type

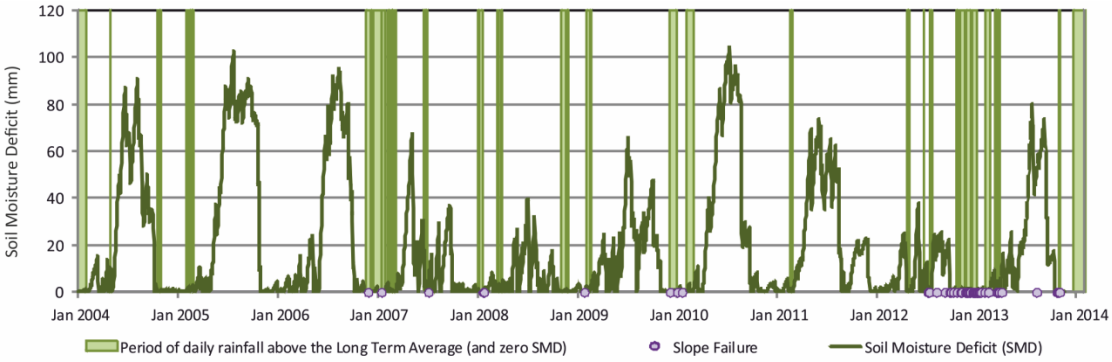

Figure 13.5 - Slope failures in England compared with of periods of low (< 1 mm) soil moisture deficit and rainfall above the 1971-2000 long term average

5) Areas of high permeability superficial geology are vulnerable to landslide events following sudden intensive rainfall (Corominas (2001), cited Tofani et al., (2006))

Figure 13.6 compares daily rainfall with landslide events within the high and low superficial permeability classes. Records from the moderate permeability class are omitted (130 records). Landslides in the high superficial permeability class are associated with high intensity rainfall (51 records). Landslides in the low superficial permeability class are associated with low intensity rainfall (18 records). Pore water pressures within high permeability soils are more likely to respond to intensive rainfall events and surface water infiltration than low permeability soils, where greater runoff occurs.

Results indicate that the presence of lower permeability bedrock (33 records; Table 13.1), does not lead to increased landslide occurrence during periods of zero SMD. Further differentiation of the permeability classes is required to explore the large number of landslide events in moderate permeability bedrock (257 records).

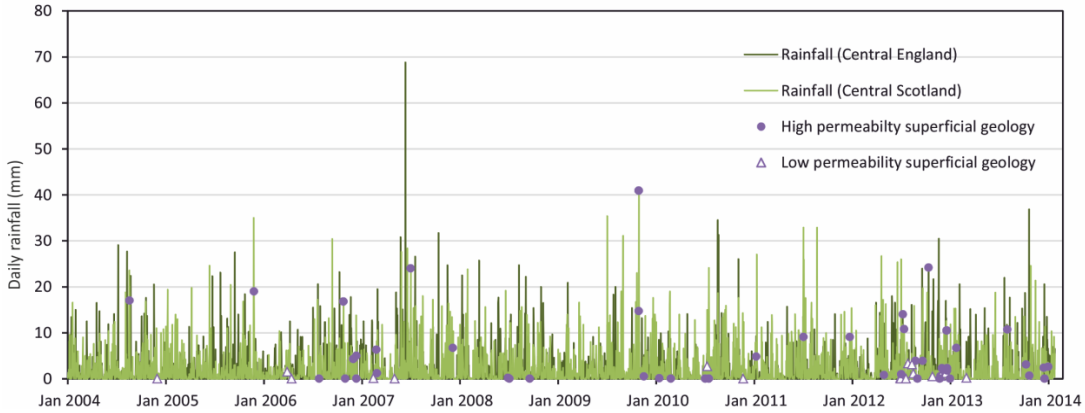

Figure 13.6 - A comparison of daily rainfall with landslides in areas of high and low permeability superficial geology (see Table 13.1)

13.1.6 Conclusions

The relationship between daily rainfall, soil moisture deficit and underlying slope geology were examined using a database of 441 landslide events between 2004 and 2014.

The data shows that a combined rainfall intensity and water balance assessment can be a useful proxy for predicting slope failure type landslide occurrence when daily rainfall is above the long term average and the soil moisture deficit is close to 0 mm. However, intense rainfall (> 10 mm per day) or rapid changes in the calculated soil moisture deficit (> 25 mm per day) were not good indicators of slope failure or other landslide failure types. Factors including the permeability of the superficial geology play a role in determining whether a slope will fail in response to an intensive rainfall event or a prolonged period of wet weather.

It is recommended that future work is undertaken to identify more localised phenomena by improving the spatial resolution of both the permeability classification and the weather data used in the SMD calculations. It is anticipated that this will benefit from continual additions to the BGS landslide database following the extremely wet winter of 2013/2014.

13.2 Field data interpretation

When interpreting field measurements, it is important to try and avoid incorrectly inferring the wrong conclusion from the way in which the data has been presented or analysed. For instance, the return periods presented in Figure 5.7 in Chapter 5 are influenced by how the data is grouped and which months are included. Figure 13.7 shows the return periods for the three modelled years with summer and winter rainfall from six-monthly periods, as opposed to the three-monthly periods in Figure 5.7. It can be seen that the return periods are significantly altered. For example, 2006 no longer appears to be a particularly dry period based on either summer or winter rainfall, although the summer of 2007 is still the most extreme (wettest) within the dataset with respect to summer rainfall and 2008 is largely unchanged in terms of return periods. This is illustrated further by Figure 13.8, which shows the cumulative probability distribution of the rainfall totals of all the years of data for several different groupings. The 50 % position on the graph represents the average of all the years, with drier years towards the left and wetter years with high cumulative probabilities on the right. For the furthermost data point to the right on each line, 100 % of the previous years fall below the total rainfall for that period. The modelled years are labelled and it can be observed that their respective positions (cumulative probabilities) vary depending on which grouping is used.

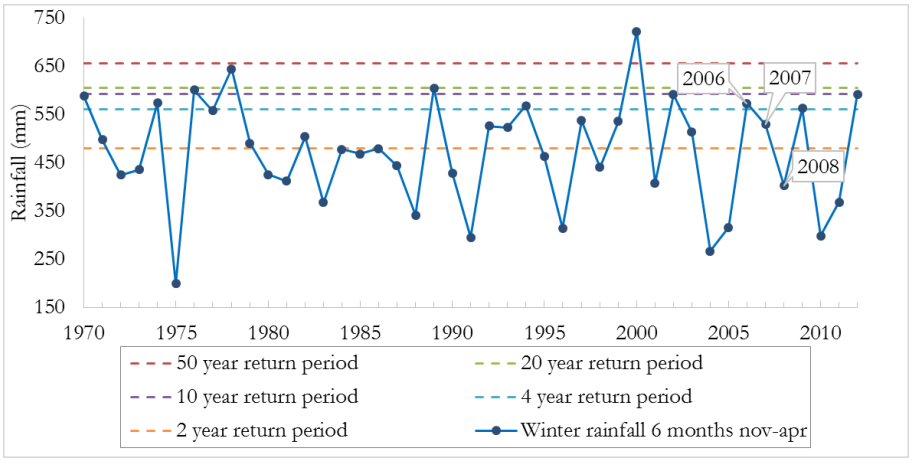

(a)

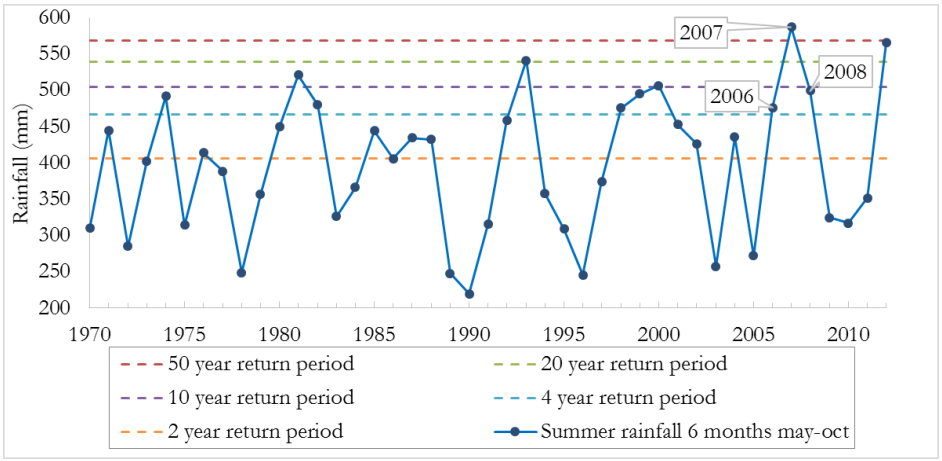

(b)

Figure 13.7 - Return periods for all years since 1970 based on (a) Total winter rainfall (November – April) and (b) Total summer rainfall (May-October) (data from (Smethurst et al., 2012))

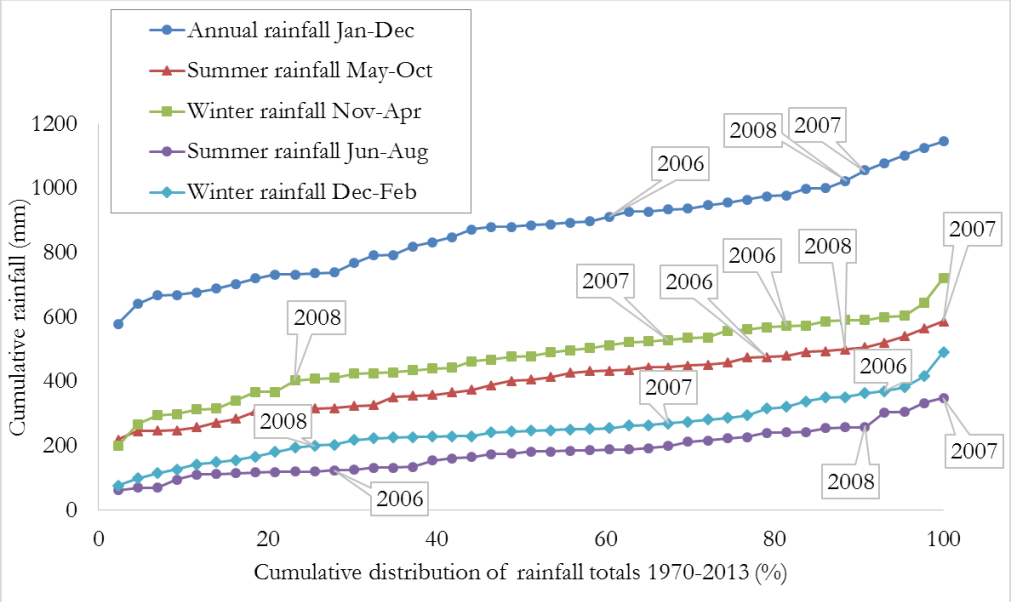

Figure 13.8 – A cumulative probability plot of annual, winter (both December-February and November-April) and summer (both May-October and June-August) rainfall totals for all years since 1970

13.3 Soil moisture deficit calculations

Table 13.2 shows that values used to calculate soil moisture deficit according to Section 3.7.

As SMD calculations involve using hourly/daily weather data from site stations, it was commonly necessary to have to estimate missing or erroneous values. Missing rainfall and temperature values were estimated by factoring data from nearby stations. Any missing wind values were approximated from the site averages. Daily maximum and minimum values of relative humidity were calculated using the assumption that $T_{dew\ point} = T_{minimum}$ and that the August-Roche-Magnus approximation can therefore be used (Allen et al., 1998; Lawrence, 2005).

Table 13.2 – Water Balance soil moisture deficit model and evapotranspiration estimation parameters, for a vegetation cover of grass and herbs at Newbury cutting (Clarke and Smethurst, 2010)

Vegetation root depth (mm)	1000
Available water (% of total soil volume)	18%
Total available water (mm)	180
Readily available water (mm)	90
Crop coefficient Kc	1
Psychrometric constant (kPa/^{0}C)	0.000665×atm. pressure
Solar constant	0.082
Latitude (rad)	0.895
Hypothetical reference crop height (m)	0.12 (Zotarelli and Dukes, 2010)
Surface resistance (s m^{-1})	70 (Zotarelli and Dukes, 2010)
Albido (or canopy) reflection coefficient	0.23 (Allen et al., 1998)
Stefan-Boltzman constant (Mj/K^4/M^2/day)	4.903×10^{-9}
Elevation above sea level (m)	105

13.4 iSMART

Part of the research presented within this thesis was conducted under the scope of the iSMART (Infrastructure Slopes Sustainable Management and Resilience Assessment) project. The project is funded by the Engineering and Physical Sciences Research Council (EPSRC) and the group comprises researchers from six different UK universities (Bath, Newcastle, Durham, Queens Belfast, Southampton, and Loughborough) as well as the British Geological Survey. The aim of the project is to coalesce on-going field, laboratory, and computing research studies within the UK infrastructure slope management and resilience fields, so as to address the current knowledge gaps.

Within iSMART there is also a heavy emphasis on collaboration with industry and several key stakeholders in the group are infrastructure asset owners (e.g. Network Rail and the Highways Agency) and engineering consultancies (e.g. Atkins and Balfour Beatty). By forming a partnership with industry, the group aims to provide research which addresses the most pertinent issues asset managers and engineers in the field currently face. The group also benefits from the input of the stakeholders in guiding research, opening up company databases of slope failures, and by allowing access to sites within their networks for field studies.

13.5 Caisson benchmark study

As part of the iSMART working group, several site-specific modelling studies were conducted in order to help improve the group's modelling capability and to provide a link to the field work and experimentation also being undertaken within the group. Prior to these case studies, it was decided to conduct a benchmark modelling study to compare modelling capability and different modelling approaches.

13.5.1 Caisson model domain

Two modelling exercises were carried out involving the wetting and drying phases of a one-dimensional caisson. The aim of this study was to identify any significant differences in the modelling criteria necessary, model assumptions, or results of the modellers from different universities. Several different modelling approaches were compared (see Glendinning et al. (2015)). The results from Hydrus and Vadose/W are shown here. Divergences from any standard assumptions outlined in the examples regarding boundary conditions, initial conditions or fluid properties were noted and compared.

The problem and benchmark results are taken from Forsyth et al. (1995). The domain, shown in Figure 13.9, is a 6 m high, 3 m wide rectangular caisson. The caisson is initially wetted using a constant infiltration surface boundary condition of 20 cm/day for 7 days in order to fully saturate the soil. It is subsequently allowed to drain freely from the bottom boundary for 100 days with no further infiltration.

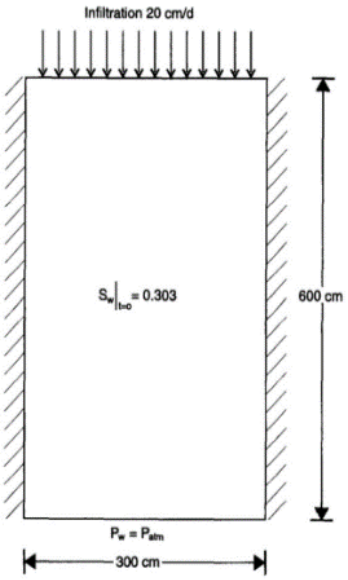

Figure 13.9 - Caisson domain for the benchmark study (Forsyth et al., 1995)

13.5.2 Initial Conditions

This exercise was conducted with an initial uniform degree of saturation of 0.303 throughout the model domain. The uniform saturation of 0.303 was set as the initial condition in Vadose/W by specifying a uniform pressure head spatial function of -7.2 m, which corresponds to a volumetric water content of 0.1 from the SWRC and a degree of saturation of 0.303. In the second case the initial condition was specified by drawing an initial water table at the base of the caisson and there was therefore a suction of 60 kPa at the surface.

13.5.3 Boundary conditions

Two separate models were set up and run, the first specifies a potential seepage face at the bottom of the caisson so that after saturation water is allowed to flow downwards through the domain. The other model specifies a potential seepage face at the top of the caisson so that after saturation no flow is allowed through the bottom of the domain and water is instead discharged over the top of the caisson. This was necessary, as failure to specify either of these boundaries as a potential seepage face during the wetting stage resulted in unconverged pressure head nodes and the model breaking down, as would be expected, as there is nowhere for the infiltration to go within the model.

In all models an infiltration flux of 200 mm/day was specified during the wetting stage for exactly 7.16 days (169.5 hours). During the drying stage, the only boundary condition applied was a seepage face at the base of the caisson. All other boundaries not mentioned above were specified as no flow boundaries.

13.5.4 Modelling parameters

The soil water retention parameters used in this example take the van Genuchten-Mualem form (see Chapter 2 Section 2.10) and are summarised in Table 13.3 along with other model inputs. Water and porous media compressibilities are assumed to be zero (Forsyth et al., 1995).

Table 13.3 – Caisson benchmark exercise model input parameters

Domain Properties	
Caisson size	3 m x 6 m
Mesh elements	200 (0.3 m x 0.3 m)
Material Properties	
SWRC	van Genuchten-Mualem form
HCF	In-built van Genuchten estimation
Parameter α	0.0143
Parameter n	1.5060
Saturated water content	0.33
Residual water content	0.0008
Saturated hydraulic conductivity	0.254016 m/day
Thermal properties	
Volumetric heat capacity	1,875 kJ/m³/°C
Thermal conductivity	138 kJ/days/m/°C
Initial temperature distribution	Uniform spatial function of 10°C
Solver properties	
Time settings	30 steps during wetting, 100 during drying
Adaptive time setting	Max change in pressure head allowed was 2.5%
Max number of iterations	500

13.5.5 Results and outcomes

Figure 13.10 shows the results obtained from Vadose/W compared to those from Hydrus for the wetting phase of the caisson exercise. The figure shows that the wetting front progresses faster through the caisson in the Vadose/W model than in the Hydrus model. Figure 13.11 shows that Vadose/W model also appears to dry faster than the Hydrus model. These results indicate that the Vadose/W model is more responsive to boundary conditions. Figure 13.11 shows that both the Vadose/W and Hydrus models appears to over-estimate the speed of initial drying after 1 day compared to experimental results from Forsyth et al. (1995). After 4 days, Vadose/W provides a closer match to the experimental results than Hydrus, although the profiles of VWC converge over the course of the simulation as the domain approaches the residual moisture content.

The caisson exercise provided a number of useful lessons regarding the process of undertaking hydrological modelling. These are discussed in further in Glendinning et al. (2015) in relation to the ISMART project.

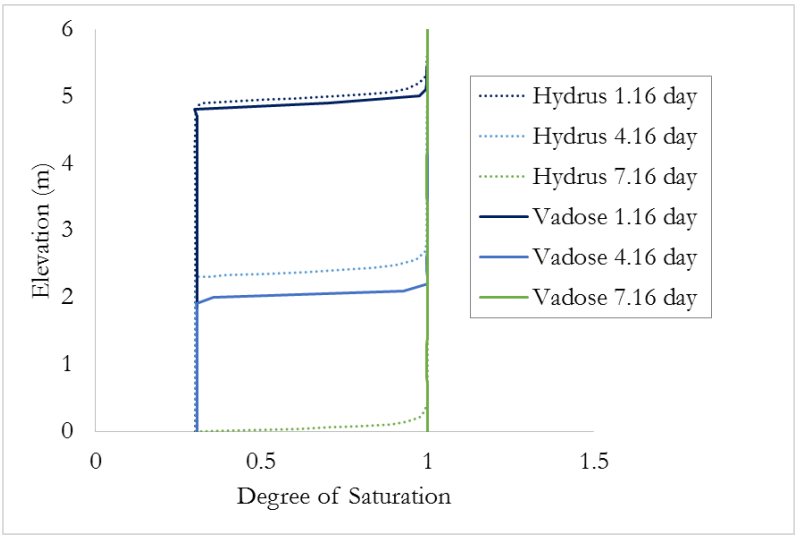

Figure 13.10 - Comparison of Vadose/W and Hydrus simulated water contents during the saturation stage

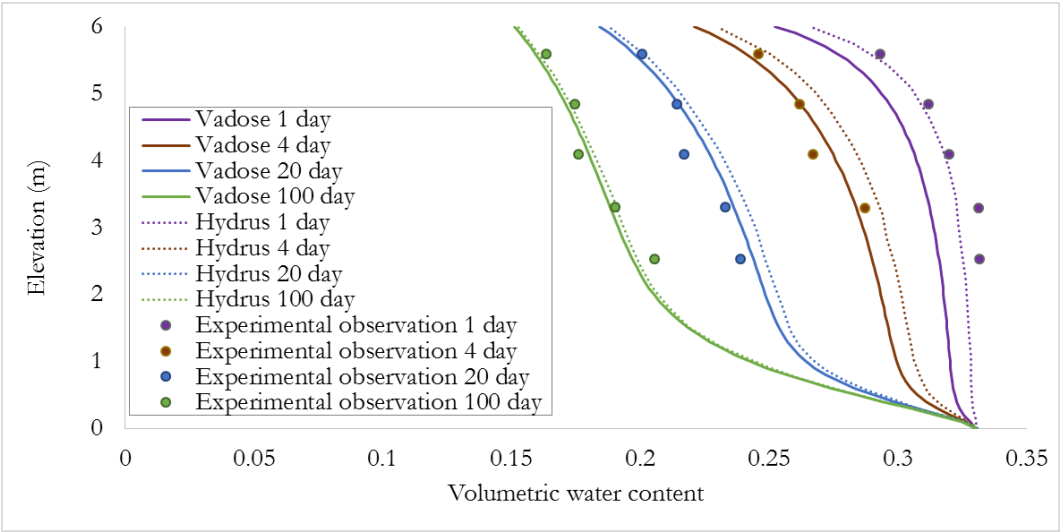

Figure 13.11 – Comparison of Vadose/W and Hydrus simulated water contents during the drainage stage as well as experimental observations from Forsyth et al. (1995)

13.6 Newbury modelling

13.6.1 Field representative model inputs

Table 13.4 shows all the specified input parameters used to construct the field representative model of Newbury cutting.

Table 13.4 – The properties and inputs used within the field representative model of Newbury cutting

Domain Properties	
Size	48 m x 17 m
Mesh elements	1 m global, 0.5 m constrained. (12 elements in 0.6 m surface layers)
Material Properties	
SWRC	Taken from drying London clay data Croney (1977)
Air entry value	20 kPa
Parameter n	1.17
Saturated water content	0.47
Residual water content	0.1
HCF	In-built van Genuchten estimation
Saturated hydraulic conductivities:	
Surface Clay (0 - 0.4m)	2.4×10^{-7} m/s (Briggs et al., 2012)
Sub Surface Clay (0.4-0.6m)	9.3×10^{-8} m/s (Briggs et al., 2012)
Weathered London Clay	5×10^{-8} m/s (Smethurst et al., 2006)
Grey London Clay	3.7×10^{-9} m/s (Smethurst et al., 2006)
Vegetation Properties	
Leaf area index	Vadose grass estimate (GEO-SLOPE, 2008)
Plant moisture limiting	(Feddes et al., 1978)
Root depth function	Grass estimate (0.5 m year round) (GEO-SLOPE, 2008)
Root depth distribution	Triangular
Thermal properties	
Volumetric heat capacity	1,875 kJ/m³/°C (Briggs, 2011)
Thermal conductivity	138 kJ/days/m/°C (Briggs, 2011)
Initial temperature distribution	Spatial function of 10 - 11°C (Briggs, 2011)
Solver properties	
Time settings	1096 time steps (adaptive time stepping used)
Adaptive time setting	Max change in pressure head allowed was 2.5 %
Max number of iterations	500

13.6.2 Initial water table justification using a repeating cycle of weather

To investigate the impact of the initial conditions set within the field representative model of Newbury cutting, a simulation was carried out in which one year of weather data (2006) was repeatedly applied as the climate boundary condition. An unrealistic initial condition would cause the simulated results to vary over time until the model eventually reaches a steady state which is no longer influenced by the initial condition. Figure 13.12 shows simulated volumetric water content at location A (0.3 m depth) within the field representative model of Newbury cutting. The figure shows that no initial delay occurs before the model starts to respond to the climate data. This indicates that the initial conditions set within the field representative model are not influencing the results obtained from the simulations discussed in Chapter 4 in an unrealistic manner.

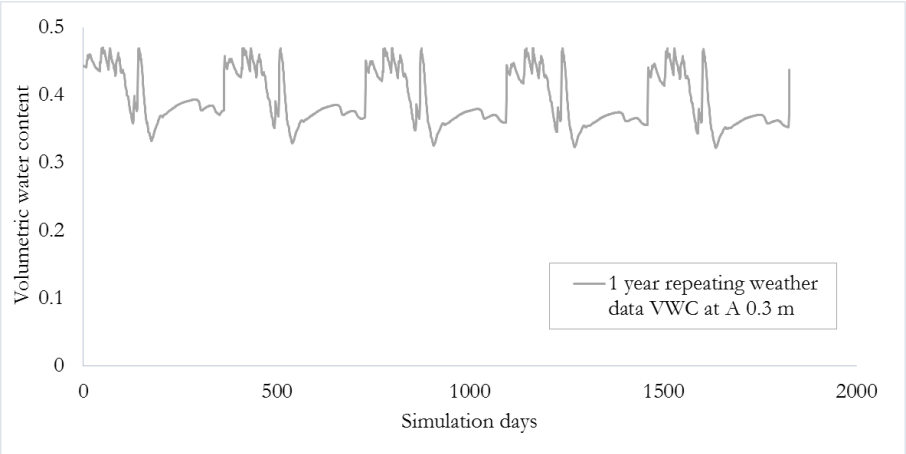

Figure 13.12 - Simulated volumetric water content at location A (0.3 m depth) within the field representative model of Newbury cutting in response to one year (365 days) of climate data (2006) repeated five times

13.7 Further sensitivity analyses

13.7.1 The influence of root depth

The root water uptake function in Vadose/W removes transpired water from within the root zone (Section 3.7). This differs from the soil moisture deficit 1D model which considers both evaporation and transpiration as one function applied at the soil surface (Equation 25). Therefore within the Vadose/W model it would be expected that increasing the root depth would result in changes in VWC occurring over a wider range of depth below the surface, as the depth over which transpiration occurs is increased.

Figure 13.13 shows the effects of varying root depth on soil moisture deficit calculated from three different Vadose/W models with differing root depths along with SMD_{1D}. Increasing the root depth from 0.8 m to 3 m results in a decrease in maximum soil moisture deficit generated. This is because SMD from the Vadose/W models is only calculated from VWC change in the top 0.8 m whereas the total VWC change during the summer of 2006 is distributed over the entire root zone in the 3 m root depth Vadose/W model. Soil moisture deficit is also less for the 0.2 m root depth model, as the entirety of the evapotranspiration is occurring near the surface and the average volume of water in the top 0.8 m is not reduced by as much as within 0.8 and 3 m root depth models.

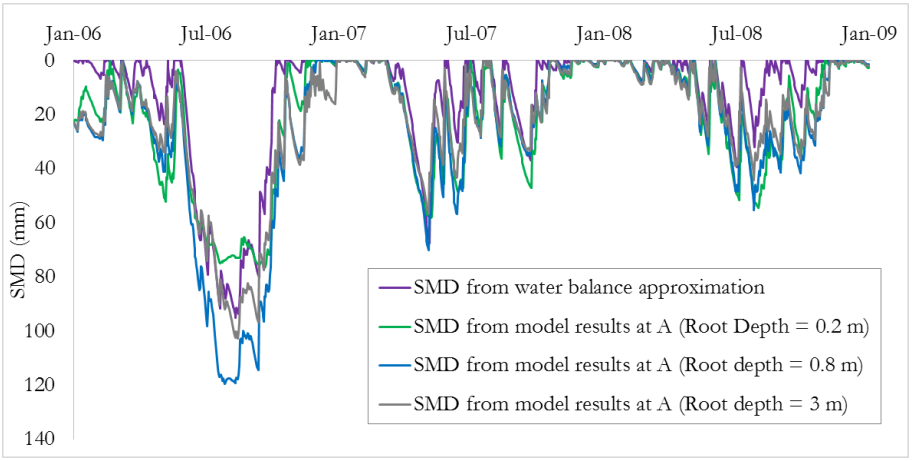

Figure 13.13 – Soil moisture deficit calculated from three different Vadose/W models, each with a different root depth, and from a 1D water balance equation

Figure 13.14 shows the impact of root depth on the minimum PWP depth profile envelopes calculated within the sensitivity Vadose/W models with root depths between 0.2 and 3 m. Using a small root depth (e.g. 0.2 m) generates a narrow band of very high suctions during the dry summer of 2006 (the driest period in the simulation) while using 3 m generates deeper suctions below 1 m depth.

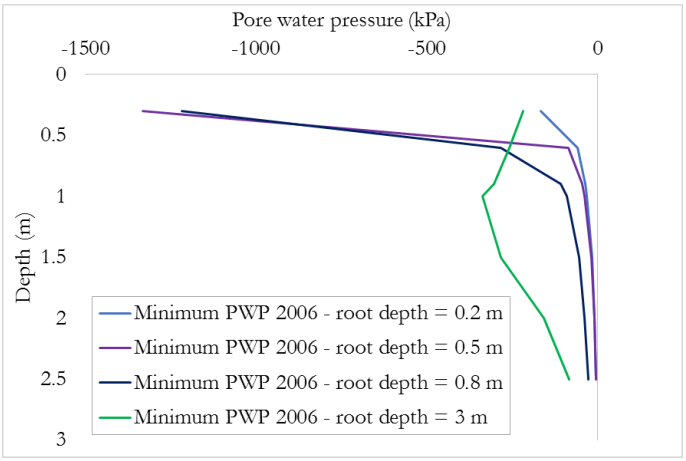

Figure 13.14 – Minimum pore water pressure depth profile envelopes at location A during 2006 calculated from four Vadose/W models each with a different root depth

The effect of the root water uptake function on PWPs within Vadose/W in the root zone is also observable from contour plots of the spatial variation of pore water pressure within the domain (Figure 13.15 & Figure 13.16). For the field representative base model with a root depth of 0.5 m no suctions are present after the winter wetting period of 2006/07. However for a Vadose/W model with root depth = 3 m (which corresponds to the root depth of mature trees), suctions are maintained throughout the winter at depth below the surface, although noticeably only within the lower permeability London clay zone and not at the top the slope.

The results from this root depth sensitivity analysis are in agreement with the findings for embankments of Briggs & Smethurst (2013) and Briggs et al. (2016). As transpiration from the root zone occurs spatially separate from surface evaporation and rainfall infiltration, vegetation with deep root systems can develop soil suctions at depth, which can be maintained throughout periods of wet winter weather. The magnitudes of these tree induced soil suctions (> 90kPa) are sufficient to significantly increase the effective stresses within a slope, and hence improve its stability (Briggs et al., 2016).

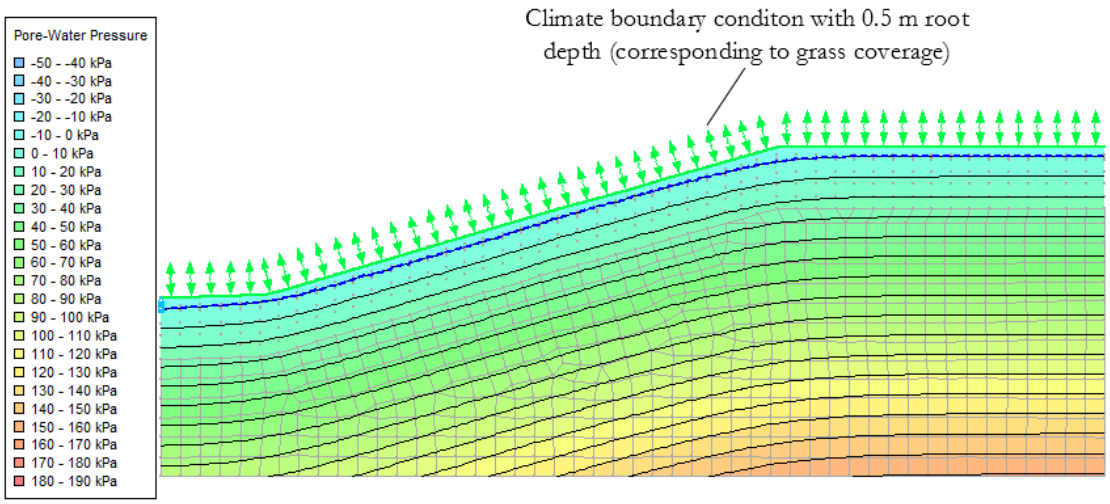

Figure 13.15 – Contour plot of the model domain of the field representative base model with root depth = 0.5 m at the end of the winter of 2006/07 (07/03/2007)

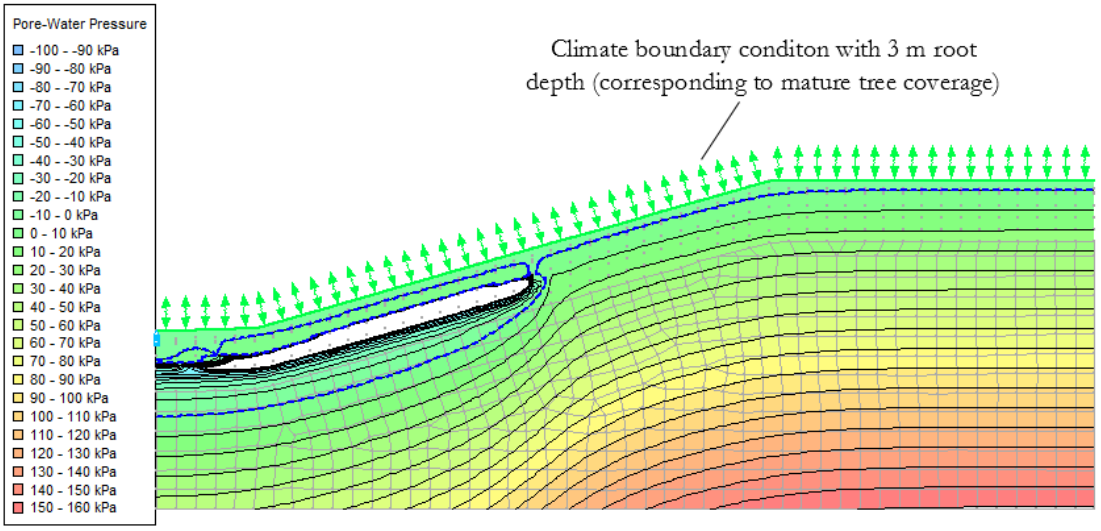

Figure 13.16 - Contour plot of the model domain of a Vadose/W model with root depth = 3 m at the end of the winter of 2006/07 (07/03/2007) (white zones indicate regions of high suctions (above -100 kPa))

13.7.2 The influence of leaf area index

As discussed in Chapter 3, the leaf area index (LAI) function defines the proportion of solar energy divided between evaporation and transpiration. Figure 13.17 shows that a variable LAI function can be defined. To investigate the impact of different LAIs on hydrological conditions within the model, indexes equal to 2.7 and 0.1 representing the extreme cases of uniform 95% transpiration and uniform 95% evaporation were modelled (Equation 35)

(Ritchie, 1972), along with a Vadose/W estimate of the LAI function corresponding to 'excellent' quality grass (GEO-SLOPE, 2008).

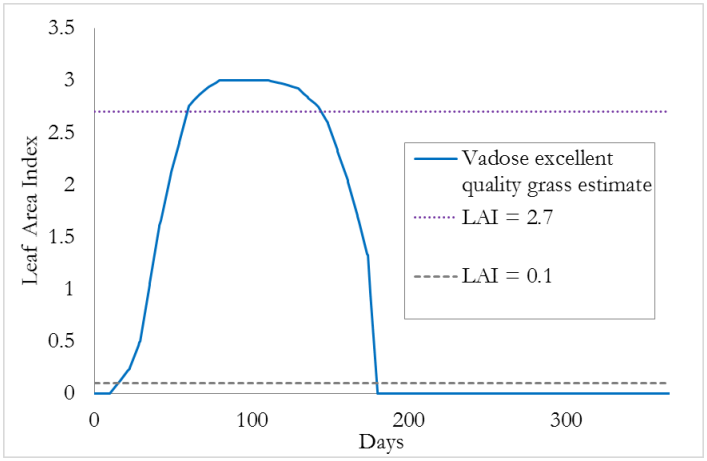

Figure 13.17 –The different leaf area index functions used within three Vadose/W (estimated grass LAI from (GEO-SLOPE, 2008))

Figure 13.18 shows the temporal variation of PWP at 1 m depth for three different Vadose/W models each with a different LAI (constant LAI of 2.7, constant LAI of 0.1 and grass estimation LAI). Throughout the modelling duration, the LAI = 2.7 model appears to match the field results well, especially during dry periods. The LAI = 0.1 model appears to underestimate suctions during the summer months, whilst the LAI grass estimate appears to take longer to rewet after the summer of 2006.

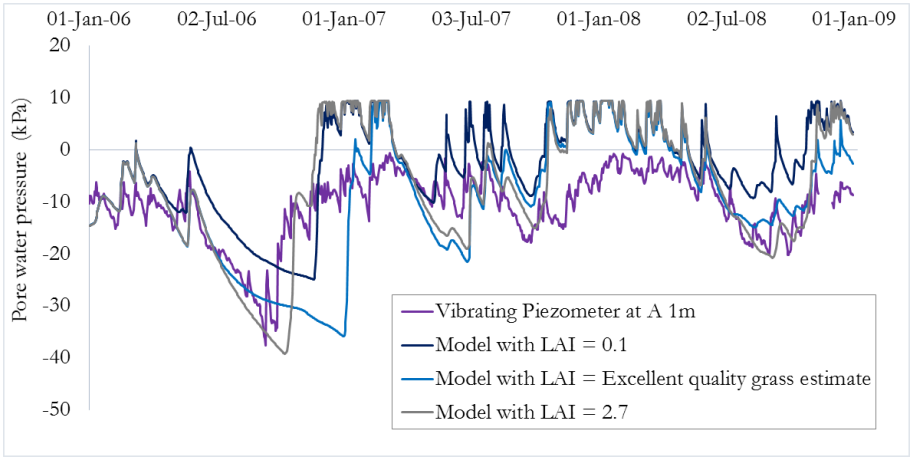

Figure 13.18 – Pore water pressure at A 1 m depth calculated for three Vadose/W models each with a different leaf area index function and field measured pore water pressure from a piezometer (Smethurst et al., 2012)

This behaviour is replicated in plots of soil moisture deficit over the model duration (Figure 13.19). The LAI = 2.7 model is much closer to SMD_{1D} in the dry summer of 2006 but the

LAI = 0.1 model is slightly closer in the other years. This may be because all the solar energy is assigned to evaporation in the LAI = 0.1 model (see Chapter 3), which has the impact that any drying from transpiration within the root zone is not taken into account. So if evaporation is reduced when the near-surface zone is desaturated, not a lot of total evapotranspiration will take place and the resulting change in VWC will be less. The LAI = 0.1 model and grass estimate model may rewet slower due to high rates of evaporation reducing infiltration in the autumn months.

The definition of leaf area index therefore has a large effect on the near surface hydrology of the modelled slope which reflects the very significant impacts of vegetation on slope hydrology in general.

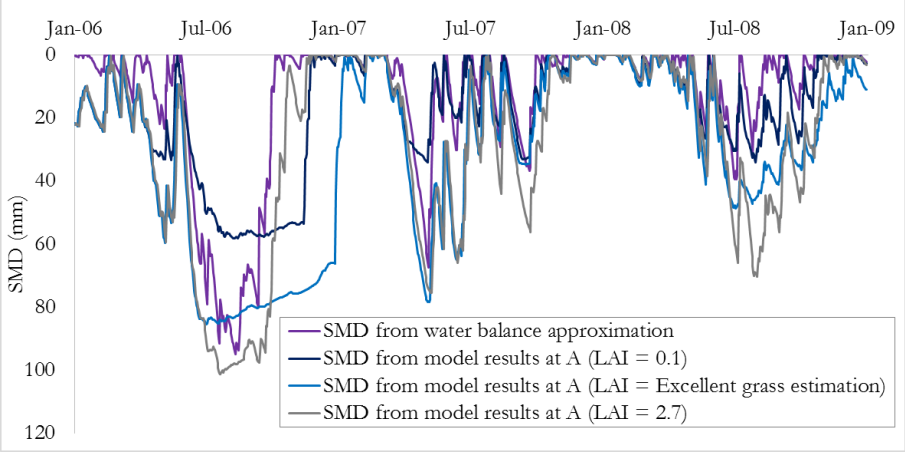

Figure 13.19 – Soil moisture deficit from three Vadose/W models each with a different leaf area index and from a water balance equation

13.7.3 Conclusions

From these sensitivity analyses it was observed that vegetation properties (root depth and leaf area index), which dictate the degree of evaporation and transpiration occurring in the near-surface zone, are very influential on calculated PWPs. Increasing the root depth can lead to suctions being maintained at depth throughout the winter months, whilst decreasing root depth leads to high suctions in the very near-surface zone. Changing the leaf area index function also has a considerable influence on the quantity of water removed from the root zone by evapotranspiration. Therefore, vegetation must be taken into consideration when examining slope hydrological behaviour and subsequent stability.